

**Advances in  
Time-of-Flight Secondary Ion Mass  
Spectrometry  
for the Analysis of Single Cells on  
Sub-Cellular Scale**

**A thesis submitted to The University of Manchester for the degree of  
Doctor of Philosophy in the Faculty of Engineering and Physical  
Sciences**

**2010**

**Sadia Rabbani**

**School of Chemical Engineering and Analytical Science**

# Contents

Abstract	5
Declaration	6
Copyright Statement	6
List of Abbreviations	7
Acknowledgements	9
<b>Chapter 1: Overview of Secondary Ion Mass Spectrometry</b>	
1.1 Introduction	10
1.2 Fundamental Principles of SIMS	15
1.2.1 Secondary Ion formation	16
1.2.1.1 Sputtering	16
1.2.1.2 Ionisation	17
1.2.2 The Basic Equation	18
1.3 History of SIMS	19
1.4 Dynamic SIMS/Depth Profiling	21
1.5 Static SIMS	22
1.6 Imaging SIMS	23
1.7 Development of new sources	24
1.7.1 Development of cluster sources	26
1.7.2 Development of polyatomic sources	28
1.7.3 Damage cross-section and secondary ion formation efficiency	31
1.8 Simulation studies	36
1.9 AIMS	40
References	42

## **Chapter 2: Development and Properties of the**

### ***J105 3D Chemical Imager***

2.1 Limitations of conventional ToF-SIMS instruments	52
2.1.1 Sensitivity	52
2.1.2 Duty Cycle	60
2.1.3 Mass Resolution	61
2.2 Concept and features of the <i>J105 3D Chemical Imager</i>	63
References	81

## **Chapter 3: Characterisation of the *J105 3D Chemical Imager***

3.1 Introduction	85
3.2 Comparison between the <i>J105</i> and the BioToF	86
3.2.1 Experimental	86
3.2.2 Results and Discussion	87
3.2.3 Conclusion	98
3.3 Tandem MS	99
3.3.1 Experimental	103
3.3.2 Results and Discussion	104
3.3.3 Conclusion	115
3.4 Limit of detection	116
3.5 Summary	120
References	121

## **Chapter 4: Molecular depth profiling using ToF-SIMS**

4.1 Introduction	124
4.2 Dept profile of Polycaprolactone	133
4.2.1 Experimental	136
4.2.2 Results and Discussion	136
4.2.3 Conclusion	141

4.3 Depth Profile of standard samples using dc $C_{60}^+$ primary ion on the J105 <i>3D Chemical Imager</i>	142
4.3.1 Experimental	143
4.3.2 Results and Discussion	144
4.3.3 Conclusion	146
4.4 Summary	147
References	148
<b>Chapter 5: Sub-cellular imaging of cells using ToF-SIMS</b>	
5.1 Introduction	152
5.2 Imaging of single cell using SIMS	158
5.2.1 Imaging of cells using Dynamic SIMS	158
5.2.2 Imaging of cells using Static SIMS	164
5.2.3 3D sub-cellular imaging of cells using SIMS	170
5.3 Sample preparation	178
5.4 Analysis of a standard cell line, HeLa using ToF-SIMS	183
5.4.1 Experimental	185
5.4.1.1 Cell Culturing	185
5.4.1.1.1 Thawing the cells	185
5.4.1.1.2 Sub-culturing (passaging) and Freezing the cells	186
5.4.1.2 ToF-SIMS analysis of cells	186
5.4.2 Results and Discussion	190
5.4.2.1 2D analysis	190
5.4.2.2 3 D analysis	198
5.4.3 Data analysis tools	208
5.4.3 Conclusion	212
5.5 Summary	213
References	214
<b>Chapter 6: Overall Conclusions and Future Work</b>	222

## The University of Manchester

**ABSTRACT OF THESIS** submitted by Sadia Rabbani

**For the degree of** Doctor of Philosophy

**Titled** Advances in Time-of-Flight Secondary Ion Mass Spectrometry for the Analysis of Single Cells on Sub-Cellular Scale

**Date of submission** 25/11/2010

Time-of-flight secondary ion mass spectrometry (ToF-SIMS) is becoming a promising technique in analysis of a biological system due to its chemical specificity and the ability to perform high spatial resolution imaging. The combination of novel cluster and polyatomic beams has allowed generating images to map the distribution of biological components in tissue sections and cell surfaces. However, under these conditions the cluster beams have to be operated in the static regime, which limits sensitivity and confines the molecular imaging to 2  $\mu\text{m}$  spatial resolution. The polyatomic beams offer the benefits of high yields and low sub-surface damage, allowing the analysis to be performed at high ion fluence and abandoning the static limit. This presents a new approach to molecular imaging in which ‘voxels’ are used rather than pixels, thus increasing sensitivity. As a result, the current SIMS instrumentation then becomes a limitation and has to be modified.

A novel SIMS instrument, the **J105 3D Chemical Imager** has been developed with Ionoptika, which allows taking full advantage of the polyatomic primary beam, particularly the  $\text{C}_{60}$  by using it in a dc mode with buncher-ToF configuration. The aim of this project was to prove the concept and the potential of this new instrument.

Initially standard organic samples have been used to show the current performance of the J105 for the analysis of organic samples with respect to a conventional ToF-SIMS instrument, the BioToF. The tandem MS capability of the instrument has been tested and proved using standard samples and a lipid mixture of brain extract.

HeLa cells, an immortalised cell line were analysed using this instrument in 2D and 3D imaging mode. The images generated show molecular localisation on a sub-cellular scale, over a practical timeframe, whilst sustaining high mass resolution at 4000. The cells were imaged using a 40 keV  $\text{C}_{60}^+$  dc beam and a clear differentiation between the material within the nuclei and lipid membrane can be made. Investigation of cell preparation suggested that the frozen-hydrated approach may be beneficial.

The data presented in this thesis validates the new instrument concept offering the advantages of higher mass detection, increase in sensitivity, and an increase in the duty cycle while at the same time allowing imaging at sub-cellular scale with higher mass resolution.

## Declaration

No portion of the work referred to in the thesis has been submitted in support of an application for another degree or qualification of this or any other university or other institute of learning

## Copyright Statement

**i.** The author of this thesis (including any appendices and/or schedules to this thesis) owns certain copyright or related rights in it (the “Copyright”) and s/he has given The University of Manchester certain rights to use such Copyright, including for administrative purposes.

**ii.** Copies of this thesis, either in full or in extracts and whether in hard or electronic copy, may be made **only** in accordance with the Copyright, Designs and Patents Act 1988 (as amended) and regulations issued under it or, where appropriate, in accordance with licensing agreements which the University has from time to time. This page must form part of any such copies made.

**iii.** The ownership of certain Copyright, patents, designs, trade marks and other intellectual property (the “Intellectual Property”) and any reproductions of copyright works in the thesis, for example graphs and tables (“Reproductions”), which may be described in this thesis, may not be owned by the author and may be owned by third parties. Such Intellectual Property and Reproductions cannot and must not be made available for use without the prior written permission of the owner(s) of the relevant Intellectual Property and/or Reproductions.

**iv.** Further information on the conditions under which disclosure, publication and commercialisation of this thesis, the Copyright and any Intellectual Property and/or Reproductions described in it may take place is available from the Head of School of Chemical Engineering and Analytical Sciences.

## List of Abbreviation

2,5-DHB	2,5-dihydroxybenzoic acid
BioToF	biological time of flight
BNCT	boron neutron capture therapy
BPA-F	<i>p</i> -boronophenylalanine
BrdU	bromodeoxyuridine
BSH	sodium borocaptate
CAD	collision activated dissociation
CID	collision induced dissociation
DAG	diacylglyceride
DCP-AES	direct current plasma-atomic emission spectroscopy
DHBA	dihydroxybenzoic acid
DMEM	Dulbecco's modified eagle medium
DMSO	dimethyl sulfoxide
DNA	deoxyribonucleic acid
DPPC	dipalmitoylphosphatidylcholine
ESA	electrostatic analyser
ESI	electrospray ionization
FAB	fast atom bombardment
FBS	fetal bovine serum
GC	gas chromatography
GGYR	Glycine-Glycine-Tyrosine-Arginine
HeLa	Henrietta Lacks
HEPES	4-(2-hydroxyethyl)-1-piperazineethanesulfonic acid
ICP-AES	inductively coupled plasma-atomic emission spectroscopy
LB	Langmuir-Blodgett
LC	liquid chromatography
LMIS	liquid metal ion sources
LN <sub>2</sub>	liquid nitrogen
LoD	limit of detection

LSCM	confocal laser scanning microscope
MAF	maximum autocorrelation factor
MALDI	matrix-assisted laser desorption
mc	maximum counts per pixel
ME	matrix enhanced
MIMS	multi-isotope imaging mass spectrometry
MS	mass spectrometry
MSI	mass spectrometry imaging
NPL	National Physical Laboratory
NRK	normal rat kidney
PBS	phosphate buffer saline
PC	phosphatidylcholine/phosphocholine
PCA	principal components analysis
PCL	polycaprolactone
PDMS	polydimethylsiloxane
PE	phosphatidylethanolamine
PET	polyethylene terephthalate
PI	phosphatidylinositol
PMMA	poly (methyl methacrylate)
POPC	palmitoyl-2-oleoyl-sn-glycero-3-phosphocholine
PS	phosphatidylserine
PSD	post source decay
RNA	ribonucleic acid
SAC	surface analysis chamber
SEM	secondary electron microscopy
SIMS	secondary ion mass spectrometry
SM	sphingomyelin
SNMS	secondary neutral mass spectrometry
TEM	transmission electron microscopy
ToF	time-of-flight
TPL	total phospholipids

## **Acknowledgement**

Firstly, I would like to express my warm and sincere thanks to my supervisors Dr. Nick Lockyer and Prof John C. Vickerman for giving me the opportunity to undertake this work as well as providing the training, facilities, input and personal support. I would also like to acknowledge Dr John Fletcher for the immense guidance, advice and contribution from the very early stages of this research, which have been vital to accomplishing this project. I am very grateful to all those who devoted their time reading this thesis and providing critical comments.

I would also like to thank previous and present SARC members particularly, Dr. Alex Henderson, Dr. A. Piwovar, Dr. Jeanette Kordys and Hua Tian for extensive discussion around my work and great friendship. I am also very grateful to my friend, Misbah Nareen for using her precious time to read this thesis and give good feedback and valuable advice.

I wish to thank Paul Blenkinsopp and Rowland Hill from Ionoptika Ltd and Steve Thompson from SAI Ltd for providing an insight into the instrumentation and stimulating discussion over a drink. I am also grateful to Dr D. Jackson and Prof S. High for providing the cells and Dr Chi W Tang for training in cell culture.

Last but not least, I would like to thank my family for their great support and prayers without which I would not have finished this project. I would also like to thank my husband Mr S. Akram for his help, endless support and love.

This thesis is dedicated to my late granddad Mr G. Rasul and my dad Mr G. Rabbani.

# 1. Overview of Secondary Ion Mass Spectrometry

## 1.1 Introduction

Complexity associated with chemical and structural properties of biological samples, particularly tissues and cells have presented many analytical measurement challenges for a biologist. Microscopy has so far been the most powerful tool in history in helping to understand the physiological processes taking place within a biological system. Images of the distribution of biological components have been possible by using fluorescent tags in combination with antibodies to the molecules of interest. However, the limitations associated with microscopy are that it provides no chemical information and the use of fluorescent tags can alter the chemical and physical properties of the labelled molecule thereby altering its intercellular distribution. Furthermore, to make the molecules of interest visible, immunofluorescent imaging techniques require a use of antibodies that are not always accessible.

More recently in the past few decades mass spectrometry (MS) has evolved as a promising technique for characterisation of molecules. MS when combined with imaging can provide molecular information from solid surfaces as well as images of the distribution of atoms and molecules at different spatial resolution. Localisation of biologically relevant compounds in cells and tissues at the sub-cellular scale is of prime importance to understand biological pathways, the mechanisms of disease and the effect of drug molecules. The MS techniques offer many advantages over microscopy such as extremely low detection limits, identification of compounds based on their molecular weight and fragments and, spatial as well as chemical information. In addition to this,

no labelling is required thus minimising modifications to the molecules of interest inside the cell. For these reasons, there is a great interest in developing and expanding the field of mass spectrometry imaging (MSI). A number of reviews on MSI have been published which provide a comprehensive overview on the methods available along with their applications [McDonnell *et al.*, 2007], [Zimmerman *et al.*, 2008] [Chughtai *et al.*, 2010]. The two most common methods that lie at the heart of MSI are matrix-assisted laser desorption ionisation (MALDI) and secondary ion mass spectrometry (SIMS), discussed below.

Figure 1.1 illustrates the MALDI-MSI technique. It was first established by the work of Caprioli and co-workers in 1997 where they analysed peptides and proteins from tissue sections using a matrix dihydroxybenzoic acid (DHBA) [Caprioli *et al.*, 1997]. The technique has rapidly developed into a huge success due to the high sensitivity and wide range of biomolecules that can be detected particularly proteins, peptides and drugs within tissues and cells [Chughtai *et al.*, 2010]. The analysis of tissue sections using MALDI-MSI has allowed the identification of biomarkers for cancer [Chaurand *et al.*, 2004] [Schwartz *et al.*, 2004] as well as Alzheimer [Stoeckli *et al.*, 2002], and Parkinson's diseases [Pierson *et al.*, 2004]. Within the pharmaceutical industry, it has been used to identify a range of pharmaceutical compounds [Earnshaw *et al.*, 2010] as well as their distribution within tissue sections [Reyzer *et al.*, 2003], [Hsieh *et al.*, 2006]. MALDI-MSI has been particularly successful in classifying and mapping the lipids within mouse tissue sections, Figure 1.2 [Woods *et al.*, 2006], [Murphy *et al.*, 2009].

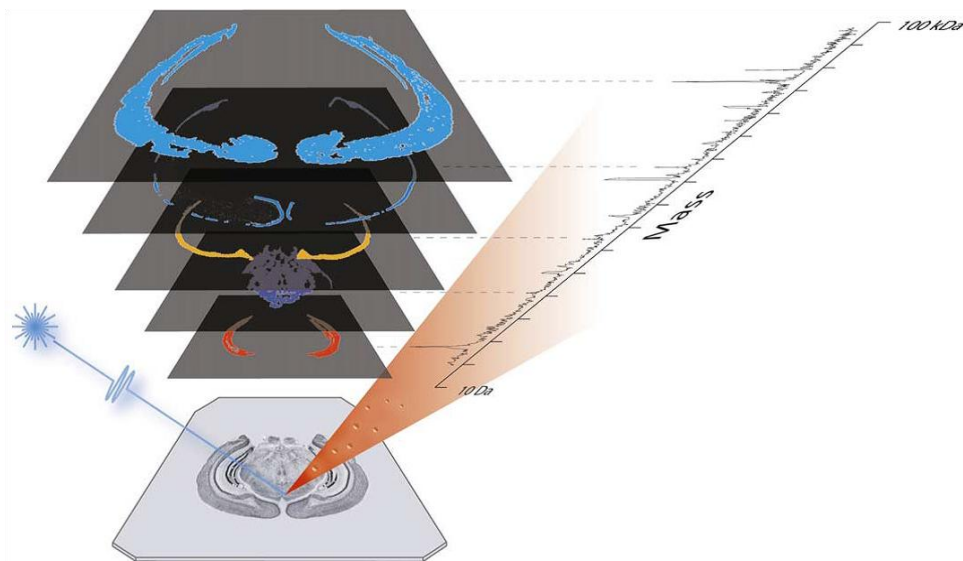


**Figure 1.1** MALDI mass spectrometric imaging. A laser is scanned over a tissue sample while acquiring a complete mass spectrum from each position, resulting in molecular images for multiple analytes. Reproduced from Rohner *et al.* 2005.

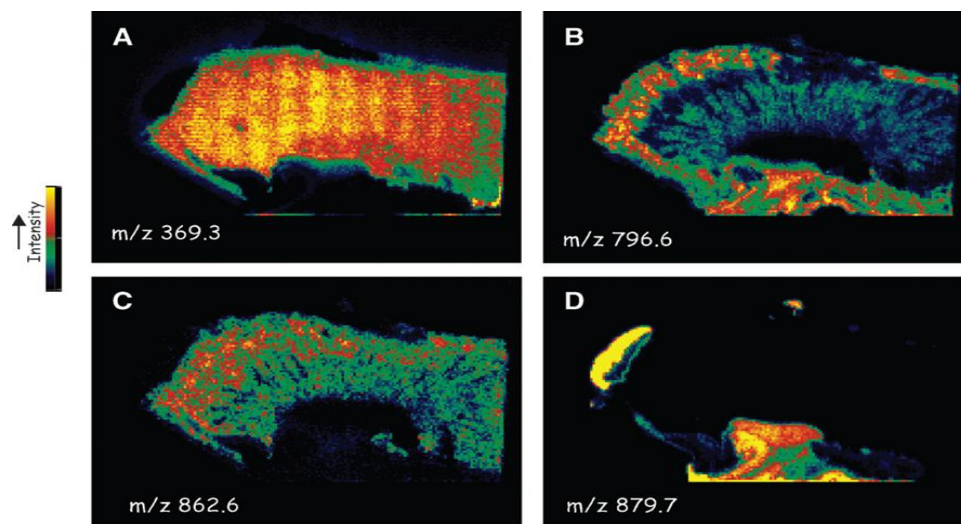


**Figure 1.2** MALDI-MSI ion images from a section of mouse kidney. A:  $m/z$  369.3,  $[M+H-H_2O]^+$ , cholesterol. B:  $m/z$  796.6  $[16:0a/18:2-PC+K]^+$ . C:  $m/z$  862.6  $[40:6-PC+H]^+$ . D:  $m/z$  879.7  $[16:0/20:4/18:1-TAG+H]^+$ . Reproduced from Murphy *et al.* 2009.

A recent success in this field has been the ability of this technique to monitor and identify the molecular changes occurring in tumour tissues when compared to healthy biopsies [Oppenheimer, 2010], [Kang *et al.*, 2010]. These studies show that MALDI-MSI has become a critical tool in the analysis of proteomics, lipidomics and pharmacokinetics and will continue to be an important analytical tool in life science.

The second method, imaging secondary ion mass spectrometry (SIMS) also allows mapping the distribution of biological components within biological systems on surface and sub-surface region at sub-micron resolution. This technique is also being widely recognised, due to the advances in instrumentation and the understanding of fundamental principles associated with it. Imaging SIMS offers the advantages of identifying low molecular weight species at a very high spatial resolution <100 nm along with high selectivity and sensitivity [Zimmerman *et al.*, 2008], [Chughtai *et al.*, 2010]. Both of these techniques, MALDI and SIMS are performed in high vacuum systems and require special sample preparation prior to analysis, which will be discussed at many points in this thesis.

MALDI and SIMS are complementary techniques but SIMS allows imaging experiments to be performed at higher spatial resolution (0-5  $\mu\text{m}$ ) with minimal sample preparation requirements. In MALDI, a matrix is required to ionise and desorb the molecules following an impact with a laser. Hence, selecting and depositing the matrix can prove to complicate the sample preparation procedure and further limits the spatial resolution to 30-50  $\mu\text{m}$ . Although this spatial resolution is adequate for providing spatial distribution of lipids and proteins within a tissue, it is insufficient for analysis of a single cell, since a diameter of an average animal cell is around 20-30  $\mu\text{m}$

[Hammond., 2010], [Solon *et al.*, 2009], [Luxembourg *et al.*, 2003]. A comparison between the two techniques, MALDI and SIMS is shown in Table 1.1.

**Table 1.1.** Comparison of MALDI and ToF-SIMS capabilities. Reproduced from Hammond, 2010.

<b>Capability</b>	<b>MALDI</b>	<b>SIMS</b>
Incident probe	Focused laser	Focused cluster ion gun
Practical mass range (Da)	>100,000	<2,000
Spatial resolution, organics ( $\mu\text{m}$ )	30–50	0–5
Mass resolution ( $M / \Delta m$ )	~10,000	~15,000
Sampling depth ( $\mu\text{m}$ )	1	<1
3-D imaging	Yes, multiple sections	Yes, $\text{C}_{60}^+$ sputtering
Molecular spectral library	Extensive	Very limited
Usual imaging approach	Stage mapping	Scanned ion gun and stage mapping

The aim of this project was to develop the technique, ToF-SIMS for the analysis of a single cell, hence, only this technique will be explained in the remaining chapters. The rest of this chapter will concentrate on the fundamental principles of SIMS and how this technique has developed over the years with reference to some relevant applications.

## 1.2 Fundamental Principles of SIMS

SIMS is a well established surface analysis technique that provides detailed chemical information about the uppermost layer of a sample as well as with depth below the initial surface under certain experimental arrangements [Vickerman *et al.*, 2001]. The basic process underlying SIMS involves bombarding a solid surface in high vacuum with a high energy (keV) primary ion beam, which can be of monoatomic, polyatomic or cluster nature. This causes a series of collisions between the primary ions and the atoms of the surface resulting in a transfer of kinetic energy to these atoms. As some of these collisions return back to the surface, the result is an emission of atoms, molecules or their clusters, some of which are ionised as they leave the surface. The ionised particles known as the “secondary ions” are analysed and detected by the mass spectrometry, Figure 1.3. There are two modes of operation, the first is dynamic SIMS, which uses a high primary ion dose to detect elements and small fragments, and the second is static SIMS, which allows the identification of molecular information by using a low primary ion flux.

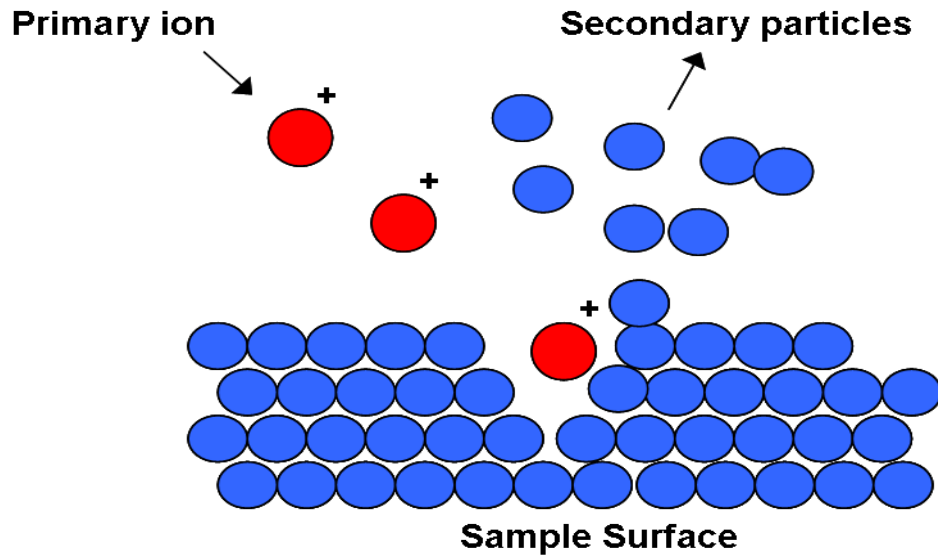


**Figure 1.3** A schematic representation of the SIMS process. Adopted and Reproduced from Vickerman, *et al.* 2001.

### 1.2.1 Secondary Ion formation

There are two processes that are used to describe the formation of a secondary ion following an impact with a primary ion beam. First is the sputtering process in which atoms and multi-atomic clusters are desorbed from the surface; and the second involves ionisation of the sputtered material that becomes charged by gaining or losing electrons.

#### 1.2.1.1 Sputtering

Sigmund's linear cascade theory (1981) has been the most successful model to explain the sputtering event caused by the impact with a monatomic primary ion beam [Sigmund, 1981]. This theory regards atoms of the solids as hard spheres that obey Newtonian mechanics and assumes that sputtering occurs by using the beam at low

current and fluence. Sigmund further classified the sputtering mechanism into a knock-on effect and electronic sputtering, but disregarded the latter since it is only valid for beams with high energies. For the low energy beam (few keV), the theory was developed into elastic collision. In this process, when the primary ion beam impacts a surface it transfers its energy to the atoms of the surface. This results in a series of collision cascading between the atoms of solids within 30 Å of a surface and as some of these collisions return back to the surface secondary particles are emitted, Figure 1.3. The emission of atoms and molecules is only possible if the energy of the beam impacting the surface is high enough to overcome the surface binding energy. This theory matches the experimental results when a medium to high energy (0-10,000 keV) primary ion beam is used to bombard a single component with yields depending on the mass and the energy of a primary particle. However in the case of multi-component system, this model may not be appropriate since the transfer of energy will be directional and not isotropic.

There has been a great effort by Garrison and Winograd to explain and model the sputtering mechanism caused by polyatomic or cluster ion beams through molecular dynamic simulations, explained further in this chapter in section 1.8.

### **1.2.1.2 Ionisation**

Ionisation of sputtered particles depends on the nature of a sample and the technique used. Only a small fraction of sputtered material during SIMS process is ionised and the yield is highly dependent on electronic properties of the matrix known as the matrix effect. Ionisation of metals occurs by swift electronic transitions whereas

organics become ionised by losing or gaining a charged species, typically a proton to form  $[M+H]^+$  or  $[M-H]^-$  ions, but salt adducts of sodium, chlorine and potassium are also commonly detected.

Various models have been developed to describe the ionisation process that occurs during a SIMS experiment. Gerhard and Plog (1983) developed the Nascent ion molecule model, which proposes that rapid electronic transitions occurring in the surface region will neutralise any ions before they can leave the surface. Emission of secondary ions occurs by neutral molecules (nascent ion molecules) undergoing non-adiabatic dissociation as they leave the surface [Gerhard *et al.*, 1983].

The desorption ionisation model was introduced by Cooks and Busch (1983) which suggests that vibrational excitation may be significant in understanding the emission of cluster(s) or molecular ion(s) from organics. This model predicts that desorption and ionisation process can be considered separately. The ions can be formed by desorption followed by two chemical reactions:

- 1) Ion/molecule reactions or electron ionisation can occur on top surface layers.
- 2) In free vacuum, the parent ion may dissociate to produce fragment ions.

### **1.2.2 The Basic Equation**

As explained above, the SIMS technique is based on the analysis of secondary ions with the yields depending on the electronic state of the surface. The relationship between the factors used to determine the number of secondary ions is represented in the SIMS equation [Vickerman, *et al.*, 1997]:

$$I_s^m = I_p Y_m \alpha^+ \theta_m \eta \quad \text{Equation 1.1}$$

Where,

$I_s^m$  = positive secondary ion current of species m

$I_p$  = primary ion flux

$Y_m$  = sputter yield of species m

$\alpha^+$  = ionisation probability of the species m to positive ions

$\theta_m$  = fractional concentration of species m in the surface layer

$\eta$  = transmission of the analysis system

Two important parameters that determine how a sample will behave under SIMS are sputter yield and ionisation probability. The sputter yield is the total yield desorbed from a surface including neutrals and ions per primary ion impact. The yield depends on the nature and topography of a sample as well as the mass, charge, energy and the current of primary ion beam. The primary ion flux is operator dependent and the transmission is generally constant for a particular system [Vickerman, *et al.*, 1997].

### 1.3 History of SIMS

The basic process underlying SIMS was first observed and identified by JJ Thompson (1910) in 1900, when he discovered that by bombarding a metal surface with a primary ion beam causes secondary ions to be emitted. However, it was not until 1949 that the first SIMS instrument was built by Herzog (1949) and Liebl (1963) and commercialised in 1960. These were dynamic SIMS instruments that used a high current primary ion beam to detect elements as a function of depth (also known as depth

profiling). This technique was primarily used in the semiconductor industry to detect very low levels (ppm) of elements within a sample, as well as to characterise the layer structure of devices. Dynamic SIMS developed rapidly in the next two decades and has become an important tool in the semiconductor industry due to its high depth resolution and very low detection limits.

Further instrumental advances led to the development of microscope and microprobe modes [Casting *et al.*, 1962], [Liebl *et al.*, 1967]. These modes allowed the construction of an image from the surface of a sample, explained later in this chapter. These instruments were also dynamic systems that used a high primary ion dose to rapidly erode the upper layer of a sample, making this technique highly destructive and providing no molecular information.

Further modification in the early 1960s by Benninghoven led to this technique to be used as a true surface analysis tool. The group showed that by bombarding a sample with a low primary ion dose, the pristine surface can be maintained. This is because at a very low ion dose the probability of striking a sample twice at the same location is very low. Thus, to ensure the mass spectrum or the image acquired represents an undamaged area of the sample, the ion dose is kept at or below  $1 \times 10^{13}$  ions/cm<sup>2</sup>, known as the ‘static limit’ [Benninghoven, 1970]. The major consequence of using low ion dose is that the information obtained only represents the uppermost layer of a sample with very low secondary ion signals. However, since the sample under analysis is still considered to be in the native state following an impact by the primary ion beam, the concept of ‘Static’ SIMS was developed. The three modes of SIMS, dynamic (depth profiling), static and imaging will be explained in more detail below.

## 1.4 Dynamic SIMS/Depth Profiling

This mode of SIMS involves using a high flux of primary ion beam to remove many monolayers of a sample to determine the concentration of a specific component as a function of depth. The depth profile experiment is performed by rastering a primary ion beam in  $x$  and  $y$  direction over a defined area on the sample surface to create an etch crater. A small area within the crater is selected for analysis in which the secondary ion signal of the species of interest is monitored [Vickerman *et al.*, 2001].

A number of different parameters have to be considered to fully understand this type of analysis as the sputtering rate of various elements in a sample will be different. At first, when sputtering begins the concentration of higher sputtered element will decrease relative to the lower sputter rate element. This suggests that the secondary ion signal of the easily sputtered element will diminish, whereas the signal of a less sputtered element will rise, and when a steady state is reached it represents the concentration of the components in *bulk* sample. Other parameters that also need to be optimised prior to analysis include depth resolution and dynamic range. The depth resolution corresponds to broadening of the measured depth profile with respect to the original concentration. Basically, it is a measurement of a sharp interface between the two species in a sample and is defined as intensity/sputter time curve or concentration/depth curve. It is reported either in  $\Delta Z$  depth on the concentration scale or  $\Delta t$  time difference on the intensity scale and a change in signal is measured over a distance of 84.13% to 15.47% on the profile graph [Honig, 1976], [Hofmann, 2000], [Vickerman *et al.*, 1997]. The dynamic range refers to a range of concentrations that are

examined for an element under analysis and monitored as a function of depth [Von Criegern *et al.*, 1990].

Although dynamic SIMS is mostly used in the semiconductor industry and for characterisation of inorganic compounds, it is now progressing towards analysis of biological species such as cells. This is discussed in more detail in Chapter 5.

## **1.5 Static SIMS**

Static SIMS allows the molecular information to be probed from the uppermost layer of a sample using a low primary ion beam current. As mentioned above this results in low secondary ion signal, and the SIMS community was faced with the challenge of increasing the sensitivity to allow analysis of more complex samples and the detection of low concentration of analytes.

Initial Static SIMS instruments were based on using a quadrupole mass analyser, which has a limited mass range and a low transmission, reducing the amount of information that can be obtained in one analysis. The quadrupole mass analyser has a low transmission as it scans over a given mass range and rejects any ions that do not possess the selective mass to charge ratio, at a given point in the scan. In addition to this since low secondary ion yields are produced during the static SIMS experiment, it is essential to use a sensitive mass analyser that will detect all the ions generated [Van der Wel *et al.*, 1990].

The introduction of the time-of-flight (ToF) mass analyser to SIMS in the late 1980s by Benninghoven (1983) and Chait (1981), led to a significant increase in the sensitivity due to high transmission and wide mass range offered by the analyser. A ToF

analyser separates ions based on the time it takes them to reach a detector, which is directly related to the mass to charge ratio of an ion. ToF mass analysers offered to satisfy almost all the requirements of a surface mass spectrometer. These included detection of all the ions generated, unlimited mass range and a high mass resolution [Benninghoven, 1994]. It was swiftly incorporated into the SIMS instrument and with an increase in the sensitivity by four orders of magnitude [Tang *et al.*, 1988], [Niehuis *et al.*, 1987], [Eccles *et al.*, 1989], it was now possible to analyse diverse sample types including polymers [Wien. 1997], bio-molecules [Luk *et al.*, 2003] and atmospheric aerosols [Peterson *et al.*, 2006].

Further improvements in sensitivity were sought through the development of new primary ion sources, discussed later in this chapter.

## **1.6 Imaging SIMS**

Imaging using SIMS can be performed using either the microscope or the microprobe modes, introduced earlier. First, the microscope mode uses a stigmatic ion optical lens system similar to an optical microscope to generate images following an impact with a defocused primary ion beam over a large area of a sample. The secondary ion optics system allows the spatial distribution of secondary ions to be maintained as they travel through the mass analyser and an image resembling the sample is produced. The spatial resolution is dependent on the instrumental features such as ion optics and mass resolution of the detector, but is independent of the beam diameter [Castaing *et al.*, 1981].

In the microprobe mode, the primary ion beam is focused to a smaller spot size and is scanned across a selected area of analysis in  $x$  and  $y$  directions. 2D images are constructed by summing images that have been collected over a period of time with each pixel containing a full mass spectrum. The spatial resolution is now highly dependent on the spot size of a beam, which should be within the range of pixel size of the analysis area [Liebl *et al.*, 1967]. If the spot size of a primary ion beam is larger than the pixel then it becomes difficult to highlight small features within a sample. Whereas if the spot size is too small there is a possibility of under-sampling and the pixel may not be truly representative of the area under analysis. Thus, to localise small components within a sample such as a cell, highly focused primary ion beam is required but this causes a loss of ion current, resulting in fewer secondary ions per shot and longer acquisition time.

## 1.7 Development of new sources

The SIMS community has long been aware of the fact that an increase in the mass of the primary ion increases the secondary ion yields, thus a shift from  $\text{Ar}^+$  to  $\text{Xe}^+$  [Kötter *et al.*, 1998] was witnessed. At the same time highly focused liquid metal ion sources (LMIS),  $\text{Ga}^+$ ,  $\text{In}^+$  [Ostrowski *et al.*, 2004],  $\text{Au}^+$  [Davies *et al.*, 2003], [Walker *et al.*, 2003] and  $\text{Bi}^+$  [Köllmer., 2004], [Touboul *et al.*, 2005] were developed for microprobe imaging. The  $\text{Ga}^+$  primary ion beam has been used to localise cholesterol in rat kidney tissue section and in leukocytes cells [Nygren *et al.*, 2003], [Nygren *et al.*, 2004] as well as for the analysis of *Paramecium* cells [Colliver *et al.*, 1997], discussed in Chapter 2 and Chapter 5. The  $\text{Au}^+$  ion source has been used for the analysis of

prostate cancer [Gazi *et al.*, 2004], macrophages and galial cells [Parry *et al.*, 2005]. However, even after numerous attempts it was still impossible to produce sub-micron molecular imaging using monoatomic primary ion source under static conditions. This is because when the atomic projectile strikes a sample, it penetrates deep below the surface, resulting in significant fragmentation of sub-surface molecules by breaking intermolecular bonds. Although by using low primary ion flux, the analysis is restricted to the outermost monolayer of the sample, it minimises the decay in the signal and reproducible spectra can be obtained. However, since the sampling depth is limited to the uppermost layer only, it is not possible to obtain in-depth compositional information. Furthermore, with corresponding loss in the sensitivity, the application of static SIMS for dilute compounds in tissue samples has been unfeasible, due to inadequate number of molecules in the surface monolayer to produce constructive images. It has been reported that for organic samples, if the ion dose exceeds the  $1 \times 10^{14}$  ion/cm<sup>2</sup>, the molecular signal will no longer be observed [Gillen *et al.*, 1998].

A non linear enhancement in the secondary ion yields was first observed in 1970 using dimer and trimer primary projectiles to analyse a range of samples [Anderson *et al.*, 1974], [Thompson *et al.*, 1979], [Wittmaack *et al.*, 1979]. Further experiments conducted by Blain and co-workers (1989) investigated the effect of using the cluster (CsI)<sub>n</sub>Cs<sup>+</sup> ion beams. These studied concluded that the secondary ion yield increases with an increase in the mass and the energy of the primary ion beam with higher yields reported for molecular secondary ions compared to atomic ions.

### 1.7.1 Development of cluster sources

At the turn of the century cluster LMIS  $\text{Au}_n^+$  [Davies *et al.*, 2003] and  $\text{Bi}_n^+$  [Köllmer, 2004] were developed for SIMS analysis. These sources quickly replaced the monoatomic,  $\text{Ga}^+$  and  $\text{In}^+$ , offering an increase in the secondary ion yields while retaining their high focusing capability.  $\text{Bi}_3^+$  cluster primary ion source has successfully been used to map the distribution of lipids in rat brain section [Touboul *et al.*, 2005], adipose tissues from chronic kidney biopsies [Sjövall, *et al.*, 2008], skeletal muscle [Magnusson *et al.*, 2008] and liver biopsies [Debois *et al.*, 2009]. The  $\text{Au}_3^+$  cluster beam has been used to determine phospholipids, cholesterol and fatty acids in cardiac tissues [Aranyosiova *et al.*, 2006]. Brunelle and co-workers (2005) used the  $\text{Au}_3^+$  cluster ion to identify three different regions of mouse leg section by localising different classes of lipids [Touboul *et al.*, 2005]. Although the behaviour characteristics of these two beams,  $\text{Au}_n^{n+}$  and  $\text{Bi}_n^{n+}$  are very similar, but  $\text{Bi}_n^{n+}$  offers a small practical advantage in that higher cluster yields are obtained due to high cluster current, Figure 1.4 [Köllmer., 2004].

Although these cluster beams allow high resolution imaging and non-linear increase in the secondary ion yields [Benguerba *et al.*, 1991], particularly at higher molecular mass species with mass up to 1000 detected; they behave very similar to the monoatomic ion sources in terms of sample damage and the analysis has to be performed within the static limit. This theory is supported by the molecular dynamic simulation, which illustrates that when the cluster beam impacts a surface, it breaks into its constituent atoms giving rise to multiple sputtering and an increase in the secondary ions. However, as the atoms still has enough energy, they penetrate and embed in the

sub-surface region of the sample. This generates chemical damage with an increase in the fluence, resulting in a loss of molecular information [Ryan *et al.*, 2007], [Rzeznik *et al.*, 2008]. Therefore, it was still not possible to probe molecular chemistry at sub-surface level using these small cluster projectiles.

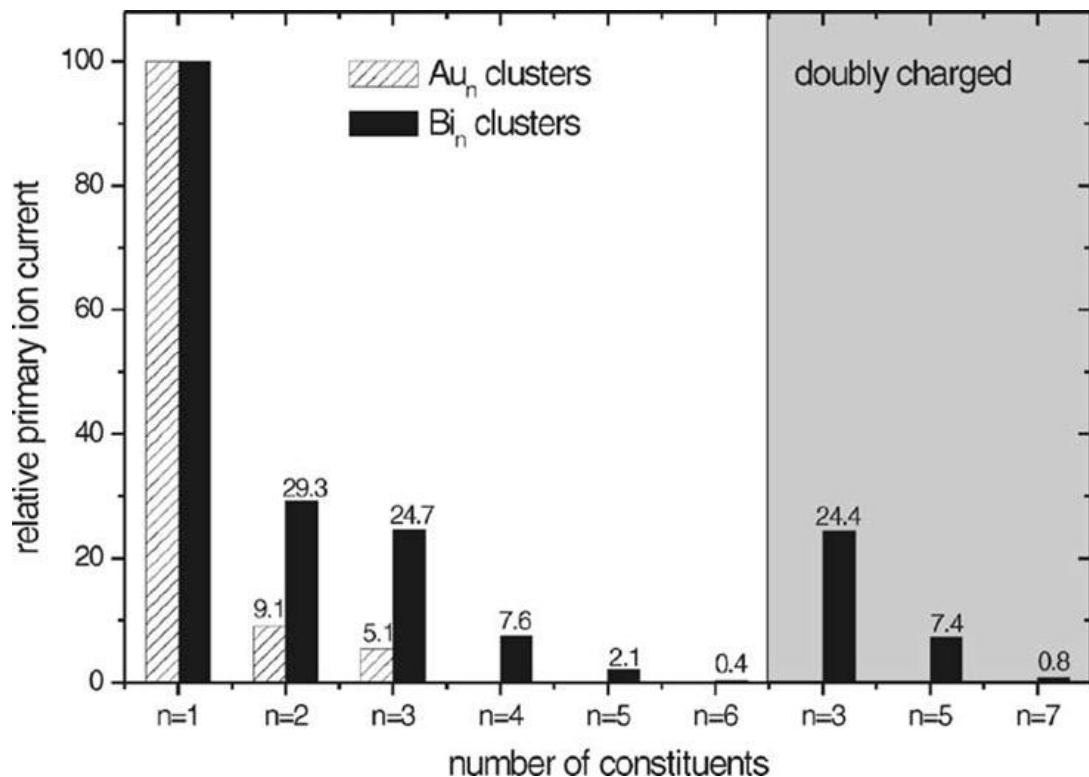


**Figure 1.4** Normalised primary ion currents for Au<sub>n</sub><sup>n+</sup> and Bi<sub>n</sub><sup>n+</sup> clusters as a function of cluster size and charge. Au<sub>1</sub><sup>+</sup> and Bi<sub>1</sub><sup>+</sup> currents are Normalised to 100%. Reproduced from Kollmer, 2004.

### 1.7.2 Development of polyatomic sources

The greatest advance in the field of ToF-SIMS in recent years has been the introduction of polyatomic primary ion beams. Appelhans *et al.* (1989) used a gas cluster source  $\text{SF}_6^0$  to show an enhancement in the secondary ion yields of pharmaceutical compounds to be 9 to 24 times greater than the monoatomic  $\text{Cs}^+$  ion beam. Benninghoven (1998) reported a non-linear increase in the secondary ion formation efficiencies of polymers when using a low energy  $\text{SF}_5^+$  polyatomic beam. Similar effect has also been reported by Gillen and co-workers when they used small carbon and caesium cluster ions [Gillen. 2000], [Gillen *et al.*, 2001].

A substantial increase in the secondary ion yields was observed by using a buckminsterfullerene,  $\text{C}_{60}$  polyatomic primary ion beam. This enhancement was first shown by the Orsay and Texas A & M groups when they carried out a number of experiments to compare the yields for  $\text{Au}_n^+$  cluster ions with large organic molecules,  $\text{C}_{60}^+$  and coronene ( $\text{C}_{24}\text{H}_{12}$ ) [Baudin, *et al.*, 1994], [Le Beyec, *et al.*, 1998], [Jacquet, *et al.*, 2002]. The findings from these experiments concluded that  $\text{Au}_n^+$  produces a non-linear increase in the secondary ion yields for organics samples such as Langmuir-Blodgett (LB) films and phenylalanine, but even higher yields up to 4-5 times more were obtained when  $\text{C}_{60}^+$  and coronene were used. This increase observed has been explained by the trim calculations estimates which show that upon impact, the  $\text{C}_{60}^+$  beam at 20 keV deposits its energy over a distance of 30 Å while the  $\text{Au}_4^+$  cluster of the same energy deposits its energy over a distance of 115 Å. The  $\text{C}_{60}^+$  primary ion beam breaks into its individual atoms and deposit more energy near the surface and produces yields higher than the  $\text{Au}_4$  cluster ion beam [Baudin, *et al.*, 1994]. Further comparison

between the  $C_{60}^+$  polyatomic projectile and monatomic,  $Ga^+$  and  $Cs^+$  on the yields of the molecular ion from phenylalanine was completed by Van Stipdonk (1996) and co-workers. They reported an increase in the secondary ion yields by an order of magnitude higher with the  $C_{60}^+$  than with the  $Cs^+$  and  $Ga^+$ .

Although these experiments were performed in 1990, a practical primary ion gun for SIMS based on a  $C_{60}$  ion source was first developed and commercialised by the Vickerman's group in collaboration with Ionoptika Ltd (Southampton) in 2003 [Weibel *et al.*, 2003], [Wong, *et al.*, 2003], [Hill *et al.*, 2004]. Figure 1.5 compares the yields of polyethylene terephthalate (PET) using three different ion projectiles,  $Au^+$ ,  $Au_3^+$  and  $C_{60}^+$ . It can be clearly seen that the  $C_{60}^+$  produces higher yields for molecular and fragment ions as compared to cluster,  $Au_3^+$  and the monoatomic,  $Au^+$  ion beam [Weibel *et al.*, 2003]. The study completed by Wong *et al.* (2004) showed that by using the  $C_{60}^+$  primary ion beam, molecular ion of Gramicidin A at  $m/z$  1881 can be detected, which is not present in the spectrum when analysed with a  $Ga^+$  ion beam. This study further highlights an increase in the yields by 20-30 times when using the  $C_{60}^+$  ion beam, particularly at higher mass. The Vickerman's group completed a number of experiments to assess the relative benefits of the  $C_{60}^+$  as compared to the monatomic and other cluster ions [Fletcher *et al.*, 2006], [Jones *et al.*, 2006]. The study by Fletcher *et al.* (2006) also investigated the effect of changing the energy of the polyatomic primary ion beam on the secondary ion yields for a range of samples. The investigators showed that with an increase in the impact energy of the primary ion beam increases the secondary ion yields, Figure 1.6.

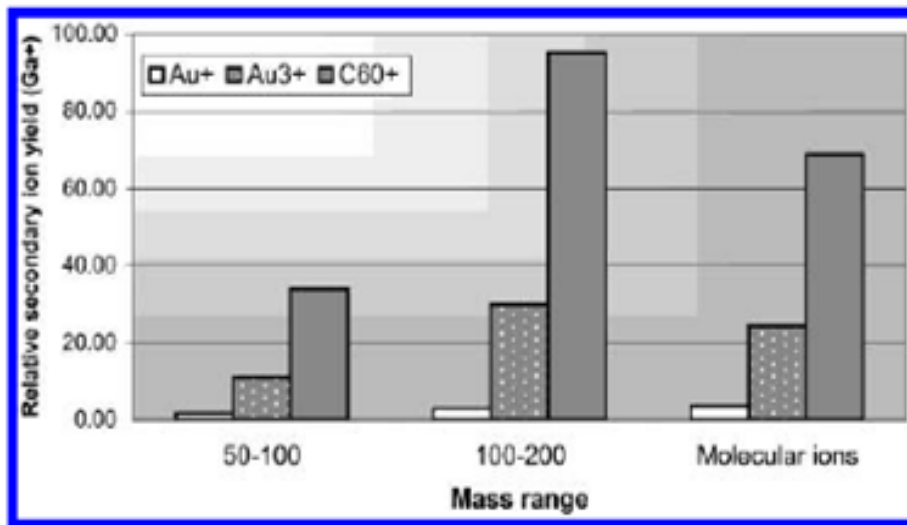


**Figure 1.5** Comparison of positive secondary ion yields during analysis of polyethylene terephthalate (PET) using  $\text{Au}^+$ ,  $\text{Au}_3^+$  and  $\text{C}_{60}^+$  primary ions at 10 keV impact energy. Reproduced from Weibel *et al.* 2003.

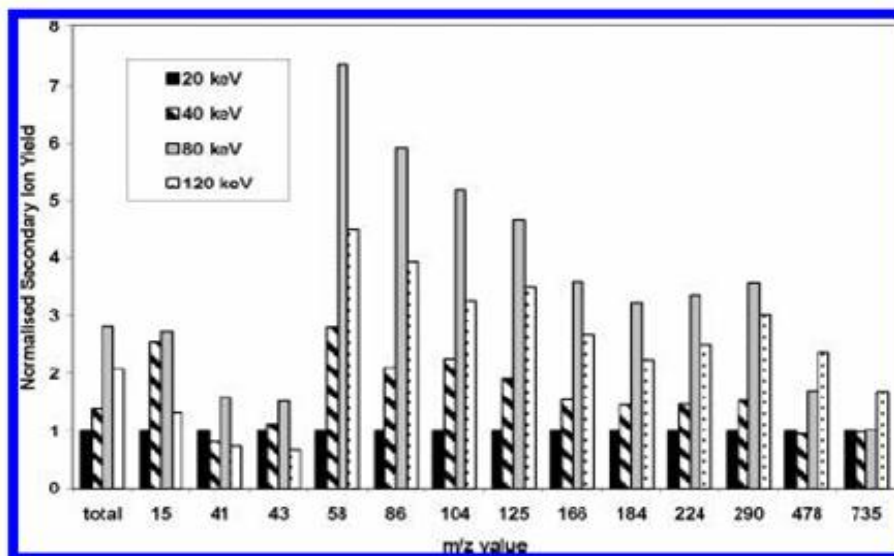


**Figure 1.6** Secondary ion yields relative to 20 keV  $\text{C}_{60}^+$  for peaks present in the SIMS spectrum of dipalmitoylphosphatidylcholine (DPPC) for 40, 80 and 120 keV  $\text{C}_{60}^+$ . Reproduced from Fletcher *et al.* 2006.

The Winograd's group suggest that the increases in the secondary ion yields obtained with cluster and particularly for polyatomic beams are caused by the increase in the sputter yields rather than the ionisation probability. An experiment undertaken by Szakal (2006) showed that the sputter yields of water from ice increases by 10 fold when switched from  $\text{Au}^+$  to  $\text{Au}_3^+$  and by 25 fold to 2500 when  $\text{C}_{60}^+$  was used. A similar effect was also observed for organic molecules trehalose and cholesterol [Cheng *et al.*, 2005]. An article published by Wucher (2006) briefly gives an overview of the secondary ion formation under cluster and polyatomic impact and the sputtering characteristics are explained by Kersting *et al.* (2004). The potential benefits observed with the 10 and 20 keV  $\text{C}_{60}^{n+}$  source led to the development of a 40 keV  $\text{C}_{60}^{n+}$  ion source for imaging with SIMS at sub-micron resolution [Fletcher *et al.*, 2006].

To provide a comparison between different beams, parameters such as secondary ion yields relative to damage cross-section and secondary ion formation efficiency have to be measured, which are defined and discussed below.

### **1.7.3 Damage cross-section and secondary ion formation efficiency**

Since, these polyatomic beams provide a great enhancement in the secondary ion yields, it is also important to investigate the damage they cause to the sample surface upon impact. This is reported in terms of 'damage cross-section', which is defined as "the average surface area depleted of the considered surface species M as a result of a single ion impact" by Kotter *et al.* (1998) and can, be determined by:

$$\sigma (X) = N_{\text{des}} / N_o \quad \text{Equation 1.2}$$

Where:

$N_{\text{des}}$  – average number of molecular species that disappears from the surface following a single primary ion impact.

$N_o$  – total number of molecular species M in the unit area of  $1 \text{ cm}^2$  of the uppermost monolayer.

Principally, it refers to the area around the sample surface that has been bombarded with the primary ion beam in which the molecules of interest have thought to be damaged. It also depends on the structure and the composition of the surface, as well as the properties of the primary ion beam and the secondary particles.

Thus, to provide a comparison between the yields and damage cross-section, the value efficiency (E) was introduced. This provides a measure of the signal available that can be acquired from an area before the surface becomes damaged. It is defined as a ratio of secondary ion yields (Y) to the damage cross-section ( $\sigma$ )

$$E (X) = Y (X) / \sigma (X) \quad \text{Equation 1.3}$$

The secondary ion yields (Y) of X can be determined by:

$$Y(X) = N(X) / N_p \quad \text{Equation 1.4}$$

Where:

$N(X)$  – number of secondary ions detected.

$N_p$  – total number of applied primary ions.

The study by Appelhans and Delomere (1989) showed that by using the polyatomic beam,  $SF_6^0$ , an increase in the secondary ion yields is obtained with a simultaneous increase in the damage, but the yield enhancement greatly outweighs the damage increase. Further, Kötter and Benninghoven (1998) accomplished an in-depth study to provide a comparison between the yields and damage cross-section of the monoatomic ion beams,  $Ar^+$  and  $Xe^+$  and the polyatomic,  $SF_5^+$  at the same energy. They reported an increase in the yields up to factor of 1000 whereas the increase in the damage was only by a factor of 6 when polyatomic,  $SF_5^+$  primary ion beam was used. A study by Gillen and co-workers (1998) evaluates the damaging behaviour of the organic films when analysed at high primary ion dose using  $SF_5^+$  and  $Ar^+$ . They show that the molecular signal can be maintained as a function of the primary ion dose when using the  $SF_5^+$  projectile, which also has the ability to remove the damage caused by the monoatomic,  $Ar^+$  primary ion beam. In addition to this, reduced damaging effects have also been reported for the polymer samples, particularly for Poly(methyl methacrylate) (PMMA) when analysed with  $SF_5^+$  ion beam [Wagner *et al.*, 2004].

On comparison of the  $C_{60}^+$  polyatomic projectile to the monoatomic, cluster and other polyatomic,  $SF_5^+$  beams, it produces higher secondary ion efficiencies and low subsurface damage [Weibel *et al.*, 2003], [Kersting *et al.*, 2004]. Table 1.2 and Table 1.3 shows the efficiencies (E) and the damage cross-section ( $\sigma$ ) reported for some of the samples from the literature.

In summary, these publications show that the  $C_{60}^+$  primary ion beam results in low disappearance cross-section ( $\sigma$ ) and an increase in the efficiency (E) as compared to the polyatomic,  $SF_5^+$  ions. Although the disappearance cross-section ( $\sigma$ ) caused by the  $C_{60}^+$  is relatively similar to the  $Ga^+$  and  $Au_3^+$ , but the efficiencies obtained with the  $C_{60}^+$  are much greater. Further, when  $Au^+$  and  $Au_3^+$  primary ion beams are used, damage accumulation occurs with an increase in the primary ion dose. This is contrast to when the sample is bombarded with the  $C_{60}^+$ , where a large decrease in the chemical damage of the sample is observed even with an ion dose up to  $1 \times 10^{15}$  ions/cm<sup>2</sup>. This could be due to the removal of any damage generated with each consecutive impact [Conlan *et al.*, 2006]. In conclusion, the literature has shown the  $C_{60}^+$  to be the most successful and favourable projectile for ToF-SIMS.

**Table 1.2** Yields (Y), disappearance cross-section ( $\sigma$ ) and secondary ions formation efficiency (E) for 10 keV Ga<sup>+</sup>, Au<sup>+</sup>, SF<sub>5</sub><sup>+</sup> (IONTOF) and C<sub>60</sub><sup>+</sup> bombardment of thin film PS2000. Reproduced from Weibel *et al.* 2003.

<b>Primary ion</b>	<b>Y (<math>1 \times 10^{-5}</math>)</b>	<b><math>\sigma</math> (<math>1 \times 10^{-3} \text{ cm}^2</math>)</b>	<b>E (<math>1 \times 10^9 \text{ cm}^2</math>)</b>
	<i>m/z 325</i>	<i>m/z 325</i>	<i>m/ z 325</i>
Ga <sup>+</sup>	14	1.33	11
Au <sup>+</sup>	62	4.23	15
SF <sub>5</sub> <sup>+</sup>	1550	5.6	277
C <sub>60</sub> <sup>+</sup>	1500	1.06	1415

**Table 1.3** Absolute values for secondary ion yields (Y), disappearance cross-sections ( $\sigma$ ) and efficiency (E) for the quasi-molecular ion [M-H]<sup>-</sup> *m/z* [C<sub>73</sub>H<sub>107</sub>O<sub>12</sub>]<sup>-</sup> of irganox 1010 with primary ion energy 12 keV Au<sup>+</sup> and 10 keV Ga<sup>+</sup>, Cs<sup>+</sup>, SF<sub>5</sub><sup>+</sup> and C<sub>60</sub><sup>+</sup>. Reproduced from Kersting *et al.* 2004.

<b>Primary ion</b>	<b>Y</b>	<b><math>\sigma</math></b>	<b>E</b>
Ga <sup>+</sup>	$1.6 \times 10^{-6}$	$2.3 \times 10^{-13}$	$7.0 \times 10^6$
Cs <sup>+</sup>	$2.0 \times 10^{-5}$	$3.3 \times 10^{-13}$	$6.1 \times 10^7$
SF <sub>5</sub> <sup>+</sup>	$2.2 \times 10^{-4}$	$5.3 \times 10^{-13}$	$4.2 \times 10^8$
Au <sup>+</sup>	$4.4 \times 10^{-5}$	$3.0 \times 10^{-13}$	$1.5 \times 10^8$
Au <sub>2</sub> <sup>+</sup>	$4.3 \times 10^{-4}$	$9.2 \times 10^{-13}$	$4.7 \times 10^8$
Au <sub>3</sub> <sup>+</sup>	$2.0 \times 10^{-3}$	$1.1 \times 10^{-12}$	$1.8 \times 10^9$
C <sub>60</sub> <sup>+</sup>	$3.2 \times 10^{-3}$	$2.1 \times 10^{-13}$	$1.5 \times 10^{10}$

## 1.8 Simulation Studies

Molecular dynamic computer simulation studies developed by the Winograd and Garrison groups have been used to explain the sputtering mechanism and the increase in the yields of the polyatomic,  $C_{60}^+$  primary ion beam [Postawa *et al.*, 2004], [Ryan *et al.*, 2007]. Figure 1.7 illustrates the difference between monoatomic  $Ga^+$  and  $C_{60}^+$  impact on a silver substrate at 15 keV [Postawa *et al.*, 2004]; and Figure 1.8 shows the difference between cluster,  $Au_3^+$  and  $C_{60}^+$  impact on the water ice substrate at 15 keV [Ryan *et al.*, 2007]. Both figures show that upon impact at 15 keV the polyatomic beam,  $C_{60}^+$  dissociates into its 60 constituents carbon atoms and each carbon atom carrying 250 eV creates its own cascade of moving particles. As the atoms deposit energy very close to the surface, it results in an increase in the amount of material removed by a single ion impact and low damage is caused which is removed by subsequent impact. Therefore, molecular information can be obtained and maintained as a function of primary ion dose.

On the other hand, when 15 keV  $Ga^+$  atomic ion beam strikes a surface, it penetrates deep into the sample and deposits energy many monolayers below the surface. This causes sub-surface mixing and less amount of material is ejected per impact. Furthermore with continuous bombardment, the damage builds up, resulting in loss of molecular information, Figure 1.7.

Figure 1.8 shows that when the cluster,  $Au_3^+$  ion beam impacts a surface, it also breaks into its constituent atoms, Au; but as each atom still possesses relatively high energy they travel considerable distance and become embedded into sub-surface region of the samples. This causes substantial damage to the samples, which builds up and is

uncovered as the sputtering proceeds. These simulation studies have been developed by the Garrison group over many years for metals but now recently effort has been devoted to the behaviour of organic films which also show the same results.

In summary, the development of the polyatomic ion beams, particularly the  $C_{60}^+$  projectiles has led to a significant increase in the secondary ion yields with very low sub-surface damage and higher efficiencies. This allows the analysis to be performed at higher primary ion dose, exceeding the static limit while maintaining molecular information which has opened up the prospect of depth profiling discussed in Chapter 4 and 3D imaging discussed in Chapter 5.

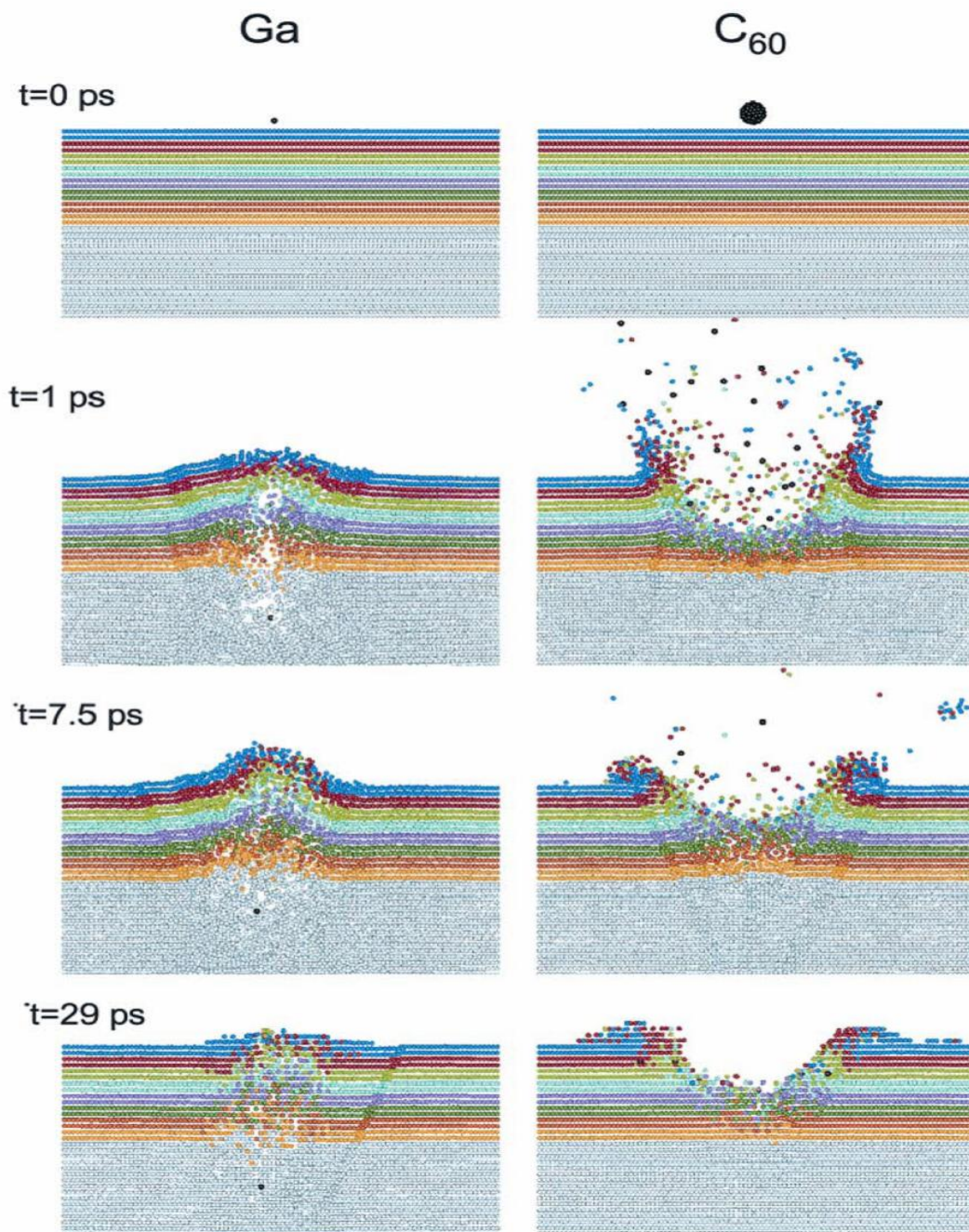


**Figure 1.7** A silver {111} surface under impact from a 15 keV Ga<sup>+</sup> (left) and 15 keV C<sub>60</sub><sup>+</sup> (right). The projectile atoms are black, the silver ions are coloured in layers to allow easier visualisation of the inter layer mixing. Reproduced from Postawa *et al.* 2004.

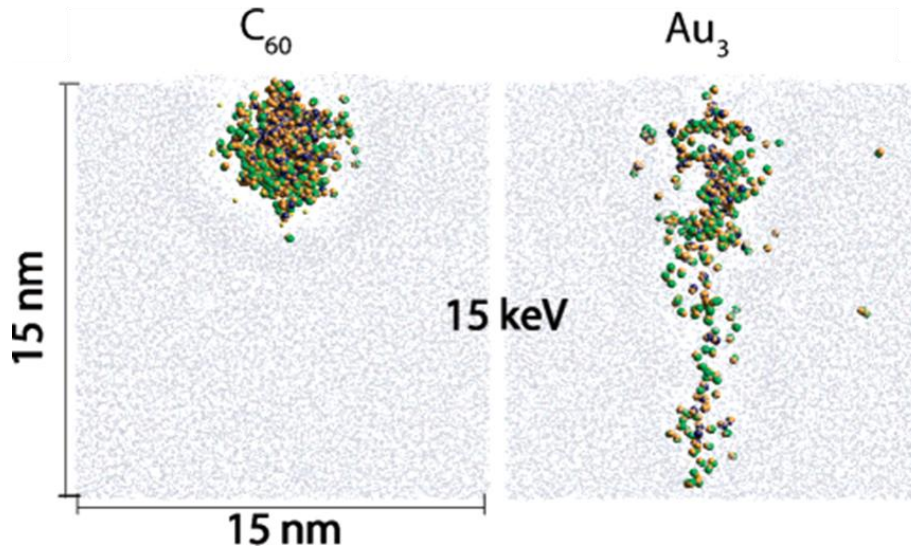


**Figure 1.8** Time snapshots of 15 keV  $C_{60}^+$  (left) and  $Au_3^+$  (right) bombardment of pure amorphous water ice. Gray and yellow spheres represent intact water molecules and projectile atoms, respectively, within a 2 nm slice through the centre of the substrate at 0.5 ps. Orange, green, and blue spheres represent the fragment species placed back in their initial positions and overlaid on the substrate at 0.5 ps. Reproduced from Ryan *et al.* 2007.

## 1.9 AIMS

In the last decade, SIMS has matured into a powerful technique in the field of MS imaging. The implementation of highly focused cluster LMIS offer the prospect of imaging at a sub 100 nm spatial resolution but the limitations of the static limit and low ionisation probability has restricted this to a 2  $\mu\text{m}$  spatial resolution [Fletcher *et al.*, 2010]. It has been shown that the secondary ion yields can be increased by using a polyatomic primary ion beam, particularly,  $\text{C}_{60}^+$ , which also offers low sub-surface damage and analysis at high ion dose. Thus, sub-micron imaging becomes a reality by using “voxels” rather than pixels with depth profiling and 3D imaging. However, the conventional ToF-SIMS as a result becomes a limitation since a pulsed ion beam has a low duty cycle resulting in long analysis time. Furthermore, while pulsing the beam it is difficult to maintain a high mass resolution and spatial resolution at the same time. A new configuration for ToF-SIMS is required to overcome these challenges and progress forward in the field of biological sciences.

Our group at the University of Manchester went into collaboration with Ionoptika Ltd (Southampton) and Surface Analysis Instruments (SAI) Ltd (Manchester) to design and build an instrument to overcome the drawbacks on the conventional ToF-SIMS instrument. This instrument, called the **J105 3D Chemical Imager** uses a dc beam for analysis and decouples SIMS process from the mass spectrometry.

The aim of this thesis is to explain the development of the new ToF-SIMS instrument, the **J105 3D Chemical Imager** and briefly outline how it differs from the conventional ToF-SIMS in terms of capability and performance. It has been shown by the Vickerman’s group that the buckminsterfullerene  $\text{C}_{60}$  polyatomic beam offers much

more to the field of biological analysis, particularly in 3D imaging of cells as compared to other polyatomic projectiles. Hence, the project explores the prospect of using  $C_{60}^+$  as a continuous beam during analysis in order to achieve a better sensitivity and a higher spatial resolution while maintaining mass resolution. A range of standard samples have been analysed to prove the concept of the J105 instrument, including tandem MS capability and limit of detection. The instrument's ability to perform sub-cellular imaging in 2D and 3D is also investigated by using a standard Henrietta Lacks (HeLa) cell line. In addition, three different sample preparation techniques, formaldehyde fixing, freeze-drying and freeze-fractured frozen-hydrated is investigated by using an improved sample handling system specifically designed for biological samples on the **J105 3D Chemical Imager**.

## References

Anderson, H.H.; Bay, H.L. **Nonlinear effects in heavy ion sputtering.** Journal of Applied Physics (1974), 45 (2), 953-954

Appelhans, A.D.; Delmore, J.E. **Comparison of Polyatomic and Atomic Primary Beams for Secondary Ion Mass Spectrometry of Organics.** Analytical Chemistry (1989), 61, 1087-1093

Aranyosiova, M.; Chorvatova, A.; Chorvat Jr, D.; Biro, Cs.; Velic, D. **Analysis of cardiac tissue by gold cluster ion bombardment.** Applied Surface Science (2006), 252, 6782-6785

Baudin, K.B.; Bolbach, G.; Brunelle, A.; Della-Negra, S.; Håkansson, P.; Le Beyec, Y. **Secondary ion emission under cluster impact at low energies (5-60 keV); influence of the number of atoms in the projectile.** Nuclear Instruments and Methods in Physics Research B (1994), 160-163

Benguerba, M.; Brunelle, A.; Della-Negra, S.; DepaUW, J.; Joret, H.; Le Beyec, Y.; Blain, M.G.; Schweikert, E.A.; Ben Assayag G.; Sudraud, P. **Impact of slow gold clusters on various solids : nonlinear effects in secondary ion emission.** Nuclear Instruments and Methods in Physics Research (1991), B62, 8-22

Benninghoven, A. **Analysis of monomolecular surface layers of solids by secondary ion emission.** Zeitschrift fuer Physik (1970), 230(5), 403-417

Benninghoven, A. **Chemical Analysis of Inorganic and Organic Surfaces and Thin Films by Static Time-of-Flight Secondary Ion Mass Spectrometry (ToF-SIMS).** Angewandte Chemie (International Edition in English) (1994), 33 (10), 1023-1043

Benninghoven, A.; Steffens, P.; Niehuis, E.; Friese, T. **Application of a new Time of Flight.** Annual Conference on Mass Spectrometry and Allied Topics (1983), 54-55

Blain, M.G.; Della-Negra, S.; Joret, H.; Le Beyec, Y.; Schweikert, E.A. **Secondary-Ion Yields from Surface Bombarded with keV Molecular and Cluster Ions.** Physical Review Letters (1989), 63 (15), 1625-1628

Caprioli, R.M.; Farmer, T. B.; Gile, J. **Molecular Imaging of Biological Samples: Localization of Peptides and Proteins Using MALDI-TOF MS.** Analytical Chemistry (1997), 69(23), 4751-4760

Castaing, R.; Slodzian, G. **Analytical microscopy by secondary ion imaging techniques.** Journal of Physics, E-Scientific Instruments (1981), 14, 1119-1127

Castaing, R; Slodzian, G. **Microanalysis by secondary ionic emission**. Journal of Microscopy (1962), 1(6), 395-410  
Chait, B.T.; Standing, K.G. **A time-of-flight mass spectrometer for measurement of secondary ion mass spectra**. International Journal of Mass Spectrometry and Ion Physics (1981), 40 (2), 185-193

Chaurand, P; Schwartz, S.A.; Caprioli, R.M. **Assessing protein patterns in disease using imaging mass spectrometry**. Journal of Proteome Research (2004), 3(2), 245-252

Cheng, J.; Winograd, N. **Depth Profiling of Peptide Films with TOF-SIMS and a C<sub>60</sub> Probe**. Analytical Chemistry (2005), 77(11), 3651-3659

Chughtai, K.; Heeren, R.M.A. **Mass Spectrometric Imaging for Biomedical Tissue Analysis**. Chemical Reviews (2010), 110(5), 3237-3277

Colliver, T.L.; Brummel, C.L.; Pacholski, M.L.; Swaneck, F.D.; Ewing, A.G.; Winograd, N. **Atomic and Molecular Imaging at the Single-Cell Level with TOF-SIMS**. Analytical Chemistry (1997), 69, 2225-2231

Conlan, X.A.; Gilmore, I.S.; Henderson, A.; Lockyer N.P.; Vickerman, J.C. **Polyethylene terephthalate (PET) bulk film analysis using C<sub>60</sub><sup>+</sup>, Au<sub>3</sub><sup>+</sup>, and Au<sup>+</sup> primary ion beams**. Applied Surface Science (2006), 252, 6562–6565

Cooks, R.G. and Busch, K.L. **Matrix Effects, Internal Energies and MS/MS Spectra of Molecular Ion Sputtered From Surfaces**. International Journal of Mass Spectrometry Ion Physics (1983), 53, 111-124

Davies, N.; Weibel, D.E.; Blenkinsopp, P.; Lockyer, N.; Hill, R.; Vickerman, J.C. **Development and experimental application of a gold liquid metal ion source**. Applied surface science (2003), 203-204, 223-227

Debois, D.; Bralet, M.P., Naour, F.; Brunelle, A.; Laprévotte, O. **In Situ Lipidomic Analysis of Nonalcoholic Fatty Liver by Cluster TOF-SIMS Imaging**. Analytical Chemistry (2009), 81, 2823-2831

Earnshaw, C.J.; Carolan, V.A.; Richards, D.S.; Clench, M.R. **Direct analysis of pharmaceutical tablet formulations using matrix-assisted laser desorption/ionisation mass spectrometry imaging**. Rapid Communications in Mass Spectrometry (2010), 24(11), 1665-1672

Eccles, A. J.; Vickerman, J. C. **The characterization of an imaging time-of-flight secondary ion mass spectrometry instrument**. Journal of Vacuum Science & Technology, A: Vacuum, Surfaces, and Films (1989), 7(2), 234-44

Fletcher, J.S.; Xavier, A.C.; Jones, E.A.; Biddulph, G.; Lockyer, N.P.; Vickerman, J.C. **TOF-SIMS Analysis Using C<sub>60</sub>. Effect of Impact Energy on Yield and Damage.** Analytical Chemistry (2006), 78, 1827-1831

Fletcher, J.S.; Lockyer, N.P.; Vickerman, J.C. **Developments in molecular SIMS depth profiling and 3D imaging of biological systems using polyatomic primary ions.** Mass Spectrometry Reviews (2010), 1-33

Gazi, E.; Dwyer, J.; Lockyer, N.; Gardner, P.; Vickerman, J.C.; Miyan, J.; Hart, C.A.; Brown, M.; Shanks, J.H.; Clarke, N. **The combined application of FTIR microspectroscopy and ToF-SIMS imaging in the study of prostate cancer.** Faraday Discussions (2004), 126, 41-59

Gerhard, W.; Plog, C. **Secondary Ion Emission by Nonadiabatic Dissociation of Nascent Ion Molecules with Energies Depending on Solid Composition.** Part I. Mathematical Formulation and Qualitative Examination of New Emission Conception from Me<sup>+</sup> Ions. Zeitschrift Fur Physik. Condensed Matter, (1983), 54 (1), 59-71

Gillen, G. in Microbeam Analysis. Proceeding of the International Conference on Microbeam Analysis, 8-15 July 2000. Institute of Physics Conference Series 165, Taylor & Francis Ltd, London 2000, p. 339

Gillen, G.; King, L.; Freibaum, B.; Lareau, R.; Bennett, J.; Chmara, F. **Negative caesium sputter ion source for generating cluster primary ion beams for secondary ion mass spectrometry analysis.** Journal of Vacuum Science and Technology, Part A: Vacuum, Surfaces and Films (2001), 19 (2), 568-575

Gillen, G.; Roberson, S. **Preliminary Evaluation of an SF<sub>5</sub><sup>+</sup> Polyatomic Primary Ion Beam for Analysis of Organic Thin Films by Secondary Ion Mass Spectrometry.** Rapid Communications in Mass Spectrometry (1998), 12, 1303-1312

Hammond, J.S. Imaging Mass Spectrometry Protocols for Mass Microscopy. **Chapter 18 Comparison of SIMS and MALDI for Mass Spectrometric Imaging.** Setou, Editor. 2010. Springer.

Herzog, R. F. K.; Viehbock, F. P. **Ion source for mass-spectrography.** Physical Review (1949), 76 855-856

Hill, R.; Blenkinsopp, P.W.M. **The development of C<sub>60</sub> and gold cluster ion guns for static SIMS analysis.** Applied Surface Science (2004), 231-232, 936-939

Hofmann, S. **Ultimate Depth Resolution and Profile Reconstruction in Sputter Profiling with AES and SIMS.** Surface and Interface Analysis (2000), 30 (1), 228-236

Honig, R.E. **Surface and thin film analysis of semiconductor materials.** Thin Solid Films (1976), 31 (1-2), 89-122

Hsieh, Y.; Casale, R.; Fukuda, E.; Chen, J.; Knemeyer, I.; Wingate, J.; Morrison, R.; Korfmacher, W. **Matrix assisted laser desorption/ionization imaging mass spectrometry for direct measurement of clozapine in rat brain tissue.** Rapid Communications in Mass Spectrometry (2006), 20(6), 965-972

Jacquet, D.; Le Beyec, Y. **Cluster impacts on solids.** Nuclear Instruments and Methods in Physics Research B (2002), 193, 227-239

Jones, E.A.; Fletcher, J.S.; Thompson, C.E.; Jackson, D.A.; Lockyer, N.P.; Vickerman, J.C. **ToF-SIMS analysis of bio-systems: Are polyatomic primary ions the solution?** Applied Surface Science 252 (2006) 6844–6854

Kang, S.; Shim, H.S.; Lee, J.S.; Kim, D.S.; Kim, H.Y.; Hong, S.H.; Kim, P.S.; Yoon, J.H.; Cho, N.H. **Molecular proteomics imaging of tumour interfaces by mass spectrometry.** Journal of Proteome Research (2010), 9 (2), 1157-1164

Kersting, R.; Hagenhoff, B.; Kollmer, F.; Möllers, R.; Niehuis, E. **Influence of primary ion bombardment conditions on the emission of molecular secondary ions.** Applied Surface Science (2004), 231–232, 261–264

Kollmer, F. **Cluster Primary Ion Bombardment of Organic Materials.** Applied Surface Science (2004), 231-232, 153-158

Kötter, F.; Benninghoven, A. **Secondary ion emission from polymer surfaces under Ar<sup>+</sup>, Xe<sup>+</sup> and SF<sub>5</sub><sup>+</sup> ion bombardment.** Applied Surface Science (1998), 133, 47-57

Le Beyec, Y. **Cluster impacts at keV and MeV energies: Secondary emission phenomena.** International Journal of Mass Spectrometry and Ion Processes (1998), 174, 101-117

Liebl, H.J. **Ion microprobe mass analyser.** Journal of Applied Physics (1967), 38(13), 5277-5283

Liebl, H.J.; Herzog, R.F.K. **Sputtering ion source for solids.** Journal of Applied Physics (1963), 34(9), 2893-2896

Luk, S. Y.; Patel, N.; Davies, M. C. **Chemical imaging of pharmaceuticals by time-of flight secondary ion mass spectrometry.** Spectroscopy Europe (2003), 15(1), 14-18

Luxembourg, S.L.; McDonnell, L.M.; Duursma, M.C.; Guo, X.; Heeren, R.M.A. **Effect of Local Matrix Crystal Variations in Matrix-Assisted Ionization Techniques for Mass Spectrometry.** Analytical Chemistry (2003), 75, 2333-2341

Magnusson, Y.; Friberg, P.; Sjövall, P.; Danardt, F.; Malmberg, P., Chen, Y. **Lipid imaging of human skeletal muscle using TOF-SIMS with bismuth cluster ion as a primary ion source.** Clinical Physiology and Functional Imaging (2008), 28, 202-209

McDonnell, L.A.; Heeren, R.M.A. **Imaging Mass Spectrometry**. *Mass Spectrometry Reviews* (2007), 26(4), 606-643

Murphy, R.C.; Hankin, J.A.; Barkley, R.M. **Imaging of lipid species by MALDI mass spectrometry**. *Journal of Lipid Research* (2009), 50, S317-322

Niehuis, E.; Heller, T.; Feld, H.; Benninghoven, A. **Design and performance of a reflectron based time-of-flight secondary-ion mass spectrometer with electrodynamic primary ion mass separation**. *Journal of Vacuum Science & Technology, A: Vacuum, Surfaces, and Films* (1987), 5(4, Pt. 2), 1243-6

Nygren, H.; Eriksson, C.; Malmberg, P.; Sahlin, H.; Carlsson, L.; Lausmaa, J.; Sjövall, P. **A cell preparation method allowing subcellular localization of cholesterol and phosphocholine with imaging TOF-SIMS**. *Colloids and Surfaces B: Biointerfaces* (2003), 30, 87-92

Nygren, H.; Malmberga, P.; Kriegeskotte, C.; Arlinghaus, H.F. **Bioimaging TOF-SIMS: localization of cholesterol in rat kidney sections**. *FEBS letters* (2004), 566 (1-3), 291-293

Oppenheimer, S.R.; Mi, D.C.; Sanders, M.E.; Caprioli, R.M. **Molecular analysis of tumour margins by MALDI mass spectrometry in renal carcinoma**. *Journal of Proteome Research* (2010), 9 (5), 2182-2190

Ostrowski, S.G.; Van Bell, C.T.; Winograd, N.; Ewing, A.G. **Mass Spectrometric Imaging of Highly Curved Membranes During Tetrahymena Mating**. *Science* (2004), 305, 71-73

Parry, S.; Winograd, N. **High-resolution ToF-SIMS imaging of eukaryotic cells reserved in trehalose matrix**. *Analytical Chemistry* (2005), 77 (24), 7950-7957

Peterson, R. E.; Nair, A.; Dambach, S.; Arlinghaus, H. F.; Tyler, B. J. **Characterization of individual atmospheric aerosol particles with SIMS and laser-SNMS**. *Applied Surface Science* (2006), 252(19)

Pierson, J.; Norris, J.L.; Aerni, H-R.; Svenningsson, P; Caprioli, R.M.; Andren, P.E. **Molecular Profiling of Experimental Parkinson's Disease: Direct Analysis of Peptides and Proteins on Brain Tissue Sections by MALDI Mass Spectrometry**. *Journal of Proteome Research* (2004), 3(2), 289-29

Postawa, Z. **Sputtering simulations of organic overlayers on metal substrates by monoatomic and clusters projectiles**. *Applied Surface Science* (2004), 231-232, 22-28

Reyzer, M.L.; Hsieh, Y.; Ng, K.; Korfmacher, W.A.; Caprioli, R.M. **Direct analysis of drug candidates in tissue by matrix-assisted laser desorption/ionization mass spectrometry**. *Journal of Mass Spectrometry* (2003), 38(10), 1081-1092

Rohner, T.C.; Staab, D.; Stoeckli, M. **MALDI mass spectrometric imaging of biological tissue sections**. *Mechanisms of Ageing and Development* (2005), 126, 177–185

Ryan, K.E.; Wojciechowski, I.A.; Garrison, B.J. **Reaction Dynamics Following keV Cluster Bombardment**. *Journal of Physical Chemistry* (2007), 111, 12822-12826

Rzeznik, L.; Czerwinski, B.; Garrison B.J.; Winograd, N.; Postawa, Z. **Molecular dynamics simulations of sputtering of organic overlayers by slow, large clusters**. *Applied Surface Science* (2008), 255, 841-843

Schwartz, S.A.; Weil, R.J.; Johnson, M.D.; Toms, S.A.; Caprioli, R.M. **Protein Profiling in Brain Tumours Using Mass Spectrometry: Feasibility of a New Technique for the Analysis of Protein Expression**. *Clinical Cancer Research* (2004), 10(3), 981-987

Sigmund, P. **Sputtering by Ion Bombardment: Theoretical Concepts**. In: Springer Series Topics in Applied Physics: Sputtering by Particle Bombardment I, Behrisch R (ed). 1981; 47:9

Sjövall, P.; Johansson, B.; Belazi, D.; Stenvinkel, P.; Lindholm, B.; Lausmaa, J.; Schalling, M. **ToF-SIMS analysis of adipose tissue from patients with chronic kidney disease**. *Applied Surface Science* (2008), 255, 1177-1180

Solon, E.G.; Schweitzer, A.; Stoeckli, M.; Prideaux, B. **Autoradiography, MALDI-MS, and SIMS-MS Imaging in Pharmaceutical Discovery and Development**. *American Association of Pharmaceutical Scientists* (2010) 12 (1), 11-26

Stoeckli, M.; Staab, D.; Staufenbiel, M.; Wiederhold, K-H.; Signor, L. **Molecular imaging of amyloid peptides in mouse brain sections using mass spectrometry**. *Analytical Biochemistry* (2002), 311(1), 33-39

Szakal, C.; Kozole, J.; Winograd, N. **Fundamental Studies of the Cluster Ion Bombardment of Water Ice**. *Applied Surface Science* (2006), 252, 6526-6528

Tang, X.; Beavis, R.; Ens, W.; Lafortune, F.; Schueler, B.; Standing, K. G. A **Secondary ion time-of-flight mass spectrometer with an ion mirror**. *International Journal of Mass Spectrometry and Ion Processes* (1988), 85(1), 43-67

Thompson, D. A.; Johar, S.S. **Nonlinear sputtering effects in thin metal films**. *Applied Physics Letters* (1979), 34 (5), 342-345

Thomson, J. J. **Scattering of Rapidly Moving Electrified Particles**. *Proc. Cam. Phil. Soc.* (1910), 15 465-71

Touboul, D.; Brunelle, A.; Halgand, F.; DeLa Porte, S.; Laprévotte, O. **Lipid imaging by gold cluster time-of-flight secondary ion mass spectrometry: Application to Duchenne muscular dystrophy.** Journal of Lipid Research (2005), 46 (7), 1388-1395.

Touboul, D.; Kollmer, F.; Niehuis, E.; Brunelle, A.; Laprévotte, O. **Improvement of Biological Time-of-Flight Secondary Ion Mass Spectrometry with a Bismuth Cluster Ion Source.** American Society for Mass Spectrometry (2005), 16, 1608-1618

Van der Wel, H.; Lub, J.; Van Velzen, P.N.T.; Benninghoven, A. **Organic surface analysis with time-of-flight SIMS.** Mikrochimica Acta (1990), 101 (1-6), 3-18

Van Stipdonk, M.J.; Harris, R.D.; Schweikert, E.A. **A Comparison of Desorption Yields from C<sub>60</sub> to Atomic and Polyatomic Projectiles at keV Energies.** Rapid Communication in Mass Spectrometry (1996), 10, 1987-1991

Vickerman, J.C. and Briggs, D. **ToF-SIMS: Surface Analysis by Mass Spectrometry** Surface Spectra, IM Publications LLP 2001

Vickerman, J.C. and Swift, A.J. **Secondary Ion Mass Spectrometry in Surface Analysis the Principle Techniques.** Edited by JC Vickerman, John Wiley and Sons Ltd., Chichester 1997

Von Criegern, R.; Weitzel, I.; Zeininger, H.; Lange-Gieseler, R. **Optimization of the Dynamic Range of SIMS Depth Profiles by Sample Preparation.** Surface and Interface Analysis (1990), 15, 415-421

Walker, A.V.; Winograd, N. **Prospects for Imaging with TOF-SIMS Using Gold Liquid Metal Ion Sources.** Applied Surface Science (2003), 203-204, 198-200

Weibel, D.E.; Wong, S. Lockyer, N.P. Vickerman, J.C. **C<sub>60</sub> Cluster Ion Bombardment of Organic Surfaces.** Applied Surface Science (2004), 231-232, 146-152

Weibel, D.E.; Wong, S., Lockyer, N.P.; Blenkinsopp, P.; Hill, R.; Vickerman, J.C. **A C<sub>60</sub><sup>+</sup> Primary Ion Beam System for Time of Flight Secondary Ion Mass Spectroscopy: Its Developments and Secondary Ion Yield Characteristics.** Analytical Chemistry (2003), 75, 1754-1764

Wien, K. **ToF-SIMS analysis of polymers.** Nuclear Instruments and Methods in Physics Research, Section B: Beam Interactions with Material and Atoms (1997), 131 (1-4), 38-54

Wittmaack, K. **Secondary-ion emission from silicon bombarded with atomic and molecular noble gas ions.** Surface Science (1979), 90, 557-563

Wong, S.C.C.; Hill, R.; Blenkinsopp, P.; Lockyer, N.P.; Weibel, D.E.; Vickerman, J.C. **Development of a C<sub>60</sub><sup>+</sup> ion gun for static SIMS and chemical imaging.** Applied Surface Science (2003), 203-204, 219-222

Woods, A.S.; Jackson, S.N. **Brain Tissue Lipidomics: Direct Probing Using Matrix-assisted Laser Desorption/Ionization Mass Spectrometry.** The APPS Journal (2006), 8 (2), E391-E395

Wusher, A. **Molecular secondary ion formation under cluster bombardment: A fundamental review.** Applied Surface Science (2006), 252 (19), 6482-6489

Zimmerman, T.A.; Monroe, E.B.; Tucker, K.R.; Rubakhin, S.S.; Sweedler, J.V. **Chapter 13 Imaging of Cells and Tissues with Mass Spectrometry. Adding Chemical Information to Imaging.** Methods in Cell Biology (2008), 89, 361-390

## **2 Development and Properties of the J105 3D Chemical Imager**

ToF-SIMS is becoming a powerful tool in molecular imaging of biological components in cells and tissues. Advances in the instrumentation, particularly the LMIS, Au<sup>+</sup>, Bi<sup>+</sup> and In<sup>+</sup> that can be focused to spot size of ~100 nm allow high spatial resolution imaging of very small biological features such as cells and this is discussed comprehensively in Chapter 5. These analyses were performed on the conventional ToF-SIMS instrument, Figure 2.1 “BioToF”, used in the Vickerman’s lab. Figure 2.2 illustrates the mechanism of operation of a similar ToF-SIMS an “IonToF”, used by many SIMS groups. Both of these systems use a pulsed primary ion beam to generate secondary ions which are extracted and accelerated into reflectron ToF where they are separated depending on their mass to charge ratio. The next pulse of the primary ion beam cannot start until the secondary ions of the first mass analyser have been separated and detected. Although impressive imaging experiments have been obtained using these instruments but issues such as sensitivity, duty cycle, mass resolution and sample preparation, discussed in detail in Chapter 5 are still preventing this technique reaching its full potential. These limitations will be reviewed in this chapter followed by the developments and properties of the new instrument, the **J105 3D Chemical Imager**.

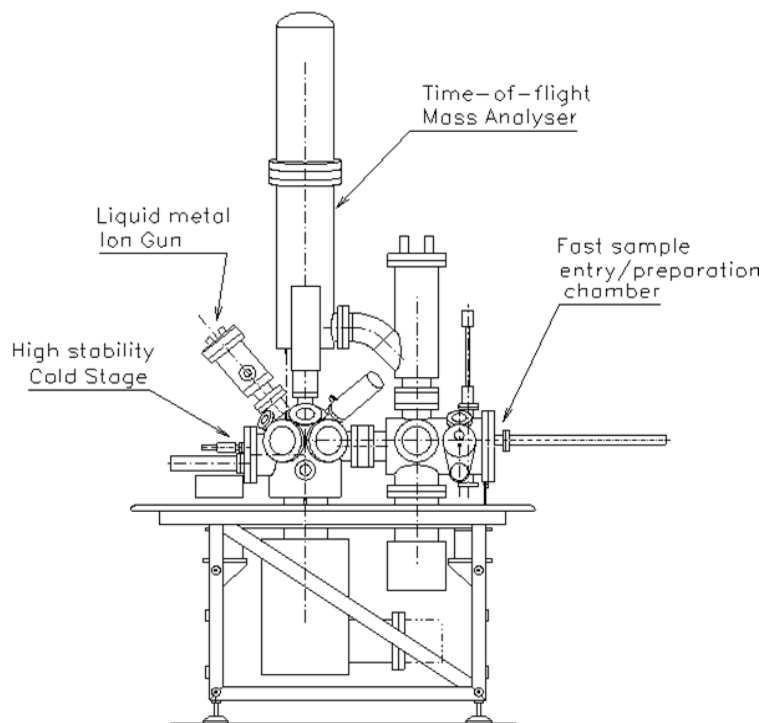


**Figure 2.1** Schematic of the BioToF. Reproduced from [www.kore.co.uk](http://www.kore.co.uk).

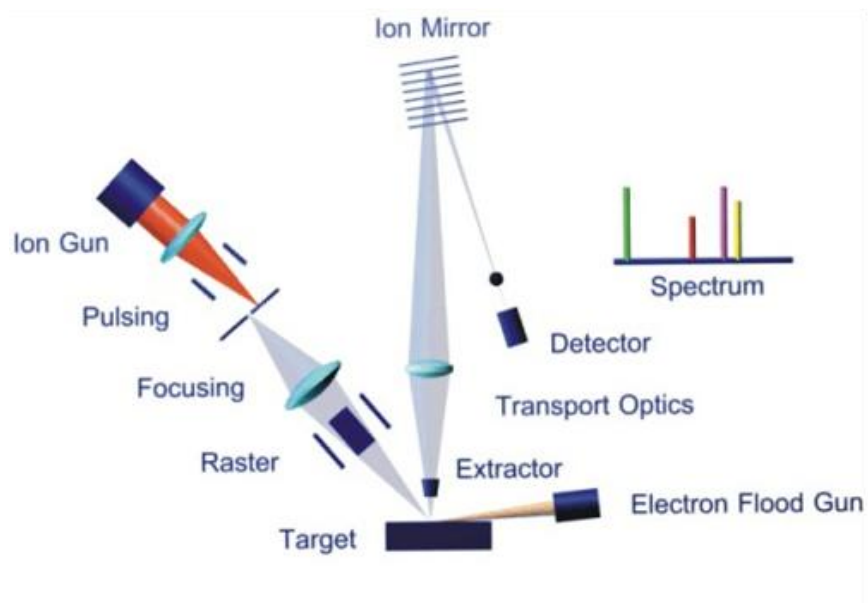


**Figure 2.2** Schematic of an IonToF. Reproduced from [http://www.fkf.mpg.de/ga/machines/sims/How\\_does\\_TOF\\_SIMS\\_work.html](http://www.fkf.mpg.de/ga/machines/sims/How_does_TOF_SIMS_work.html).

## 2.1 Limitations of conventional ToF-SIMS instruments

### 2.1.1 Sensitivity

Sensitivity refers to a proportion of the amount of a sample available that can be detected using a technique of interest. In dynamic SIMS, the primary ion beam is used in continuous mode but this causes damage to the sample and the secondary ions detected are in the form of elemental ions and small fragments [Lorey II *et al.*, 2001]. The modality of static SIMS allows molecular information to be obtained using monoatomic LMIS, but due to the damaging characteristics of these beams the analysis is performed under static conditions. This results in restricting the analysis to the upper layer of the sample only, limiting sensitivity. Nevertheless, these beams are routinely utilized in SIMS imaging as they generate very sharp images.

Winograd and co-workers (1997) used  $\text{Ga}^+$  primary ion beam to image freeze-fractured single *Paramecium* cells [Colliver *et al.*, 1997]. When the inorganic peaks  $\text{Na}^+$  and  $\text{K}^+$  were imaged they co-localise with the cells but the hydrocarbons appear more uniformly distributed on the cell surface. The *Paramecium* cells were also doped with cocaine and dimethyl sulfoxide (DMSO) to image the distribution of these molecules in a biological matrix. The characteristic peaks used to image cocaine were  $m/z$  105 and  $m/z$  304 which localise in the *Paramecium* cells. This study provides a good example of using ToF-SIMS for an application at sub-cellular resolution. However, the signal levels for organic species are extremely low and as a result the cocaine signal only appears to be slightly higher in the cell than in the background. Although, the inorganic species are detected with high intensity when single ions  $\text{Na}^+$  and  $\text{K}^+$  are imaged to outline the

*Paramecium* cell, it is very difficult to differentiate the cell from background, shown in Figure 2.3.

In some laboratories it was observed that increasing the mass of the primary ion beam increases the secondary ion yields which led to the use of the heavier primary ion,  $\text{In}^+$ . Ostrowski *et al.* (2004) used ToF-SIMS to analyse protozoan *Tetrahymena thermophila* cell system using  $\text{In}^+$  primary ion source. During the fusion process, two adjacent lipid bilayers of a *Tetrahymena* cell combine to form fusion pores at the conjugation site. This radical transformation of the shape causes the lipid bilayer to adopt a high curvature structure and as a result the lipid composition changes in that area. ToF-SIMS imaging of freeze fractured *Tetrahymena* cells show that the hydrocarbon fragment  $m/z$  69 is uniformly distributed across the conjugation site whereas the phosphatidylcholine fragment,  $m/z$  184, rapidly decreases in the conjugation junction, Figure 2.4. This analysis was performed using primary ion beam fluence below the static limit which is restricting the total amount of material available, hence limiting sensitivity.

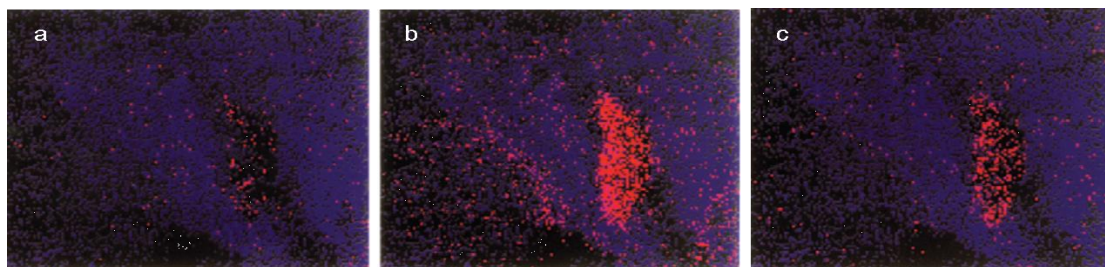


**Figure 2.3** TOF-SIMS images of a *Paramecium* sample previously exposed to a 10  $\mu\text{M}$  cocaine solution. The cocaine image in (a) was produced by creating a two-colour overlay of the parent cocaine ion  $[\text{M} + \text{H}]^+$  with  $m/z$  304 (the range of counts was 0-1) and a characteristic fragment  $m/z$  105 (both in red) with water (blue). This image is compared to overlays of  $\text{K}^+$  and  $\text{Na}^+$  with water in (b) and (c), respectively. The field of view is  $100 \times 100 \mu\text{m}^2$ . Reproduced from Colliver *et al.* 1997.

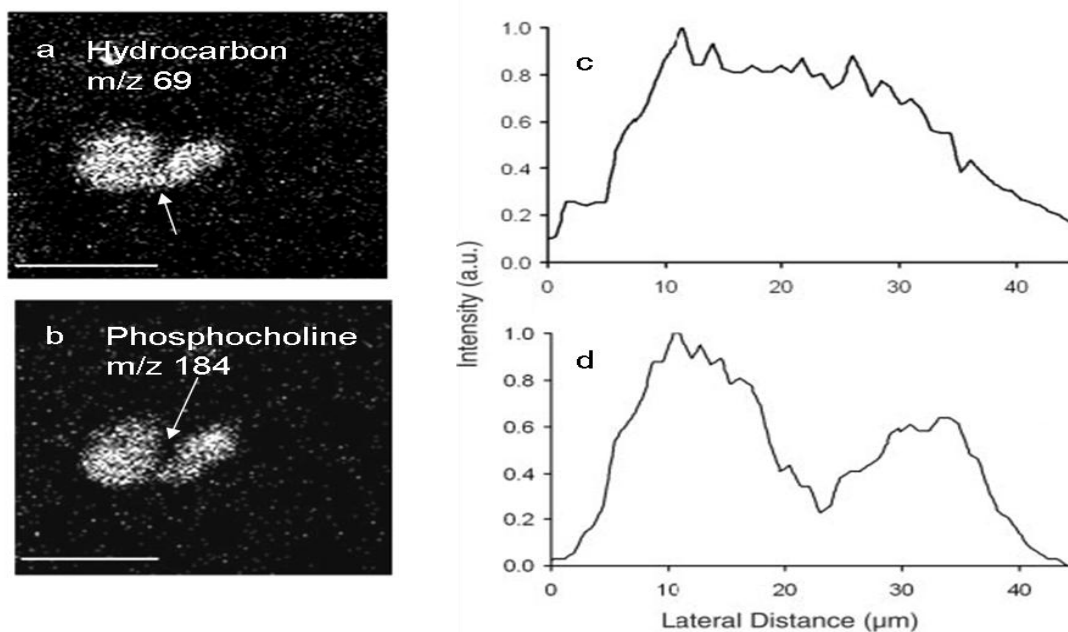


**Figure 2.4** ToF-SIMS images of fusing cells using 200 nm beam spot size. (a)  $\text{C}_5\text{H}_9^+$ :  $m/z$  69; (b) Phosphocholine:  $m/z$  184; (c): Line scan of  $m/z$  69 intensity across fusion region and (d) Line scan of  $m/z$  184 intensity across fusion region. Adapted and reproduced from Ostrowski *et al.* 2004.

Other methods used for enhancing secondary ion yields and hence sensitivity included silver printing, matrix enhancement and laser post ionisation. Nygren *et al.* (2003) and Sjövall *et al.* (2003) explored the use of silver imprinting to identify and localise lipid distribution in leucocytes. This involved pressing a clean and etched silver (Ag) foil against the glass surface covered with cells and once the material was transferred, the sample was analysed on the Ag surface using ToF-SIMS. This method offers two advantages; firstly, the sensitivity of the sample is enhanced as high secondary ion yields are obtained on silver substrate; secondly, an increase in specificity is also observed due to reduction in fragmentation of the molecular ion [Sjövall *et al.*, 2003].

In the above two studies, Ag was used as a matrix which although successful, results in uncontrolled fracturing of cells during imprinting due to the pressure applied. The SEM images displayed high residues from many cells being transferred when a high pressure was applied compared to only few cells whose content is visible using low pressure. As a result, the images of the cells obtained may not be truly representative of the original sample. Accordingly, the group used an alternative approach in which Ag was deposited onto the sample [Nygren *et al.*, 2004]. Leucocyte cells were freeze-dried in ammonium formate and Ag was sputtered onto a layer of cells using an agar sputtering coater with an argon pressure of 0.08 mbar for 15 s. Following an analysis with ToF-SIMS, principal components analysis (PCA) was performed which allowed differentiation between nuclear and non-nuclear regions of the cells.

All of these studies demonstrate that Ag imprinting/depositions is successful in increasing the yields by the formation of silver cationised species  $[M+Ag]^+$ . Figure 2.5

shows the localisation of phosphocholine and cholesterol to the cells. However on inspecting the spectrum, the phosphocholine peak  $m/z$  184 is not cationised and therefore not enhanced. According to Fletcher (2009) the Ag could be suppressing the signal since it transfers the molecular ion into the  $[M+Ag]^+$  species. Furthermore, since this is static SIMS, it would be expected that the cells are covered with both cholesterol and phosphocholine in the image acquired, but cholesterol only appears in the peripheral region and phosphocholine in the nuclear. This raises the question whether during Ag imprinting the cells are becoming deformed and artefacts into the images are introduced [Fletcher, 2009].

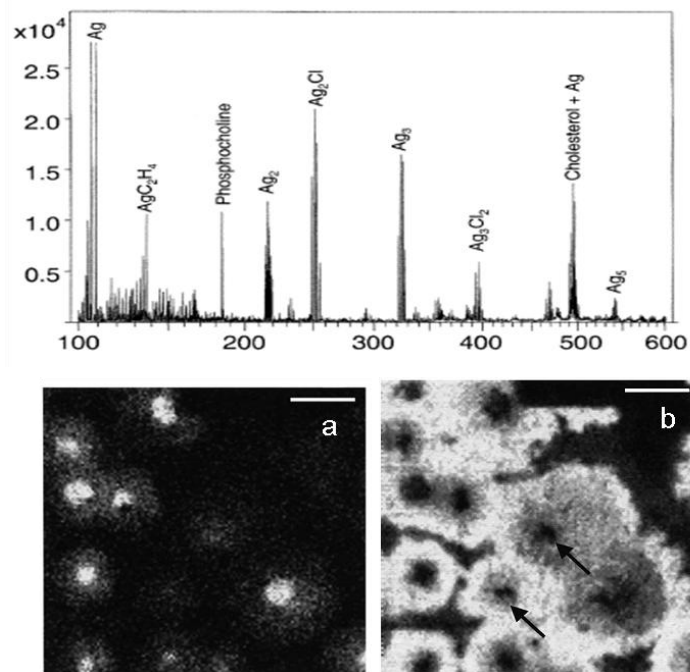


**Figure 2.5** ToF-SIMS high mass resolution, positive secondary ion mass spectrum from cell imprint on silver (100-600 amu, analysis area  $100 \times 100 \mu\text{m}^2$ ). In addition to typical silver cluster ions, specific signals from phosphocholine ( $m/z$  184) and cationised cholesterol ( $m/z$  493) are demonstrated. Secondary ion images,  $m/z$  184 (a) and 493 (b) obtained from silver imprints of glass-adhering leukocytes (PMNLs). The scale represents relative intensity with white as maximum. Image area;  $100 \times 100 \mu\text{m}$ , bar =  $20 \mu\text{m}$ . Arrows indicate spots with low levels of ionisation. Reproduced from Nygren *et al.* 2003.

Matrix enhanced (ME) SIMS involves using an organic species as a matrix to increase the ionisation efficiency of the analyte, similar to MALDI matrix. The effect of elemental matrices on the atomic yields using SIMS was first studied in late 1970 [Deline *et al.*, 1978], [William, 1982]. At the same time Jonkman and co-workers explored the use of frozen Argon (Ar) as a matrix to measure small molecules [Jonkman

*et al.*, 1978]. Few years later Busch and associate reported an increase in the signals of quaternary ammonium salt mixed with an ammonium chloride matrix [Busch *et al.*, 1983]. This was followed by a publication by Gillen *et al.* (1993) who demonstrated that by using a frozen glycerol matrix an enhancement in the signal of small biomolecules can be achieved. ME-SIMS involves using an organic matrix and mixing it with the analyte at various concentration ratios, resulting in an increase in the signal. This increase is attributed to two mechanisms. First, the matrix can act as a proton donor and provides protons for the analytes to become ionised and detected by the mass spectrometry. The second mechanism, involves the matrix to absorb high energy when the beam impacts a surface. This energy is transferred to the other molecules during collisions in the sub-surface region resulting in less fragmentation and high molecular yields. Thus, the matrix is providing a softer but more efficient desorption and ionisation of the chemical species under bombardment [Adriaensen *et al.*, 2005]. The literature shows 2,5-dihydroxybenzoic acid (2,5-DHB) to be the most efficient matrix and masses up to 10000 Da can now be detected by applying this technique [Jen Wu *et al.*, 1996], [Altelaar *et al.*, 2005, 2006], [McDonnell *et al.*, 2005]. However, the drawbacks associated with this technique are that an optimal analyte/matrix mixture has to be found for a maximum increase in the signal which is effected by the type and the concentration of the matrix utilized. Also the presence of matrices can cause the relative ion intensities to change in the ToF-SIMS spectra [Adriaensen *et al.*, 2005].

During the sputtering process a large amount of neutrals are also generated compared to the secondary ions, resulting in a lot of information being lost. Laser post ionisation SIMS also known as secondary neutral mass spectrometry (SNMS) involves

firing a laser into the sputtered material prior to extraction to ionise the neutrals so they can be detected in the mass spectrometer. This approach has proved to be successful in characterising elements and molecules in cells and tissues [Fartmann *et al.*, 2004], [Arlinghaus *et al.*, 2006]. However, SNMS is a very specific technique in that it will only enhance yields of particular elements or molecules, as a universal laser set up is not yet available to ionise all the neutral species generated. Furthermore, it is particularly useful to ionise and image ultra trace elements within a biological sample rather than the organics since the laser can cause damage and result in fragmentation of the organic species [Arlinghaus, 2008].

Although these techniques, ME-SIMS, laser post ionisation and an increase in the mass of the primary ion beam led to an increase in the secondary ion yields, a further significant effect was observed with the introduction of cluster ion sources, as mentioned in Chapter 1 [Andersen *et al.*, 1974], [Wittmaack, 1979], [Johar *et al.*, 1979], [Blain *et al.*, 1989, 1990]. Cluster projectiles,  $\text{Au}_n^{n+}$  [Davies *et al.*, 2003] and  $\text{Bi}_n^{n+}$  [Kollmer, 2004] were found to give a significant enhancement in the secondary ion yields for organic species, particularly at high mass compared to the monoatomic ions and the increase is non-linear with respect to primary particle nuclearity [Benguerba *et al.*, 1991]. However as described in Chapter 1, these sources too had to be operated under static conditions which also limits sensitivity.

A major advance in the field of ToF-SIMS has been the development of polyatomic ion sources [Appelhans *et al.*, 1989], [Kötter *et al.*, 1998], [Gillen, 2000], predominantly the  $\text{C}_{60}$  ion beams [Wong *et al.*, 2003], [Weibel *et al.*, 2003], discussed in Chapter 1. These ion sources,  $\text{SF}_5^+$  and  $\text{C}_{60}^+$ , provide the advantages of higher

secondary ion yields and an enhancement of molecular information, but they also produce low sub-surface damage [Garrison *et al.*, 2008] allowing ion fluence beyond the static limit to be used. These beams offer great enhancement in sensitivity, particularly in cellular imaging as by using a high ion flux it is now possible to access ‘voxels’ rather than pixels, and if there is enough signal available 3D molecular imaging is possible. However, to fully exploit the use of these beams for chemical imaging at sub-micrometer *lateral resolution*, the current ToF technology has to be modified, discussed later in this chapter [Fletcher *et al.*, 2009, 2010].

### **2.1.2 Duty Cycle**

The duty cycle term refers to the time it takes from firing the primary ion beam to acquiring a spectrum. On a conventional ToF-SIMS instrument, the primary ion beam is pulsed for a short time (ns) and the secondary ions generated are extracted with energies in the order of few keV. The path length of the reflectron employed is 1-3 m and the secondary ions require flight times in the order of a few hundred microseconds to reach the detector. Repetition rates cannot exceed 10 kHz and this makes the duty cycle very low, increasing the duration of the experimental time. The operator is usually forced to accept a compromise in sensitivity to allow the experiment to finish in a reasonable time [Fletcher *et al.*, 2009, 2010].

When the beam is tuned for a high lateral imaging experiment it has to be passed through a smaller aperture to obtain a highly focussed small spot size. This results in a very low beam current (typically pA) for high brightness LMIS and the electron impact sources used to produce  $C_{60}^+$  ions. Therefore, many ToF cycles are needed to generate

images with useful levels of secondary ion signal in each pixel, which makes the generation of 2D images time consuming. This becomes even more challenging when the depth profile has to be carried out to generate 3D images as this will take even longer. An approach that is often adopted on conventional ToF-SIMS instruments is to acquire a spectrum and then sputter etch the sample by turning the beam on a continuous mode. Although this approach allows the experiment to be completed on a reasonable time scale, valuable sample is wasted during the etch cycles, as the current ToF-SIMS instrumentation does not allow for detection of material during sputtering [Fletcher *et al.*, 2009, 2010].

### 2.1.3 Mass Resolution

The duty cycle and the short pulsed primary ion beam can affect the mass resolution, which is defined as the ability to distinguish between two peaks of similar masses [Hoffmann *et al.*, 2007].

$$\text{Mass Resolution} = \frac{M}{\Delta M} = \frac{M_1}{M_1 - M_2} \quad \text{Equation 2.1}$$

Where:

$M_1 = m/z$  ratio of the first ion

$M_2 = m/z$  ratio of the second ion

Fundamentally ToF-SIMS is capable of acquiring at a high mass resolution and accuracy, but the problem arises when one wants to carry out high mass resolution imaging. The mass resolution is directly related to the length of the primary ion beam pulse and to maintain high mass resolution, short (<10 ns) pulses are required which limits spatial resolution. This is because the short pulse will produce an unstable beam resulting in blurry images being recorded. It is usually preferred to perform imaging at a high spatial resolution by instantaneously blanking the beam following an impact, rather than moving it across the sample and use long pulses to obtain a stable spot at each pixel. As a result, the requirement for a stable spot and rapid acquisition has led to many experiments being performed with a long pulse length (>50 ns) to acquire spectra, in which the peaks are only resolved to nominal mass. Therefore, it is not normally possible to perform analysis at high mass resolution and high spatial resolution at the same time [Fletcher *et al.*, 2010].

A further constraint arises from the topography variation across electrically insulating sample because the secondary ions produced are extracted from different positions at different times in the extraction field. This produces an energy spread which cannot be compensated by the standard reflectron ToF-analyser. This results in a loss of mass accuracy and each spectrum has to be calibrated before an image is generated and even then differences in mass calibration across the image are observed. Variation in topography presents more problems during 3D analysis where the topography may change through the depth profile [Fletcher *et al.*, 2010].

## 2.2 Concept and features of the J105 3D Chemical Imager

Fletcher *et al.* (2008) explain that the best set up for imaging small cells would be to use a primary ion beam that causes no or minimal sub-surface damage. Further, it should be easily focussed into a small spot size while at the same time maintaining reasonable sample current. At present, the  $C_{60}^+$  primary ion beam appears to produce less damage on the sample surface, but an approach is required to compensate for the low current when it is focussed down to “sub-micrometer diameter” spot sizes. Thus, to take full advantage of the benefits offered by the polyatomic primary ion beams and to overcome the limitations on the application of conventional ToF-SIMS instruments to biological samples, it has been necessary to develop novel instrumental configurations for the analysis of these samples by ToF-SIMS. Our groups at the University of Manchester and Winograd group at Penn State have been working in parallel to achieve this aim and radical changes to the conventional ToF-SIMS have emerged.

The Winograd group adapted a high-performance hybrid quadrupole orthogonal MALDI instrument (Applied Biosystems Q-Star XL) to explore the combination of cluster SIMS and MALDI on the same instrumental platform [Carado *et al.*, 2008]. The Q-STAR XL has been modified to incorporate a 20 keV  $C_{60}^+$  primary ion beam to be used as an alternative to the laser beam, Figure 2.6. The cluster ion source is orientated at  $45^\circ$  to the sample and operated in continuous mode. The secondary ions produced are extracted using a flow of nitrogen gas and focussed into a collisionally focusing RF-only quadrupole before passing through two further quadrupoles. These can either be employed in RF only mode for standard analysis or used for precursor ion selection and collisional dissociation in tandem MS mode.

A small section of ions generated are pulsed into an orthogonally orientated ToF spectrometer for mass analysis. As the sputtering process is decoupled from the mass spectrometry, high mass resolution ( $m/\Delta m \sim 14000$ ) is maintained in all modes while using the primary ion beam in dc mode. The new configuration of the instrument allows complementary MALDI and SIMS data to be obtained.

Carado *et al.* (2008) used the modified Q-Star instrument for the analysis of mouse lung and brain tissues. The authors successfully identified and localised diacylglyceride (DAG) ions in the lung and phosphocholine ( $m/z$  184) and  $m/z$  439.31 to the periphery of the mouse brain slice, Figure 2.7. The analysis was completed using a 20 keV  $C_{60}^+$  primary ion beam in dc mode and ion dose of  $3 \times 10^{12}$  ions/cm<sup>2</sup> over an area of  $4.4 \times 9.1$  mm<sup>2</sup>. If this experiment was carried out on the conventional ToF-SIMS instrument using the same ion dose but in pulsed mode it would have taken 2.2 years to complete. Appropriately this study shows the potential of using SIMS for the analysis of these samples, particularly highlighting the advantages of using primary ion beam in a dc mode.

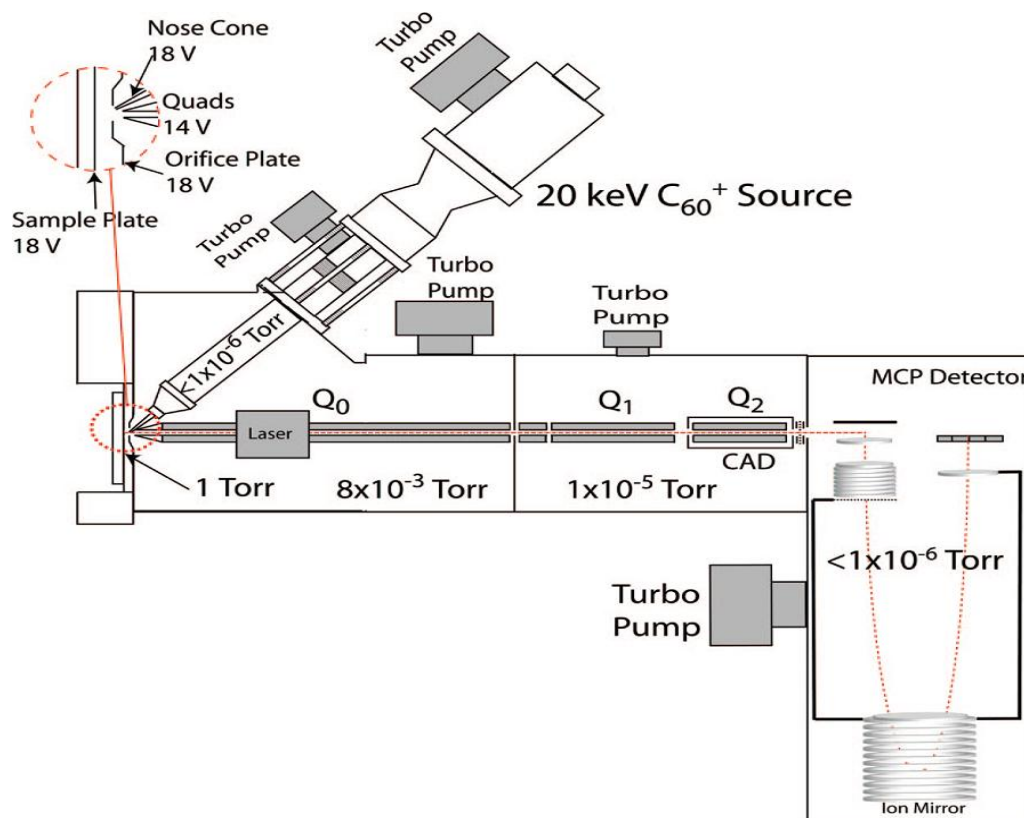


**Figure 2.6** Schematic diagram of the modified QSTAR XL hybrid QqTOF mass spectrometer. Reproduced from Carado *et al.* 2008.

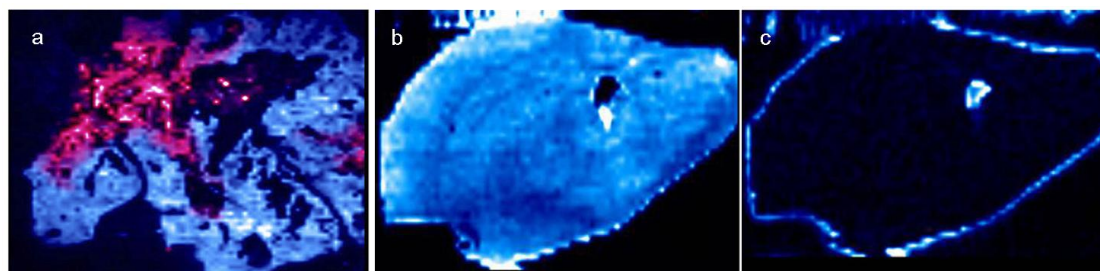


**Figure 2.7** ToF-SIMS images of selected ions. (a) lung tissue showing the 1-palmitoyl-2-oleoyl-glycerol ion ( $m/z^+$  577.5), pink and phosphocholine head group ( $m/z^+$  184) blue; (b)  $m/z^+$  184 distributed uniformly over the mouse brain cross-section; (c)  $m/z^+$  439.31 localised to the periphery of the tissue slice. Adopted and reproduced from Carado *et al.* 2008.

However in the prototype instrument the primary ion beam cannot be rastered and the stage moves in 10  $\mu\text{m}$  steps during imaging experiments, making single cell analysis impractical. Also due to the needle attached to the nose cone of the  $\text{C}_{60}^+$ , it cannot be focused to a sub-micrometer spot size. Furthermore, the image acquisition rate is also limited because until the secondary ions reach the detector the primary ion source cannot move to the next pixel. Therefore unless the drawbacks of these technologies are overcome, this instrument is still limited in its ability to perform very high spatial resolution imaging.

Our group at the University of Manchester took an alternative route and developed a new ToF-SIMS instrument using a novel methodology of mass spectrometry in collaboration with Ionoptika Ltd (Southampton, UK) and SAI Ltd (Manchester, UK) [Fletcher *et al.*, 2008]. This instrument, called the **J105 3D Chemical Imager**, has been specifically designed for the analysis of biological samples in 2D and 3D. It allows the analysis to be performed using a dc primary ion beam similar to Q-star and combines a linear buncher with a harmonic reflectron ToF analyser, Figure 2.8. The J105 instrument is an ultra-high vacuum system and is more comparable to a conventional ToF-SIMS instrument than the Q-Star hybrid in terms of sample handling, ion generation and electrostatic extraction of secondary ions.

A continuous stream of secondary ions is generated from a sample bombarded with a dc primary ion beam on the J105. This is contrast to conventional SIMS instruments mentioned above where a pulsed primary ion beam is used to generate a pulse of secondary ions. This greatly increases the analysis time as the next pulse cannot start until the secondary ions from the first pulse have been analysed. The

secondary ions generated on the J105 are extracted electrostatically and collisionally cooled in an RF only quadrupole filled with a suitable collision gas (N<sub>2</sub>) and the secondary ion stream is further energy filtered by the electrostatic analyser (E.S.A). This process results in all the ions having energy spread of 100 eV before they are injected into the linear buncher. The charged particle buncher, Figure 2.9, is approximately 30 cm long and was invented by SAI Ltd in 2006 for mass spectrometry instruments such as Gas Chromatography (GC) and MALDI and more recently on the SIMS instrument [Parr *et al.*, 2006]. It contains a series of evenly spaced electrodes arranged to generate a shaped electric field. The first buncher fitted on the J105 instrument had 30 plates and later was modified to include 60 electrodes each with an aperture through which a charged particle passes. An upgrade of the buncher consisting of 30 plates has been developed at Ionoptika with greatly improved electronic control and has been recently installed.

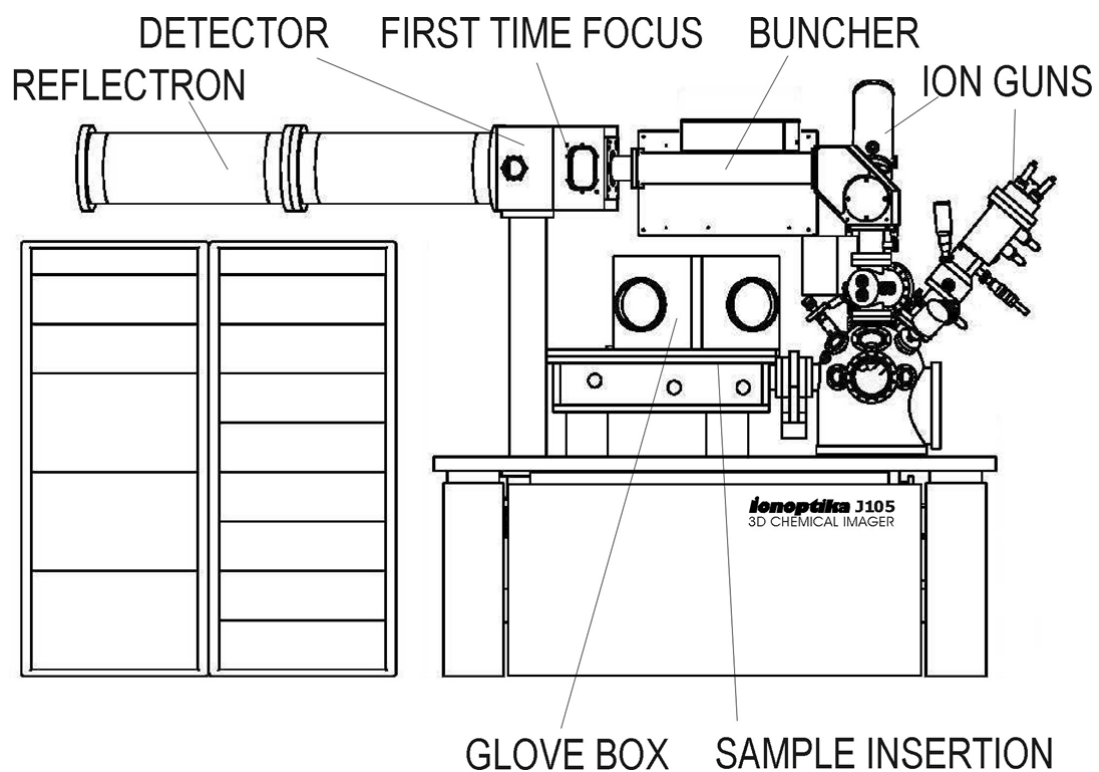


**Figure 2.8** Schematic diagram of the **J105 3D Chemical Imager** showing the coupling of the buncher to the harmonic reflectron. Reproduced from Fletcher *et al.* 2008.

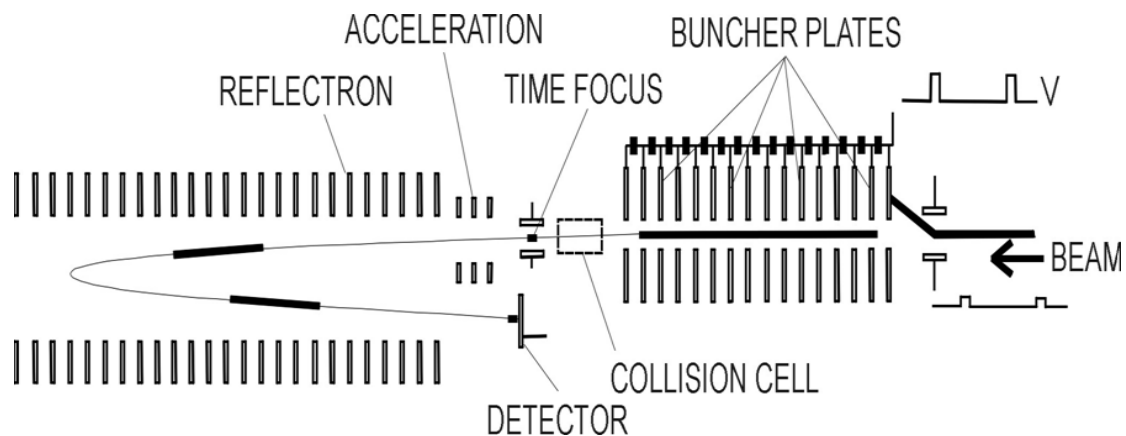


**Figure 2.9** A section of secondary ions are bunched in the time focus and accelerated into reflectron. Reproduced from Fletcher *et al.* 2008.

The buncher is filled with secondary ions for  $\sim 90 \mu\text{s}$  which is controlled by a blanker while the electric field is held at a 100 V. After  $\sim 90 \mu\text{s}$  the buncher ‘fires’ by applying an instantaneous accelerating field that varies from 7 kV at the back (entrance) to 1 kV at the front (exit). This process (which takes  $\sim 10 \mu\text{s}$ ) accelerates ions at the back faster than those at the front and ensures all the ions with the same mass reach a focus point beyond the exit of the buncher but in the same plane as the detector and at the same time. This creates a time focus at the entrance of the ToF mass analyser and the mass resolution is now dependent on the width of this tight packet of secondary ions and is independent of sample topography and sputtering events similar to the Q-star instrument. The short time primary ion pulse that determines the mass resolution in the conventional SIMS mentioned above has been replaced by the focus of this tight packet of ions leaving the buncher. Once the ions have been emitted, the field is turned off in the buncher and it is filled again with the secondary ions. The cycle repeats every 100  $\mu\text{s}$  and a duty cycle of 90% is obtained in terms of transmission for mass 500 amu and above. The ions travelling at a faster speed are reduced in transmission in line with the following equation [Hill *et al.*, 2010]:

$$\text{Transmission} = \frac{l}{t} \sqrt{\left[ \frac{m}{2Vq} \right]} * 100 \quad \text{Equation 2.2}$$

$l$  = length of the buncher

$V$  = transport voltage

$t$  = buncher filling time

This arrangement results in high transmission for molecular ions while sacrificing transmission of fragment and elemental ions. Due to the acceleration in the buncher the ions now have a 6 keV energy spread and a harmonic field ToF reflectron is required to compensate for this energy spread. In a normal ToF reflectron the ions are accelerated by an electric field of a known strength, which results in all the ions having the same kinetic energy. Thus, the time it takes for the ions to travel down the flight tube is determined by the velocity, which in turn depends on the mass to charge ratio. However, this design does not work with the buncher since the ions leaving the buncher have a very high energy spread (6 keV). This cannot be compensated by the normal ToF reflectron and a harmonic type reflectron is required in which the path of the ions is only dependent on the mass to charge ratio and not on the kinetic energy. The ions undergo half a period of simple harmonic motion in the reflectron before impacting a detector with the same time spread as the focus from the buncher.

The instrument is currently delivering mass resolution of  $m/\Delta m \sim 6000$  at 500 amu but the upgrade referred to above is expected to produce  $m/\Delta m$  in excess of 10,000. Hence by decoupling the sputtering mechanism from the mass spectrometry, an imaging instrument has been developed that enables the primary ion beam in dc mode to be exploited, together with the parallel mass detection and a mass range of the ToF analyser. Furthermore, for the first time it is now possible to carry out nanoscale imaging using ToF-SIMS without sacrificing mass resolution. In addition, mass calibration of each spectrum is no longer required and a mass accuracy of 5 ppm is observed.

The instrument is fitted with 40 kV  $C_{60}^{n+}$  and 40 kV  $Au_n^+$  ion guns. The  $C_{60}$  ion beam operates in a dc mode and can be focused down to 200 nm, Table 2.1, and is capable of producing pure 120 keV  $C_{60}^{3+}$  using a Wien filter. The gold ion gun operates in a collimated or crossover mode and can be focused to deliver ultimate spot sizes of 50 nm, Table 2.2 and Table 2.3.

**Table 2.1** Current and spot size of the 40 keV  $C_{60}^+$  primary ion beam available on different apertures, provided by Ionoptika Ltd.

Aperture ( $\mu\text{m}$ )	Current (nA)	Spot size ( $\mu\text{m}$ )
1000	1.056	40
300	0.100	15
100	0.045	08
100	0.005	03
30	0.001	0.8
30	0.0006	0.5

**Table 2.2** Current and spot size of the 40 keV  $Au_3^+$  primary ion beam available on different apertures, provided by Ionoptika Ltd.

Aperture ( $\mu\text{m}$ )	Current (nA)	Spot size (nm)
1000	> 90	< 400
100	> 0.008	< 150
30	> 0.001	< 100

**Table 2.3** Current and spot size of the 40 keV Au<sup>+</sup> primary ion beam available on different apertures, provided by Ionoptika Ltd.

Aperture (μm)	Current (nA)	Spot size (nm)
1000	> 2.00	< 500
300	> 1.00	< 300
100	> 0.15	< 150
30	> 0.015	< 100

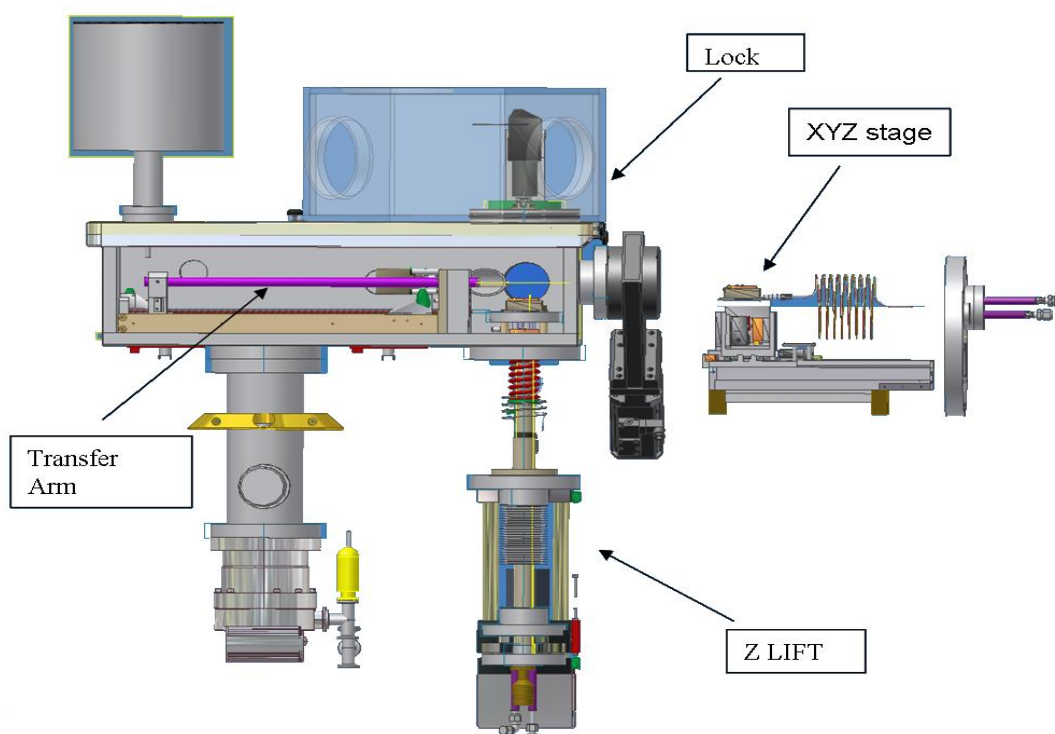


**Figure 2.10** Schematic of J105 sample handling system with main components Transfer Arm, Lock, Z lift, XYZ stage. Reproduced from the Sample Handling Manual courtesy of Ionoptika.

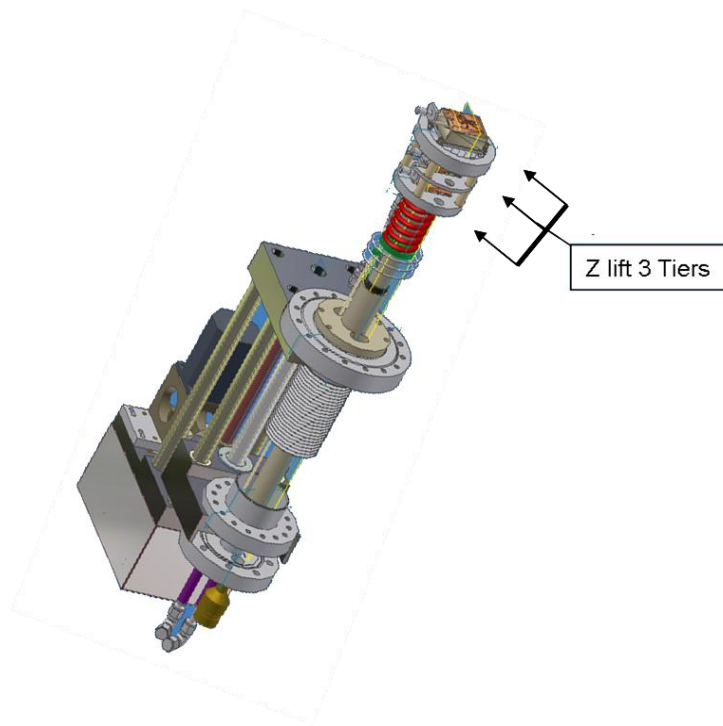


**Figure 2.11** Z lift to show the three tiers to hold three sample stubs. Reproduced from the Sample Handling Manual courtesy of Ionoptika.

One of the difficulties encountered when analysing biological samples using ToF-SIMS is their handling and manipulation under a high vacuum. The J105 has an automated sample handling system which allows the sample to be inserted and transferred easily. It consists of three parts, a Z lift, a transfer arm in the Preparation Chamber and XYZ stage in the Surface Analysis Chamber (SAC), Figure 2.10.

The Z-lift is a vertical stage inside the Preparation Chamber that moves up and down only. To insert the sample the Z-lift is brought up into the lock position where it seals against the lid of the Preparation Chamber so that the load lock can be vented. The sample is placed on the top tier and the lock is pumped out using a rotary pump and then a fine pumping line connected to the Preparation Chamber. Once a pressure of

$1 \times 10^{-5}$  mbar has been achieved, the sample is transferred down into the Preparation Chamber. The sample handling system is designed so that it can accommodate three samples stubs in the Preparation Chamber but only the top one can be heated or cooled, Figure 2.11. A specifically designed steel plate is used as a substrate and is placed on the copper sample holder which is 40 mm long  $\times$  30 mm wide  $\times$  12 mm thick, Figure 2.12. Once the sample has been pumped down and pressure of  $1 \times 10^{-6}$  mbar has been achieved in the Preparation Chamber the sample is transferred to the XYZ stage in the SAC using a transfer arm. The transfer arm can also be used to transfer sample stubs between different tiers of the Z-lift and although it is not heated or cooled it transfers the sample rapidly enough to maintain the temperature required. The XYZ stage is the analysis stage in the SAC and the height of this can be adjusted through computer control to accommodate different sample thicknesses.

The instrument is fitted with two cameras, one is on Load Lock, where the sample is inserted but focuses on the sample surface when the Z-lift is lowered into the Preparation Chamber. This provides a complete view of the sample stub and the picture can be saved and imported into the sample handling software and used to navigate around the sample. The second camera is fitted on the SAC, showing the area of analysis and it only focuses when the sample is at the correct height.

The SED imaging system controls the rastering of the ion beam and is used to acquire and save a secondary electron microscopy (SEM) image of the sample. It is used to measure the sample current into a Faraday cup on sample stub as well as to tune the focus of the ion guns in preparation for imaging experiments.

The instrument also incorporates an electron gun (10 eV to 1 keV) used for neutralising the sample. As a sample surface is bombarded with a positive primary ion beam the potential of the surface increases due to the positive charge input and emission of secondary electrons. The sample becomes charged and results in a loss of secondary ions because the kinetic energy of the emitted ions is so large that it is not accepted by the analyser. In order to counteract this charging an electron flood gun is used which bombards the surface with low energy electrons. These electrons are attracted to the region of positive charge on the surface and the potential of the surface returns back to neutral. It is important to select a correct dose of electrons because if it is too low the sample surface will not be neutralised and if it is too high it can damage the surface [Gilmore *et al.*, 2002].

Analysis of biological samples including cells and tissue using SIMS is an important research area of many labs. Sample preparation, discussed in detail in chapter 5 has a significant effect on the results obtained. The literature shows that the freeze-fractured frozen-hydrated technique to be successful to some degree in maintaining the sample's physical and chemical morphology [Colliver *et al.*, 1997], [Strick *et al.*, 2001]. However, frozen-hydrated and freeze-fractured samples are not routinely analysed on ToF-SIMS instruments due to the complexity of the procedure.

The automated sample handling facility on the J105 allows these experiments to be carried out more routinely. Both the Z lift and the XYZ stage are each connected to separate liquid nitrogen (LN<sub>2</sub>) dewers containing copper coils. During the frozen-hydrated experiment, LN<sub>2</sub> is poured into these dewers and nitrogen gas is passed through the coils, which in turn passes through the sample carriers and then out of the

instrument and vented to the atmosphere. As the gas passes through the coils it is cooled close to the LN<sub>2</sub> temperature and this transfer of heat is then passed to the sample carrier. The Z lift and XYZ stage are designed to be temperature controlled between 95 K to 700 K and to achieve this they are fitted with a PT100 sensor. The temperature control unit allows the operator to control and measure the temperature accurately and efficiently in the Preparation Chamber in the Z lift and XYZ stage in the SAC. The sample stubs are also fitted with a PT100 sensor which allows one to measure the sample temperature, Figure 2.12. This was previously not possible on our conventional ToF-SIMS instrument, the Bio-ToF since a high voltage is applied to the stage during an acquisition which hinders the measurement of the temperature of the sample. Figure 2.13 shows the temperature plot acquired during testing of the instrument.

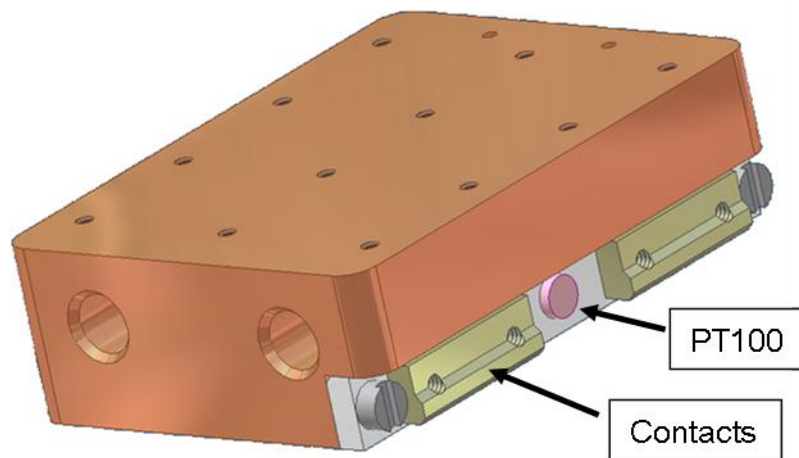


**Figure 2.12** Sample holder for the J105 made up of copper with dimensions of 40 mm long × 30 mm wide × 12 mm thick. Reproduced from the Sample Handling Manual courtesy of Ionoptika.

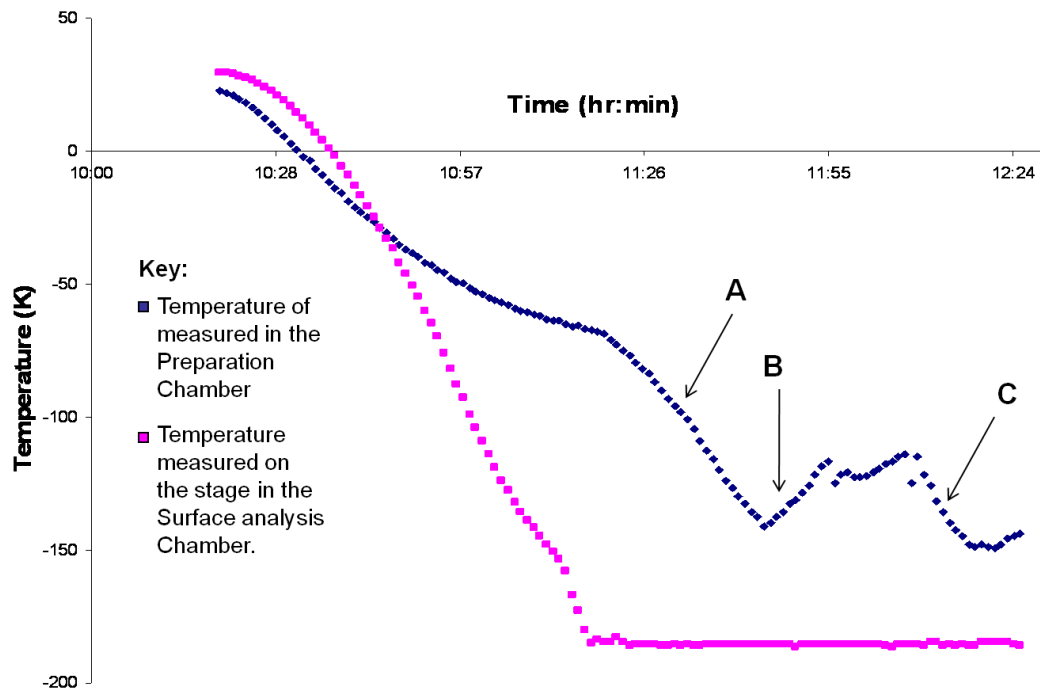


**Figure 2.13** Temperature plot acquired during cooling the instrument. Key: blue- temperature measured on the Z-lift in the Preparation Chamber; pink- temperature measured on the stage in the Surface analysis Chamber (SAC). A: The dewers were refilled again for cooling; B: Warming up; C: Cooling again.

The instrument also has a novel facility for carrying out automated freeze-fracture of biological sample *in situ* using a special device called the “mousetrap”, Figure 2.14. The sample is sandwiched between the two metal plates and rapidly frozen in liquid nitrogen-cooled propane. The frozen sample is then transferred to a liquid nitrogen flask containing the freeze-fracture device and the sample is mechanically fixed on it while under nitrogen. The sample is transferred to an argon purged glove box fitted above the sample insertion flange. The glove box is purged for 10 minutes prior to

sample transfer to prevent water deposition on the sample and on the pre-cooled sample holder on the Z-lift which is exposed during sample insertion. Once inserted in the lock position and pumped, the sample is transferred to the Preparation Chamber and the sample is fractured *in situ* by pushing the trigger on the device. This action automatically releases the top plate of the steel which flips backwards fracturing the sample. Unlike previous vacuum freeze fracture devices, the two surfaces of material are retained and available for analysis. The fractured sample is transferred to the pre-cooled analysis stage and cells are analysed in a frozen-hydrated state. The instrument also incorporates a cryo-shield fixed above the sample Preparation Chamber to minimise re-condensation of water vapour once the sample is fractured. Using this device, the cold sample is never exposed to damp atmosphere and it is already cold when it enters the vacuum system, avoiding long cooling times or sample degradation during pump down. This facility combined with the instrument's ability to analyse simultaneously at high spatial resolution and high mass resolution provides a powerful tool for tissue analysis and even individual cell analysis.

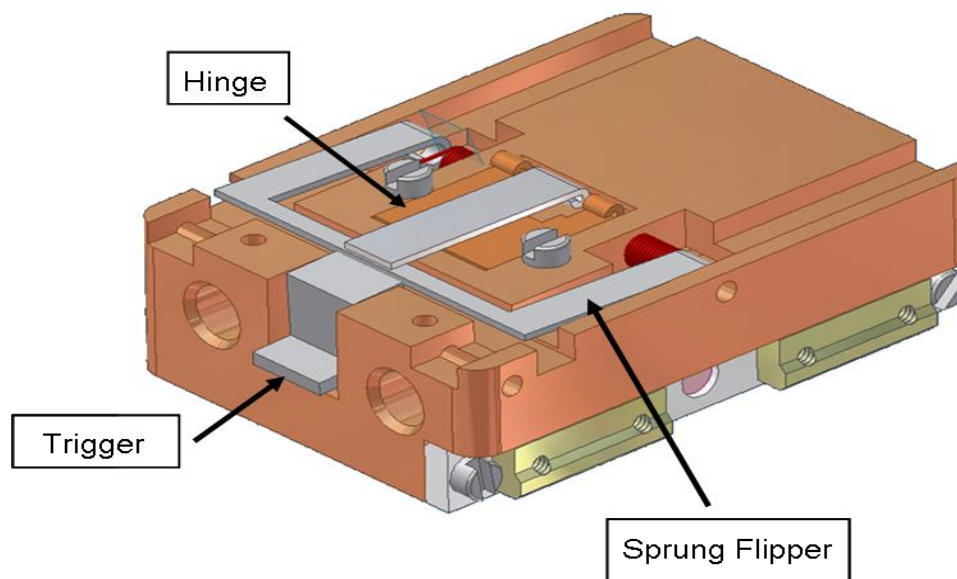


**Figure 2.14** Mousetrap freeze-fractured device as developed by Ionoptika Ltd for the J105 instrument. Reproduced from the Sample Handling Manual courtesy of Ionoptika.

A further requirement of the instrument was its ability to perform tandem MS/MS on pure and complex samples such as cells to help identify the unknown peaks routinely observed during the analysis of these samples. In the J105 MS/MS analysis is performed in ToF-ToF configuration. The ions leaving the buncher pass through a cell containing a suitable collision gas such as nitrogen, helium or argon where they are fragmented. Since the collision takes place after the buncher and as the collision energy is in the range of 1-7 kV it causes all of the ions to fragment. However, as the collision takes place in a field free region of the instrument the parent ion and the associated daughter ions continue to travel at the same speed and a timed ion gate is used to select the parent ion of interest along with its daughter ions. These are passed into to the ToF analyser for the analysis.

The analysis software was developed by SAI Ltd and is similar to that provided for their MALDI instrument. It allows tuning the instrument, switching from positive to negative mode as well as saving presets. Further, the software allows the acquisition of a single tiled image or a series of tiled images for depth profiling experiments as well as multiple tiled images for a large area analysis required for tissue imaging. The rate at which the data is generated using the J105 is extremely high and new approaches for data processing visualisation and manipulation are required, discussed further in Chapter 5.

In summary, the **J105 3D Chemical Imager** instrument is able to fully exploit the properties of polyatomic ion beams while providing high mass resolution imaging using a continuous primary ion beam, increasing the duty cycle and improving the quality of the mass spectra. The increase in duty cycle allows depth profile and 3D imaging experiments to be carried out without the interleaved analyse/etch method, thus maximising sensitivity. The increase in the acquisition rate also aids in large area imaging of tissue sections.

## References

Adriaensen, L.; Vangaever, F.; Lenaerts, J.; Gijbels, R. **Matrix-enhanced secondary ion mass spectrometry: the influence of MALDI matrices on molecular ion yields of thin organic films.** Rapid Communications in Mass Spectrometry (2005), 19, 1017-1024

Altelaar, A. F. M.; Klinkert, I.; Jalink, K.; de Lange, R. P. J.; Adan, R. A. H.; Heeren, R. M. A.; Piersma, S. R. **Gold-Enhanced Biomolecular Surface Imaging of Cells and Tissue by SIMS and MALDI Mass Spectrometry.** Analytical Chemistry (2006), 78, 734-742

Altelaar, A. F. M.; Minnen, J. V.; Jiménez, C. R.; Heeren, R. M. A.; Piersma, S. R.; **Direct Molecular Imaging of Lymnaea Stagnalis Nervous Tissue at Subcellular Spatial Resolution by Mass Spectrometry.** Analytical Chemistry (2005), 77, 735-741

Andersen, H. H.; Bay, H. L. **Nonlinear effects in heavy-ion sputtering.** Journal of Applied Physics (1974), 45 (2), 953-954

Appelhans, A. D.; Delmore, J. E. **Comparison of polyatomic and atomic primary beams for secondary ion mass spectrometry of organics.** Analytical Chemistry (1989), 61 (10), 1087-1093

Arlinghaus, H. F.; Kriegeskotte, C.; Fartmann, M.; Wittig, A.; Sauerwein, W.; Lipinsky, D. **Mass spectrometric characterization of elements and molecules in cell cultures and tissues.** Applied Surface Science (2006), 252, 6941-6948

Arlinghaus, H.F. **Possibilities and limitations of high-resolution mass spectrometry in life science.** Applied Surface Science (2008), 255, 1058-1063

Benguerba, M.; Brunelle, A.; Della-Negra, S.; Depa UW, J.; Joret, H.; Le Beyec, Y.; Blain, M. G.; Schweikert, E. A.; Assayag, G. B.; Sudraud, P. **Impact of slow gold clusters on various solids : nonlinear effects in secondary ion emission.** Nuclear Instruments and Methods in Physics Research (1991), B62, 8-22

Blain, M. G.; Della-Negra, S.; Joret, H.; Le Beyec, Y.; Schweikert, E. A. **Secondary-ion yields from surfaces bombarded with keV molecular and cluster ions.** Physical Review Letters (1989), 63 (15), 1625-1628

Blain, M. G.; Della-Negra, S.; Joret, H.; Le Beyec, Y.; Schweikert, E.A. (1990) J. Vac. Sci. Technol., 8, 2265

Busch, K.L.; Hsu, B.H.; Xie, Y.-X.; Cooks, R.G. **Matrix effect in secondary ion mass spectrometry.** Analytical Chemistry (1983), 55 (7) 1157-1160

Carado, A.; Passarelli, M. K.; Kozole, J.; Wingate, J. E.; Winograd, N.; Loboda, A. V. **C<sub>60</sub> secondary ion mass spectrometry with a hybrid-quadrupole orthogonal time-of-flight mass spectrometer**. *Analytical Chemistry*, (2008), 80 (21), 7921-7929

Carado, A.; Kozole, J.; Passarelli, M.; Winograd, N.; Loboda, A.; Bunch, J.; Wingate, J.; Hankin, J.; Murphy, R. **Biological tissue imaging with a hybrid cluster SIMS quadrupole time-of-flight mass spectrometer**. *Applied Surface Science* (2008), 255, 1572–1575

Colliver, T. L.; Brummel, C. L.; Michael L. Pacholski, M. L.; Swanek, F. D.; Ewing, A. G.; Winograd, N. **Atomic and Molecular Imaging at the Single-Cell Level with TOF-SIMS**. *Analytical Chemistry* (1997), 69, 2225-2231

Davies, N.; Weibel, D. E.; Blenkinsopp, P.; Lockyer, N.; Hill, R.; Vickerman, J. C. **Development and experimental application of a gold liquid metal ion source**. *Applied Surface Science* (2003), 203-204, 223-227

Deline, V.R.; Katz, W.; Evans, Jr.; C.A.; Williams, P. **Mechanism of the SIMS matrix effect**. *Applied Physics Letters* (1978), 33(9), 832-835

Fartmann, M.; Kriegskotte, C.; Dambach, S.; Wittig, A.; Sauerwein, W.; Arlinghaus, H. F. **Quantitative imaging of atomic and molecular species in cancer cell cultures with TOF-SIMS and Laser-SNMS**. *Applied Surface Science* (2004), 428, 231–232

Fletcher, J.S. **Cellular imaging with secondary ion mass spectrometry**. *Analyst* (2009), 134, 2204–2215

Fletcher, J.S.; Henderson, A. Biddulph, G.X.; Vaidyanathan, S.; Lockyer, N.P.; Vickerman, J.C. **Uncovering new challenges in bio-analysis with ToF-SIMS**. *Applied Surface Science* (2008), 255, 1264–1270

Fletcher, J.S.; Lockyer, N.P.; Vickerman, J.C. **A new SIMS paradigm for 2D and 3D molecular imaging of bio-systems**. *Analytical and Bioanalytical Chemistry* (2010), 396, 85-104

Fletcher, J.S.; Lockyer, N.P.; Vickerman, J.C. **Developments in molecular SIMS depth profiling and 3D imaging of biological systems using polyatomic primary ions**. *Mass Spectrometry Reviews* (2010)

Fletcher, J.S.; Rabbani, S.; Henderson, A.; Blenkinsopp, P.; Thompson, S.P.; Lockyer, N. P.; Vickerman, J. C. **A new dynamic in mass spectral imaging of single biological cells**. *Analytical Chemistry*, (2008), 80 (23), 9058-9064

Garrison, B.J.; Postawa, Z. **Computational view of surface based organic mass spectrometry**. *Mass Spectrometry Reviews* (2008), 27 (4), 289-315

Gillen G. In Proceedings of the International Conference on Microbeam Analysis, 8-15 July 2000, Institute of Physics Conference Series (2000), 165, 339

Gillen, G.; Hues, S.M. **Doped gelatin films as a model matrix for molecular secondary ion mass spectrometry studies of biological soft tissue.** Journal of the American Society for Mass Spectrometry (1993), 4(5), 419-423

Gilmore, I. S.; Seah, M.P. **Electron flood gun damage in the analysis of polymers and organics in time-of-flight SIMS.** Applied Surface Science (2002), 187 (1-2), 89-100

Hill, R.; Blenkinsopp, P.; Thompson, S.P.; Fletcher, J.S.; Vickerman, J.C; Surface Interface Analysis (2010), submitted

Hoffmann, E.; Stroobant, V. **Mass Spectrometry Principles and Applications.** John Wiley and Sons Ltd, Chichester 2007

Jen Wu, K.; Odom, R.B. **Matrix-Enhanced Secondary Ion Mass Spectrometry: A Method for Molecular Analysis of Solid Surfaces.** Analytical Chemistry (1996), 68, 873-882

Johar, S. S.; Thompson, D. A. **Spike effects in heavy-ion sputtering of Ag, Au and Pt thin films.** Surface Science, (1979) 90 (2), 319-330

Jonkman, H.T.; Michl, J.; King, R.N.; Andrade, J.D. **Low-temperature secondary positive ion mass spectrometry of neat and argon-diluted organic solids.** Analytical Chemistry (1978), 50 (14), 2078-2082

Kollmer, F. **Cluster primary ion bombardment of organic materials** Applied Surface Science (2004), 231-232, 153-158

Kötter, F.; Benninghoven, A. **Secondary ion emission from polymer surfaces under Ar<sup>+</sup>, Xe<sup>+</sup> and SF<sub>5</sub><sup>+</sup> ion bombardment.** Applied Surface Science (1998), 133 (1-2), 47-57

Lorey II, D.R.; Morrison, G.H.; Chandra, S. **Dynamic secondary ion mass spectrometry analysis of boron from boron neutron capture therapy drugs in co-cultures: Single-cell imaging of two different cell types within the same ion microscopy field of imaging.** Analytical Chemistry (2001), 73 (16), 3947-3953

McDonnell, L.; Piersma, S. R.; Altelaar, A. F. M.; Mize, T. H.; Luxembourg, S .L.; Verhaert, P. D. E. M.; Minnen, J.V.; Heeren, R.M.A. **Subcellular imaging mass spectrometry of brain tissue.** Journal of Mass Spectrometry (2005), 40, 160-168

Nygren, H.; Eriksson, C.; Malmberg, P.; Sahlin, H.; Carlsson, L.; Lausmaa, J.; Sjövall, P. **A cell preparation method allowing subcellular localization of cholesterol and phosphocholine with imaging TOF-SIMS.** Colloids and Surfaces B: Biointerfaces (2003), 30, 87-92

Nygren, H.; Malmberg, P. **Silver deposition on freeze-dried cells allows subcellular localization of cholesterol with imaging TOF-SIMS.** Journal of Microscopy (2004), 215, 156–161

Ostrowski, S. G.; Van Bell, C. T.; Winograd, N.; Ewing, A. G. **Mass Spectrometric Imaging of Highly Curved Membranes During Tetrahymena Mating.** Science (2004), 305, 71-73

Parr, V.C.; Thompson, S.P.; Mills, M.D. **Charged Particle Buncher.** United State Patent, May 2006.

Sjövall, P.; Lausmaa, J.; Nygren, H.; Carlsson, L.; Malmberg, P. **Imaging of Membrane Lipids in Single Cells by Imprint-Imaging Time-of-Flight Secondary Ion Mass Spectrometry.** Analytical Chemistry (2003), 75, 3429-3434

Strick, R.; Strissel, P.L.; Gavrillov, K.; Levi-Setti, R. **Cation-chromatin binding as shown by ion microscopy is essential for the structural integrity of chromosomes.** Journal of Cell Biology (2001), 155 (6), 899-910

The Sample Handling Manual by Ionoptika (private communication)

Weibel, D.; Wong, S.; Lockyer, N.; Blenkinsopp, P.; Hill, R.; Vickerman, J.C. **A C<sub>60</sub> primary ion beam system for time of flight secondary ion mass spectrometry: Its development and secondary ion yield characteristics.** Analytical Chemistry (2003), 75 (7), 1754-1764

Williams, P. **On mechanism of sputtered ion emission.** Applications of Surface Science (1982), 13 (1-2), 241-259

Winograd, N. **The magic of cluster SIMS.** Analytical Chemistry (2005), 77 (7), 142A-A149A

Wittmaack, K. **Secondary-ion emission from silicon bombarded with atomic and molecular noble-gas ions.** Surface Science (1979), 90 (2), 557-563

Wong, S.C.C.; Hill, R.; Blenkinsopp, P.; Lockyer, N.P. Weibel, D.E.; Vickerman, J.C. **Development of a C<sub>60</sub><sup>+</sup> ion gun for static SIMS and chemical imaging.** Applied Surface Science (2003), 203-204, 219-222

## 3 Characterization of the J105 3D Chemical Imager

### 3.1 Introduction

The new instrument, the Ionoptika **J105 3D Chemical Imager**, was delivered in March 2008 and installed at the University of Manchester by engineers from Ionoptika, SAI and research associate J.S. Fletcher in the Vickerman group. This Chapter discusses the current performance of the J105 for the analysis of organic samples with respect to a conventional ToF-SIMS instrument, the BioToF [Braun *et al.*, 1998]. Further, the instrument's ability to perform tandem MS is also explored followed by a sensitivity test to determine the lowest concentration of a compound that produces a peak.

Once in operation, the instrument was tuned using an inorganic standard, caesium iodide (CsI), typically used in SIMS to study ion cluster formation and emission [Honda *et al.*, 1978], [Barlak *et al.*, 1981], [Ens *et al.*, 1983]. Since it is relatively stable under bombardment by the primary ion, it is commonly used for tuning and calibration of the SIMS instruments. The behaviour of CsI cluster formation has also been investigated by fast atom bombardment (FAB) tandem MS [Baldwin *et al.*, 1983].

The analysis of CsI on the J105 was performed by using a 20 keV  $C_{60}^+$  primary ion beam in a dc mode. Figure 3.1 shows the spectra of CsI clusters  $(Cs_{n+1}I_n)^+$  with the main peaks  $[Cs]^+$   $m/z$  132.905 and  $[Cs_2I]^+$   $m/z$  392.715 used for tuning the quadrupole, electrostatic analyser (E.S.A) and the buncher voltages to obtain the maximum counts per ion impact.

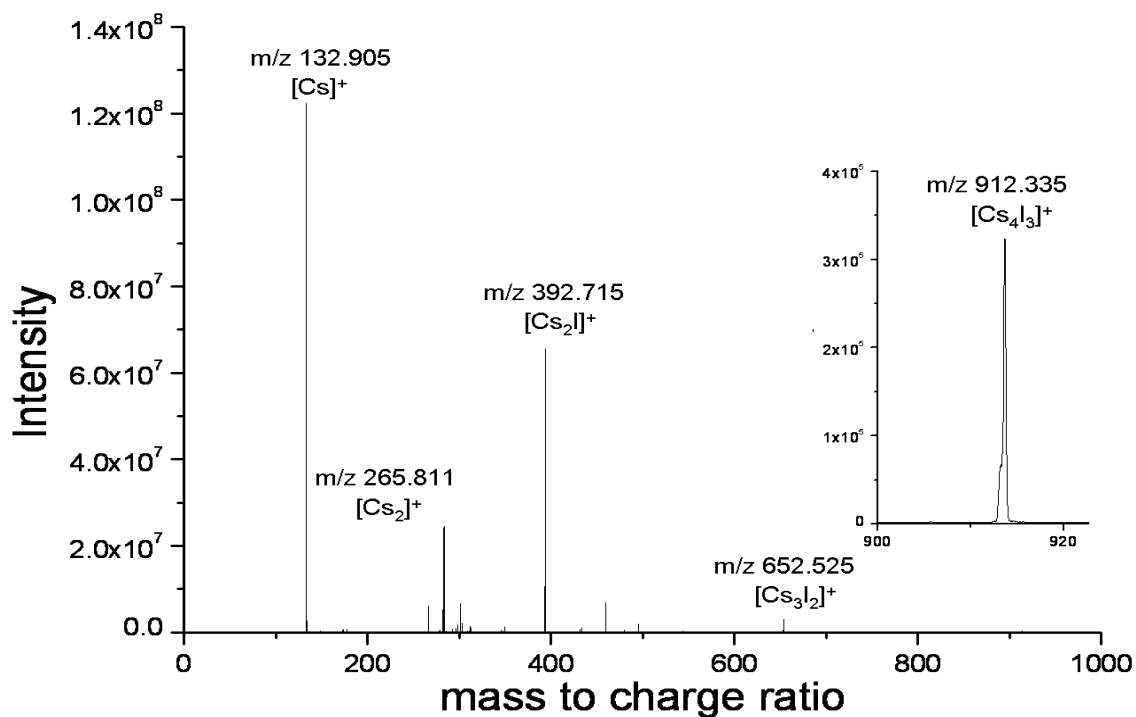


**Figure 3.1** ToF-SIMS spectrum of CsI acquired using 20 keV  $C_{60}^+$  primary ion beam over an area of  $500 \times 500 \mu\text{m}^2$  with  $32 \times 32$  pixels and ion fluence of  $1 \times 10^{13}$  ions/cm<sup>2</sup>.

## 3.2 Comparison between the J105 and the BioToF

### 3.2.1 Experimental

Thick films of arginine, cholesterol and a tetrapeptide (Glycine-Glycine-Tyrosine-Arginine) (GGYR) were prepared by using dried droplets on Si wafers to obtain a fractional coverage of 1. Static surface spectra of these samples were acquired on the J105 using a 20 keV  $C_{60}^+$  primary ion beam (110 pA) with  $32 \times 32$  pixels over an area of  $500 \times 500 \mu\text{m}^2$  covering a mass range of 0-1200 amu. The BioToF data,

provided by A. Piwowar for comparison, was also acquired under static conditions using a 20 keV  $C_{60}^+$  ion beam.

### 3.2.2 Results and Discussion

The standard spectra acquired on the J105 shows the current performance of the instrument which changes with tuning of the voltages or any upgrade on the instrument. Arginine is a basic amino acid with a monoisotopic molecular mass of 174.11 g/mol, and empirical formula  $C_6H_{14}N_4O_2$ , Figure 3.2. Following bombardment with a primary ion beam, arginine forms a molecular ion  $[M+H]^+$  at  $m/z$  175.119 with diagnostic fragment ions at  $m/z$  158.093 formed due to loss of  $NH_3$ ,  $m/z$  130.098 an immonium ion and  $m/z$  112.087 formed by loss of  $NH_3$  from ion at  $m/z$  129.114 shown in Figure 3.3 and 3.4. The formation of the fragment ions of arginine are discussed later in this chapter.

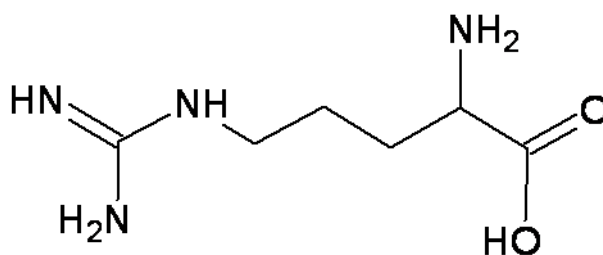


**Figure 3.2** The chemical structure of arginine,  $C_6H_{14}N_4O_2$ , monoisotopic mass 175.11 g/mol.

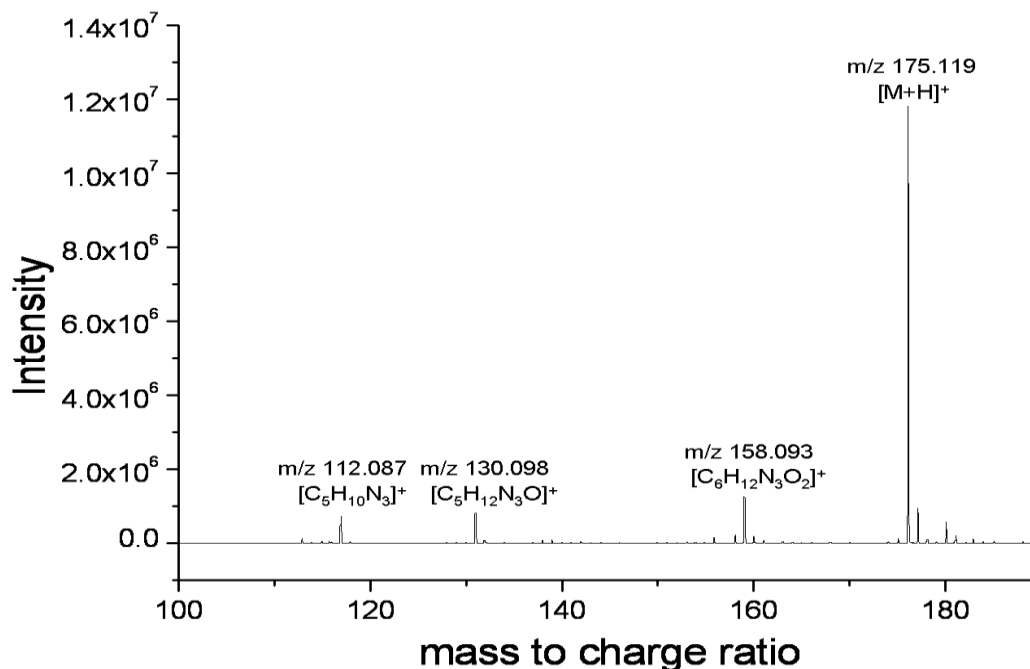


**Figure 3.3** ToF-SIMS spectrum of arginine acquired on the J105 with 20 keV  $C_{60}^+$  at ion dose of  $1 \times 10^{13}$  ions/cm<sup>2</sup>.

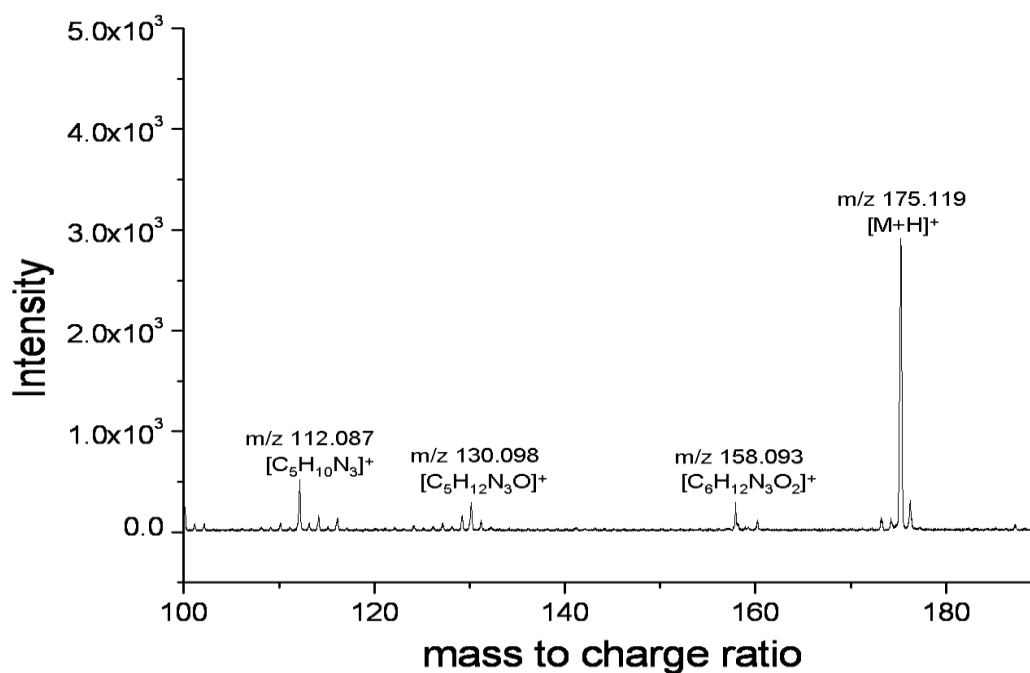


**Figure 3.4** ToF-SIMS spectrum of arginine acquired on the BioToF with 20 keV  $C_{60}^+$  at ion dose of  $1 \times 10^{13}$  ions/cm<sup>2</sup>.

Cholesterol is a steroid with a monoisotopic molecular mass of 386.35 g/mol, and empirical formula  $C_{27}H_{46}O$ , Figure 3.5. It is also classed as a sterol due to the OH group which gives it an amphiphilic character. It is highly abundant in the cell membrane where it helps to maintain the membrane permeability as well as play a key role in assisting cells to communicate with each other. It is also present in the membrane of other organelles such as mitochondria and endoplasmic reticulum. Following an impact with a primary ion beam, cholesterol forms a pseudo-molecular ion  $[M-H]^+$   $m/z$  385.347 and a diagnostic fragment ion at  $m/z$  369.352 formed by a loss of OH, Figure 3.6 and Figure 3.7.

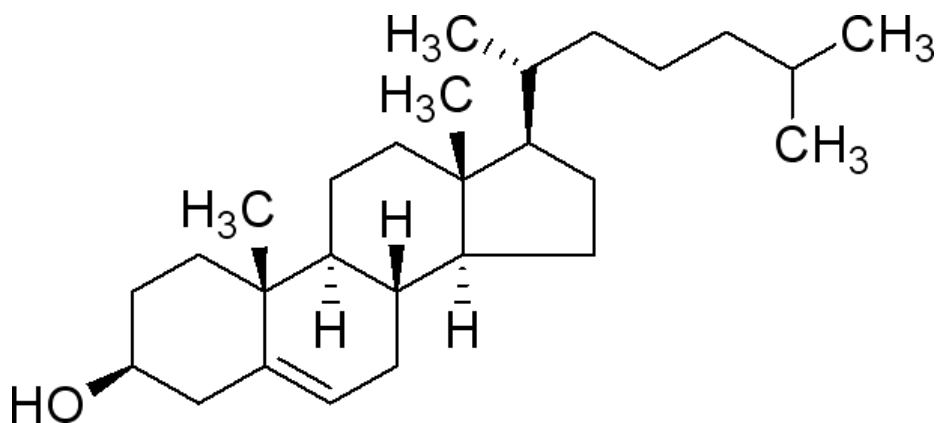


**Figure 3.5** The chemical structure of cholesterol,  $C_{27}H_{46}O$ , monoisotopic mass 386.35 g/mol.

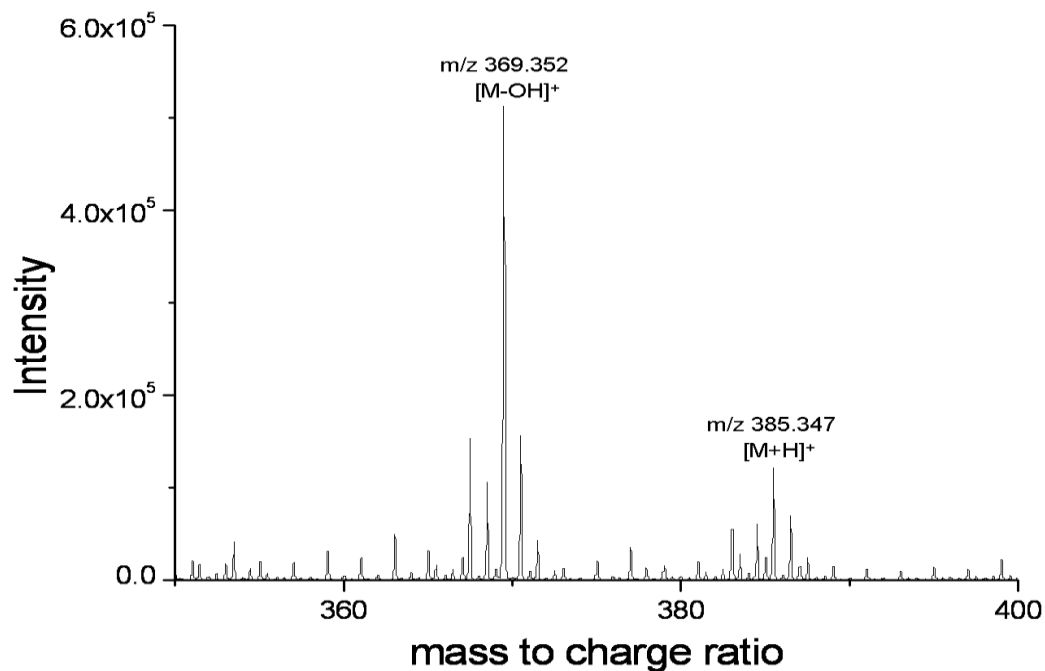


**Figure 3.6** ToF-SIMS spectrum of cholesterol acquired on the J105 with 20 keV  $C_{60}^+$  at ion dose of  $1 \times 10^{13}$  ions/cm<sup>2</sup>.

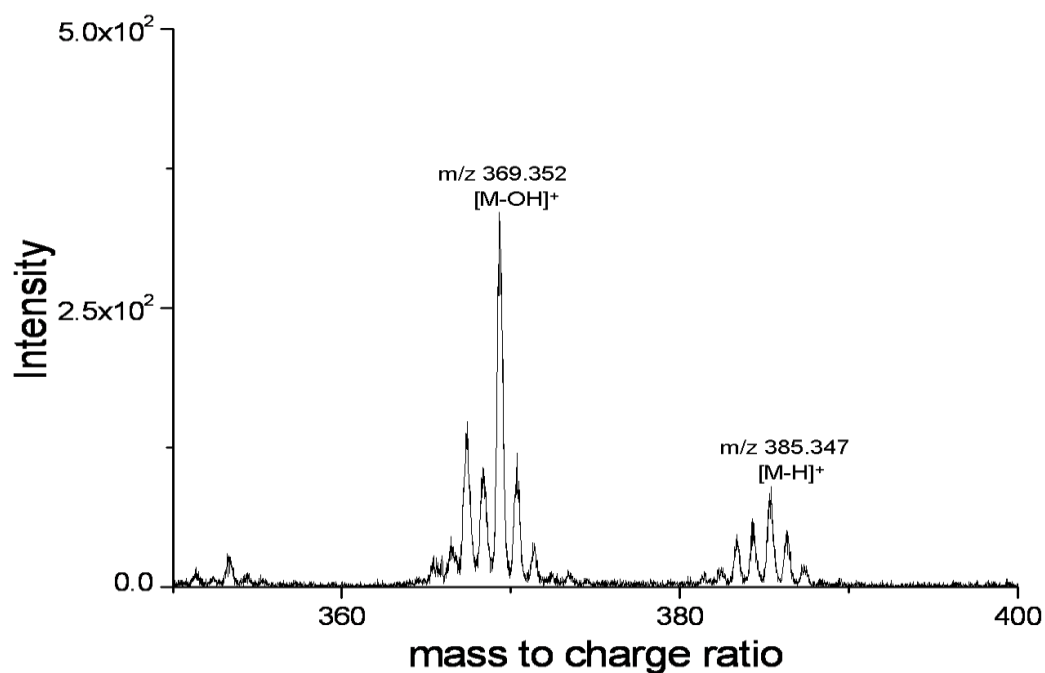


**Figure 3.7** ToF-SIMS spectrum of cholesterol acquired on the BioToF with 20 keV  $C_{60}^+$  at ion dose of  $1 \times 10^{13}$  ions/cm<sup>2</sup>.

The tetrapeptide consists of four amino acids Glycine-Glycine-Tyrosine-Arginine (GGYR) and has a monoisotopic mass of 451.23 g/mol, and empirical formula  $C_{19}H_{29}N_7O_6$ , Figure 3.8. The mechanism for the formation of fragment ions from a peptide was first devised by Roepstorff and Fohlman in 1984 which was later modified by Johnson and co-workers in 1987. The scheme for the formation of fragment ions is shown in Figure 3.9. The authors' show that a peptide can fragment to give ions classed as a, b or c if the charge is retained on the N terminal fragment. However, if the charge is preserved on the C terminal then the ions are classified as x, y or z ions, show in Figure 3.10 [Roepstorff *et al.*, 1984], [Johnson *et al.*, 1987]. The molecular ion  $[M+H]^+$  of the peptide is clearly visible at  $m/z$  452.226 which fragments to produce many characteristics ions, Figure 3.11 and Figure 3.12. Following the fragmentation mechanism of a peptide in Figure 3.9 and Figure 3.10, the tetrapeptide (GGYR), Figure 3.8, produces numerous fragments shown in Table 3.1.

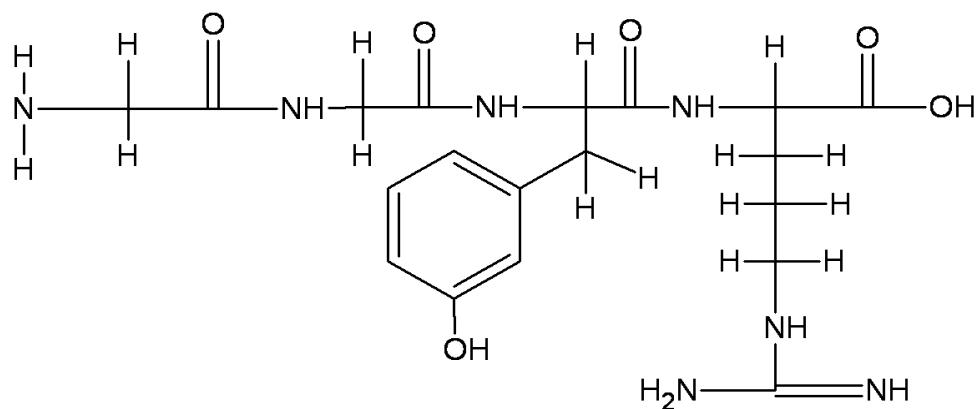


**Figure 3.8** The chemical structure of the tetrapeptide (GGYR),  $C_{19}H_{29}N_7O_6$ , monoisotopic mass 451.23 g/mol.

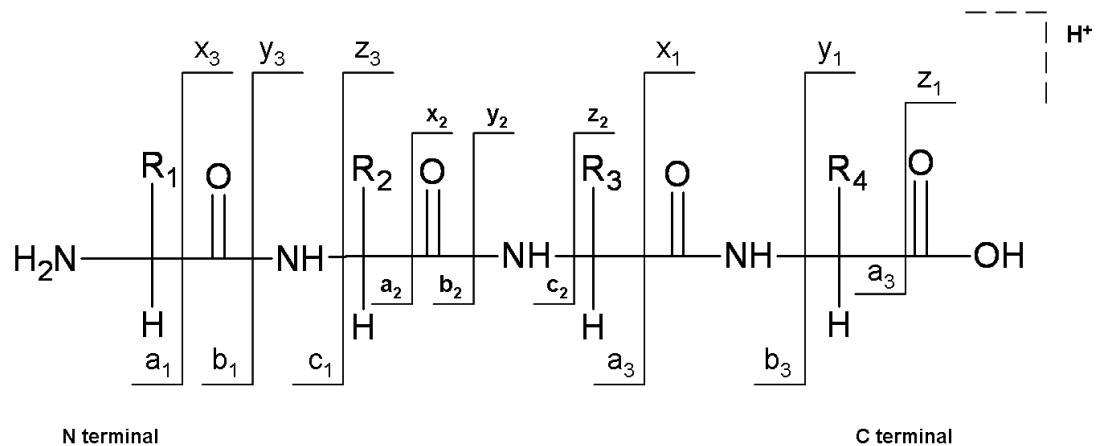


**Figure 3.9** Scheme for the formation of fragment ions in a peptide as suggested by Roepstorff *et al.* 1984 and Johnson *et al.* 1987.

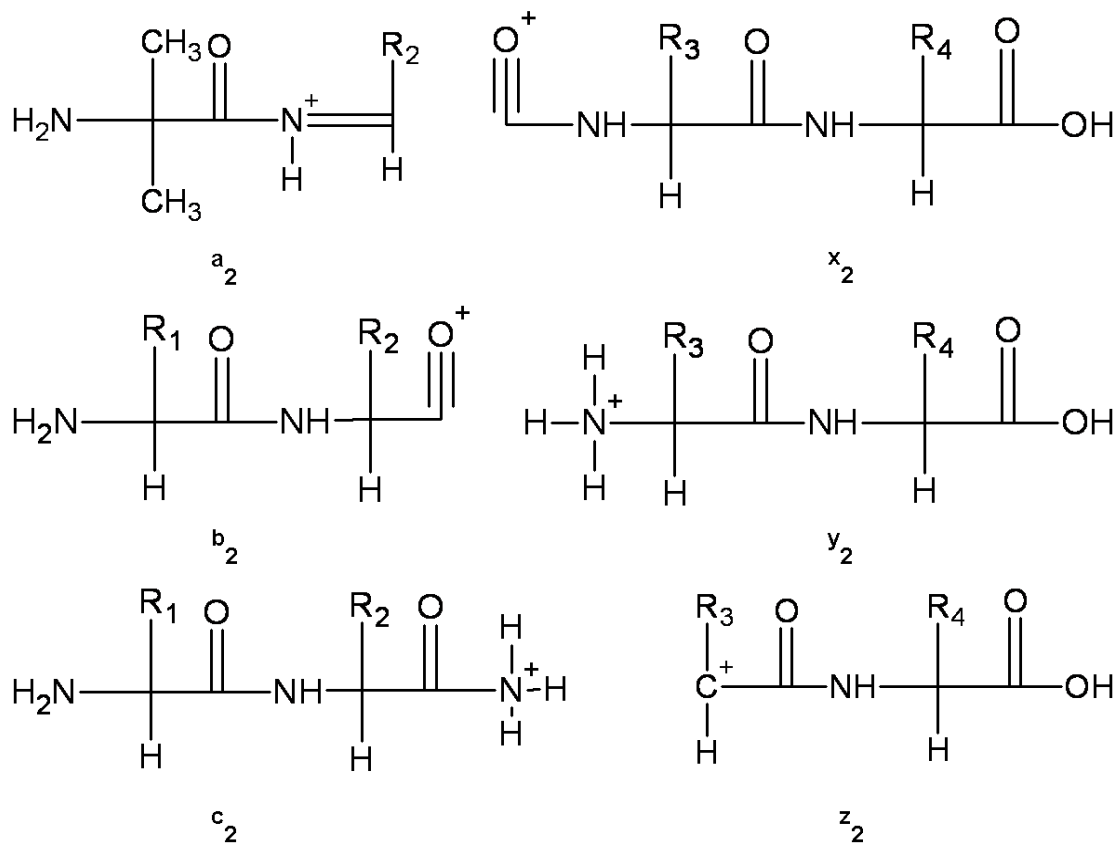


**Figure 3.10** Structures of the charged sequence fragment ion, as suggested by Roepstorff *et al.* 1984 and Johnson *et al.* 1987.

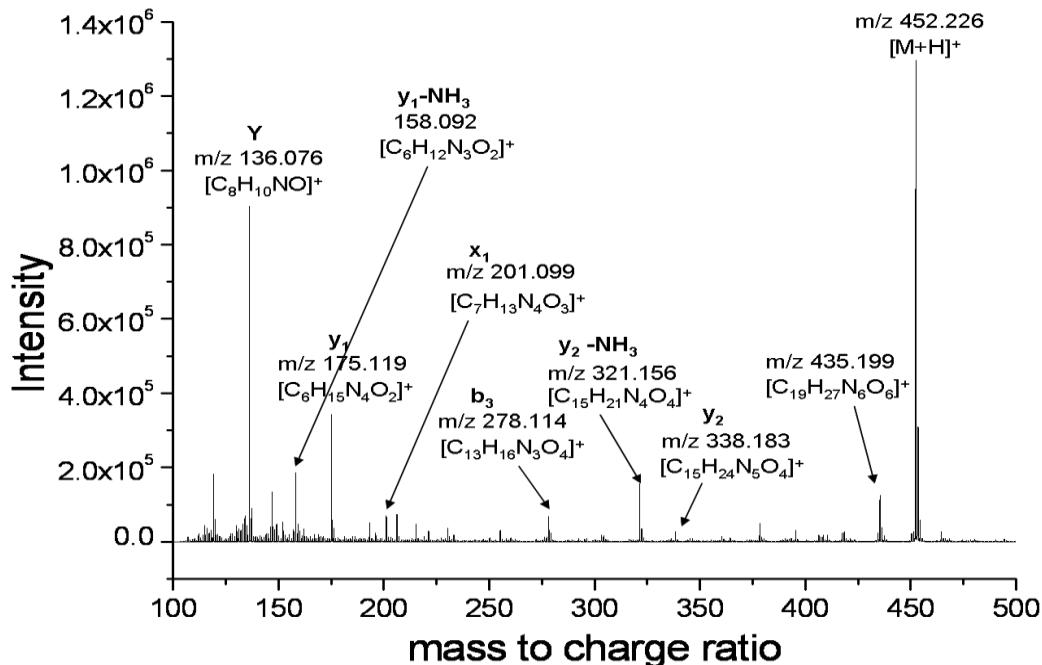


**Figure 3.11** ToF-SIMS spectrum of the tetrapeptide (GGYR) acquired on the J105 with 20 keV  $C_{60}^+$  at ion dose of  $1 \times 10^{13}$  ions/cm<sup>2</sup>.

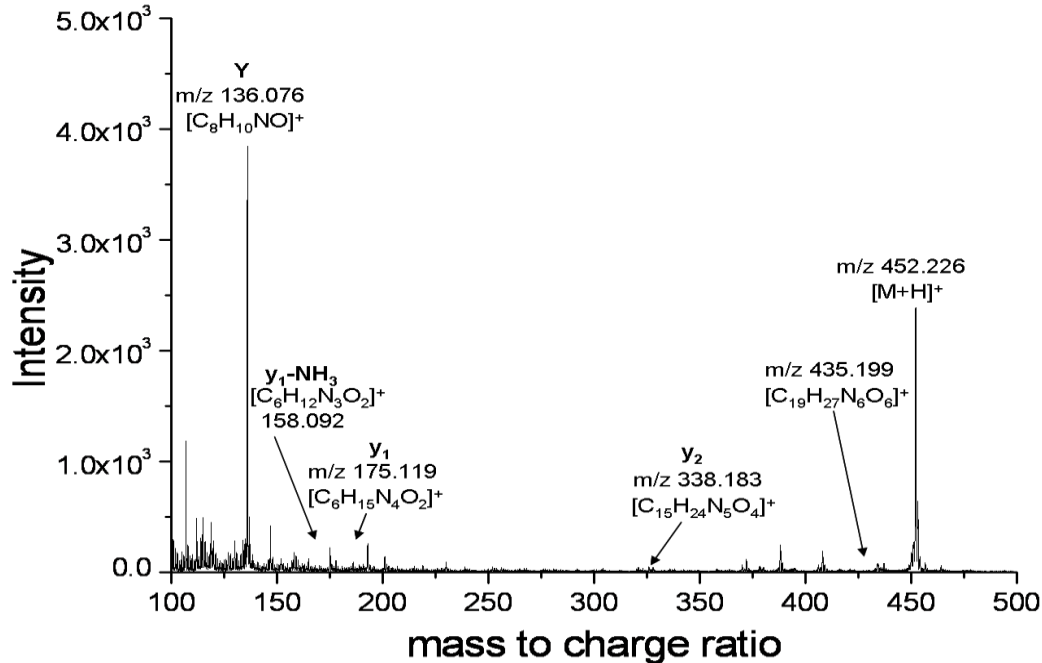


**Figure 3.12** ToF-SIMS spectrum of the tetrapeptide (GGYR) acquired on the BioToF with 20 keV  $C_{60}^+$  at ion dose of  $1 \times 10^{13}$  ions/cm<sup>2</sup>.

**Table 3.1** Shows the fragment ions observed on the ToF-SIMS MS spectrum of the tetrapeptide (GGYR).

<b>Ion</b>	<b>Formula</b>	<b><i>m/z</i></b>
$[M+H]^+$	$[C_{19}H_{30}N_7O_6]^+$	452.226
$[M+H]^+ - NH_3$	$[C_{19}H_{27}N_6O_6]^+$	435.199
$y_2$	$[C_{15}H_{24}N_5O]^+$	338.183
$y_2 - NH_3$	$[C_{15}H_{21}N_4O_4]^+$	321.156
$x_1$	$[C_7H_{13}N_4O_3]^+$	201.099
$y_1$	$[C_6H_{15}N_4O_2]^+$	175.119
$y_1 - NH_3$	$[C_6H_{12}N_3O_2]^+$	158.092
<b>Y</b>	$[C_8H_{10}NO]^+$	136.076

On comparison of the surface spectra of arginine, cholesterol and the tetrapeptide (GGYR) acquired on the J105 and on the BioToF, it can be seen that similar peaks are detected on both instruments. However, the intensities of these peaks vary with higher intensities observed on the J105, Figure 3.3, as compared to with the BioToF, Figure 3.4. Further, the intensity of fragment ions compared to the molecular ion is also different and the intensity ratio of the fragment ions to the molecular ion in the low mass region (0-150) is higher on the BioToF, Figure 3.12, in contrast to the J105, Figure 3.11. There are number of factors which can affect the measured secondary ion yields in ToF-SIMS. These include the projectile used, the nature of the sample surface and the transmission of the instrument. With regards to the projectile, the yields can fluctuate with the energy, mass and angle of incidence of the projectile [Miyayama *et al.*, 2008], [Kozole *et al.*, 2008]. The nature of the sample can also affect the yields, a

thick layer of organic film will produce different yields to a thin layer [Fletcher *et al.*, 2006]. The same ion beam type at the same impact energy was used on both instruments to look at similar samples thus, allowing comparisons to be made that result from the difference in instrument design and operation only. On the J105, a sample is bombarded with a dc primary ion beam which produces a continuous stream of secondary ions, increasing signal levels for the samples where the use of  $C_{60}^+$  prevents damage accumulation. However, on the BioToF, a pulsed primary ion beam generates secondary ions which have to be detected before the beam can strike again. Hence, the BioToF has a much lower duty cycle and experiments are normally performed under static conditions even when using  $C_{60}^+$  primary ion beam.

The ratio of fragment ions to the molecular ion is low in the low mass range on the J105 as compared to the BioToF, caused by reduced transmission of low mass ions on the J105. The J105 instrument is more complex, it requires the secondary ions to pass through a number of stages before they can be detected. On the BioToF, the ions leaving the surface are extracted directly into the flight tube to the detector. However, on the J105 the ions leaving the surface are extracted and then decelerated as they enter an RF only quadrupole where they are collisionally cooled and then subsequently energy filtered by the E.S.A, described in detail in Chapter 2. This results in all the ions having 100 eV energy when they enter the buncher. Once the buncher is filled, it ‘fires’ by applying an instantaneous accelerating field of 7 kV at the entrance dropping down to 1 kV at the exit producing a tight bunch of ions, referred to as a time focus, at the entrance of the reflectron. Since all the ions leaving the buncher now have an energy

spread of 6 keV they are analysed using a quadratic field reflectron [Fletcher *et al.*, 2008].

Thus, there are two critical stages on the J105 which can effect the transmission of low mass ions; the collisional cooling quadrupole and the buncher. For example, if the quadrupole is only optimised for high mass ions then the ions with low mass will lose so much energy during collisions that they become motionless. These ions can no longer be extracted to the E.S.A and are lost. Therefore, it is vital to set the collision cell for an 'optimal mass' for maximum transmission [Thompson. 2006]. During the acquisition of the above data set, the quadrupole was optimised for the detection of the molecular ion for each compound resulting in low transmission of low mass ions.

The effect of the buncher on transmission is fundamental and part of the instrument's design. All the ions entering the buncher have the same energy, 100 eV, so the ions with low mass will move faster as determined by their floating velocity which is proportional to the reciprocal of root mass. Thus, if ions with mass of 500 amu are filling the buncher, then the ions with mass of 50 amu will approximately have 3 times the velocity and will overfill the buncher and are lost. Also, the transmission of low mass ions alters with respect to operating the instrument at 5 kHz or 10 kHz. If the analysis is performed at a low mass <650 amu, the instrument operates at 10 kHz in which the transmission of the low mass ions is 20% with respect to transmission the high mass ions. In contrast, if the analysis is performed at 5 kHz, the transmission of the low mass ions will fall to 10% with respect to transmission the high mass ions [Thompson. 2006]. During the acquisition of the above data set, the mass range was set

to 0-1200 amu causing the transmission of low mass ions to fall as the instrument was operating at 5 kHz.

The signal to noise ratio defined as signal power to noise power corrupting the signal is larger on the J105 as compared to the BioToF, outlined in Table 3.2. Furthermore, since the mass resolution is greater on the J105, the peaks are better resolved and a peak at every mass is detected. This is not attainable on the BioToF as shown on Figure 3.12 where the peak at  $m/z$  338.183 is merged with other peaks and is not distinguishable, whereas on the J105 spectrum it is clearly resolved, Figure 3.11.

**Table 3.2** Signal to noise levels on the J105 and the BioToF.

<b>m/z</b>	<b>Signal to noise level on J105</b>	<b>Signal to noise level on BioToF</b>
175.119	5272	47
136.076	978	92
452.226	1500	65

### **3.2.3 Conclusion**

From the data acquired, it is shown that higher signal levels are obtained on the J105 as compared to the BioToF. Although there is a drawback of loss in transmission for low mass ions, the J105 offers many more advantages, higher sensitivity, higher mass detection and an increase in duty cycle which allows depth profiling and 3D molecular imaging to be performed on a reasonable time frame. In addition, the signal to noise ratio is greater on the J105 in comparison to the BioToF allowing the real peaks to be distinguished from background noise. Furthermore, due to higher mass resolution on the J105, the peaks are better resolved, one of the foremost requirements of sub-cellular imaging.

### 3.3 Tandem MS

Tandem mass spectrometry (MS/MS) has become an extremely valuable tool in biochemical research to elucidate the structure of unknown compounds, particularly in determining protein and nucleotide sequences. It involves two stages of mass analysis, Figure 3.13. The precursor ion is selected in the first mass analyser and focused into a collision region where it collides with inert gas atoms or molecules causing the precursor ion's translational energy to be converted into an internal energy. This results in an unstable excited precursor ion which fragments into product/daughter ions in a process known as the 'collision induced dissociation' (CID) also referred to as 'collision activated dissociation' (CAD). The product ions are analysed in the second mass analyser and a daughter spectrum is produced. It is vital to choose an inert gas that prevents a reaction between ions and the gas molecules and causes little scattering of the fragments. The most common gases used are helium (He), Xenon (Xe) and argon (Ar) since they are nonreactive, monatomic with high ionisation probability [Hoffmann *et al.*, 2006].

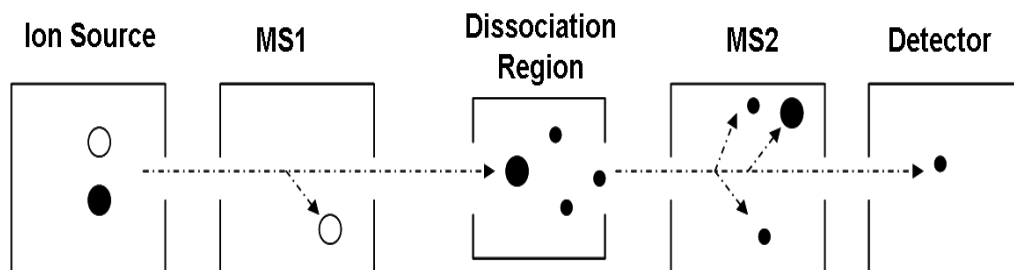


**Figure 3.13** Scheme representation of a tandem MS experiment. Reproduced from Downard, 2004.

MS/MS is widely available in MS instruments such as Gas Chromatography (GC), Liquid Chromatography (LC) and MALDI mass spectrometers but it is extremely rare in commercial SIMS instruments. The first tandem MS SIMS instrument was devised by the Vickerman's group in mid 1980 which was based on a Vacuum Generator system that used triple quadrupole to perform MS/MS analysis on polymers [Leggett *et al.*, 1990]. The triple quadrupole analysers offers the advantages of high sensitivity, improved mass resolution and was relatively easy to switch between negative and positive modes as compared to magnetic sector analysers. This system was based on a VG MM 12-12 SIMS but fitted with a VG 12-12 3S triple quadrupole in place of single quadrupole for tandem MS analysis, Figure 3.14. The main aims of these studies were to accurately determine the structure of secondary ions and the fundamental process that oversees the formation of secondary ions and the fragmentation in the MS/MS mode. The study by Leggett and co-workers (1992) suggested that the fragmentation occurring during CAD is similar to the fragmentation taking place at the solid surface during the sputtering process. Further, the group investigated a range of collision gases and found Xe to be the most effective followed by Ar, but He proved to be unsuccessful. Nitrogen (N<sub>2</sub>) was found to behave similar to Ar [Leggett *et al.*, 1990], [Leggett *et al.*, 1992].

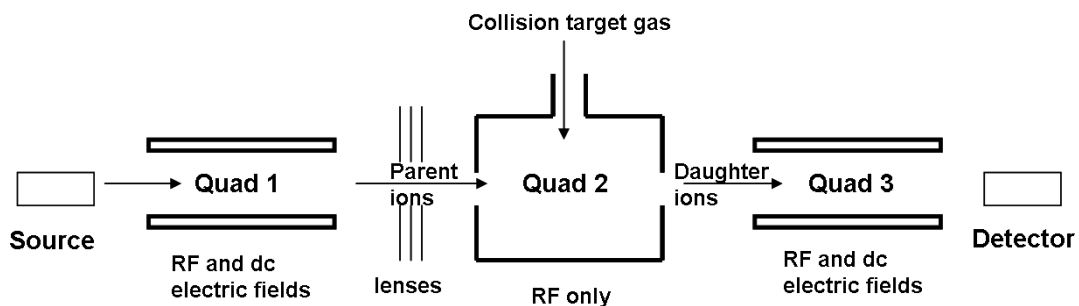


**Figure 3.14** A triple quadrupole mass spectrometer. Reproduced from Leggett *et al.* 1990.

Tandem MS has also been used to differentiate between the secondary ions of analyte from the secondary ions of tissue, chicken liver. Acetylcholine chloride and methylphenylpyridinium iodide were deposited onto the tissue matrix and the distribution of these compounds was mapped using SIMS and confirmed by using MS/MS SIMS [Todd *et al.*, 1995].

Brunelle and co-workers (2006) used ToF-SIMS and the post source decay method (PSD) to perform tandem MS analysis on model molecules; the phosphocholine ion, phosphatidylcholines, cholesterol and vitamin E. The PSD method refers to measuring and detecting the fragment ions produced from a selected precursor ion. The precursor ion undergoes dissociation in the flight tube after leaving the source and produces fragment ions which are detected in the reflector. The amount of fragmentation can be increased by either using a collision cell or higher intensity laser in MALDI [Sandler, 2003].

In the study by Brunelle (2006) PSD measurements were applied to pure lipid compounds and tissue sections and same ions were detected with relatively similar abundances. The analysis of an ion  $m/z$  184 from pure phosphatidylcholine produced

ions at  $m/z$  60, 86, 104, 125 and 166, also detected in MALDI MS/MS. These ions were also observed in the MS spectrum of the phosphocholine produced due to in source decay of the molecular ion  $[M+H]^+$   $m/z$  758.6 of this compound. Further, these ions have been imaged on the edge of a corpus callosum of a rat brain section to map their distribution within a tissue section [Touboul *et al.*, 2006].

The above studies highlight the importance and potential benefits of MS/MS on SIMS instrumentation since it allows determination of the composition and structure of complex substances, as well assisting in understanding the formation of secondary ions produced when the sample is bombarded with a primary ion beam.

The  $C_{60}^+$  ion beam equipped QSTAR XL system, developed by the Winograd group also has the facility to perform MS/MS SIMS analysis, described in Chapter 2. They used this instrument to perform MS/MS analysis on the fragment ion of cholesterol  $m/z$  369  $[M-OH]^+$  and the resultant spectrum was used to identify the fragments previously unidentified in the MS spectrum. Following this, these fragments were imaged in a model cell system, J774 macrophages doped with cholesterol, to map the distribution of the cholesterol in cells as well as to confirm that these fragments are produced from this compound. Further, a peak at  $m/z$  147.117 identified as a fragment of cholesterol was distinguished from the commonly occurring contamination peak at  $m/z$  147.065 from poly-dimethyl-siloxane (PDMS). This study also highlights the importance of tandem MS methodology for ToF-SIMS bioimaging as well as the need of acquiring data at high mass resolution to differentiate between the real peaks and possible interferences [Piehowski *et al.*, 2008].

MS/MS on the J105 is performed using a ToF-ToF configuration, described in detail in Chapter 2. In the MS/MS mode the ions leaving the buncher pass through a collision cell containing a collision gas, N<sub>2</sub>. Since, the ions have an energy spread of 1-7 kV they all fragment when colliding with the gas. However, as these collisions take place in a field free region, the daughter ions and the parent ion travel at same velocity to the ToF analyser. Following a short distance into the ToF region, a timed ion gate is used to select the precursor ion and its associated daughter fragment ions which are then passed into ToF analyser for detection [Fletcher *et al.*, 2008].

### 3.3.1 Experimental

The standards, arginine and the tetrapeptide (GGYR) used for MS/MS analysis were obtained from Sigma (UK) except the lipid mixture (brain extract) which was obtained from the Avanti Polar Lipids (USA) by Winograd's group and sent to Manchester. A small amount of arginine and the tetrapeptide (GGYR) were dissolved in water solvent, whereas the lipid mixture was dissolved in glycerol. 10 µl droplets of each solution were deposited onto a clean steel plate and air dried.

ToF-SIMS MS and MS/MS analysis was performed using a 40 keV C<sub>60</sub><sup>+</sup> primary ion beam. MS/MS of the molecular ion peak of arginine was performed using a range of gas pressure to determine an optimum collision gas pressure for the tandem MS analysis. It is not possible to measure the gas pressure directly in the collision cell and is monitored using the ToF pressure gauge. However, this is only an approximation and the pressure in the cell is expected to be a much higher. Here arbitrary numbers, 2, 10, 20, 25 and 30 have been used which correspond to the time the valve is open to

allow the collision gas to enter. During the acquisition of the data set the calibration was slightly different on the spectra with respect to the exact mass to charge ratio of molecular and fragment ions of the samples analysed.

### 3.3.2 Results and Discussion

Amino acids have been studied extensively in normal MS and tandem MS mode. It is a molecule that consists of an amine group, carboxylic acid and a side chain R which varies with different amino acids, Figure 3.15. They are a vital part of life and have many functions in metabolism, particularly in building proteins.

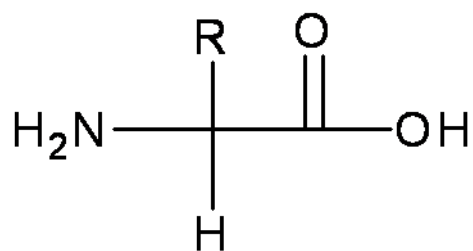


**Figure 3.15** General structure of an amino acid, side chain R varies with the amino acid.

Arginine, shown previously in Figure 3.2 is a basic amino acid, also referred to as an alpha amino acid because the amine and carboxyl group are attached to the same carbon atom. The literature shows that the protonated arginine exhibits the most complex fragmentation pattern as compared to other alpha amino acids [Kulik *et al.*, 1988], [Dookeran *et al.*, 2006], [Piraud *et al.*, 2003], [Gogichaeva *et al.*, 2007]. Figure 3.16, shows the MS/MS spectrum of the protonated arginine  $[M+H]^+$   $m/z$  175.119 which produces nine main diagnostic product ions. The first daughter ion, at  $m/z$  158.093  $[C_6H_{12}N_3O_2]^+$  is formed by a loss of ammonia from the protonated arginine. A

study by Zwinselmann and co-workers showed that the loss of ammonia occurs through the amine group attached to the alpha C forming a cyclic protonated molecular ion of arginine before it fragments [Zwinselman *et al.*, 1983]. Dookeran *et al.* (1996) show that in FAB MS/MS of arginine a peak at  $m/z$  157  $[\text{C}_6\text{H}_{13}\text{N}_4\text{O}]^+$  is also produced due to a loss of water, but this peak is not observed in the SIMS ToF-ToF and in the MALDI ToF-ToF. Further, daughter ions detected include immonium ions at  $m/z$  130.098  $[\text{C}_5\text{H}_{12}\text{N}_3\text{O}]^+$  formed by a loss of CO and  $\text{NH}_3$  and 129.114  $[\text{C}_5\text{H}_{13}\text{N}_4]^+$  corresponding to a loss of CO and  $\text{H}_2\text{O}$ , also illustrated in the study of Zwinselmann *et al.* (1983) and Piraud *et al.* (2003). However, these characteristic ions  $m/z$  157, 158.093 and 129.114 are not detected when the arginine is analysed in the MALDI TOF-TOF. According to Chait *et al.* (1981) the ion at  $m/z$  130.122  $[\text{C}_5\text{H}_{14}\text{N}_4]^+$  can also be formed by a loss of CHO from the protonated arginine when analysed by  $^{252}\text{Cf}$  plasma desorption. This difference in the composition of the ion at  $m/z$  130 could be due to the difference in ionisation of the two techniques.

The daughter ion  $m/z$  60 arises due to the protonation of guanidine group  $[(\text{NH}_2)_3\text{C}]^+$  on the arginine, shown by Dookeran and co workers (1996), Figure 3.17. The authors explain that at low collision energy (2-50 eV), a proton is transferred to form a protonated guanidine but at higher internal energy the guanidine group fragments as a neutral molecule prior to proton transfer. This causes the remaining residue to form a protonated cyclic ring proline which is detected at  $m/z$  116  $[\text{C}_5\text{H}_{10}\text{NO}_2]^+$ , Figure 3.16. This is most abundant in the MALDI ToF-ToF and is also detected with reasonable intensity in SIMS ToF-ToF. The author further explain that the protonated proline decomposes to produce an immonium ion at  $m/z$  70  $[\text{C}_4\text{H}_8\text{N}]^+$  which

dominates the spectrum at all energies in electrospray ionisation (ESI), FAB and SIMS but not in MALDI ToF-ToF. The ToF-SIMS MS/MS of the protonated arginine, Figure 3.16 corresponds to the ToF-SIMS MS of standard arginine, Figure 3.3. This suggests the process underlying the formation of secondary ions is similar to the formation of the fragment ions produced during the CID of arginine in MS/MS, also shown by the earlier literature [Leggett *et al.*, 1990], [Leggett *et al.*, 1992].

MS/MS analysis of the arginine on the J105 was performed at 5 different gas pressures to determine an optimum gas pressure for MS/MS analysis. Figure 3.18 shows that the ratio of fragment ions to molecular ion increases with an increase in the gas pressure. This effect is observed because with an increase in the gas pressure, there is an increase in the number of successive collisions between the gas N<sub>2</sub> and the selected precursor ion causing an increase in the intensity of daughter ions.

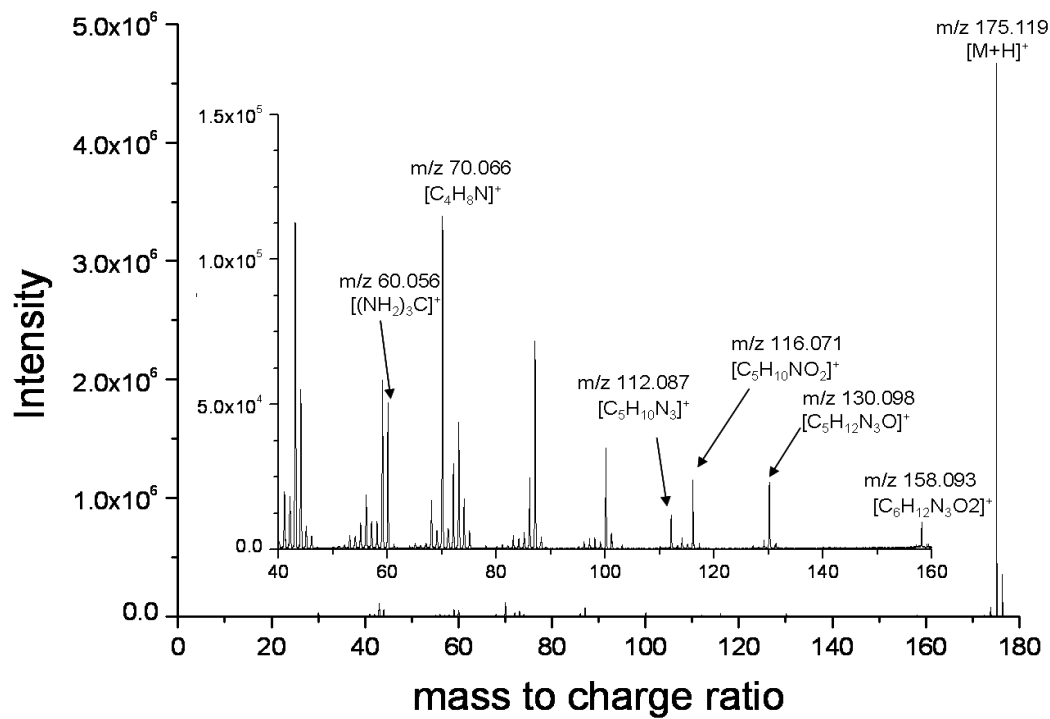


**Figure 3.16** ToF-SIMS MS/MS spectrum of  $[M+H]^+$   $m/z$  175.119 of 0.3 M arginine acquired at  $64 \times 64$  pixels over an area of  $600 \times 600 \mu\text{m}^2$  with ion dose of  $1 \times 10^{13}$  ions/cm<sup>2</sup>.

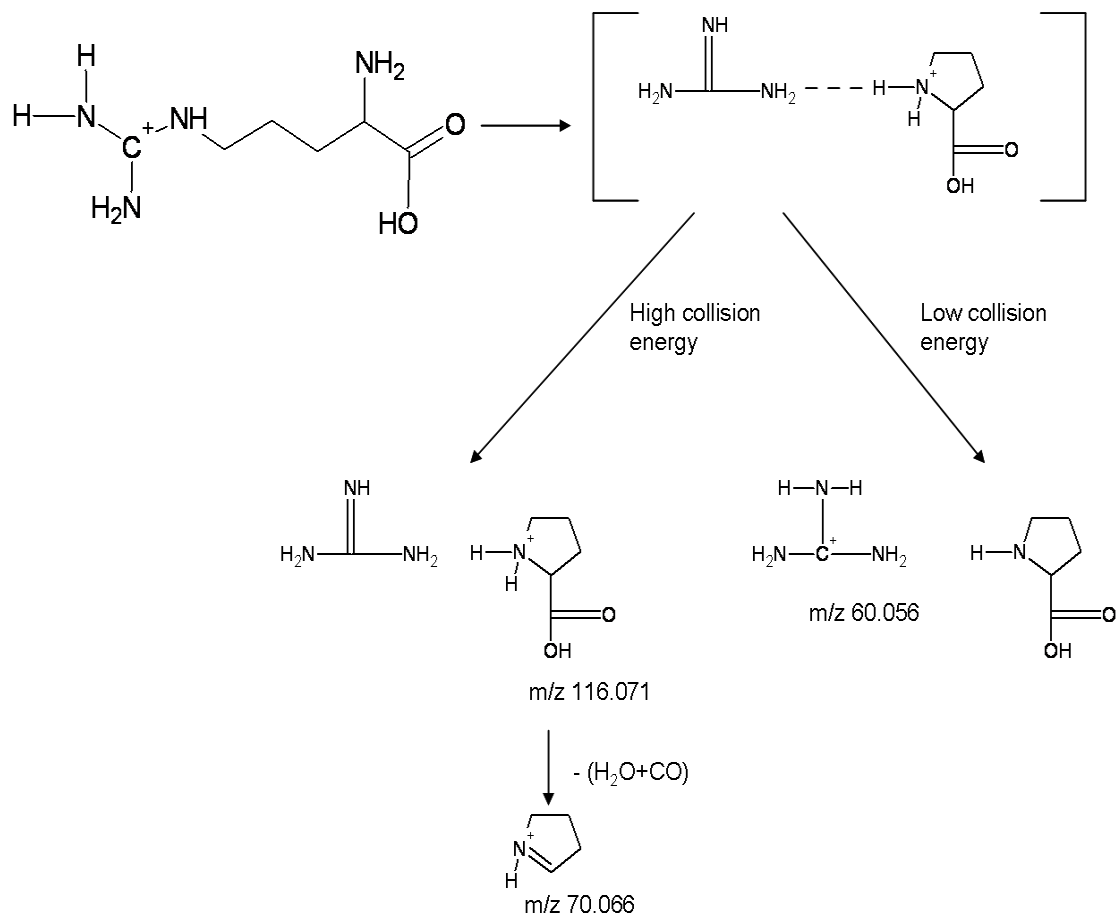


**Figure 3.17** Fragmentation mechanism of arginine as suggested by Dookeran and co-workers. Reproduced from Dookeran *et al.* 1996.

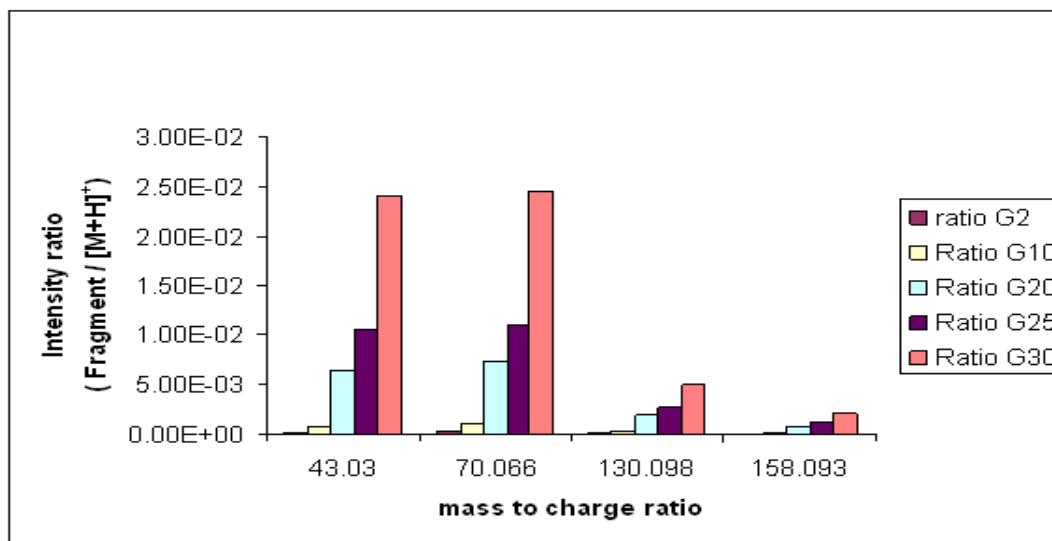


**Figure 3.18** Graph to show the effect of changing the gas pressure in the collision cell on the intensity ratio of fragment to molecular ion. Higher collision gas pressure produces higher intensity of the fragment ions.

MS/MS analysis of the molecular ion  $[M+H]^+$   $m/z$  452.226 of the tetrapeptide (GGYR) is shown in Figure 3.19. Upon collisions with the gas, the molecular ion produces four main diagnostic daughter ions at  $m/z$  158.092,  $m/z$  136.076,  $m/z$  87.055 and immonium ions at  $m/z$  112.087,  $m/z$  100.087 and  $m/z$  70.066, labelled as R on Figure 3.19. These ions were assigned following the scheme of the formation peptide fragmentation as shown in Figure 3.9 and 3.10. This contrasts with a FAB MS/MS of tetrapeptide performed by Tang and co-workers (1992). They show that the molecular ion  $[M+H]^+$  fragments to produce numerous daughter ions, similar to that seen in ToF-SIMS MS of the tetrapeptide, Figure 3.11. Although both processes were performed at relatively high energy, it is not yet clear why the MS/MS of the molecular ion of the

tetrapeptide is different. Further investigation is required to determine what is causing this difference.

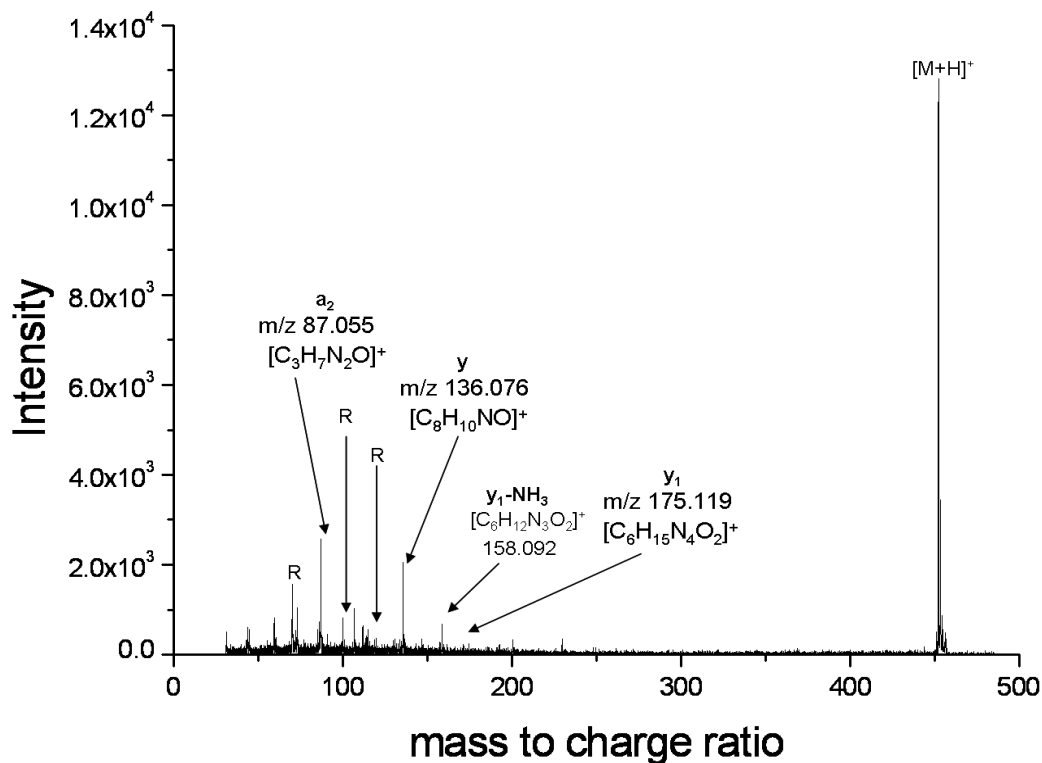


**Figure 3.19** ToF-SIMS MS/MS spectrum of  $[M+H]^+$   $m/z$  452.226 of the tetrapeptide (GGYR) acquired at  $64 \times 64$  pixels over an area of  $600 \times 600 \mu\text{m}^2$  with an ion dose of  $1 \times 10^{13}$  ions/cm<sup>2</sup>.

The composition of the lipid mixture (brain extract) is shown in Table 3.3. Following an impact with the primary ion beam six main ions are produced  $m/z$  184.06, 734.6, 760.6, 788.6, 943.6, 971.8, Figure 3.20. The spectrum is dominated by the ion at  $m/z$  184.06 which corresponds to a fragment of phosphatidylcholine (PC) head group and is easily detected in SIMS. There are many phosphatidylcholine containing phospholipids but 1,2-Dipalmitoyl-sn-glycero-3-phosphatidylcholine (DPPC),

$C_{40}H_{81}NO_8P$ , monoisotopic molar mass of 733.57 g/mol and 1-Palmitoyl-2-oleoyl-sn-glycero-3-phosphocholine (POPC),  $C_{42}H_{82}NO_8P$ , monoisotopic mass of 759.58 have been repeatedly analysed in MS mode by ToF-SIMS. The ions at  $m/z$  734.6 and  $m/z$  760.6 detected in the MS spectrum of the lipid mixture can be assigned to molecular ion of PC containing lipids but further verification is required by the MS/MS of these ions. The MS/MS spectrum of the precursor ion  $m/z$  734.6 produced four daughter ions,  $m/z$  224.105  $[C_8H_{19}NO_4P]^+$ ,  $m/z$  184.074  $[C_5H_{15}NO_4P]^+$  and  $m/z$  86.097  $[C_5H_{12}N]^+$  Figure 3.21. On comparison of the MS/MS of the  $m/z$  734.6 to the standard spectrum of DPPC [SIMS Library], similar ions are detected in both MS and MS/MS mode. This allows correctly assigning the ion at  $m/z$  734.6 detected in ToF-SIMS of lipid mixture to phosphocholine containing lipid.

The MS/MS spectrum of  $m/z$  760.6 also produced daughter ions at  $m/z$  166.063  $[C_5H_{13}NO_3P]^+$ ,  $m/z$  184.067  $[C_5H_{15}NO_4P]^+$  and 86.097  $[C_5H_{12}N]^+$ , Figure 3.22. On comparison of the daughter ions to the ions produced when standard POPC was analysed on ToF-SIMS it can be confirmed that the ion at 760.6 on the MS of the lipid mixture belongs to the phosphocholine containing lipid, POPC.

Due to the time constraints, only these two ions were analysed in the MS/MS mode and further MS/MS analysis of other ions is required to assign other lipids.

**Table 3.3** Composition of the lipid mixture, brain extract. Reproduced from Avanti Polar Lipids.

<b>Brain lipid extract Component</b>	<b>Total Extract Percent /Wt</b>
Phosphatidylethanolamine	16.7
Phosphatidylserine	10.6
Phosphatidylcholine	9.6
Phosphatidic acid	2.8
Phosphatidylinositol	1.6
Other	58.7

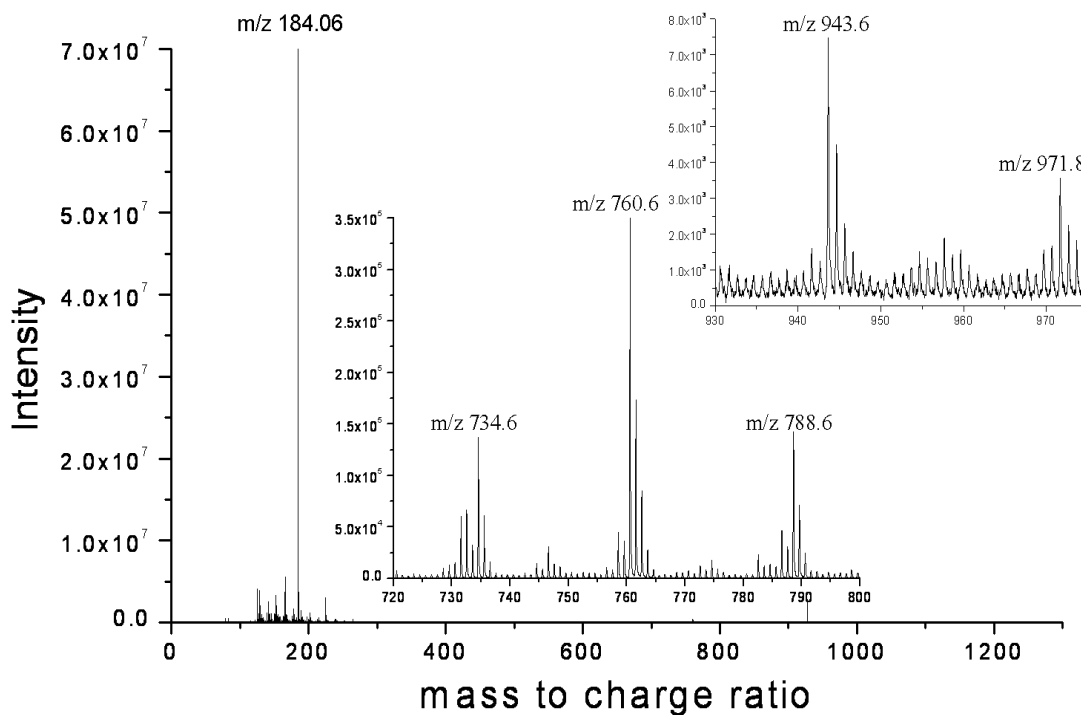


**Figure 3.20** ToF-SIMS MS spectrum of the lipid mixture dissolved in glycerol acquired at  $32 \times 32$  pixels over an area of  $1000 \times 1000 \mu\text{m}^2$  with an ion dose of  $5 \times 10^{12}$  ions/cm<sup>2</sup>.

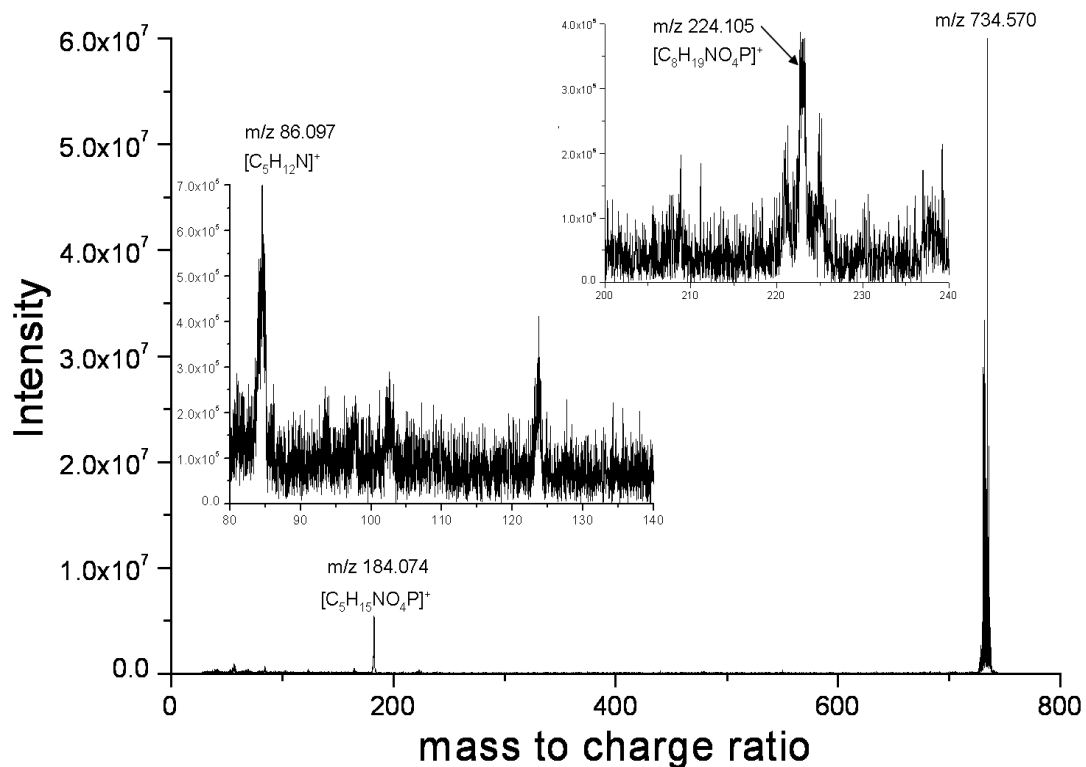


**Figure 3.21** ToF-SIMS MS/MS spectrum of  $m/z$  734.570 of the lipid mixture dissolved in glycerol acquired at  $32 \times 32$  pixels over an area of  $1000 \times 1000 \mu m^2$  using ion dose of  $3 \times 10^{13}$  ions/cm<sup>2</sup>. The intensity has been multiplied by a factor of 1000. This ion has been assigned to the PC containing lipid in the lipid mixture. The  $m/z$  values are slightly low in mass due to the off calibration during the acquisition of the data set.

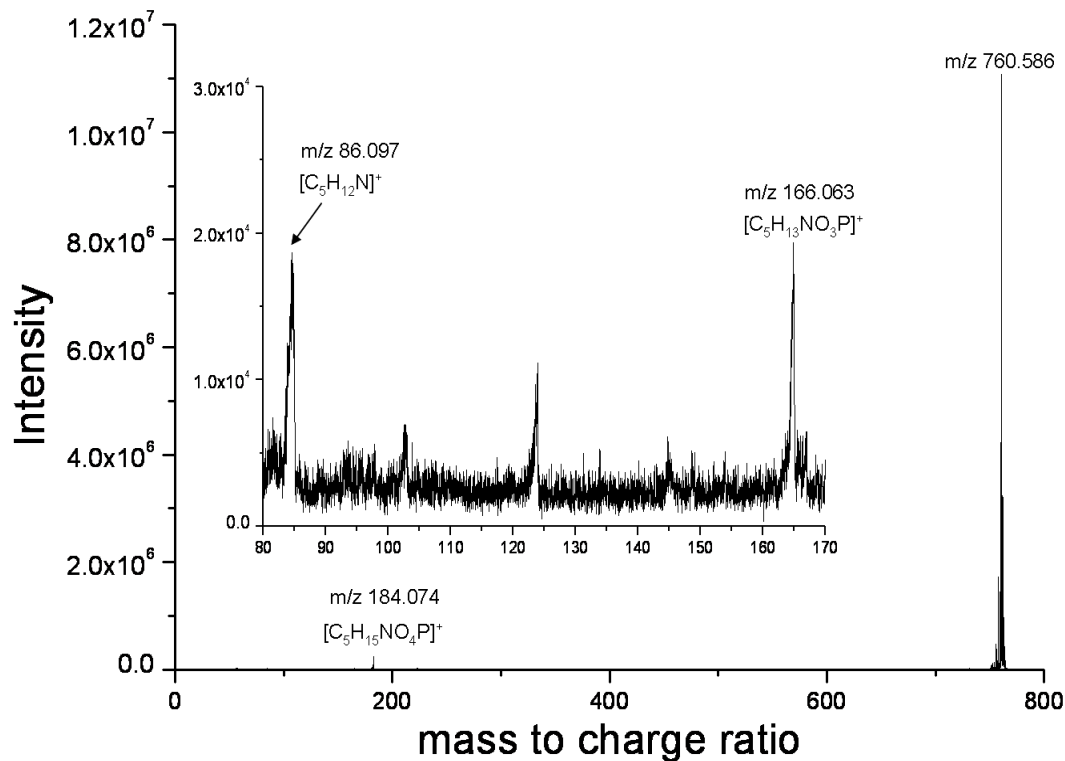


**Figure 3.22** ToF-SIMS MS/MS spectrum of  $m/z$  760.586 of the lipid mixture dissolved in glycerol acquired at  $32 \times 32$  pixels over an area of  $1000 \times 1000 \mu\text{m}^2$  using an ion dose of  $3 \times 10^{13}$  ions/cm<sup>2</sup>. The intensity has been multiplied by a factor of 10. This ion has been identified as POPC in the lipid mixture. The  $m/z$  values are slightly low in mass due to the off calibration during the acquisition of the data set.

### 3.3.3 Conclusion

MS/MS capability of the J105 has been tested using standard molecules, arginine, the tetrapeptide (GGYR) and a lipid mixture from brain extract. The secondary ions produced during normal ToF-SIMS MS mode correspond to the ions produced during CID of molecular ion  $[M+H]^+$  in the ToF-SIMS MS/MS mode. This suggests that the process underlying secondary ion formation is similar to the CID fragmentation. On comparison of the MS/MS of the lipid mixture and standard lipid spectra it was possible to identify  $m/z$  734.6 and  $m/z$  760 to phosphocholine containing lipids. The above data shows the importance and benefits of tandem MS/MS on the SIMS instrument. It is powerful method that offers the sensitivity and selectivity to identify unknown species particularly in cells and tissues.

### 3.4 Limit of detection

Limit of detection (LoD) refers to the minimum surface concentration that can be detected with a given analytical method. It can either be determined using a statistical approach or an empirical (experimental) approach [Armbruster *et al.*, 2008]. The former approach involves measuring replicates of a blank sample (a sample without analyte) and LoD can be calculated by:

$$\text{Mean of the blank} + (3 \times \text{standard deviation of the mean blank})$$

This approach assumes that in the presence of the analyte, a signal greater than this value will be produced. Although this is a relatively quick and easy method for estimating the LoD, it does not provide the real data that can be used to distinguish signal from analytical noise. This method of detection has also been criticised by some researchers as “the ability to measure nothing” [Needleman *et al.*, 1990].

The empirical (experimental) approach consists of measuring increasingly dilute concentrations of the analyte until a signal or a peak can no longer be detected under the conditions. This method offers the advantage over the statistical approach in that real data is used to provide a comparison between the analytical response of a blank and low concentration of sample to determine the lowest concentration of a sample detectable [Armbruster *et al.*, 2008].

Determining LoD is highly important in the forensic drug testing, where the presence or the absence of drug can provide critical information to the regulatory body

of prohibited substances. It can also play a significant role in medicine, for example monitoring "biochemical relapse" in prostate cancer [Katz *et al.*, 1973].

SIMS offers the advantage of high sensitivity with detection limits in ppm and ppb range [Fralick, *et al.*, 1977], [Lockyer. 2007]. The polyatomic beams offer the advantages of high ion efficiencies, low sub-surface damage as well as very low detection limits [Ravanel *et al.*, 2008] [Poleunis *et al.*, 2006]. A publication by Achiwawanich and co workers (2007) show that the temperature dependent concentrations of trace transitional metals such as Cr and Cu can be determined by ToF-SIMS at a level that cannot be measured by XPS.

Limit of detection on the J105 has been determined using the empirical (experimental) approach in which increasingly dilute concentrations of arginine have been measured. A working solution of arginine with concentration of  $3 \times 10^{-1}$  M was prepared and was diluted to  $3 \times 10^{-2}$  M.....up to  $3 \times 10^{-10}$  M. Each concentration consisting of 1  $\mu$ l was deposited onto a clean Si wafer and analysed using 40 keV  $C_{60}^{+}$  primary ion beam (110 pA),  $32 \times 32$  pixels,  $4 \times 4$  dynamic stage (to analyse the whole droplet) over an area of  $1000 \times 1000 \mu m^2$  with 200 shots. A blank was also taken.

The intensity of the molecular ion peak  $[M+H]^{+}$   $m/z$  175.115 was used to determine the LoD on the J105. The results demonstrate that the increase in the dilution decreases the intensity of the molecular ion peak, but not by a factor 10 and minimum concentration detected at  $3 \times 10^{-5}$  M after which the signal can be regarded as belonging to the blank, Table 3.4.

**Table 3.4** The intensity of  $[M+H]^+$   $m/z$  175.115 vary with change in concentration of arginine.

Concentration of Arginine (M)	Intensity (Counts)
$3 \times 10^{-1}$	141087
$3 \times 10^{-2}$	474360
$3 \times 10^{-3}$	505165
$3 \times 10^{-4}$	242297
$3 \times 10^{-5}$	15015
$3 \times 10^{-6}$	332
$3 \times 10^{-7}$	270
$3 \times 10^{-8}$	300
$3 \times 10^{-9}$	323
$3 \times 10^{-10}$	290
Blank	372

As a consequence, the minimum numbers of moles of arginine that can be detected are  $3 \times 10^{-11}$  mol, which is equivalent to  $1.807 \times 10^{13}$  molecules, determined as shown below:

$$M = n/V$$

Equation 3.1

Where

M: concentration of solution in mol/L

n: moles of a substance

V: volume of substance in L

Thus

$$n = M \times V$$

$$n = 3 \times 10^{-5} \text{ ML}^{-1} \times 1 \times 10^{-6} \text{ L}$$

$$n = 3 \times 10^{-11} \text{ mol}$$

$$N = nN_A$$

Equation 3.2

Where

N: number of molecules

n: number of mol

$N_A$ : Avogadro number  $6.022 \times 10^{23} \text{ mol}^{-1}$

Thus

$$N = (3 \times 10^{-11} \text{ mol}) \times (6.022 \times 10^{23} \text{ mol}^{-1})$$

$$N = 1.807 \times 10^{13}$$

### 3.5 Summary

This chapter has studied the current performance of the new instrument J105 *3D Chemical Imager* compared to the conventional ToF-SIMS instrument, the BioToF. The data showed that although the transmission of low mass ions is low on the J105, this instrument provides the advantages of higher mass detection, increase in sensitivity and better peak resolving power compared to the BioToF. The tandem MS capability of the J105 has been tested and proved and two lipids have been identified in the lipid mixture of brain extract. It was also determined that the fragmentation mechanism for the secondary ions is similar to the ions produced during collision induced dissociation. The tandem MS technique has become a powerful tool for the identification of unknown peaks and the analysis of complex material.

Following limit of detection test, it was determined that currently the lowest concentration of arginine that produces a peak on the J105 instrument is  $3 \times 10^{-5}$  M which is equivalent to  $1.807 \times 10^{13}$  molecules.

## References

Achiwawanich, S.; James, B.D.; Liesegang, J. **XPS and ToF-SIMS analysis of natural rubies and sapphires heated in an inert (N<sub>2</sub>) atmosphere.** Applied Surface Science (2007), 253, 6883–6891

Armbruster, D.A.; Pry, T. **Limit of Blank, Limit of Detection and Limit of Quantitation.** Clinical Biochemistry Review (2008), S49-S52

Avanti Polar Lipids website <http://www.avantilipids.com> visited 5-01-2010

Baldwin, M.A.; Proctor, C.J. Amster, L.J. Mclafferty, F.W. **The behaviour of caesium iodide cluster ions produced by fast-atom bombardment.** International Journal of Mass Spectrometry and Ion Processes (1983), 54, 97-107

Barlak, T. M.; Campana, J. E.; Colton, R. J.; DeCorpo, J. J.; Wyatt, J. R. **Secondary Ion Mass Spectrometry of Metal Halides. 1. Stability of Alkali Iodide Clusters.** The Journal of Physical Chemistry (1981), 85 (25), 3840-3844

Braun, R.M., Blenkinsopp, P., Mullock, S.J., Corlett, C., Willey, K.F., Vickerman, J.C., Winograd, N. **Performance characteristics of a chemical imaging time-of-flight mass spectrometer** Rapid Communications in Mass Spectrometry (1998), 12 (8), 1246-1252

Chait, B.T., Agosta, W.C., Field, F.H. **Fission fragment ionization (252Cf) mass spectrometry. Positive and negative spectra and decomposition mechanisms for seven compounds.** International Journal of Mass Spectrometry and Ion Physics (1981), 39 (3), 339-366

Dookeran, N.N.; Yalcin, T.; Harrison, A.G. **Fragmentation Reactions of Protonated alpha Amino Acids.** Journal of Mass Spectrometry (1996), 31, 500-508

Downard, K. **Mass Spectrometry A Foundation Course.** The Royal Society of Chemistry, UK, 2004

Ens, W.; Beavis, R.; Standing, K.G. **Time-of-Flight Measurements of Caesium-Iodide Cluster Ions.** Physical Review Letters (1983), 50 (1), 27-30

Fletcher, J.S., Rabbani, S., Henderson, A.; Blenkinsopp, P.; Thompson, S.P.; Lockyer, N.P., Vickerman, J.C. **A new dynamic in mass spectral imaging of single biological cells.** Analytical Chemistry (2008), 23, 9058-9064

Fletcher, J.S.; Conlan, X.A., Jones, E.A.; Biddulph, G., Lockyer, N.P.; Vickerman, J.C. **ToF-SIMS analysis using C<sub>60</sub>. Effect of impact energy on yield and damage.** Analytical Chemistry (2006), 78 (6), 1827-1831

Fralick, R.D.; Conrad, R.L. **Quantitative Multielement Analysis with SIMS**. *RD Res Dev* (1977), 28 (3), 32-34, 36, 38

Gogichaeva, N.V.; Williams, T. **MALDI TOF/TOF Tandem Mass Spectrometry as a New Tool for Amino Acid Analysis**. *American Society for Mass Spectrometry* (2007), 18, 279–284

Hoffmann, E.; Stroobant, V. **Mass Spectrometry Principles and Applications**. John Wiley and Sons Ltd, Chichester 2007

Honda, F.; Lancaster, G.M.; Fukuda, Y.; Rabalais, J.W. **SIMS study of the mechanism of cluster formation during ion bombardment of alkali halides**. *The Journal of Physical Chemistry* (1978), 69 (11), 4931-4937

Johnson, R.S.; Martin, S.A.; Biemann, K. **Novel Fragmentation Process of Peptides by Collision- Induced Decomposition in a Tandem Mass Spectrometer: Differentiation of Leucine and Isoleucine**. *Analytical Chemistry* (1987), 59, 2621-2625

Katz, S.M.; Di Silvio, T.V. **Ascorbic acid effects on serum glucose values**. *Journal of the American Medical Association* (1973), 224 (5), 628

Kozole, J.; Willingham, D.; Winograd, N. **The effect of incident angle on the C<sub>60</sub><sup>+</sup> bombardment of molecular solids**. *Applied Surface Science* 255 (2008) 1068–1070

Kulik, W., Heerma, W. **A Study of the Positive and Negative Ion Fast Atom Bombardment Mass Spectra of  $\alpha$ -Amino Acids**. *Biomedical and Environmental Mass Spectrometry* (1988), 15, 419-427

Leggett, G.J.; Briggs, D.; Vickerman, J.C. **Collision Target-gas Effects during the Tandem Secondary-ion Mass-spectrometric Analysis of Polymers**. *Journal of Chemical Society. Faraday Transition* (1990), 86 (10), 1863-1872

Leggett, G.J.; Vickerman, J.C. **Applications of Tandem Quadrupole Mass Spectrometry in SIMS**. *Surface and Interface Analysis* (1990), 16, 3-8

Leggett, G.J.; Vickerman, J.C. **Surface Studies by Static Secondary Ion Mass Spectrometry: Cluster Ion Formation studied by Tandem Mass-spectrometric Techniques**. *Journal of Chemical Society. Faraday Transition* (1992), 88 (3), 279-309

Lockyer, N.P. **Static secondary ion mass spectrometry for biological and biomedical research**. *Methods in Molecular Biology* (2007), 369, 543-567

Miyayama, T.; Sanada, N.; Iida, S.; Hammond, J.S.; Suzuki, M. **The effect of angle of incidence to low damage sputtering of organic polymers using a C<sub>60</sub> ion beam**. *Applied Surface Science* (2008), 255, 951–953

Needleman S.B.; Romberg R.W. **Limits of linearity and detection for some drugs of abuse.** Journal of Analytical Toxicology.(1990), 14(1), 34-8

Piehowski, P.D.; Carado, A.J.; Kurczy, M.E.; Ostrowski, S.G. Heien, M.L., Winograd, N., Ewing, A.G. **MS/MS Methodology To Improve Subcellular Mapping of Cholesterol Using TOF-SIMS.** Analytical Chemistry (2008), 80, 8662–8667

Piraud, M.; Vianey-Saban, C.; Petritis, K.; Elfakir, C.; Steghens, J.P.; Morla, A.; Bouchu, D. **ESI-MS/MS analysis of underivatized amino acids: a new tool for the diagnosis of inherited disorders of amino acid metabolism. Fragmentation study of 79 molecules of biological interest in positive and negative ionization mode.** Rapid Communications in Mass Spectrometry (2003), 17, 1297-1311

Poleunis, C.; Delcorte, A.; Bertrand, P. **Determination of organic contaminations on Si wafer surfaces by static ToF-SIMS: Improvement of the detection limit with C60+ primary ions** Applied Surface Science 252 (2006) 7258–7261

Ravanel, X.; Trouiller, C. Juhel, M.; Wyonc, C.; Kwakman, L.F.T.; Léonard D. **Static time-of-flight secondary ion mass spectrometry analysis of microelectronics related substrates using a polyatomic ion source.** Applied Surface Science (2008), 255 1440–1442

Roepstorff, P.; Fohlman, J. **Proposal for a common nomenclature for sequence ions in mass spectra of peptides.** Biomedical Mass Spectrometry (1984), 11 (11), 601

Sandler Mass Spectrometry User's Group Meeting 2003  
<http://www.msg.ucsf.edu/agard/maldi/IntrotoMALDITOF.ppt>. visited on 20-08-2010

Tang, X.; Boyd, R.K. **An Investigation of Fragmentation Mechanisms of Doubly Protonated Tryptic Peptides.** Rapid Communications in Mass Spectrometry (1992), 6, 651-657

Thompson, S.P. **SIMS ToF Mass Spectrometer Design Report** (2006). Private communication.

Todd, P.J.; McMahon, J.M.; Short, R.T. **Secondary ion emission and images from a biologic matrix.** International Journal of Mass Spectrometry and Ion Processes (1995), 143, 131 – 145

Touboul, D.; Brunelle, A.; Lapr evote. **Structural analysis of secondary ions by post-source decay in time-of-flight secondary ion mass spectrometry.** Rapid Communications in Mass Spectrometry (2006), 20, 703-709

Zwinselman, J.J.; Nibbering, N.M.M.; van der Greef, J., Ten Noever de Brauw, M.C. **A <sup>15</sup>N labelling, FD and FAB Study of Ammonia Loss from Protonated Arginine Molecules.** Organic Mass Spectrometry (1983), 18 (12), 525-529

## 4 Molecular depth profiling using ToF-SIMS

### 4.1 Introduction

The concept of depth profiling was introduced in Chapter 1. It is a process in which the composition of a sample can be determined as a function of depth. In dynamic SIMS a dc primary ion beam is used to profile chemical changes of sample as a function of depth. However, with the emergence of static SIMS in 1960 [Benninghoven, 1970], followed by incorporation of ToF analysers in 1980 [Benninghoven, 1983], the primary ion beam could no longer be used in a dc mode and had to be operated in a pulsed mode. This resulted in a low duty cycle and a depth profile of a sample took a long time to complete. Consequently, to accomplish the experiment over a reasonable time, an alternating analysis and etch cycle method is adapted. This involves using a primary ion beam in a dc mode to raster over a large area on the surface and as it sputters down several microns below the surface, an etch crater is produced. Following this, the same or a different ion beam in a pulsed mode is used to analyse within this etch crater and the secondary ions produced are detected by a mass spectrometer, Figure 4.1. The dual beam approach allows the analyst to select the finest analysis beam and etching beam for a study under investigation [Iltgen *et al.*, 1997].

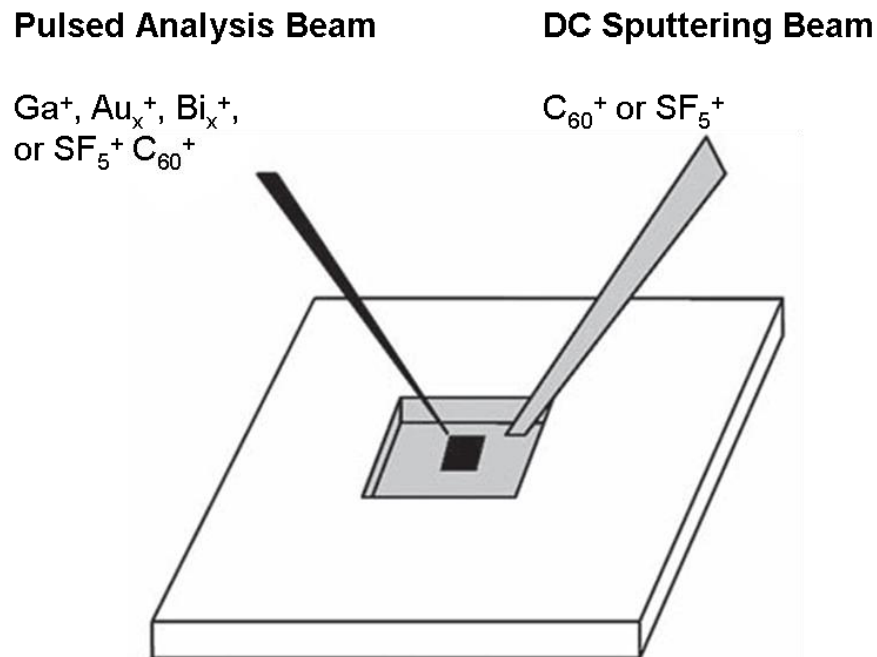


**Figure 4.1** Schematic of the dual beam approach to ToF-SIMS depth profiling and 3D analysis. Reproduced from Hammond, 2010.

Although, the concept of depth profiling has been known for decades and is particularly useful in the semiconductor industry, the implementation of molecular depth profiling was only accomplished with the development of polyatomic ion sources. The molecular depth profiling of organic and biological material was practically impossible with the monoatomic beams due to the damage characteristics associated with these beams, described in Chapter 1.

The very first molecular depth profiling study using polyatomic projectiles was reported by Gillen and co-workers in 1998. In this work the authors' depth profiled various polymer and organic films using a monoatomic ion beam,  $\text{Ar}^+$  and a polyatomic beam,  $\text{SF}_5^+$ . This study illustrated that under  $\text{SF}_5^+$  impact not only high secondary ion

yields can be obtained but the molecular signal can also be maintained as a function of primary ion fluence, until a substrate is reached, Figure 4.2b. However, under the bombardment with  $\text{Ar}^+$  the signal rapidly degrades with an increase in the primary ion dose, Figure 4.2.a [Gillen *et al.*, 1998].

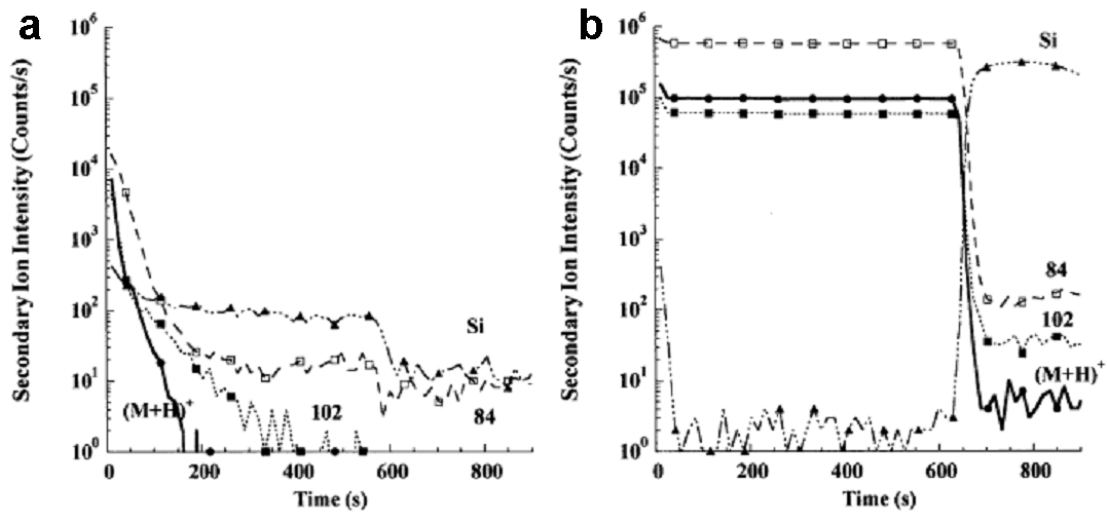


**Figure 4.2** Comparison of depth profiles obtained from 180 nm thick, vapour-deposited glutamate films (a) under  $\text{Ar}^+$  and (b) under  $\text{SF}_5^+$  primary ions under dynamic SIMS conditions. The  $\text{SF}_5^+$  primary ion dose to reach the silicon was  $1.4 \times 10^{15}$  ions/cm<sup>2</sup>. Reproduced from Gillen *et al.* 1998.

The authors explained that when the  $\text{SF}_5^+$  beam impacts a surface, the energy is divided between the sulfur and fluorine atoms and is deposited very close to the surface. This results in an increase in the sputter yields and the damage is limited to the surface region which is removed by subsequent impacts. Thus, during the depth profile using polyatomic beam, a pristine surface is analysed following each impact and a loss in the molecular signal is not observed. This is in contrast to the behaviour of the monoatomic

beam because when it strikes a sample it deposits its energy deep into the sub-surface region of the sample causing damage deep into the sample and generating low sputter yields. Furthermore, with continuous impact the damage accumulates in the sample and a rapid decay in the signal intensity of molecular ions is observed [Postawa *et al.*, 2004].

This work was followed by another study in which carbon cluster ions  $C_2^-$  to  $C_8^-$  were used to depth profile glutamate film yielding similar results as to the  $SF_5^+$  [Gillen *et al.*, 2001]. The polyatomic,  $SF_5^+$  projectile has been used extensively to depth profile polymers in submonolayer [Brox *et al.*, 2000] and multilayer films [Wagner, 2005] as well as doped with drugs [Mahoney *et al.*, 2004], [Mahoney *et al.*, 2006], [Belu, *et al.*, 2008].

With the development of the buckminsterfullerene,  $C_{60}^+$  ion source [Wong, *et al.*, 2003], it was also shown that this source too has the capabilities to depth profile a sample. Initial studies, conducted by Winograd and co-workers, were based on profiling inorganic and organic multilayer films to identify fundamental depth profiling characteristics of the  $C_{60}^+$  projectile [Sun *et al.*, 2004], [Sostarecz *et al.*, 2004]. These experiments were completed using a dual beam approach in which  $C_{60}^+$  ion beam was used for etching and  $Ga^+$  beam for analysis between etch cycles. These studies show that the  $C_{60}^+$  was able to clearly identify all the individual layers in a multilayer film and offers significant advantages over other beams; in terms of higher secondary yields, reduction in interlay mixing and enhanced depth resolution. Depth resolution, described in Chapter 1, is the ability to measure a sharp interface between the two layers. It has been shown to decrease with an increase in the roughness of the sample. Higher depth resolution is attained when polyatomic projectiles are used as compared to monoatomic

beams due to the shallow penetration of these beams upon impact and the energy deposited is limited only to the surface. As a consequence, there is low interlayer mixing and topographic roughness which improves the depth resolution [Sun *et al.*, 2004].

Similar effects have also been reported by Gillen and co-worker (1998) and Yamada and associate (1995) who demonstrate that a smoother surface is produced when a sample is bombarded with polyatomic projectile,  $\text{SF}_5^+$  and gas clusters as compared to atomic ion beams [Gillen *et al.*, 2008], [Yamada *et al.*, 1995].

Winograd and co-workers also carried out a series of depth profiles of polypeptide films using the  $\text{C}_{60}^+$  ion beam for both analysis and etching cycles [Cheng *et al.*, 2005], [Cheng *et al.*, 2006], [Cheng *et al.*, 2007]. In the first study the investigators show the ability of  $\text{C}_{60}^+$  to depth profile a biological material, trehalose which also enhances the stability of the polypeptide signal under bombardment [Cheng *et al.*, 2005]. This work was followed by another study in which organic multilayer films were depth profiled using the  $\text{C}_{60}^+$  ion beam. In this work trehalose was embedded between two chemical species, aluminium (Al), silicon (Si), silver (Ag) and ice to produce a number of multilayer films Al/trehalose/Si, Al/trehalose/Al/Si, Ag/trehalose/Si and ice/trehalose/Si, and following a depth profile it was established that best profiles were only obtained when the mass of the atoms in the top layer is less than or equivalent to the mass of atoms in the embedded molecules [Cheng *et al.*, 2006].

Cheng *et al.* (2007) published an article in which a direct comparison between the LMIS cluster,  $\text{Au}_3^+$  and polyatomic,  $\text{C}_{60}^+$  projectile was made on thin films of peptide doped trehalose and dipalmitoylphosphatidylcholine (DPPC). The profiles show

a decrease in the signal and increase in the fragmentation under  $\text{Au}_3^+$  impact as compared to the  $\text{C}_{60}^+$ .

At the same time, depth profiling studies using  $\text{C}_{60}^+$  were also being performed in the Vickerman lab. A number of articles have been published in which three different beams,  $\text{Au}^+$ ,  $\text{Au}_3^+$  and  $\text{C}_{60}^+$  have been used to depth profile a range of biological systems to explore the potential and benefits of the  $\text{C}_{60}^+$  projectile as compared to LMIS [Fletcher *et al.*, 2006], [Fletcher *et al.*, 2006], [Jones *et al.*, 2007]. The authors also report on the success of  $\text{C}_{60}^+$  to depth a profile cellulose film, previously not possible using  $\text{SF}_5^+$ , which highlights the feasibility of  $\text{C}_{60}^+$  to analyse and depth profile a range of biological samples [Fletcher *et al.*, 2006].

Jones *et al.* (2007) completed a comprehensive study on depth profiling of standard biological compounds, cholesterol and DPPC to determine a protocol for possible tissue depth profiling. Figure 4.3 shows that under  $\text{C}_{60}^+$  bombardment, the molecular ion  $[\text{M-H}]^+$   $m/z$  385 and fragment ion  $[\text{M-OH}]^+$   $m/z$  369 of cholesterol reach a steady state, whereas with  $\text{Au}_3^+$  and  $\text{Au}^+$  the signal rapidly decays with an increase in the primary ion fluence. A similar effect was also observed during the depth profile of DPPC film.

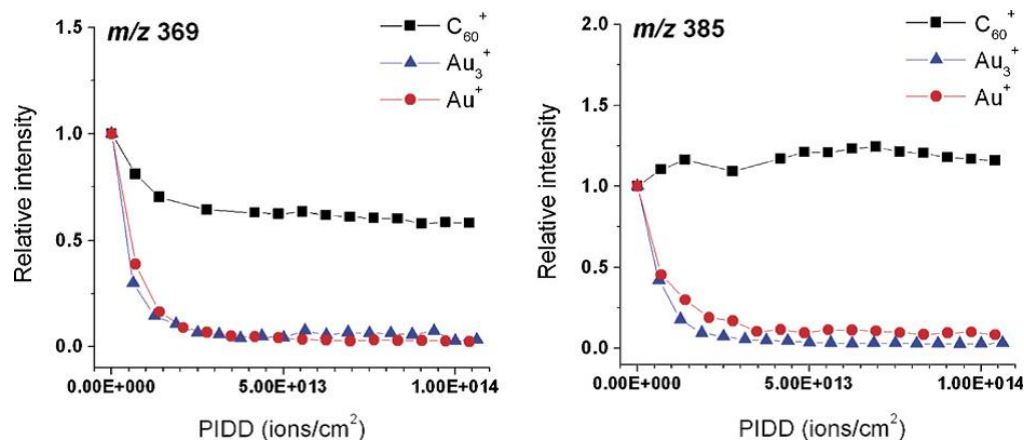


**Figure 4.3** A comparison of the stability of quasi-molecular ion intensity from a cholesterol film under prolonged bombardment by Au<sup>+</sup>, Au<sub>3</sub><sup>+</sup> and C<sub>60</sub><sup>+</sup> primary ion beams all at 15 keV. The plots show the relative peak intensity from the [M-OH]<sup>+</sup> *m/z* 369 (left) and [M-H]<sup>+</sup> *m/z* 385 (right) with respect to primary ion dose. Reproduced from Jones *et al.* 2007.

The literature shows that there are a number of parameters that can affect a depth profile of a sample, the beam used, angle and energy of the beam, as well as the temperature. The above studies demonstrate that the best molecular depth profiles are obtained using the polyatomic beams as compared to monoatomic or metal cluster ions.

With regards to the beam energy, higher sputter and secondary ion yields are obtained with an increase in the polyatomic beam energy [Bolotin *et al.*, 2006], [Fletcher *et al.*, 2006], [Shard *et al.*, 2007]. Furthermore, the molecular signal can also be maintained for longer period of time as a function of primary ion fluence at higher beam energy [Fisher *et al.*, 2008], [Wucher *et al.*, 2008]. However, this also increases the roughness of the sample which results in a loss of depth resolution. Winograd and

co-workers carried out a study in which they investigated the effect of a range of kinetic energies 20, 40, 80 and 120 keV of  $C_{60}^+$  ion beam on the depth resolution. The authors found that the energies between 20 and 40 keV provide better depth resolution of 18 nm as compared to higher energies [Wucher *et al.*, 2008].

Recently the National Physical Laboratory (NPL) have developed a model multilayer organic sample comprising of Irganox 1010 and Irganox 3114, to provide a comparison between different instrumentation, ion sources and experimental conditions for the depth profiling of organic films. Shard *et al.* (2008) depth profiled this reference delta layers sample in 'interlaced' mode using  $Bi_3^+$  for analysis and  $C_{60}^+$  for sputtering at various energies 5, 10, 20 and 30 keV. The results illustrate that as the energy of the sputtering beam is increased, the erosion depth increases and more layers are identified. However, this also increases the roughness of the sample which limits the depth resolution. This study shows that at lower energies greater depth resolution is obtained.

With respect to the beam incident angle, the literature shows that the angle at which the beam impacts a surface can also affect a depth profile of a sample. Winograd and co-workers used a cholesterol film deposited on Si to show the effect of varying the angle of incidence from  $40^\circ$  to  $73^\circ$  on molecular depth profiling. The investigators showed that at glancing angle,  $73^\circ$  the signal can be maintained for a long time and low damage is caused to the sample as compared to  $40^\circ$  incident angle [Kozole *et al.*, 2008]. Hence, it is preferred to perform depth profiling at glancing incident angle. A similar effect was also observed by Miyayama and co-workers when they depth profiled a polymer using  $C_{60}^+$  ion beam at different angle of incident [Miyayama *et al.*, 2008].

The temperature plays a crucial role in depth profiling experiments. Mahoney and co-workers identified that temperature can have a significant effect on the success of profiling organic samples, particularly polymers. This is since the physical and chemical properties of the polymers vary with temperature and which will also effect the sputtering rates. The authors showed that profiling Poly(methyl methacrylate) (PMMA) at low temperature results in an increase in the secondary ion stability, low interface width as well as a reduced topography effect with an increase in erosion as compared to depth profiling at room temperature [Mahoney *et al.*, 2006], [Mahoney *et al.*, 2007]. A study by Zheng *et al.* (2008) also shows that at cryogenic temperature, the high mass signal and sputtering of LB multilayer film remains stable with an increase in primary ion dose, but at room temperature the signal slowly degrades. Recently a paper by Sjövall and associates also report on the same trend. In this study, the authors used the NPL reference delta layers to show that at low temperature, better profiles can be obtained while maintaining constant sputter and secondary ion yields [Sjövall *et al.*, 2010]. These effects have also been observed and confirmed by a recent study undertaken in the Vickerman lab where the investigators depth profiled a range of bio-samples at low temperature [Piwowar *et al.*, 2010]. These studies conclude that high quality profiles of organic samples can be achieved at cryogenic temperatures.

In summary, the developments of polyatomic ion beams have instigated molecular depth profiling of organic and biological molecules as monolayer as well as in multilayer systems. These beams, particularly  $C_{60}^+$  offer the benefits of higher secondary ion yields, reduction in interlayer mixing and reduced topographic roughness with an improved depth resolution.

The aim of this chapter is to discuss the ability of cluster and polyatomic beams to remove the damage induced by the monatomic beam, thus regenerating the original surface to establish a protocol for *high lateral resolution* 3D ToF-SIMS imaging of bio-samples using polycaprolactone. Further, it explores the use of polyatomic beam  $C_{60}^+$  as a dc beam for molecular depth profiling on the J105 using organic standards samples, arginine and a tetrapeptide (GGYR).

## 4.2 Dept profiling of Polycaprolactone

Polycaprolactone (PCL) is biodegradable polyester that can be prepared by a ring opening polymerisation mechanism of  $\epsilon$ -caprolactone, Figure 4.4. It has a low melting point of  $60^\circ\text{C}$  and is used as an additive for resin to enhance their processing characteristics and operating properties. PCL can be hydrolyzed by its ester linkage in physiological conditions and has been used as an implantable material [Wikipedia, 2007].

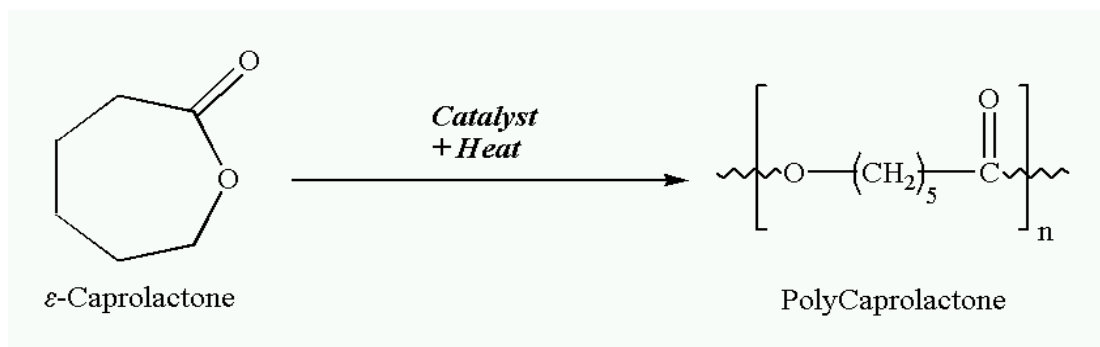


**Figure 4.4** Ring opening polymerization of  $\epsilon$ -caprolactone. Reproduced from Wikipedia, 2007

Roberson *et al.* (2003) used ToF-SIMS to complete a bio-compatibility study of PCL using a  $\text{Ga}^+$  primary ion beam. The authors disclose that this technique can be useful in correlating the contact angle measurement, as well as determining a change in the chemical composition of the PCL surface.

PCL is one of the most commonly biodegradable polymers used as matrix for drug delivery and has been depth profiled using monoatomic and polyatomic projectiles. Mahoney *et al.* (2004) depth profiled a series of biodegradable polymers including PCL doped with model drugs using monoatomic,  $\text{Ar}^+$  and  $\text{Cs}^+$  and polyatomic  $\text{SF}_5^+$  primary ion beams. The aim of this study was to investigate the behaviour of the polymers as a function of primary ion dose as well as monitor the distribution of drugs as a function of depth. The results show that the secondary ion signal of polymers and drugs remains stable under polyatomic beam,  $\text{SF}_5^+$  for ion dose as high as  $5 \times 10^{15}$  ion/cm<sup>2</sup> as compared to the monoatomic beams.

Further, depth profiles of PCL were completed by Fletcher *et al.* (2006) using  $\text{C}_{60}^+$ ,  $\text{Au}^+$  and  $\text{Au}_3^+$  to provide a comparison between the different primary ion beams. This study also illustrates that PCL remains stable under polyatomic beams, but higher sputter yields are produced when  $\text{C}_{60}^+$  is used as compared to  $\text{SF}_5^+$  ion beam. The PCL was found to be unstable when depth profiled using monoatomic  $\text{Au}^+$  and the small cluster ion,  $\text{Au}_3^+$ , Figure 4.5.

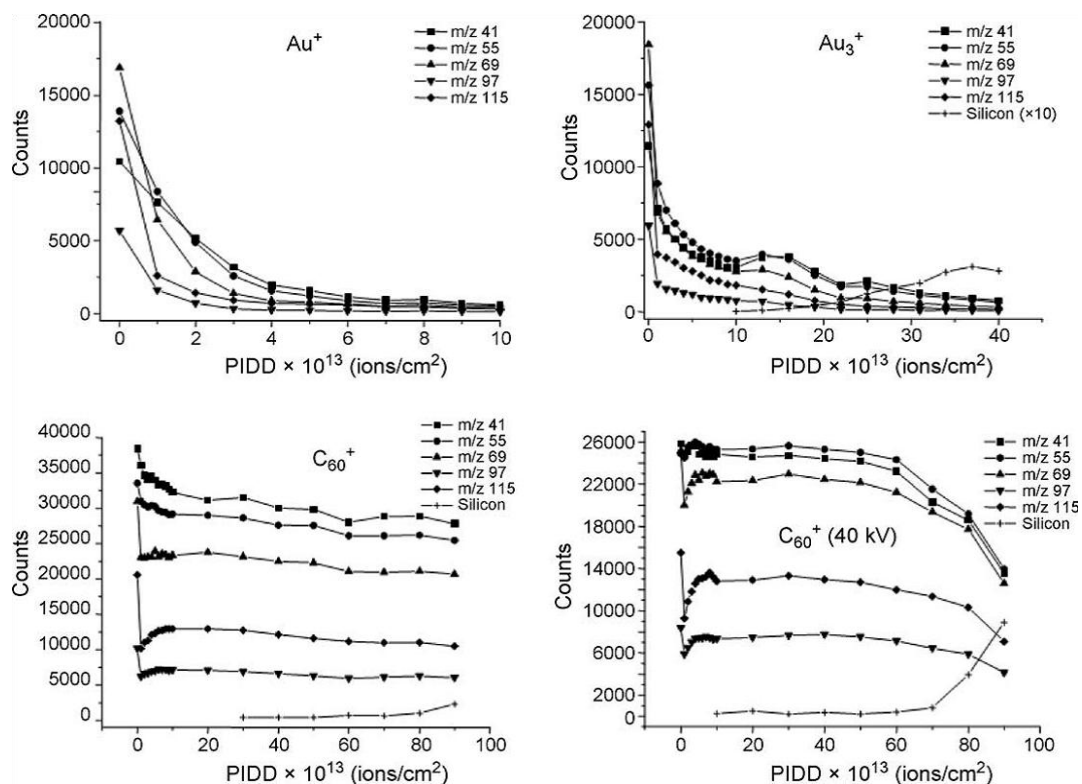


**Figure 4.5** Variation in absolute intensity of the fragments associated with polycaprolactone (PCL) with increasing dose. Profiles acquired with 20 keV Au<sup>+</sup>, Au<sub>3</sub><sup>+</sup> and C<sub>60</sub><sup>+</sup> and 40 keV C<sub>60</sub><sup>+</sup> primary ions. Reproduced from Fletcher *et al.* 2006.

A short study was undertaken to determine the ability of cluster, 20 keV Au<sub>3</sub><sup>+</sup> and the polyatomic ion beam, 20 keV and 40 keV C<sub>60</sub><sup>+</sup> to remove the damage induced by the monoatomic, 20 keV Au<sup>+</sup> following a depth profile on the conventional ToF-SIMS instrument, the BioToF.

### 4.2.1 Experimental

PCL (Sigma Aldrich, UK) was dissolved in chloroform to form  $10^{-3}$  M solution and a thick film was prepared by spin casting 10  $\mu$ l droplets onto silicon substrate. The film was allowed to dry for 10 minutes and the sample was mechanically attached to the copper sample stub and transferred into the BioToF. The depth profile analysis of the biopolymer PCL was carried out using 20 keV  $\text{Au}^+$  with ion dose of  $1 \times 10^{13}$  ions/cm<sup>2</sup> per analysis and  $128 \times 128$  pixels over an area of  $300 \times 300 \mu\text{m}^2$ . The depth profile continued until a dose of  $1 \times 10^{14}$  ions/cm<sup>2</sup> was reached. Following this, the sample was imaged depth profile by using 20 keV  $\text{Au}_3^+$ , 20 keV  $\text{C}_{60}^+$  and 40 keV  $\text{C}_{60}^+$ . An electron gun was also used for charge compensation.

### 4.2.2 Results and Discussion

Figure 4.6 shows the standard spectra of PCL acquired with 20 keV  $\text{Au}^+$  with 5 main peaks at  $m/z$  41 [ $\text{C}_3\text{H}_5^+$ ],  $m/z$  55 [ $\text{C}_4\text{H}_7^+$ ],  $m/z$  69 [ $\text{C}_5\text{H}_9^+$ ],  $m/z$  97 [ $\text{C}_6\text{H}_9\text{O}^+$ ] and a molecular specific fragment  $[\text{M}+\text{H}]^+$  at  $m/z$  115. The depth profile results are depicted in Figure 4.7 in which the secondary ion intensities of molecular signal  $[\text{M}+\text{H}]^+$   $m/z$  115 is plotted as a function of increasing ion dose for three beams,  $\text{Au}^+$ ,  $\text{Au}_3^+$  and  $\text{C}_{60}^+$ . This figure illustrates that under bombardment with 20 keV  $\text{Au}^+$ , there is a rapid decrease in the molecular ion  $[\text{M}+\text{H}]^+$  with an increase in the primary ion dose. This has also been reported previously by Fletcher *et al.* (2006), Figure 4.5. This decrease in the signal is attributed to the damaging characteristics of the monoatomic beam when it is operated at ion dose higher than the static limit. It has been described above and in Chapter 1 that when the monoatomic beam impacts a surface, it penetrates deep into the sample

causing the molecular bonds to break in deep regions of the sample. Thus following an initial etch, the beam is subsequently impacting an increasingly damaged surface and preventing the ability to depth profile molecular sample.

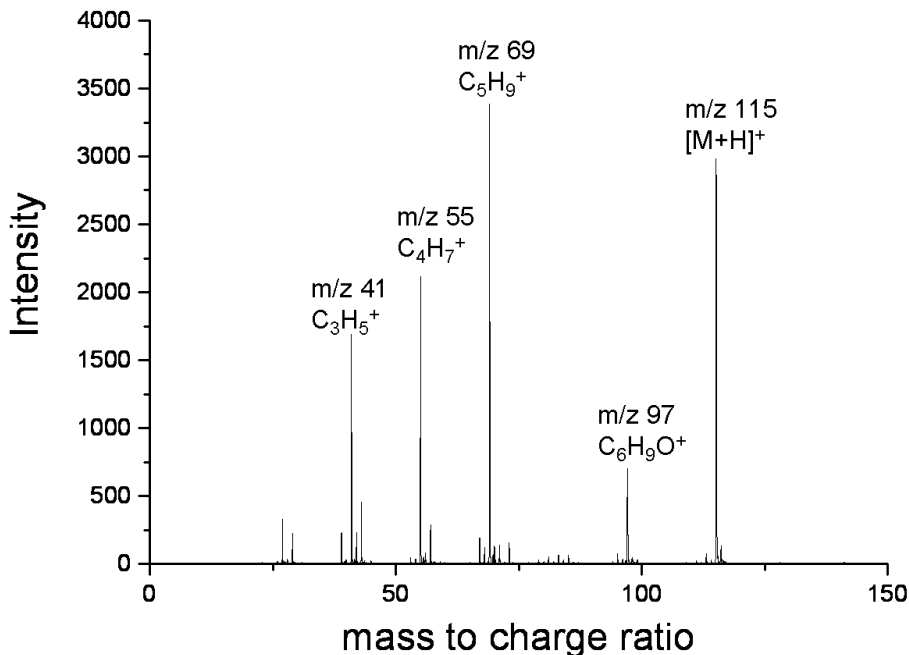


**Figure 4.6** ToF-SIMS spectrum of polycaprolactone (PCL) acquired with 20 keV Au<sup>+</sup> with ion dose of  $1 \times 10^{13}$  ion/cm<sup>2</sup> over an area of  $300 \times 300 \mu\text{m}^2$ .

PCL was depth profiled using 20 keV Au<sup>+</sup> up to ion dose of  $1 \times 10^{14}$  ions/cm<sup>2</sup> after which an image depth profile was performed using cluster, Au<sub>3</sub><sup>+</sup> and polyatomic, C<sub>60</sub><sup>+</sup> ion beams. Under the 40 keV C<sub>60</sub><sup>+</sup> bombardment, an initial drop in the [M+H]<sup>+</sup> signal is observed, Figure 4.7, but following subsequent alternating etch and analysis cycles the signal increases and a plateau is attained between  $1.5 \times 10^{14} - 2.0 \times 10^{14}$

ions/cm<sup>2</sup>. A similar pattern was also observed when the damaged surface was bombarded with 20 keV C<sub>60</sub><sup>+</sup>. Thus the C<sub>60</sub><sup>+</sup> bombardment not only recovers the molecular signal by removing the damage induced by the Au<sup>+</sup> ion beam but also maintains the molecular signal as a function of primary ion fluence. Furthermore, higher secondary ion signals are obtained when the sample is interrogated with 40 keV C<sub>60</sub><sup>+</sup> than with 20 keV C<sub>60</sub><sup>+</sup> ion beam. This is because at higher energy, the beam impacts deeper into the sample causing more material to be ejected and increasing the sputter yields [Fletcher *et al.*, 2006]. This observation is also supported by the simulation studies which show that as the impact energy of the C<sub>60</sub><sup>+</sup> ions on silver is increased, the impact diameter decreases while the depth of the crater increases, resulting in higher sputter yields [Postawa *et al.*, 2004].

However, this is in contrast to the results obtained when the sample is imaged depth profiled using the cluster, 20 keV Au<sub>3</sub><sup>+</sup> ion beam, where the [M+H]<sup>+</sup> signal decays further with an increase in the ion dose. These results are also exemplified in the images generated from the image depth profile, Figure 4.8.

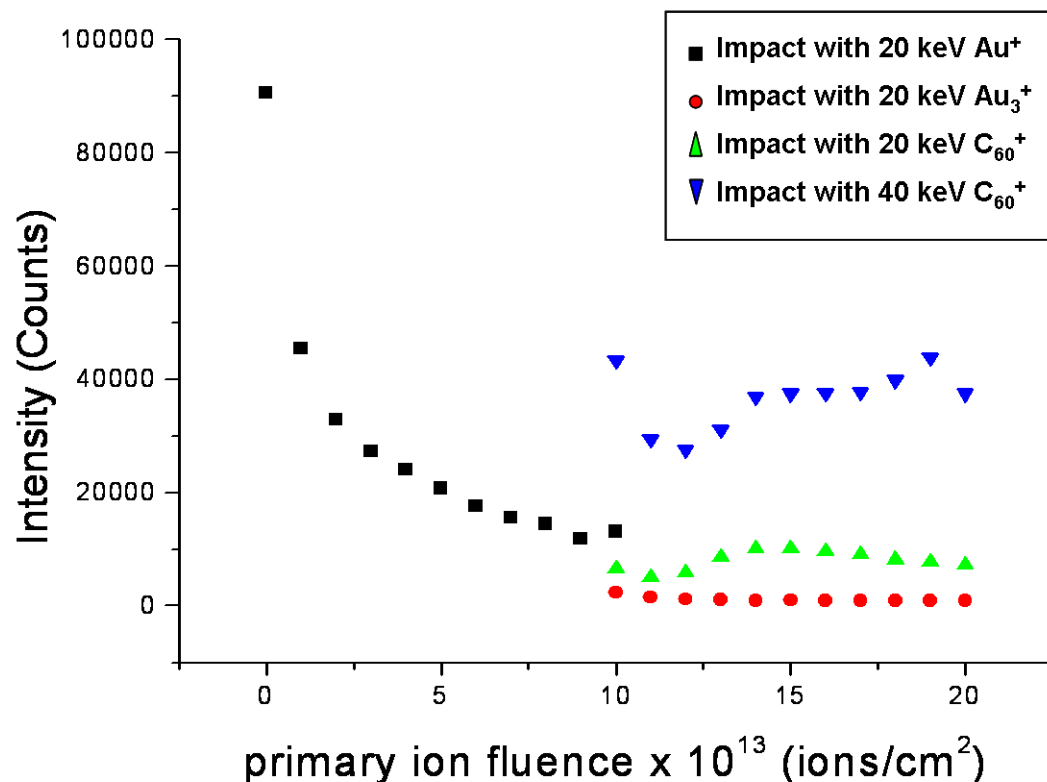


**Figure 4.7** Secondary ion signal  $[M+H]^+$   $m/z$  115 of polycaprolactone (PCL) plotted as function of primary ion dose. Black: Data acquired with 20 keV Au<sup>+</sup> up to ion dose  $1 \times 10^{14}$  ions/cm<sup>2</sup>. Red: Data acquired with 20 keV Au<sub>3</sub><sup>+</sup>. Green: Data acquired with 20 keV C<sub>60</sub><sup>+</sup>. Blue: Data acquired with 40 keV C<sub>60</sub><sup>+</sup>.

Figure 4.8 shows that at primary ion dose  $2 \times 10^{14}$  ions/cm<sup>2</sup> the 40 keV C<sub>60</sub><sup>+</sup> is able to fully recover the damage; whereas the 20 keV C<sub>60</sub><sup>+</sup> is only able to remove some at the same dose. The Au<sub>3</sub><sup>+</sup> is unable to eradicate any of the damage implanted by Au<sup>+</sup> and in addition to this destroys the surface further. This is because when the Au<sub>3</sub><sup>+</sup> impacts a surface it breaks into its constituent atoms but each atom still has enough energy to penetrate deep into the sub-surface of the sample. As a consequence, the sample is significantly damaged which builds up and is uncovered as the depth profile

proceeds, explained in Chapter 1. Similar results have also been reported by Gillen and co-workers where they show the success of polyatomic beam  $\text{SF}_5^+$  to successfully remove the damage caused by the monoatomic,  $\text{Ar}^+$  beam from the surface [Gillen *et al.*, 1998].

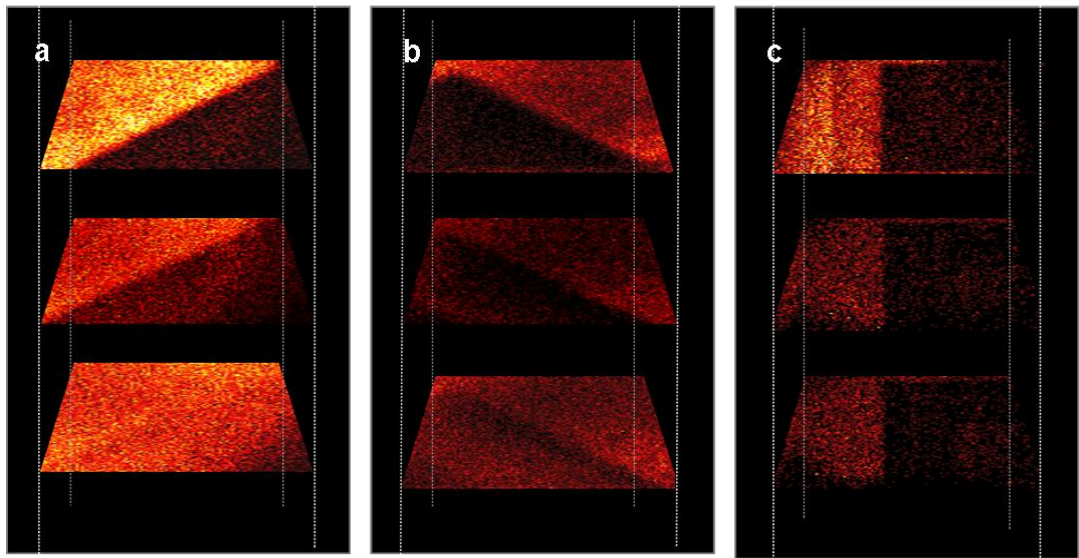


**Figure 4.8** Image depth profile of polycaprolactone (PCL), half of the area was bombarded with 20 keV  $\text{Au}^+$  and then half was restored using cluster and polyatomic beams (a) Right triangle bombarded with 20 keV  $\text{Au}^+$ ; Left triangle restored with 40 keV  $\text{C}_{60}^+$ . (b) Left triangle bombarded with 20 keV  $\text{Au}^+$ ; Right triangle restored with 20 keV  $\text{C}_{60}^+$ . (c) Right triangle bombarded with 20 keV  $\text{Au}^+$ ; Left triangle restored with 20 keV  $\text{Au}_3^+$ . From top to bottom the primary ions fluence is  $1.1 \times 10^{14}$ ,  $1.3 \times 10^{14}$  and  $1.6 \times 10^{14}$  ions/cm<sup>2</sup>.

### 4.2.3 Conclusion

The development of novel cluster and polyatomic ion beams has opened up the possibility for molecular depth profiling using ToF-SIMS which opens up the prospects of 3D molecular imaging, described in Chapter 5. The PCL study shows that the polyatomic beam,  $C_{60}^+$  is able to fully remove the damage caused by the monoatomic beam and recover the molecular signal whereas the cluster,  $Au_3^+$  ion beam causes more damage to the surface. In addition, the  $C_{60}^+$  beam maintains secondary ion signal as a function of primary ion fluence allowing the ability to depth profile organic samples successfully.

This research outlines the prospect of performing *high lateral resolution* 3D imaging using dual beam approach in which highly focused LMIS,  $Au_n^+$  or  $Bi_n^+$  can be used to acquire images with high spatial resolution, and polyatomic  $C_{60}^+$  or  $SF_5^+$  for removing the damage caused by the LMIS. Although this interleaved method is frequently used by the SIMS community for molecular depth profiling and *high lateral resolution* 3D imaging of cells and tissues, the sputter rates calculated using Atomic Force Microscope (AFM) indicate that the dose required to remove the damage caused by  $Au^+$  ion corresponds to the removal of 25-30 nm material by 40 keV  $C_{60}^+$ . This results in a loss of valuable molecular information from the top 20-30 nm of the sample.

### 4.3 Depth Profile of standard samples using dc $C_{60}^+$ primary ion on the J105 3D Chemical Imager

It has been recognised in the above study and in the literature that the dual beam approach allows performing depth profiling at *high lateral resolution* over a reasonable time frame. However, a lot of valuable sample is also lost during the sputtering cycles. Furthermore, the ion dose of monoatomic and metal cluster beams has to be kept within the static limit to prevent damage to the sample, which limits sensitivity. Thus as described in Chapter 2, an approach was required in which depth profiling experiments could be performed using a primary ion beam with high fluence beyond the static limit which causes little or no damage to the sample. Besides, the depth profile could be completed over a practical time frame while analysing the whole sample without needing a separate etch cycle. As discussed previously the  $C_{60}^+$  ion beam promises to meet these requirements but to fully explore the properties of this beam the conventional ToF-SIMS had to be modified. This led to the design and development of the new instrument J105 *3D Chemical Imager*, described in Chapter 2. On this instrument the polyatomic beam can be used in dc mode and focussed to a small spot size while retaining high current for *high lateral resolution* imaging. Depth profile experiments on the J105 are performed in similar manner to dynamic SIMS but by using the polyatomic beam molecular information is obtained. Moreover, since the dual beam approach is no longer used, a loss of sample during the etch cycle is avoided which maximises sensitivity with an increase in duty cycle, Figure 4.9.

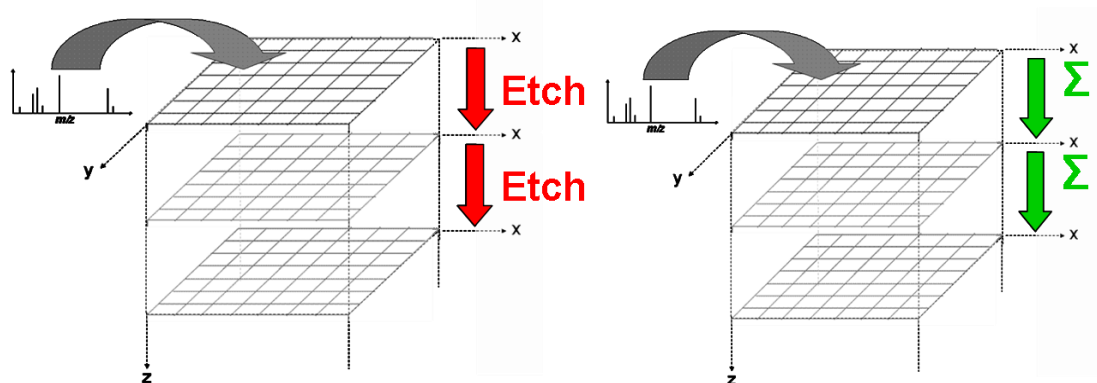


**Figure 4.9** Depth profiling by ToF-SIMS. (a) Depth profiling using a conventional SIMS which requires the use of dual beam in which one is used for imaging followed by etching which wastes valuable sample. (b) The use of a continuous analysis beam on the J105 means that all the material is sampled [Reproduced from Hill *et al.*, 2009].

Experiments were undertaken to explore the ability of  $C_{60}^+$  to depth profile standard organic films, arginine and a tetrapeptide (GGYR) in dc mode.

### 4.3.1 Experimental

Thin films of arginine and a tetrapeptide (GGYR) were prepared as dried droplets on Si wafers. These samples were depth profiled using 40 keV  $C_{60}^+$  primary ion beam (120 pA) with an ion dose of  $1 \times 10^{13}$  ions/cm<sup>2</sup> per layer with  $32 \times 32$  pixels over an area of  $330 \times 330 \mu\text{m}^2$ . In total 31 layers were acquired with total ion dose of  $3.0 \times 10^{14}$  ions/cm<sup>2</sup> was used.

### 4.3.2 Results and Discussion

ToF-SIMS spectra of arginine and tetrapeptide (GGYR) acquired on the J105 have been shown previously, see Figure 3.3 and Figure 3.11 in Chapter 3. Arginine produces many diagnostic ions, but three ions  $[M+H]^+$   $m/z$  175,  $[C_5H_{12}N_3O]^+$   $m/z$  130 and  $[C_4H_8N]^+$   $m/z$  70 were selected to show the behaviour of arginine when it is interrogated with a continuous primary ion beam, Figure 4.10. When the sample is depth profiled with 40 keV  $C_{60}^+$ , an initial drop in signal intensity for molecular and the fragment ions is observed after which the signal reaches a steady state between an ion dose of  $3 \times 10^{13}$  ions/cm<sup>2</sup> to  $3.1 \times 10^{14}$  ions/cm<sup>2</sup>. Arginine has also been previously depth profiled using 20 keV  $C_{60}^+$  primary ion beam at room temperature and in a frozen hydrated state [Piwowar *et al.*, 2009]. In both of these conditions molecular signal is maintained with an increase in the primary ion dose with high yields being reported at frozen hydrated state.

Upon depth profiling, the tetrapeptide (GGYR) with 40 keV  $C_{60}^+$  in dc mode a similar pattern is also observed in which the signal is maintained as a function of primary ion dose, Figure 4.11.

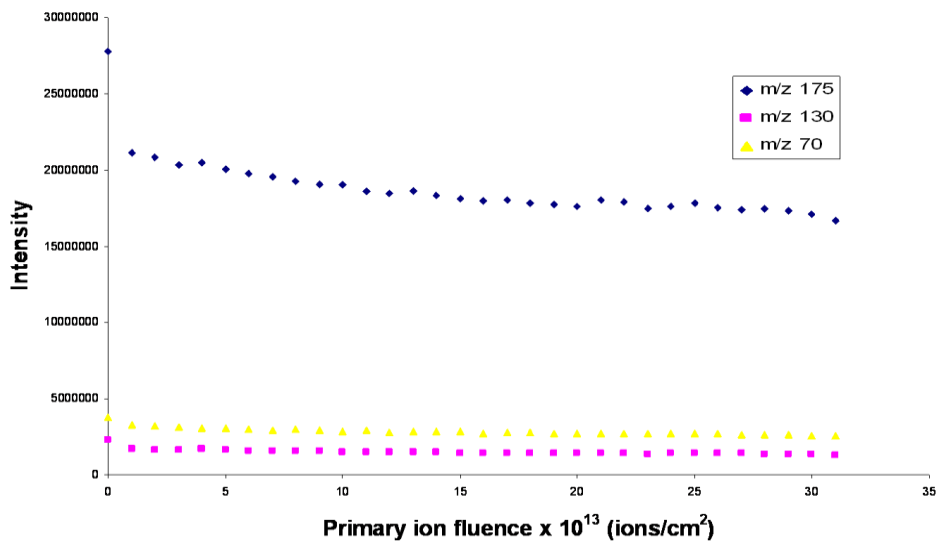


**Figure 4.10** Plot of secondary ion signal of arginine as a function of 40 keV  $C_{60}^+$  primary ion fluence. Blue:  $[M+H]^+$   $m/z$  175. Pink:  $[C_5H_{12}N_3O]^+$   $m/z$  130. Yellow:  $[C_4H_8N]^+$   $m/z$  70.

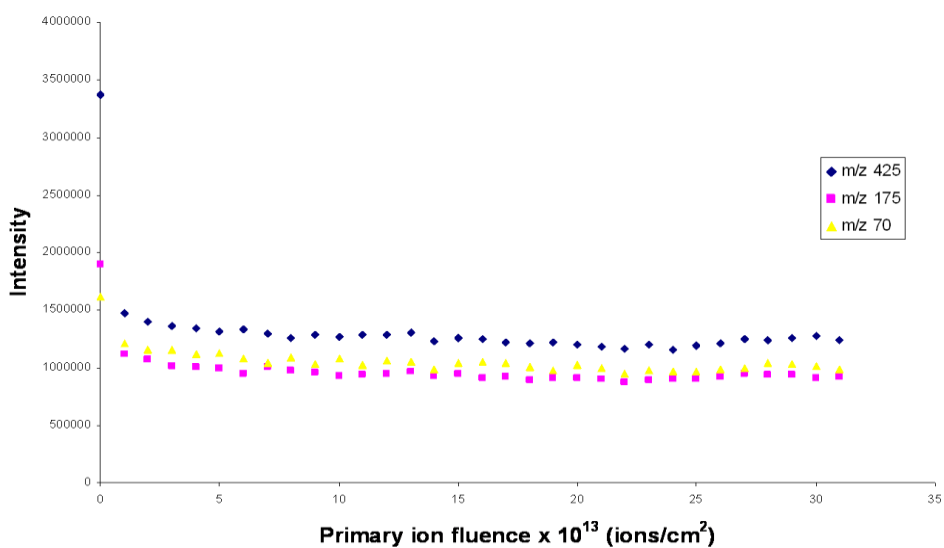


**Figure 4.11** Plot of secondary ion signal of a tetrapeptide (GGYR) as a function of 40 keV  $C_{60}^+$  primary ion fluence. Blue:  $[M+H]^+$   $m/z$  425. Pink:  $[C_6H_{15}N_4O_2]^+$   $m/z$  175. Yellow:  $[C_4H_8N]^+$   $m/z$  70.

### 4.3.3 Conclusion

This study shows that the  $C_{60}^+$  ion beam can be used in dc mode to molecular depth profile organic samples. Additionally, higher secondary ion signals are obtained which can be maintained as a function of primary ion dose. On the conventional ToF-SIMS instrument, BioToF this experiment could only be accomplished by using alternating analysis and etch cycles which would have wasted substantial amounts of valuable sample resulting in decrease in sensitivity. Thus the benefits of performing depth profile experiments on the J105 could be realised.

The depth profile experiment was stopped at ion dose  $3.1 \times 10^{13}$  ions/cm<sup>2</sup> and could have been carried until the substrate was reached.

## 4.4 Summary

In this chapter molecular depth profiling has been reviewed. Advances in the instrumentation particularly polyatomic ion beams has extended the capability of ToF-SIMS to molecular depth profile various biological molecules and is continuously evolving to meet the needs of biological community. It has been shown that factors such as type of beam, beam energy, beam angle and temperature greatly influence depth profile results and these factors need to be carefully considered prior to the experiment to obtain high quality results.

A dual beam approach is often used by the analyst in which monoatomic or cluster ion beam is used for analysis and polyatomic beam for sputtering. However, sputter rates calculated for the PCL study show that the dose required by the polyatomic beam,  $C_{60}^+$  to remove the damage caused by the monoatomic beam, corresponds to the removal of 25-30 nm material from the sample. Although successfully implied for *high lateral resolution* 3D imaging, it results in a large quantity of valuable sample to be wasted during the etch cycles. Thus and an alternative approach is required where a whole material can be sampled and detected.

The new instrument, the J105 allows using the polyatomic beam,  $C_{60}^+$  in a dc mode, thus sampling a whole material and increasing sensitivity. Furthermore, due to low damage cross-section the molecular signal can be maintained as a function of primary ion fluence and in-depth chemistry to be probed. The J105 allows exploiting the capabilities of the polyatomic beams thoroughly making the prospect of rapid 3-D molecular imaging of cells and tissue a reality.

## References

- Belu, A.; Mahoney, C.; Wormuth, K. **Chemical imaging of drug eluting coatings: Combining surface analysis and confocal Raman microscopy**. *Journal of Controlled Release* (2008), 126 (2), 111-121
- Benninghoven, A. **Analysis of monomolecular surface layers of solids by secondary ion emission**. *Zeitschrift fuer Physik* (1970), 230(5), 403-417
- Benninghoven, A.; Steffens, P.; Niehuis, E.; Friese, T. **Application of a new Time of Flight**. *Annual Conference on Mass Spectrometry and Allied Topics* (1983), 54-55
- Bolotin, I.L.; Tetzler, S.H.; Hanley, L. **Sputtering yields of PMMA films bombarded by keV C<sub>60</sub><sup>+</sup> ions**. *Applied Surface Science* (2006), 252 (19), 6533-6536
- Brox, O.; Hellweg, S.; Benninghoven A. **Dynamic SIMS of polymer films?** *Proc 12th International Conference Secondary Ion Mass Spectrometry* (2000), 12, 777–780
- Cheng, J.; Kozole, J.; Hengstebeck, R.; Winograd, N. **Direct Comparison of Au<sub>3</sub><sup>+</sup> and C<sub>60</sub><sup>+</sup> Cluster Projectiles in SIMS Molecular Depth Profiling**. *Journal of the American Society for Mass Spectrometry* (2007), 18 (3), 406-412
- Cheng, J.; Winograd, N. **Depth profiling of peptide films with TOF-SIMS and a C<sub>60</sub> probe**. *Analytical Chemistry* (2005), 77 (11), 3651-3659
- Cheng, J.; Wucher, A.; Winograd, N. **Molecular depth profiling with cluster ion beams**. *Journal of Physical Chemistry B* (2006), 110 (16), 8329-8336
- Fisher, G.L.; Dickinson, M.; Bryan, S.R.; Moulder, J. **C<sub>60</sub> sputtering of organics: A study using TOF-SIMS, XPS and nanoindentation**. *Applied Surface Science* (2008), 255 (4), 819-823
- Fletcher, J.S.; Conlan, X.A.; Lockyer, N.P.; Vickerman, J.C. **Molecular depth profiling of organic and biological materials**. *Applied Surface Science* (2006), 252, 6513–6516
- Fletcher, J.S.; Xavier, A.C.; Jones, E.A.; Biddulph, G.; Lockyer, N.P.; Vickerman, J.C. **TOF-SIMS Analysis Using C<sub>60</sub>. Effect of Impact Energy on Yield and Damage**. *Analytical Chemistry* (2006), 78, 1827-1831
- Gillen, G.; King, L.; Freibaum, B.; Lareau, R.; Bennett, J.; Chmara, F. **Negative caesium sputter ion source for generating cluster primary ion beams for secondary ion mass spectrometry analysis**. *Journal of Vacuum Science and Technology, Part A: Vacuum, Surfaces and Films* (2001), 19 (2), 568-575

Gillen, G.; Roberson, S. **Preliminary Evaluation of an SF<sub>5</sub><sup>+</sup> Polyatomic Primary Ion Beam for Analysis of Organic Thin Films by Secondary Ion Mass Spectrometry**. *Rapid Communication in Mass Spectrometry* (1998), 12, 1303–1312

Hammond, J.S. **Imaging Mass Spectrometry: Protocols for Mass Microscopy**, Chapter 18 Comparison of SIMS and MALDI for Mass Spectrometric Imaging, Springer 2010

Hill, R.; Blenkinsopp, P.; Everest, C.; Barber, A.; Vickerman, J.C.; Fletcher, J.S.; Thompson, S.P. **A New Instrument for 3-Dimensional Imaging SIMS**. UK SAF Meeting (2009), Private Communication

Iltgen, K.; Bendel, C.; Benninghoven, A. **Optimized time-of-flight secondary ion mass spectroscopy depth profiling with a dual beam technique**. *Journal of Vacuum Science and Technology A* (1997), 15 (3), 460-464

Jones, E.A.; Lockyer, N.P.; Vickerman, J.C. **Mass spectral analysis and imaging of tissue by ToF-SIMS—The role of buckminsterfullerene, C<sub>60</sub><sup>+</sup>, primary ions**. *International Journal of Mass Spectrometry* (2007), 260 146–157  
Kozole, J.; Willingham, D.; Winograd, N. **The effect of incident angle on the C<sub>60</sub><sup>+</sup> bombardment of molecular solids**. *Applied Surface Science* (2008), 255 (4), 1068-1070

Mahoney, C.M.; Yu, J.; Fahey, A. ; Gardella Jr.; J.A. **SIMS depth profiling of polymer blends with protein based drugs**. *Applied Surface Science* (2006), 252 (19), 6609-6614

Mahoney, C.M.; Fahey, A.J.; Gillen, G.; Xu, C.; Batteas, J.D. **Temperature-controlled depth profiling in polymeric materials using cluster secondary ion mass spectrometry (SIMS)**. *Applied Surface Science* (2006), 252 (19), 6502-6505

Mahoney, C.M.; Fahey, A.J.; Gillen, G.; Xu, C.; Batteas, J.D. **Temperature-controlled depth profiling of poly(methyl methacrylate) using cluster secondary ion mass spectrometry. 2. Investigation of sputter-induced topography, chemical damage, and depolymerization effects**. *Analytical Chemistry* (2007), 79 (3), 837-845

Mahoney, C.M.; Roberson, S.; Gillen, G. **Dynamic SIMS utilizing SF<sub>5</sub><sup>+</sup> polyatomic primary ion beams for drug delivery applications**. *Applied Surface Science* (2004), 231-232, 174-178

Piwowar, A.M.; Fletcher, J.S.; Kordys, J.; Lockyer, N.P.; Winograd, N.; Vickerman, J.C. **Effects of Cryogenic Sample Analysis on Molecular Depth Profiles with TOF-Secondary Ion Mass Spectrometry** *Analytical Chemistry* (2010), published online

Miyayama, T.; Sanada, N.; Iida, S.; Hammond, J.S.; Suzuki, M. **The effect of angle of incidence to low damage sputtering of organic polymers using a C<sub>60</sub> ion beam.** Applied Surface Science (2008), 255 (4), 951-953

Postawa, Z. **Sputtering simulations of organic overlayers on metal substrates by monoatomic and clusters projectiles.** Applied Surface Science (2004), 231-232, 22-28

Roberson, S.; Sehgal, A.; Fahey, A.; Karim, A. **Time-of-flight secondary ion mass spectrometry (ToF-SIMS) for high-throughput characterization of biosurfaces.** Applied Surface Science (2003), 203-204, 855-858

Shard, A.G.; Brewer, P.J.; Green, F.M.; Gilmore, I.S. **Measurement of sputtering yields and damage in C<sub>60</sub> SIMS depth profiling of model organic materials.** Surface and Interface Analysis (2007), 39 (4), 294-298

Shard, A.G.; Green, F.M.; Gilmore, I.S. **C<sub>60</sub> ion sputtering of layered organic materials.** Applied Surface Science (2008), 255 (4), 962-965

Sjövall, P.; Rading, D.; Ray, S.; Yang, L.; Shard, A.G. **Sample Cooling or Rotation Improves C<sub>60</sub> Organic Depth Profiles of Multilayered Reference Samples: Results from a VAMAS Interlaboratory Study.** Journal of Physical Chemistry B (2010), 114 (2), 769-774

Sostarecz, A.G.; Sun, S.; Szakal, C.; Wucher, A.; Winograd, N. **Depth profiling studies of multilayer films with a C<sub>60</sub><sup>+</sup> ion source.** Applied Surface Science (2004), 231-232, 179-182

Sun, S.; Szakal, C.; Roll, T.; Mazarov, P.; Wucher, A.; Winograd, N. **Use of C<sub>60</sub> cluster projectiles for sputter depth profiling of polycrystalline metals.** Surface and Interface Analysis (2004), 36, 1367-1372

Sun, S.; Wucher, A.; Szakal, C.; Winograd, N. **Depth profiling of polycrystalline multilayers using a Buckminsterfullerene projectile.** Applied Physics Letters (2004), 84 (25) 5177-5179

Wagner, M.S. **Molecular depth profiling of multilayer polymers films using time-of-flight secondary ion mass spectrometry.** Analytical Chemistry (2005), 77 (3), 911-922

Wikipedia <http://en.wikipedia.org/wiki/Polycaprolactone> accessed on 7-08-2009

Wong, S.C.C.; Hill, R.; Blenkinsopp, P.; Lockyer, N.P.; Weibel, D.E.; Vickerman, J.C. **Development of a C<sub>60</sub><sup>+</sup> ion gun for static SIMS and chemical imaging.** Applied Surface Science (2003), 203-204, 219-222

Wucher, A.; Cheng, J.; Winograd, N. **Molecular depth profiling using a C<sub>60</sub> cluster beam: The role of impact energy.** *Journal of Physical Chemistry C* (2008), 112 (42) 16550-16555

Yamada, I.; Matsuo, J.; Insepov, Z.; Akizuki, M. **Surface modifications by gas cluster ion beams.** *Nuclear Instrument and Methods in Physics Research, B* (1995), 106 (1-4), 165-169

Zheng, L.; Wucher, A.; Winograd, N. **Depth resolution during C<sub>60</sub><sup>+</sup> profiling of multilayer molecular films.** *Analytical Chemistry* (2008), 80 (19), 7363-7371

## 5 Sub-cellular imaging of cells using ToF-SIMS

### 5.1 Introduction

A cell is a basic, living, structural and functional unit of a body with the main function of allowing material to move across the cell membrane, cell division and protein synthesis. There are two types of cells, eukaryotes and prokaryotes, with the major difference being the presence of a nucleus in eukaryotes and absent in prokaryotes. In this project, a eukaryotic cell line was used and this will form the main part of discussion.

Figure 5.1 shows a generalised view of a typical animal cell which can be divided into three main parts; plasma membrane, cytoplasm and a nucleus. The plasma membrane forms the outside boundary of the cell which separates the cell's internal environment from outside as well as controlling the movement of substances into and out of the cell. The fundamental structure of the plasma membrane is of a lipid bilayer containing three types of lipid molecules; phospholipids, cholesterol and glycolipids, Figure 5.2. Table 5.1 presents the composition of the lipid species in the plasma membrane of an average mammalian cell. Phospholipids form the major constituent of the cell membrane and consist of a glycerol head-group which gives it a hydrophilic character and two fatty acid tail groups that account for the hydrophobic non-polar part. Figure 5.3, shows a general structure of a phospholipid with  $R_1$  and  $R_2$  representing the fatty acid chains and X the different head-group which differentiates the lipids into different classes. The lipids contained within the plasma membrane are distributed asymmetrically as demonstrated in a study by Rothman *et al.* (1977) on human red

blood cell membrane in which the outer leaflet consists mainly of sphingomyelin (SM) and phosphatidylcholine (PC); whereas the inner leaflet consists mainly of phosphatidylethanolamine (PE) and phosphatidylserine (PS), Figure 5.4.

The cytoplasm of a cell consists of cellular content between the plasma membrane and nucleus which can be divided into two components; the cytosol and organelles. The cytosol is a fluid mainly containing water and solutes. The organelles, ribosomes, the endoplasmic reticulum, golgi complex, peroxisomes, cytoskeleton, lysosomes and mitochondria are highly organised sub-cellular structures within a cell, with each having its own characteristic shape and particular function. Finally, the main part of the cell is the nucleus which contains genes that control cellular structure and functions such as the cell division and protein synthesis [Tortora *et al.*, 2000].

Established imaging techniques such as optical, fluorescence, confocal, scanning electron microscopy, transmission electron microscopy and more recently atomic force microscopy are routinely utilized to identify and localise the distribution of biological components in cells to understand the physiological processes taking place at the surface and within the cells. However, the limitations associated with these techniques are that they provide no chemical information and require the use of fluorescent labels to image the molecules of interest, discussed in Chapter 1.

Lately, Mass Spectral imaging (MSI), particularly SIMS is becoming a powerful technique to image the distribution of biological components within a single cell. SIMS offers the benefits of high sensitivity, very high spatial resolution (<100 nm) and the capability of label free monitoring of the distribution of native bio-molecules and xenobiotics at the sub-cellular scale with high selectivity [Fletcher *et al.*, 2010].

Imaging using SIMS can be performed by using either the microscope or the microprobe modes, introduced earlier in Chapter 1. Briefly in the microscope mode, an image of the selected secondary ion is generated using a broad beam over a large area; whereas in the microprobe, the beam is focused to a small spot size and is rastered across a defined area of analysis. In the latter mode, mass spectral data collected is directly related to the position of the beam, which allows mapping the distribution of the ions in the given area. The spatial resolution in this mode is dependent on the spot size of the primary ion beam; while in the microscope mode the spatial localisation of the secondary ions is preserved by the secondary ion optics system [Castaing *et al.*, 1981], [Liebl *et al.*, 1967].

This chapter reviews the current literature on imaging of single cells using SIMS and the factors limiting the technique reaching its full potential. Further, the ability of operating the  $C_{60}^+$  as a dc beam on the new instrument, **J105 3D Chemical Imager** to image at sub  $\mu\text{m}$  spatial resolution and examine the chemistry below the surface is explored. In addition to this, different sample preparation techniques, formalin fixed, freeze-dried and freeze-fractured frozen-hydrated are also investigated using a novel sample handling system on the J105, specifically designed for the biological samples.

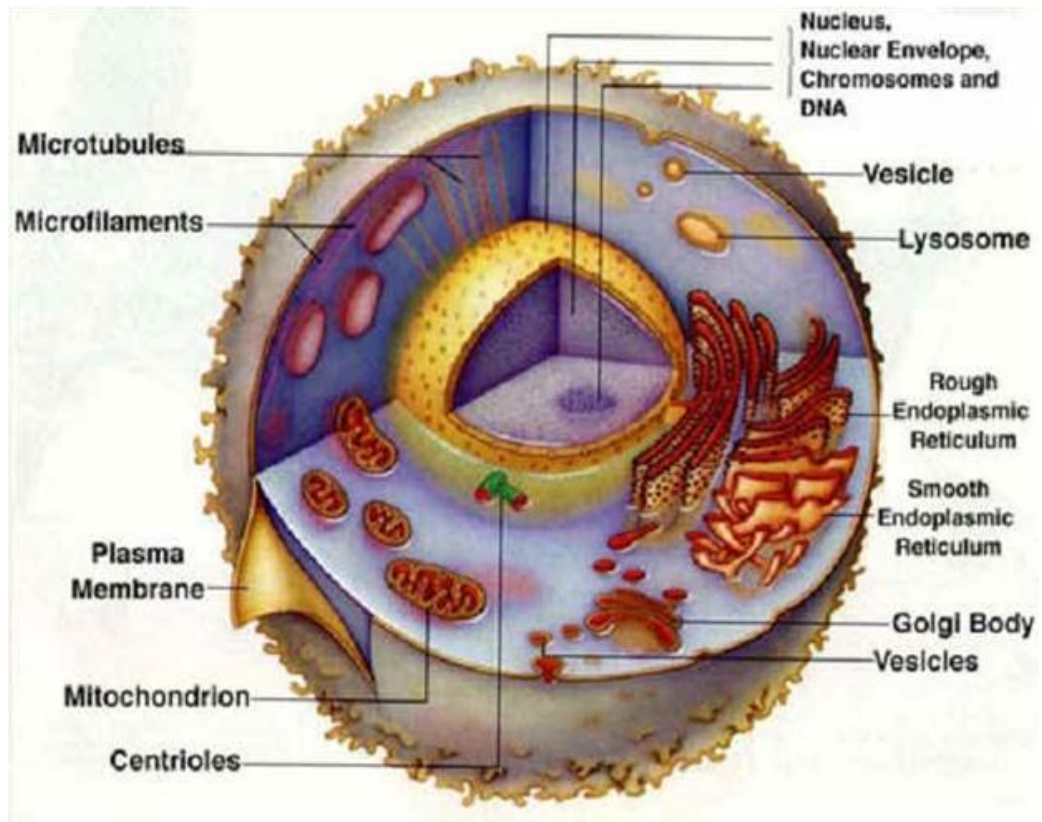


**Figure 5.1** Typical view of an animal cell. Reproduced from [http://asweknowit.net/images\\_edu/DWA%205%20eukaryote.jpg](http://asweknowit.net/images_edu/DWA%205%20eukaryote.jpg)

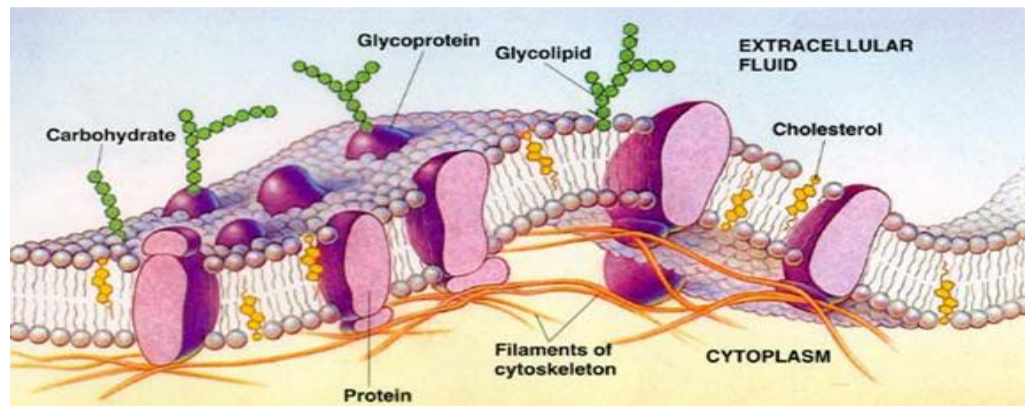


**Figure 5.2** Plasma membrane in fluid mosaic arrangement of lipids and proteins. Reproduced from <http://www.colorado.edu/intphys/Class/IPHY3730/image/membrane.jpg>.

**Table 5.1** Membrane lipid composition in an average mammalian cell. Reproduced from

<http://employees.csbsju.edu/hjakubowski/classes/ch331/lipidstruct/oldynamicves.html>

<b>LIPIDS</b>	<b>%</b>
<b>Phospholipids</b>	
Phosphatidylcholine (PC)	45-55
Phosphatidylethanolamine (PE)	15-25
Phosphatidylinositol (PI)	10-15
Phosphatidylserine (PS)	5-10
Phosphatidic Acid (PA)	1-2
<b>Sphingomyelin (SM)</b>	5-10
<b>Cardiolipin (bis-Phosphatidylglycerol)</b>	2-5
<b>Cholesterol</b>	10-20

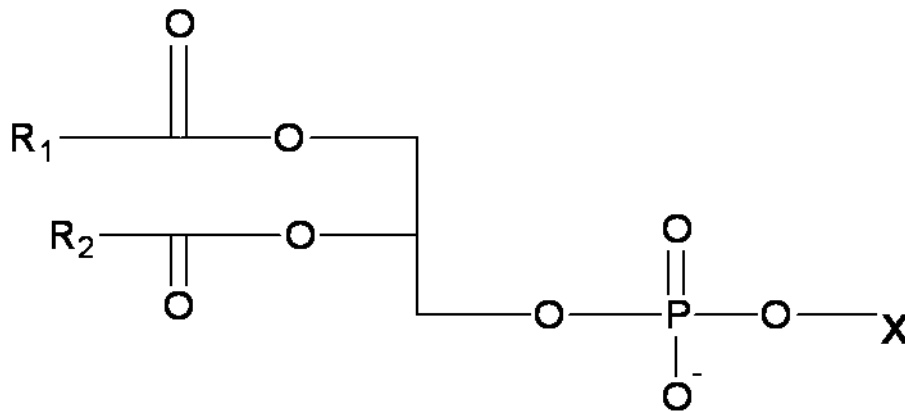


**Figure 5.3** General structure of a phospholipid. R<sub>1</sub> and R<sub>2</sub> represent the fatty acid chains, X represent the different head-groups.

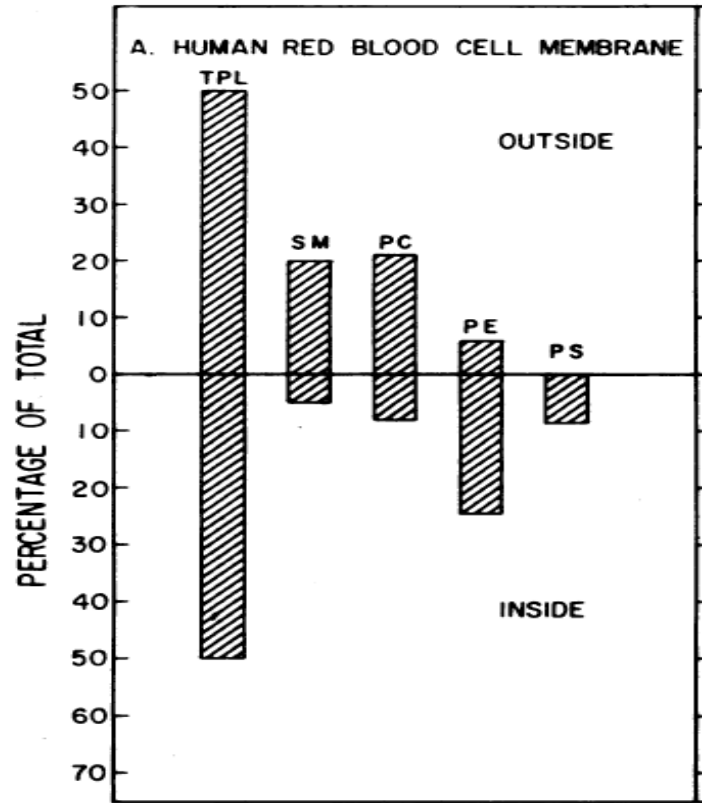


**Figure 5.4** Asymmetrical distribution of phospholipids in membranes of human red blood cells. Abbreviations: *TPL*, total phospholipids; *PC*, phosphatidylcholine; *SM*, sphingomyelin; *PE*, phosphatidylethanolamine; *PS*, phosphatidylserine; and *PI*, phosphatidylinositol. Reproduced from Rothman *et al.* 1977.

## 5.2 Imaging of single cell using SIMS

### 5.2.1 Imaging of cells using Dynamic SIMS

The very first mass spectral images of cells were obtained using a dynamic SIMS instrument based on ‘ion microscopy’ technology that was commercialised by Cameca [Morrison *et al.*, 1975]. The instrument operates in the microscope mode, by bombarding the sample with a defocused primary ion beam over a larger field of view. The secondary ions emitted are accelerated in the same electrostatic field through an immersion lens. This produces an unfiltered global image containing many ion images, one for each isotope present in the sample. Thus, a filtering system was required to separate ions based on their  $m/z$  to generate an image corresponding to the element selected.

The Cameca instrument was successfully employed in a range of applications such as geology, solid-state physics, environmental science and biology, particularly imaging the distribution of biological significant element, calcium in transversal section of an insect abdomen and dentine in the human tooth [Morrison *et al.*, 1975].

Although at the time of analysis only one secondary ion species either atomic or small fragment ion is detected, this approach offered the advantage of high spatial resolution as demonstrated by studies on mapping the distribution of pharmaceutical compounds within cells and tissues [Larras-Regard *et al.*, 1995], [Clerc *et al.*, 1997], [Bennett *et al.*, 1992].

A very successful application of this imaging SIMS technique has been in the development of boron neutron capture therapy (BNCT) for the treatment of cancerous cells, particularly brain tumours [Smith *et al.*, 2001]. BNCT is based on the fission

reaction in which  $^{10}\text{B}$  atoms capture a neutron and slowly decay to form alpha particles and lithium nuclei causing the death of cancerous cells. Prior to the development of SIMS ion microscopy, other techniques such as direct current plasma-atomic emission spectroscopy (DCP-AES) and inductively coupled plasma-atomic emission spectroscopy (ICP-AES) were used to detect boron in BNCT studies, but these methods required pre-treatment of biological cells before analysis, which alters the native distribution of chemical species in the cells. SIMS based ion microscopy offers the advantages of high sensitivity and spatially resolved 3D images of isotopes without manipulating the sample. 3D imaging on the microscope dynamic SIMS instruments is performed by recording a series of secondary ion intensities versus time of impact with the primary ion beam [Chandra *et al.*, 2000].

A study by Chandra *et al.* (2007) investigated the boron uptake from two different BNCT drugs *p*-boronophenylalanine (BPA-F) and sodium borocaptate (BSH) in different co-cultured cell lines and it was possible to differentiate between the cells lines from optical images as well as image uptake and accumulation of boron within the cells. This was followed by another experiment by the same group where they treated the cells with  $^{13}\text{C}$   $^{15}\text{N}$ -labelled phenylalanine to compare the uptake of boron from phenylalanine amino acids with the BPA-F drug. The SIMS images obtained show that although the mechanism for up-taking boron from the two compounds is the same, the processing is different, particularly in mitochondria. This study also investigated uptake of boron from the BPA drug during different stages of the cell cycle. The cells were treated with the BPA drug and bromodeoxyuridine (BrdU), a thymidine analogue that binds to DNA during the s-phase of the cell cycle. The SIMS images illustrate the

capability of the instrument and show an increase in uptake and accumulation of boron from BPA in nuclear region of cells in the s-phase compared to non replicating cells, Figure 5.5.

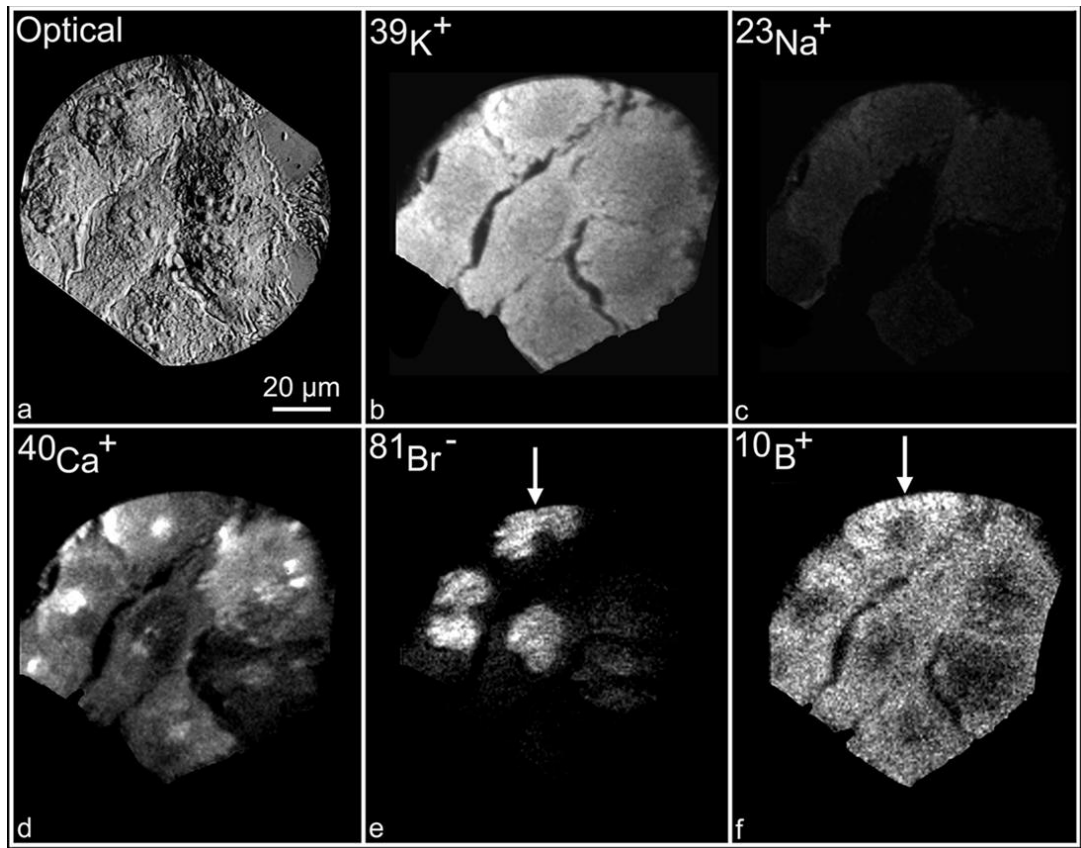


**Figure 5.5** Correlative reflected light (a) and SIMS imaging (b-f) of fractured freeze-dried cells T98G human glioblastoma cells. SIMS images of inorganic  $^{39}\text{K}$ ,  $^{23}\text{Na}$ ,  $^{40}\text{C}$   $^{81}\text{Br}$  and  $^{10}\text{B}$  from the same cell shown in (b-f) respectively. The s-phase cells show bright  $^{81}\text{Br}^-$  signal from the nucleus indicated with an arrow (e) which also contains high level of  $^{10}\text{B}^+$  (f, indicated with the arrow). Reproduced from Chandra *et al.* 2007.

Levi-Setti and co-workers used the ion microprobe imaging mode with spatial resolution of 50 nm to map the distribution of halogens and calcium isotopes in individual chromosomes bound to  $\text{Mg}^{2+}$  and  $^{44}\text{Ca}$  [Levi-Setti *et al.*, 2004], [Strissel *et al.*, 2004]. 3D imaging in the microprobe mode is completed by assembling the images as they are acquired. The above studies demonstrate dynamic SIMS to be a valuable tool to further our understanding on the mechanism of disease and the effect of drugs.

The development of new primary ion sources,  $\text{Cs}^+$ ,  $\text{O}_2^-$ ,  $\text{In}^+$  and parallel mass detection in the magnetic sector detector instrument led to the development of new methods for imaging intercellular molecules. Nanometer-scale, secondary ion mass spectrometry (NanoSIMS) is a technique developed for the analysis of trace elements and isotope of fine features in animal tissues and cells [Slodzian *et al.*, 1992]. It operates in dynamic imaging microprobe mode and uses stable isotope markers such as  $^{13}\text{C}$ ,  $^{15}\text{N}$  and  $^{18}\text{O}$  to label molecules and map their distribution within an animal tissue or cells. It offers the advantage of *high lateral resolution* (50 nm) while maintaining extremely high sensitivity (ppm in elemental imaging) and high mass resolution ( $M/\Delta M = 5000$  with 60% transmission,  $M/\Delta M = 7500$  at 40% transmission and  $M/\Delta M = 15,000$  with 10% transmission) [Guerquin-Kern *et al.*, 2005], [Grovenor *et al.*, 2006]. NanoSIMS 50 ion microprobe (Cameca) was used to image the membrane binding protein B-subunit of Shiga toxin in Henrietta Lacks (HeLa) cells to investigate the sub-cellular distribution and intracellular transport pathway [Römer *et al.*, 2006].

A prototype of NanoSIMS was developed by Lechene *et al.* (2006) named multi-isotope imaging mass spectrometry (MIMS) which combines SIMS with tracer methods to determine and map the distribution of molecules labelled with stable

isotopes in sub-cellular compartments. Samples ranging from human hair cross-section to tissue section were studied but the most impressive image generated was of a whole single endothelial cell, Figure 5.6. An overlay of the images  $^{12}\text{C}$ ,  $^{12}\text{C}^{14}\text{N}$  and  $^{31}\text{P}$  was generated which shows clear differences within the cell. The region in red indicates the nucleus and cytoplasm which contains high nitrogen signal with the periphery (lamellipodium) being high in phosphorus and low in nitrogen. The outermost layer of the cell contains more carbon than in the lamellipodium area. Small and thin protrusions at the edge of the cells also contain high nitrogen which the authors suggest could be filpodia.

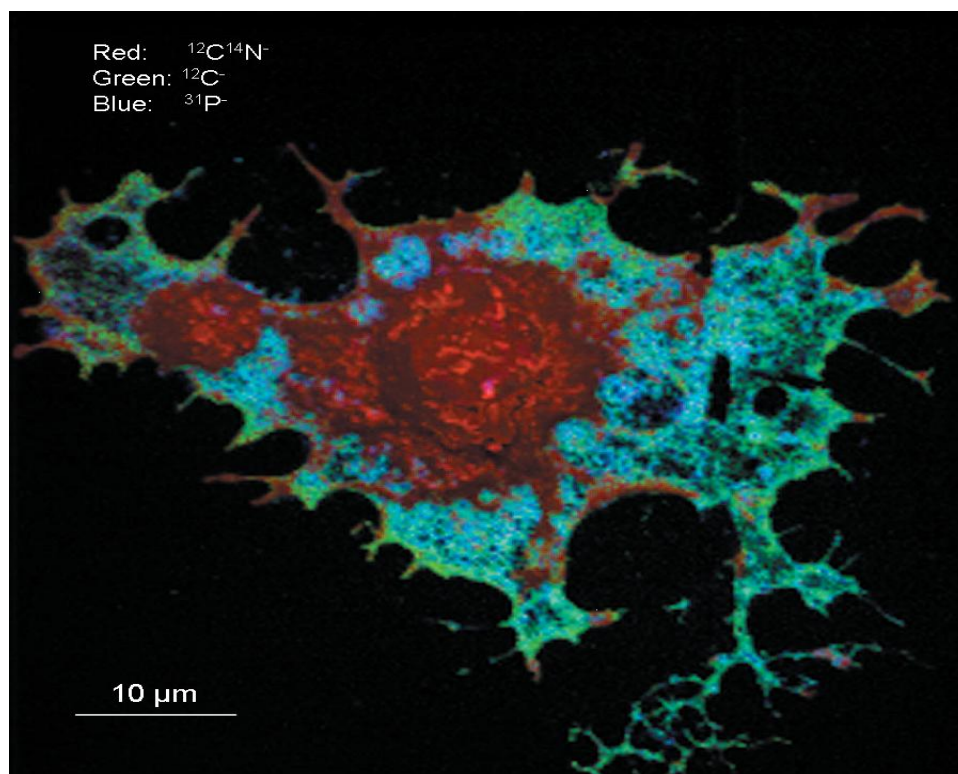


**Figure 5.6** Analysis of gross differences in composition within an unlabelled cell. Endothelial cells were cultured on silicon supports, fixed on the support, dried, and analysed with multi-isotope imaging mass spectrometry (MIMS). Quantitative mass images of the surface of a whole endothelial cell were recorded in parallel at masses  $^{12}\text{C}^-$ ,  $^{12}\text{C}^{14}\text{N}^-$  and  $^{31}\text{P}^-$ . An overlay of these images is shown, with  $^{12}\text{C}^{14}\text{N}$  in red,  $^{12}\text{C}$  in green, and  $^{31}\text{P}$  in blue. Scale bar = 10  $\mu\text{m}$ . Reproduced from Lechene *et al.* 2006.

Although very impressive images can be generated using the dynamic SIMS instrument with stable isotope markers, this technique is destructive causing severe damage to organic molecules and only providing elemental and small fragment information.

### 5.2.2 Imaging of cells using Static SIMS

With the development of static SIMS, ToF analysers and LMIS that can be focused down to a spot size of 50 nm, it is now possible to probe the molecular information from the cell surfaces. In recent years, a number of applications have been published to show the ability of ToF-SIMS to spatially resolve the distribution of biochemical species on the cell surfaces using LMIS sources.

Winograd and co-workers imaged hydrocarbon, inorganic and doped molecules (cocaine and dimethylsiloxane (DMSO)) in a freeze-fractured frozen-hydrated single *Paramecium* cell using a  $\text{Ga}^+$  primary ion beam, see Figure 2.1, Chapter 2, [Colliver *et al.*, 1997]. This was followed by a number of subsequent studies by the same group using a  $\text{Ga}^+$  primary ion beam to image lipids in freeze-fractured freeze-dried human red blood cells [Pacholski *et al.*, 1998], and cellular sections of the fractured rat pheochromocytoma (PC12) cells, as well as in combination with *in situ* fluorescence microscopy using a fluorescent label DiI in the PC12 cells [Roddy *et al.*, 2002].

As mentioned in Chapter 2, when performing *high lateral resolution* imaging on ToF-SIMS the sensitivity to molecular species was extremely low. Thus, to increase the signal levels,  $\text{In}^+$  [Ostrowski *et al.*, 2004],  $\text{Au}_n^+$  [Davies *et al.*, 2003] and  $\text{Bi}_n^+$  [Kollmer *et al.*, 2004] LMIS were developed, where large impacting ions helped to improve the sputter yields. Winograd and co-workers describe the use of ToF-SIMS to image lipid composition of cryogenically preserved rat oligodendrocyte single cells [Piehowski *et al.*, 2008], as well show the change in lipid composition during *Tetrahymena* mating [Ostrowski *et al.*, 2004]. Furthermore, Ostrowski *et al.* (2007) used the  $\text{In}^+$  primary ion beam to investigate the distribution of cholesterol between the plasma membrane of two

cells. Cholesterol is a sterol which is an important structural component of the cell membrane required for maintaining membrane permeability and fluidity, discussed in Chapter 3. Most of the cholesterol required by the body is synthesised by the body, but it can also be ingested through diet. It is highly concentrated in lipids rafts and is a crucial molecule for the normal cell functions such as metabolising fat soluble vitamins and signal transduction. However, abnormal cholesterol levels within blood can exacerbate many diseases such as heart disease and Alzheimer. Therefore, it is essential to understand the role of cholesterol in mammalian cells. In this study, the cells (macrophages cell line, J774) were treated with Chol-BCD solution and labelled with a fluorescent tag, DiD and second population of J774 cells (control) were incubated only in media and labelled with DiI fluorescent tag. The samples were fractured and only cells that still had a membrane intact, as verified by the presence of fluorescence tag, were imaged. This study provided a proof of concept in the identification of cells by fluorescence in the vacuum system as well as mapping the distribution of cholesterol using a characteristic peak  $[M+H-H_2O]^+$  at  $m/z$  369 on the cell surface, Figure 5.7. This study shows the ability of ToF-SIMS to successfully detect cholesterol within cells, but also yet again highlights low signal levels obtained using the technique.

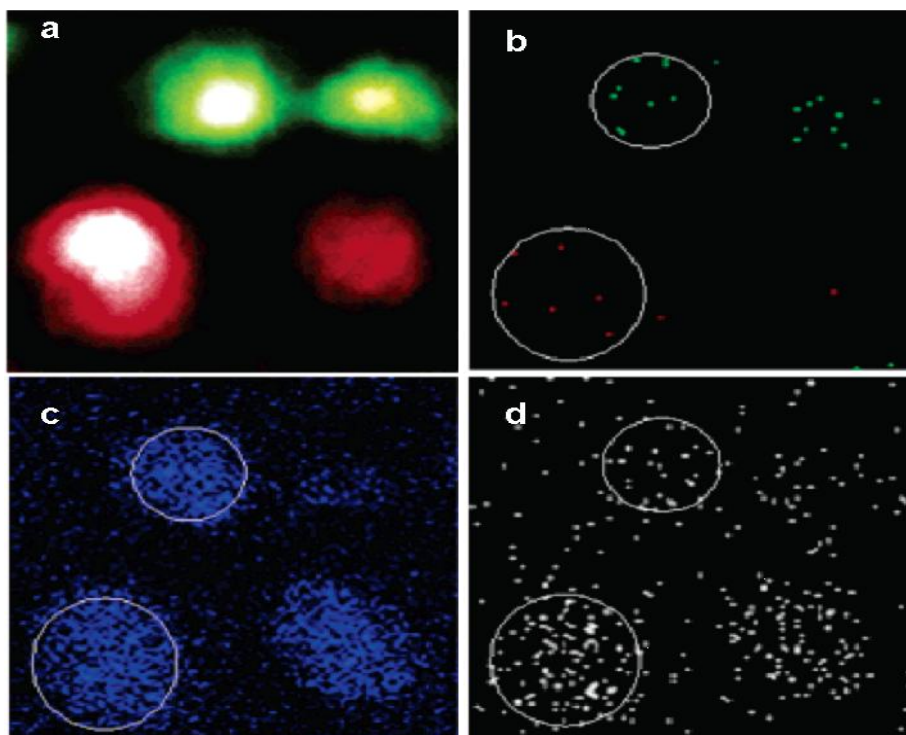


**Figure 5.7** Fluorescence and SIMS images of cholesterol-treated and control J774 cells ( $100 \times 100 \mu\text{m}^2$  field of view). Fluorescence and SIMS images were aligned manually using imaging software. (a) *In situ*, two-colour fluorescence image of several freeze-fractured J774 cells. The treated cells were arbitrarily coloured red, and the control cells are shown in green. (b-d) Positive ion molecule-specific images of J774 cells that correlate with the fluorescence image in (a). In all SIMS images, black pixels indicate an absence of signal. (b) SIMS composite image for DiD ( $m/z$  860; red) and DiI ( $m/z$  834; green). (c) SIMS image for  $\text{C}_5\text{H}_9^+$  hydrocarbon ( $m/z$  69; blue). (d) SIMS image for cholesterol ( $m/z$  366-370; white). Reproduced from Ostrowski *et al.* 2007.

Nygren and co-workers used a  $\text{Ga}^+$  primary ion beam to localise cholesterol and lipids in the membrane of single cells. The authors used silver (Ag) printing to enhance secondary ion yields and were able to localise cholesterol and phospholipids, Figure 5.8 [Sjövall *et al.*, 2003]. Although imprinting increases secondary ion signals, it results in a loss of *lateral resolution* as well as introducing artifacts into the images, mentioned previously in Chapter 2.

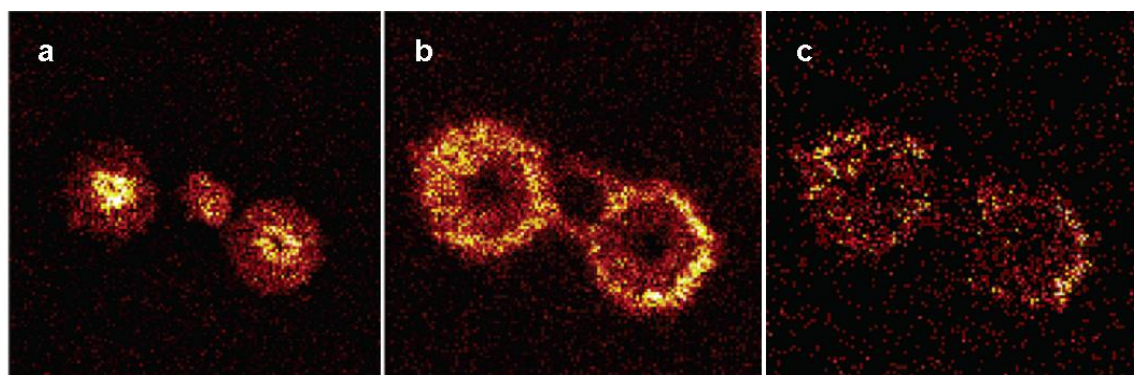


**Figure 5.8** Positive TOF-SIMS images from a cell-imprinted Ag surface obtained after pre-moistened imprinting at 0.6 MPa. The images show the intensity distributions of (a) phosphocholine  $\text{C}_5\text{H}_{15}\text{NPO}_4^+$ , (b)  $(\text{cholesterol-Ag})^+$  (c)  $(\text{cholesterol}_2\text{-Ag})^+$ . Field of view,  $77 \times 77 \mu\text{m}^2$ . Reproduced from Sjövall *et al.* 2003.

The Vickerman group developed a static SIMS instrument “BioToF” in collaboration with the Winograd group (Penn State) and Kore Technology Ltd for the analysis of biological samples [Braun *et al.*, 1998]. This instrument was used by Cliff *et al.* (2003) to demonstrate the application of ToF-SIMS as a valuable tool in pharmacological studies. Clofazimine is an antibiotic used to treat various bacterial infections including tuberculosis but the exact mechanism of action is unknown. ToF-

SIMS has been utilized to study yeast cells, *C. glabrata* incubated in Clofazimine to determine whether the drug can be retained by the outer cell wall or incorporates into phospholipid bilayer. The samples were freeze-fractured and ToF-SIMS images were acquired using 15 keV Au<sup>+</sup>. Figure 5.9 shows the localisation of the Clofazimine drug to the cell surface and does not penetrate through into the cell interior [Cliff *et al.*, 2003].

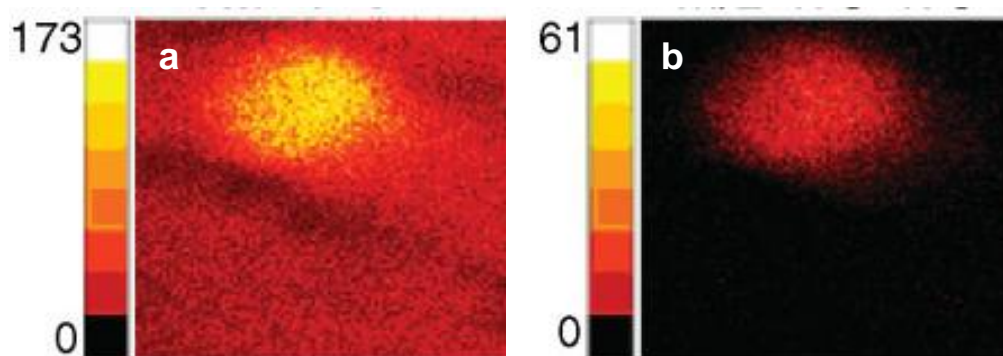


**Figure 5.9** ToF-SIMS images of intact *Candida* incubated in presence of drug Clofazimine over an area of  $50 \times 50 \mu\text{m}^2$ . (a) Total Ion; (b) Clofazimine  $m/z$  473-475. Adapted and reproduced from Cliff *et al.*, 2003.

Furthermore, the group used this instrument to characterise prostate cancer cell line (PC-3) cells. The cells were analysed in freeze-fractured and freeze-dried states using Ga<sup>+</sup> and Au<sub>2</sub><sup>+</sup> ion beams. Various species including K, Ca, and Mg can be localised to the cytoplasm with cholesterol and dipalmitoylphosphocholine (DPPC) to the lipid membrane. In addition, an increase in the yields by a factor of 20 for DPPC fragment  $m/z$  184 is observed when changing the primary ion beam from Ga<sup>+</sup> to Au<sub>2</sub><sup>+</sup> [Gazi *et al.*, 2004].

The Winograd group used the  $\text{Au}^+$  primary ion beam to map the distribution of lipids in macrophages J774 and Glial cells in a trehalose matrix. The authors successfully preserved the morphology and chemistry of these cells in the matrix and images of the distribution of lipids in the sub-cellular regions were produced. Some of the cell samples were deposited with Ag which although has been shown to enhance the secondary ion signal, it also results in a loss of *lateral resolution* [Parry *et al.*, 2005]. This was followed by another study on *high lateral resolution* imaging in which the lipid response to phagocytosis on the macrophage cells was investigated using a  $\text{Au}^+$  primary ion beam [Parry *et al.*, 2008].

The  $\text{Bi}_n$  cluster primary ion beam has been used extensively by Nygren and co-workers for molecular imaging of lipids in cells and tissues to determine their distribution and understand their function within cells [Börner *et al.*, 2007]. Malm *et al.* (2009) also used  $\text{Bi}_3^+$  primary ion beam to investigate different sample preparation techniques for ToF-SIMS, see below.

Although above studies show some of the extraordinary work produced in the history of SIMS, it also highlights the challenges faced in the application of static SIMS for the analysis of biological samples using monoatomic LMIS sources. This is because the damage characteristics of these beams mean that the analysis has to be carried out within the static limit which reduces sensitivity, described in detail in Chapter 2. The development of cluster LMIS sources  $\text{Au}_n^+$  and  $\text{Bi}_n^+$  yielded a non-linear increase in the secondary ion yields, while maintaining high spatial resolution, but the static limit still has to be adhered to when using these beams, thus yet again limiting sensitivity.

With the introduction of polyatomic ion sources using  $C_{60}^+$  [Wong *et al.*, 2003], and  $SF_5^+$  [Kötter *et al.*, 1998], a significant increase in the secondary ion yields was observed with greatly reduced sample damage, described in Chapter 1. This allowed the static limit to be relaxed and opened up the possibility of molecular depth profiling, Chapter 4 and 3D chemical imaging, discussed below.

### 5.2.3 3D sub-cellular imaging of cells using SIMS

Cellular and sub-cellular analysis of cells is of great importance to understand and follow the evolution of biochemistry with depth, hence the need for 3D imaging. Current approaches adopted are to use optical microscopes such as confocal microscopy to look inside the cell and construct 3D images from a series of 2D images recorded. Although very powerful and successful, this technique requires fluorescent labelling of the molecules of interest before analysis so they can be detected. ToF-SIMS offers the advantage of being able to generate chemically specific images as a function of depth without having to tag the molecules with active markers that can change the chemistry of cells. Moreover, when using light microscopy one is limited in the number of analogues that can be incorporated for one experiment, whereas with ToF-SIMS the possibilities are much greater allowing simultaneous analysis of more than 5 tags at once with monitoring of molecules and elemental halogens.

Chandra *et al.* (2004) used the dynamic SIMS instrument, described above to perform 3D sub-cellular imaging of single cells, human T98G glioblastoma. The cells were fractured freeze-dried in the mitotic stage and images of single masses  $^{12}C^+$ ,  $^{23}Na^+$ ,  $^{24}Mg^+$ ,  $^{39}K^+$  and  $^{40}Ca^+$  were recorded. In this study, the distribution of  $^{40}Ca^+$  was also

monitored as a function of depth to determine the concentration of  $^{40}\text{Ca}^+$  in the mitotic spindle region. This study highlights the importance of looking beneath the cell surfaces.

The ability of cluster and polyatomic primary ion beams to successfully depth profile organic systems, described in Chapter 4, opened up the prospect to depth profile and image single cells using a dual beam approach on static SIMS instruments. However, depth profiling of a preserved cell was challenging due to the complex nature of the sample and the sputtering characteristics of these beams. A cell is a multi-component system which when analysed produces variations in the intensity with depth that represents changes in the chemistry. This is contrast to a single component system where similar information is produced regardless of the depth [Jones *et al.*, 2007]. Also, the sputtering behaviour of the polyatomic beams differs when a single species is analysed as compared to a complex biological system. To investigate this issue further, Kozole *et al.* (2006) constructed a DPPC-sucrose multilayer system to be used as a model for 3D molecular imaging of a biological cell. The DPPC was used as the plasma membrane of the cell and the sucrose solution as a cell cytoplasm. The sample was frozen in liquid nitrogen to preserve the native biological environment and depth profiled using the  $\text{C}_{60}^+$  primary ion beam. The depth profile plots show that the  $\text{C}_{60}^+$  beam can be used to remove a lipid film up to 20 nm and a molecular signal from the underlying biological species can be detected. This study shows the potential of using  $\text{C}_{60}^+$  primary ion for the analysis of single cells in 3D. Over the years, a series of papers have been published where the researchers have constructed membranes to mimic the

cells and depth profiled them [McQuaw *et al.*, 2005, 2006], [Baker *et al.*, 2008], [Zheng *et al.*, 2008].

Eventually a breakthrough came from the Manchester group when they published a 3D molecular image from a cell, *Xenopus laevis* oocyte using the  $C_{60}^+$  projectile [Fletcher *et al.*, 2007]. *Xenopus laevis* oocyte is a large frog egg about 1 mm in diameter, whose cell organelles are easily visualised and analysed but the variation in topography meant a loss in mass resolution during analysis due to the size and only the outer section of oocyte could be analysed. Despite this limitation, the sample proved the concept of molecular depth profiling of a single cell using the  $C_{60}^+$  primary ion beam. This study was completed on a conventional ToF-SIMS instrument equipped with a 40 keV  $C_{60}^+$  primary ion beam which was used in a pulsed mode to sputter, etch and record a series of 2D images to characterise chemical changes with depth. This analysis took a number of days to complete and the data was collected in both positive and negative ion modes, with the detection of masses up to  $m/z$  1000, even after using the primary ion dose of  $1 \times 10^{15}$  ions/cm<sup>2</sup>. The main organic peaks detected and imaged were cholesterol  $m/z$  369, diacylglyceride and phospholipids fragments and a series of recorded 2D images were stacked to generate 3D images, Figure 5.10.

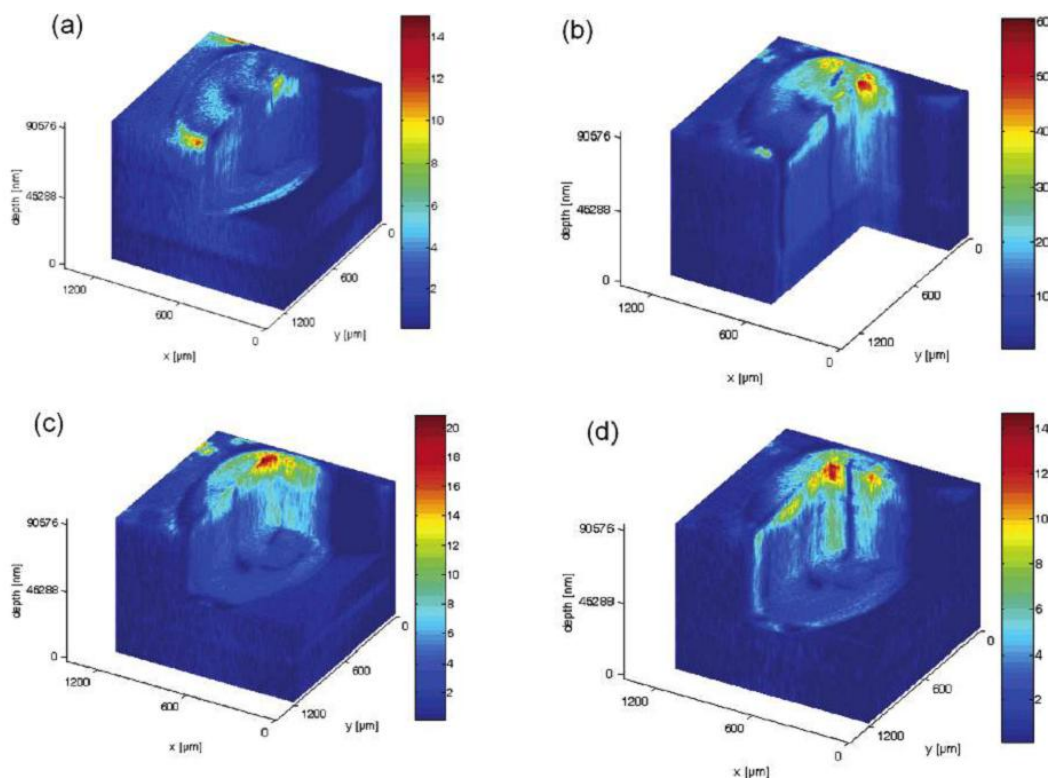


**Figure 5.10** 3D biochemical images of freeze-dried oocyte, showing changes in (a) phosphocholine peaks  $m/z$  58, 86, 166, and 184, (b) signal summed over the  $m/z$  range 540-650, (c) signal summed over the  $m/z$  range 815-960, and (d) cholesterol peak at  $m/z$  369. Colour scale Normalised for total counts per pixel for each variable ( $m/z$  range). Reproduced from Fletcher *et al.* 2007.

This experiment demonstrates the potential of using the  $C_{60}^+$  polyatomic primary ion beam as an imaging beam to map the distribution of bio-chemicals present laterally and as a function of depth, even with high primary ion fluence that exceeds the static limit. However, the  $C_{60}^+$  polyatomic primary ion beam is a gas cluster ion source which is difficult to focus to a spot size comparable to the LMIS while maintaining enough current to allow analysis to be completed in a useful time. An approach which is often

adopted for imaging experiments on the conventional ToF-SIMS instrument is to employ dual beams, in which a pulsed metal cluster beam such as  $\text{Au}_n^+$  or  $\text{Bi}_n^+$  is applied to acquire an image and a continuous polyatomic beam such as  $\text{SF}_5^+$  or  $\text{C}_{60}^+$  is used to sputter the material. This interleaved dual beam approach allows the analysis to be completed on a practical useful time scale [Nygren *et al.*, 2008], [Malmerg *et al.*, 2008].

The dual beam approach was adopted by Brietenstein *et al.* (2007) to perform 3D imaging on smaller cells, normal rat kidney cells, using the  $\text{C}_{60}^+$  for sputtering and  $\text{Bi}_3^+$  for imaging. The aim was to detect endogenous chemicals present in the cell and to validate the 3D ToF-SIMS protocol using a well known cellular system. Six confluent layers of cells were grown on glass cover-slips and chemically fixed with gluteraldehyde before analysis. The cells are 20  $\mu\text{m}$  in diameter and were analysed using a ToF-SIMS IV instrument (ION-TOF, Germany) equipped with 25 keV  $\text{Bi}_3^+$  used for imaging and 10 keV  $\text{C}_{60}^+$  to remove the layers and in total 60 cycles were acquired to go through 6 layers of cells. Images were acquired at nominal mass resolution and the spectrum was recorded in bunched mode with mass resolution of 5000-10000. In this study, the authors were able to detect and image phospholipids and amino acids as shown in Figure 5.11.

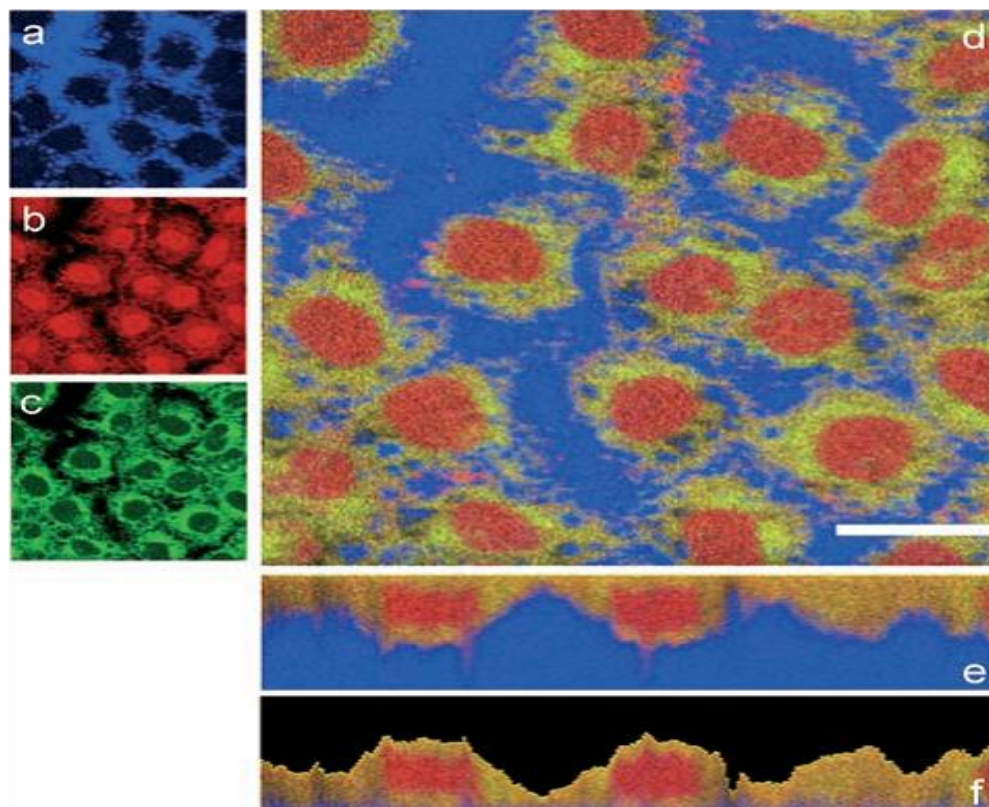


**Figure 5.11** 2D images of NRK cells after 45<sup>th</sup> sputter cycle. Summed signals of amino acid fragment ions are represented in red (b), those of phospholipids in green (c), and substrate-derived secondary ions are depicted in blue (a). The scale bar in (d) corresponds to 20  $\mu\text{m}$ . a)–d) Horizontal xy sections and e), f) vertical xz sections through the sample. Reproduced from Brietenstein *et al.* 2007.

This was impressive work which showed that ToF-SIMS can be employed to reconstruct 3D imaging of cells using the dual beam approach and without the need to label with fluorophores. However, the limitation that lies with this approach is that valuable sample is wasted in the sputter cycle and the analysis with  $\text{Bi}_3^+$  has to be restricted to static conditions limiting the yield per pixel. The authors predict that this

technique can be used to detect drugs in cells which are the ultimate aim for 3D SIMS imaging. However, the approach adopted by these labs raises the issue whether there will be enough sensitivity during the static analysis step to detect extremely low concentration of these molecules [Fletcher *et al.*, 2009].

In another study, a similar approach is adopted in which 3D imaging of freeze-fractured freeze-dried thyroid carcinoma cell line is reported using  $C_{60}^+$  for sputtering and  $Bi_3^+$  for imaging. The authors claim that they can image internal compartments of the cell but they were only able to detect and image the PC head-group  $m/z$  184, inorganic ions Na  $m/z$  23, K  $m/z$  39 and  $m/z$  86. A high intensity signal of  $m/z$  86 was observed in the centre as well as at the periphery part of the cells that could not be identified but was said to be a fragment of PC or amino acids leucine/isoleucine [Nygren *et al.*, 2007].

In both of these studies, the images were acquired at low mass resolution by using a long pulsed primary ion beam and the mass spectrum of the cell was recorded at a high mass resolution using a bunched primary ion beam to assign the peaks. High mass resolution imaging instruments are commonly operated in this mode. This is because rapid pulsing results in a loss of focus of the primary ion beam and if the beam is focused to a small spot size the current is so low that it can take few days to complete an experiment. Therefore, the aim is usually to increase acquisition time by increasing the current of primary ion beam which results in low quality mass spectrum.

From above studies, it can be concluded that while using a conventional ToF-SIMS instrument, it is difficult to operate with high mass resolution and high spatial resolution at the same time. This is because the instability of the pulsed primary ion

beam has to be overcome, forcing the analyst to use long pulses. The pulsed beam also results in a low duty cycle and depth profiling and imaging experiments can take a long time to complete. The dual beam approach in which a pulsed metal cluster beam such as  $\text{Au}_n^+$  or  $\text{Bi}_n^+$  is used to acquire an image and a continuous polyatomic beam such as  $\text{SF}_5^+$  and  $\text{C}_{60}^+$  to sputter the material allows the analysis to be completed on a useful time scale, but results in a loss of valuable data during sputtering, described in Chapter 4 [Nygren *et al.*, 2008].

The J105 *3D Chemical Imager* was developed to further explore the capabilities of ToF-SIMS in imaging of biological samples [Fletcher *et al.*, 2008]. This instrument has been described in detail in Chapter 2 but briefly, it differs from conventional ToF-SIMS instrumentation in that the mass spectrometry is decoupled from the sputtering process. This allows a polyatomic primary ion beam in dc mode to be used providing optimum conditions for rapid 2D and 3D analysis. Also, the dc mode allows the analysis to be performed at a high mass resolution while maintaining spatial resolution irrespective of sample topography and sample type. Furthermore, using the polyatomic beam in a dc mode on the J105 allows analysis of the whole sample without the need of the dual beam experiment, see Figure 4.9 in Chapter 4.

### 5.3 Sample Preparation

Sample preparation plays a significant role in acquiring useful and meaningful data when analysing samples using ToF-SIMS, particularly during sub-cellular imaging of biological samples. This is because these samples contain a high water content which if introduced directly into high vacuum causes the cells to rupture and molecules to relocate during water evaporation in the vacuum. The main challenge that the SIMS community is presented with is to maintain the biological integrity of these samples when it is placed in the high vacuum instrument.

Over the years, different sample preparation approaches such as freeze-dried, freeze-fractured, frozen-hydrated and fixative techniques have been developed in various SIMS labs to address this issue, discussed below.

Freeze-drying involves rapidly freezing the sample in liquid nitrogen, propane or isopentane and then transferred in vacuum for several hours for slow and controlled warm up to a room temperature before analysis to allow the ice to sublime. Fast freezing is essential to limit the relocation of small molecules or the formation of ice crystals which can rupture or damage the cell. The sample can also be analysed in a frozen hydrated state (discussed below) if a cryogenic stage is available [Grovenor *et al.*, 2006], [Kurczy *et al.*, 2008].

Kurczy *et al.* (2008) used *Tetrahymena* cells to show that the cells retain their two dimensional morphology when freeze-dried but this process causes residues from media to deposit on and around the cells and when analysed the spectrum is dominated by Na and polydimethylsiloxane (PDMS). This results in hindering the signal from organic secondary ions, particularly the PC fragment  $m/z$  184 which gives a high

intensity signal in SIMS. Berman *et al.* (2008) suggested using nonreactive gas such as argon to gently blow away the media residues residing on the cell surfaces. However, this protocol requires great care since vigorous drying can cause the cells to rupture and a loss in molecular information. Furthermore, only blowing by the gas is not sufficient to obtain interference free spectrum of cells and further washing is required before freezing. Kurczy *et al.* (2008) used de-ionised water to remove all the contaminants from the cells prior to freeze drying. Although, this increased the signal of the PC fragment  $m/z$  184, it caused the cells to swell due to osmotic pressure and resulted in altering the morphology of the cells. This effect was also observed by Berman *et al.* (2008) when they washed human breast cancer cells, MCF7 with de-ionised water.

As a result, Berman *et al.* (2008) suggested that an iso-osmotic wash solution is required to preserve the morphology of the cells and they investigated a range of washing solutions, 4-(2-hydroxyethyl)-1-piperazineethanesulfonic acid (HEPES), magnesium acetate, sodium chloride and ammonium acetate. They found ammonium acetate to work best due to the volatility of this solution, in removing the contaminants from the cells surface, maintaining the physical morphology of the cells as well as allowing depth profile of chemicals present in the cytosol.

Another volatile solution that is more routinely used in SIMS is ammonium formate to remove salts accumulating on the biological sample particularly tissue sections. This has been extensively used by Sjövall and co-workers and by washing the samples with 0.15 M ammonium formate for 30s allows to depth profile samples with characteristics molecular ion and lipids detected through the whole samples [Sjövall *et al.*, 2004], [Nygren *et al.*, 2003]. This protocol washing in ammonium formate for

approx 10-15s followed by freeze-drying was adopted by Vickerman's group to successfully analyse biological samples using ToF-SIMS [Jones *et al.*, 2008], [Fletcher *et al.*, 2008].

Freeze-fractured, frozen-hydrated involves putting the sample between two substrates with a spacer bead of same height as the cells, to prevent squashing them and the sandwich is rapidly frozen in liquid propane, nitrogen or isopentane. Once frozen, the top substrate is pulled away and the sample is fractured. This method exposes cell interior for analysis without requiring the washing step or chemical pre-treatment [Chandra, 2008]. The sample is immediately transferred and analysed on a cryogenic stage *i.e.* frozen-hydrated. The freeze-fractured technique was first reported in early 1957 and has been widely used for cell analysis using microscopy. This concept was adapted and modified by Chandra and Morrison for preparation of cell for imaging using SIMS [Chandra *et al.*, 1992]. The authors used this sample preparation to map the distribution of Ca in cell undergoing mitosis and cytokinesis as well as localise boron in brain tissue for BNCT [Chandra, 2005], [Chandra *et al.*, 2000].

The Winograd group also developed the freeze-fractured sample preparation in their laboratory in which a sample is placed onto a silicon wafer and is covered with a silicon shard followed by rapidly freezing in liquid propane. The frozen cells are rapidly transferred to the cryogenic stage and the sample is fractured *in situ* to expose the fractured cell surface for analysis. The group have used this method to localise membrane lipids in single cells as well as identified cellular sections following freeze-fracture. This strategy is the most successful in maintaining the integrity and

morphology of the cell in 3D and has been regarded as a “gold standard” by Kurczy *et al.* (2008).

However, it can be difficult to separate the two surfaces under cryogenic liquid and fracturing can cause undesirable topography as well as produce low amount of fractured cells. It can also result in high level of sample charging which cannot be compensated, even with an electron flood gun. Furthermore, unless the sample can be rapidly transferred from insertion chamber to the analysis chamber, it can warm up swiftly resulting in chemical smearing of the sample [Berman *et al.*, 2008].

Thus, to keep the sample preparation, simpler methods such as using a matrix, trehalose and glycerol [Parry *et al.*, 2005] to help keep the sample in its native have been reported. Another method which is widely used in microscopy is chemically fixing the cells. This involves using 70% ethanol, gultraldehyde [Malm *et al.*, 2009] or 4% formaldehyde to chemically fix the cells. However, by using this method there is danger of changing the chemistry of the sample under analysis as well as destroying the native composition of the living cell [Grovenor *et al.*, 2006].

Sjövall and co-workers published a nice study in which they compare the fixative and drying sample preparation and their effect on the morphology and chemical structure of the human fibroblast cells. In this study, the authors show that the morphology of the cells is preserved if the sample is cryo-fixed followed by freeze-drying. This method is preferred over fixation with gulteraldehyde which is better than alcohol-drying [Malm *et al.*, 2009].

Another novel method currently under development in the Vickerman’s group is cytospinning which involves cytospinning cells or nuclei in solutions onto a clean

substrate. The data presented in this paper shows this sample preparation technique to be robust, allowing biochemistry and architecture of cells to be maintained [Jackson *et al.*, 2010].

In summary, the literature shows that the best sample preparation method for maintaining the cell morphology is to use the freeze-fractured, frozen-hydrated strategy. However, due to the complexity associated with handling of these samples in vacuum they are not routinely analysed using ToF-SIMS. The J105 has been specifically designed for biological samples in that it has an automated sample handling system as well as cryogenic analysis facilities. It has a novel ability to perform an automated fracturing using a specially designed sample holder referred to as a “mousetrap”, described in details in Chapter 2. This design has also been adapted by the group in Sweden to design a “spring-loaded trap system” device for *in situ* freeze-fracturing single cells. The group reported ToF-SIMS analysis of freeze-fractured rat pheochromocytoma (PC12) cells using this device. A Bi<sup>+</sup> primary ion beam was used to generate single cell chemical images with sub-cellular *lateral resolution* [Lanekoff *et al.*, 2010].

This Chapter discusses the analysis of a model cell line (HeLa) to demonstrate the functionality of the new instrument and to provide a comparison between three different sample preparation techniques, formalin fixed, freeze-dried and freeze-fractured cells analysed in frozen-hydrated state.

## 5.4 Analysis of a standard cell line, HeLa using ToF-SIMS

HeLa cells are an immortalised cell line that was derived from cervical cancer cells taken from a patient called Henrietta Lacks, who later died from this disease in 1951. These cells were isolated and have since been cultured and are now extensively used in research to gain an understanding and knowledge of biological processes. The typical size of these cells is 20-25  $\mu\text{m}$  with many different strains and they continue to evolve by sub-culturing. Since, HeLa cells have a large nucleus they are widely used by biologists to understand the cell cycle, particularly the deoxyribonucleic acid (DNA) replication that occurs in the s-phase. Figure 5.12, shows the three stages of the s-phase of HeLa cells acquired using Confocal Laser Scanning Microscope (LSCM) after labelling the cells BrdU. The s-phase can be divided into three parts, early, mid and late s-phase. In the early s-phase, Figure 5.12a, transcriptionally active regions become replicated; in the mid phase transcriptional inactive regions replicate, Figure 5.12b and in the late s-phase more condensed heterochromatin found at the centromeric region replicate, Figure 5.12c, [Tortora *et al.*, 2000]. The ultimate aim is to use ToF-SIMS to study the organisation of DNA replication in HeLa cells and thus these cells were used as a model system in this project.

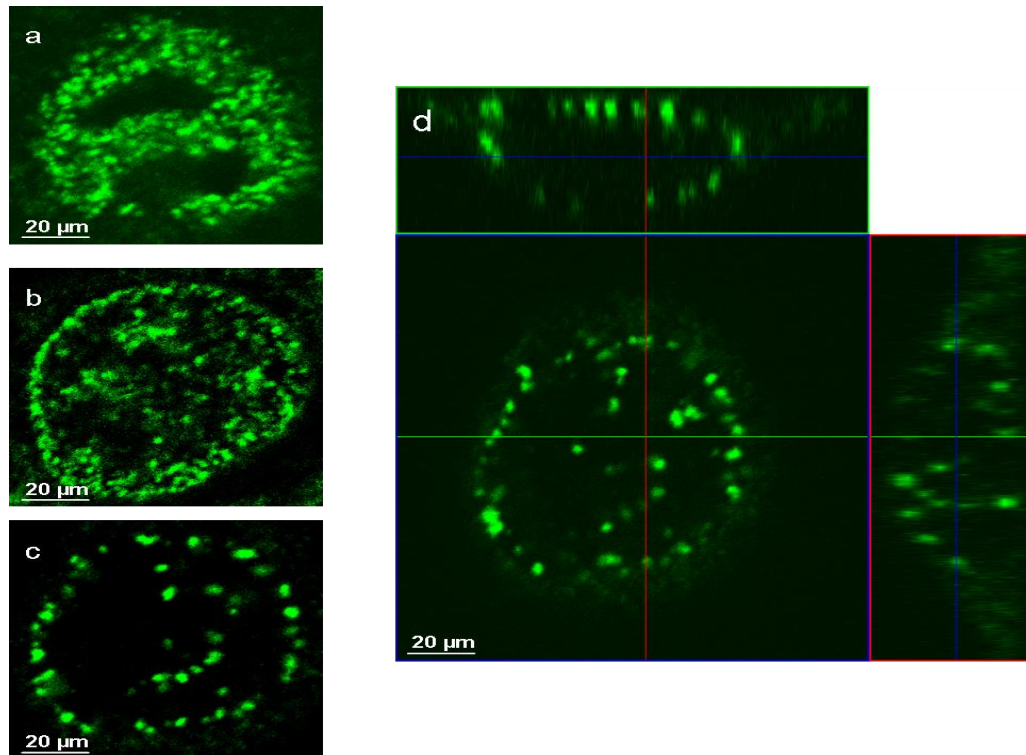


**Figure 5.12** Shows the DNA replication s-phase of HeLa cells labelled with 5-bromodeoxyuridine acquired using Confocal Laser Scanning Microscope (LSCM). (a) Early s-phase: most chromatin replicates; (b) Mid s-phase: replication foci appears as discrete perinuclear sites; (c) Late s-phase: replication foci form large donout shapes and (d) 3D image of late s-phase.

## **5.4.1 Experimental**

### **5.4.1.1 Cell Culturing**

Frozen HeLa cell lines were obtained from Dr D. Jackson and Prof. S. High at the University of Manchester and were cultured and maintained during the research project over the two years.

#### **5.4.1.1.1 Thawing the cells**

Two small cryogenic tubes containing frozen HeLa cells at  $-80\text{ }^{\circ}\text{C}$  were placed in a warm water bath at  $37\text{ }^{\circ}\text{C}$  for 1 min after which 1 ml of warm ( $37\text{ }^{\circ}\text{C}$ ) media (Dulbecco's modified eagle medium (DMEM) with 10% fetal bovine serum (FBS)) was added. The DMEM with 10% FBS is prepared by adding 5 ml of a mixture of penicillin and streptomycin, 7.5 ml of non-essential amino acids, 7.5 ml of sodium pyruvate, 50 ml of bovine serum and 5 ml of L- glutamine to 500 ml of DMEM. The cells were re-suspended slowly with a pipette and 0.5 ml of cell solution was transferred to four 25 ml flasks. An aliquot of the media (5ml) was added to each flask and placed in an incubator at  $37\text{ }^{\circ}\text{C}$  and an atmosphere of 5%  $\text{CO}_2$ . The cells were grown until 80% confluence was obtained in each flask and the media was changed every two days. Once enough confluence of cells was obtained, the cells were split (passage) every three consecutive days. Some cells were frozen at  $-80\text{ }^{\circ}\text{C}$  for future use because high number of sub-culturing (passage) can cause the cell morphology to change over time. Thus, it is recommended to passage one cell line 35 times.

#### **5.4.1.1.2 Sub-culturing (passaging) and Freezing the cells**

Old media was removed from the flask and the cells were washed with 3 ml of phosphate buffer saline (PBS). 0.5 ml of trypsin was added to the cells and incubated for 5 min. Once the cells have become detached 2 ml of fresh media was added and the cells were homogenised, after which 0.5 ml is transferred to the new T 25 flasks. 5 ml of fresh media was added to the flask and the cells were incubated until enough confluence is achieved. Some cells were frozen for future use by transferring the remaining solution containing cells to a 15 ml tube and spun down using a centrifuge at 185 g for 10 min. The media was aspirated and 2 ml of solution containing FBS + 10% dimethyl sulfoxide (DMSO) was added slowly and the cells were re-suspended in this solution. 0.5 ml of the cell solution was transferred to the cryogenic tubes and stored in -80 °C freezer.

#### **5.4.1.2 ToF-SIMS analysis of cells**

The cells were grown on two substrates, Si wafers and steel (specifically designed for the J105 instrument) after coating their surface with 0.1% poly-l-lysine for 15 min. Poly-lysine, a small peptide is routinely used in cell culture as an adhesive for the attachment of cells and tissues to a solid surface. Polycationic molecules of the poly-l-lysine bind to the solid surface, leaving the cationic sites to interact with anionic surfaces of the cells. After aspirating the poly-l-lysine, the substrates were allowed to dry before placing in the culture plate with cells and incubated for 24 hrs at 37 °C and an atmosphere of 5% CO<sub>2</sub>.

Secondary electron microscopy (SEM) images were recorded on the J105 using a 40 keV  $C_{60}^+$  primary ion beam after focusing it to match pixel size as verified using a transmission electron microscopy (TEM) grid. The SEM images show that the cells grown on poly-l-lysine substrate spread with more defined structure and visible nucleus, Figure 5.13a, whereas the cells grown on the substrate without any poly-l-lysine fold up in a ball structure, Figure 5.13b.

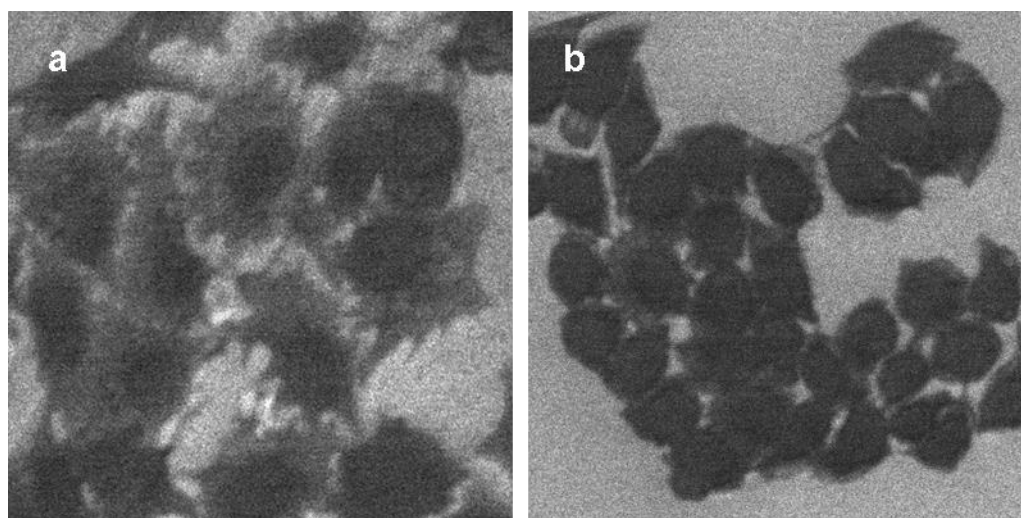


**Figure 5.13** SEM images of HeLa M cells grown on steel substrate recorded using 40 keV  $C_{60}^+$  over an area of  $256 \times 256 \mu\text{m}^2$ . (a) Steel substrate coated with poly-l-lysine. (b) Steel substrate not coated with poly-l-lysine.

Prior to the analysis of biological samples using ToF-SIMS, they have to be washed in a volatile solution to remove salts that accumulate on the surface. Various solutions have been investigated by different groups but ammonium formate was found to work best and is now widely used within the SIMS community. Once a protocol for

growing cells on the substrate as well as removing salts from the surfaces was developed, the cells were ready to be analysed by ToF-SIMS.

Following a wash in the ammonium formate, the cells were rapidly frozen and freeze-dried in vacuum before analysis. The analysis was performed on the J105 instrument equipped with a 40 keV  $C_{60}^+$  and 40 keV  $Au_3^+$  primary ion beam operating in a d.c. mode with bombardment angle of  $45^\circ$ . Two different mode of analysis were performed. Firstly, a single 2D image was acquired in which a whole cell is consumed using the 40 keV  $Au_3^+$  primary ion beam with current of 250 fA over an area of  $107 \times 107 \mu m^2$  and  $256 \times 256$  pixels and total ion dose of  $3 \times 10^{14}$  ions/cm<sup>2</sup>. This was followed by another experiment in which freshly prepared cells were analysed using the 40 keV  $C_{60}^+$  primary ion beam over an area  $256 \times 256 \mu m^2$  and  $256 \times 256$  pixel with a current of 6 pA. A single 2D image was acquired using a total ion fluence of  $3 \times 10^{14}$  ions/cm<sup>2</sup>.

In the second mode of analysis, a series of single image “slices” were acquired using the primary ion fluency of  $3 \times 10^{13}$  ions/cm<sup>2</sup> per layer to generate a 3D image. A total of ten single images were acquired in which a total of  $3 \times 10^{14}$  ions/cm<sup>2</sup> primary ion fluence was used to remove the entire cell. These cells were prepared using three different sample preparation techniques, formalin fixation, freeze-drying and frozen-hydrated analysis following vacuum freeze-fracture of a cell sandwich.

1. Formalin fixed cells were prepared by aspirating the media from the cells grown on a Si substrate and washed with PBS three times. Then the cells were chemically fixed by incubating them with 4% formalin for 15 min at  $4^\circ C$ . After fixation

the cells were washed with PBS five times followed by Millipore water three times and finally with 0.15 M ammonium formate for 1 minute to remove salts.

2. Freeze-dried cells were prepared by immediately freezing the cells grown on a Si substrate in liquid nitrogen following a wash in 0.15 M ammonium formate for 1 min. Then the sample was transferred into the preparation chamber under Ar to prevent water deposition and freeze-dried in vacuum for 2 hrs.

3. Frozen-hydrated cells were prepared by growing the cells for 24 hrs on poly-l-lysine coated steel, a hinged two plate substrate specifically designed to fracture biological samples. After aspirating the culture media and washing in 0.15 M ammonium formate for 1 minute, the cells were sandwiched between the two metal plates and rapidly frozen in liquid nitrogen-cooled propane. The frozen cells were transferred to liquid nitrogen where the steel substrate is mechanically attached onto a freeze-fractured device “mousetrap” and inserted into the instrument under Ar. The device was then transferred to a pre-cooled preparation chamber (168 K) and the sample was fractured *in situ* by pushing the trigger on the device. This action automatically releases the top plate of the steel which flips backwards and the sample is fractured. The fractured sample was transferred to the cryogenic analysis stage (148 K) and cells were analysed in the frozen-hydrated state. The instrument also incorporates a cryo-shield fixed above the sample preparation chamber to minimise re-condensation of water vapour, once the sample is fractured.

The analysis software developed by the SAI Ltd allows viewing and generating single ion images. Matlab routines have also been developed by A. Henderson in the Vickerman’s group to generate better contrast single ion images.

## 5.4.2 Results and Discussion

The main aim behind the development of this instrument was to fully exploit the potential of ToF-SIMS for single cells imaging. Although, this is extensively being researched in ToF-SIMS, the technique is confined to reaching its full prospective due to the limitations associated with the pulsed primary ion beam. The J105 has been fitted with two primary ion sources operating in a dc mode,  $\text{Au}_n^{n+}$  cluster ion and the polyatomic  $\text{C}_{60}^{n+}$  projectile. The cells were analysed in 2D and 3D modes, discussed below.

### 5.4.2.1 2D analysis

Firstly, the cells were analysed in a 2D mode in which a whole cell is consumed using a dc primary ion beam,  $\text{Au}_3^+$  cluster and polyatomic  $\text{C}_{60}^+$  to provide a comparison between the two beams. The 2D image generated is more comparable to a bright-field microscope image of a cell except that no labelling is required in ToF-SIMS.

Figure 5.14 show a single 2D ToF-SIMS total ion image of rapidly frozen freeze-dried HeLa cells, acquired using  $\text{Au}_3^+$  cluster primary ion beam, focused to 300 nm over 3.5 hrs. A 2D image of cells was also acquired using a 40 keV  $\text{C}_{60}^+$  polyatomic beam focussed to 700 nm with an ion fluence of  $3 \times 10^{14}$  ions/cm<sup>2</sup> over 3.5 hrs (image not shown). The figure shows that a highly focused total ion image can be obtained using LMIS in which the beam can be focused to a smaller spot size as compared to the gas cluster  $\text{C}_{60}^+$  projectile.

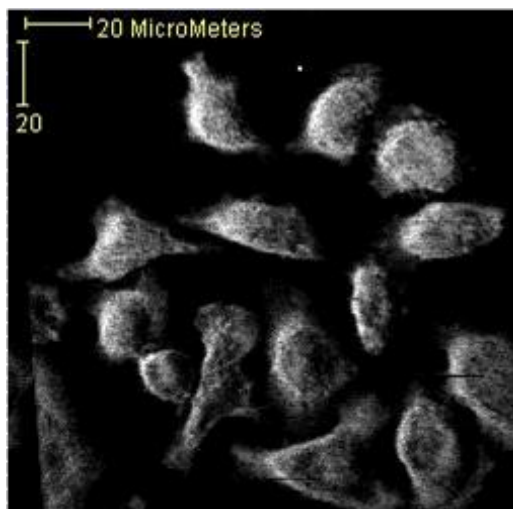


**Figure 5.14** 2D total ion ToF-SIMS image of HeLa cells acquired on the J105 3D *Chemical Imager* using acquired using the 40 keV  $\text{Au}_3^+$  primary ion beam over a field of view of  $107 \times 107 \mu\text{m}^2$ ,  $256 \times 256$  pixels and total ion dose of  $3 \times 10^{14}$  ions/ $\text{cm}^2$ .

Some of the ions commonly imaged in the cells and the tissues in ToF-SIMS literature were selected to generate single images to map their distribution in the HeLa cells. Firstly, fragment of lipids were selected, which form a major component of living cells and tissues and are easily ionised relative to other bio-molecules. The PC head-group  $m/z$  184, a highly abundant lipid in the cell that has also been used as a biomarker for cells is frequently imaged in cells and tissues following ToF-SIMS analysis [Brietenstein *et al.* 2007], [Nygren *et al.*, 2005]. Figure 5.15 shows the distribution of the PC head-group  $m/z$  184 and its associated fragments  $m/z$  86 (which can also be assigned to an ammonium ion of leucine) and  $m/z$  104, generated following  $\text{Au}_3^+$  impact, Figure 5.15 a-c and  $\text{C}_{60}^+$ , Figure 5.15 d-f. On examining the figure one can see immediately a huge difference between the two beams. The PC head-group  $m/z$  184 clearly localises to the plasma membrane of the HeLa cells when imaged following  $\text{C}_{60}^+$

bombardment, Figure 5.15f; whereas when imaged using the  $\text{Au}_3^+$  the signal is more spread over the cells, Figure 5.15c.

Further, amino acid ions were also imaged using both beams, Figure 5.16. Again it is evident that the distributions of amino acids  $m/z$  120 fragment of phenylalanine, glycine or methionine, Figure 5.16d;  $m/z$  130 fragment of glutamic acid, glutamine or tryptophan, Figure 5.16e; and  $m/z$  170 fragment of tryptophan, Figure 5.16f, are distributed inside the cells when imaged using the  $\text{C}_{60}^+$ . However, when these ions are imaged using the  $\text{Au}_3^+$ , they appear to be scattered and localise at the same place as the lipid fragments, Figure 5.16 a-c.

A similar result is seen when the DNA and ribonucleic acid (RNA) bases are imaged, Figure 5.17. A cell consists of two types of nucleic acids; DNA which contains genetic information and RNA which transmit instructions from genes for protein synthesis. DNA is double strand polymer chains, composed of nucleotides which consist of a nitrogen base, deoxyribose sugar and a phosphate group. There are four different bases in DNA, adenine, guanine, cytosine and thymine. RNA differs from DNA in that it is a single strand consisting of a ribose sugar and uracil base instead of thymine. There are three different types of RNA, messenger RNA, ribosomal RNA and transfer RNA and each possess a specific function in protein synthesis [Tortora *et al.*, 2000]. When the nitrogenous bases, adenine fragments  $m/z$  119 [ $\text{C}_5\text{H}_3\text{N}_4$ ]<sup>+</sup>, Figure 5.17a,  $m/z$  136 [ $\text{C}_5\text{H}_6\text{N}_5$ ]<sup>+</sup> (can also be assigned to an immonium ion of amino acid tyrosine), Figure 5.17b, guanine fragments  $m/z$  135 [ $\text{C}_5\text{H}_3\text{N}_4\text{O}$ ]<sup>+</sup>, Figure 5.17c, thymine fragment 127 [ $\text{C}_5\text{H}_7\text{N}_2\text{O}_2$ ]<sup>+</sup>, Figure 5.17d, cytosine 223 [ $\text{C}_8\text{H}_{11}\text{N}_6\text{O}_2$ ]<sup>+</sup>, Figure 5.17e and uracil  $m/z$  225 [ $\text{C}_8\text{H}_9\text{N}_4\text{O}_4$ ]<sup>+</sup>, Figure 5.17f, are imaged using the  $\text{C}_{60}^+$  they localise to the

centre of the cells as they arise from the nuclear DNA and RNA. However, when these ions are imaged using the  $\text{Au}_3^+$  ion beam, the signal levels appears to be low and dispersed over the whole cell , data not shown [Fletcher *et al.*, 2008], [Rabbani *et al.*, 2010].

This effect is seen because upon impact the LIMIS,  $\text{Au}_3^+$  sources penetrate deeper than the polyatomic sources causing damage to the sub-surface region; and at ion fluence higher than the static limit an increasingly damaged surface is analysed resulting in a decrease in the signal levels of secondary ion

However, the polyatomic beam  $\text{C}_{60}^+$  offers the advantages of higher secondary ion signal and low sub-surface damage, allowing the static limit to be relaxed. By using the  $\text{C}_{60}^+$  beam at high ion dose, one can access a whole sample referred to as ‘voxels’ rather than pixels which also increases the sensitivity. Thus, by analysing HeLa cells using the  $\text{C}_{60}^+$  primary ion beam a clear differentiation between the lipid membrane and nuclear material can be made.

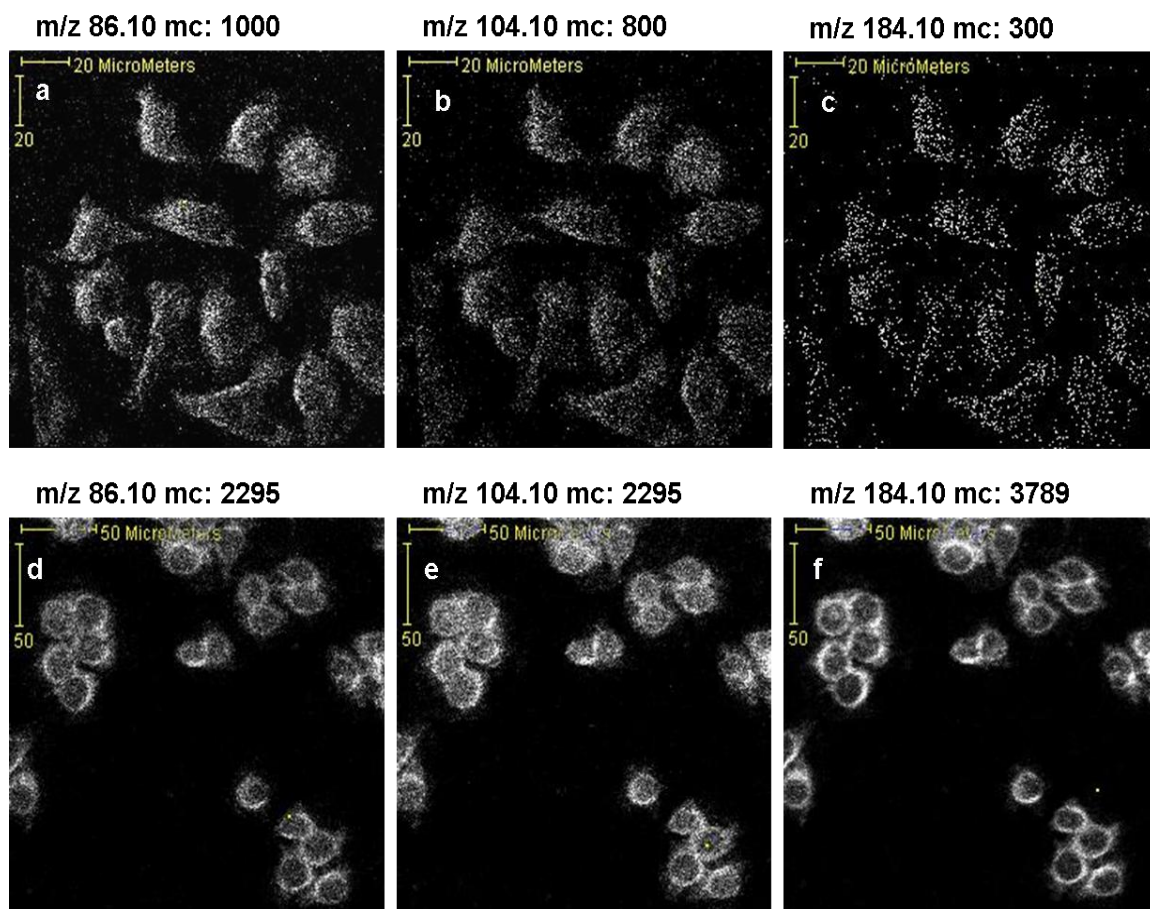


**Figure 5.15** 2D ToF-SIMS images of PC head-group  $m/z$  184 and its fragments of rapidly frozen freeze-dried HeLa cells acquired on the J105 with cluster LMIS  $\text{Au}_3^+$  (a-c) and polyatomic  $\text{C}_{60}^+$  (d-f). (a) and (d)  $m/z$  86.10 and (b) and (e)  $m/z$  104.10 fragment of PC head-group. (c) and (f)  $m/z$  184.10 PC head-group. Maximum counts per pixel (mc) for each mass is displayed.

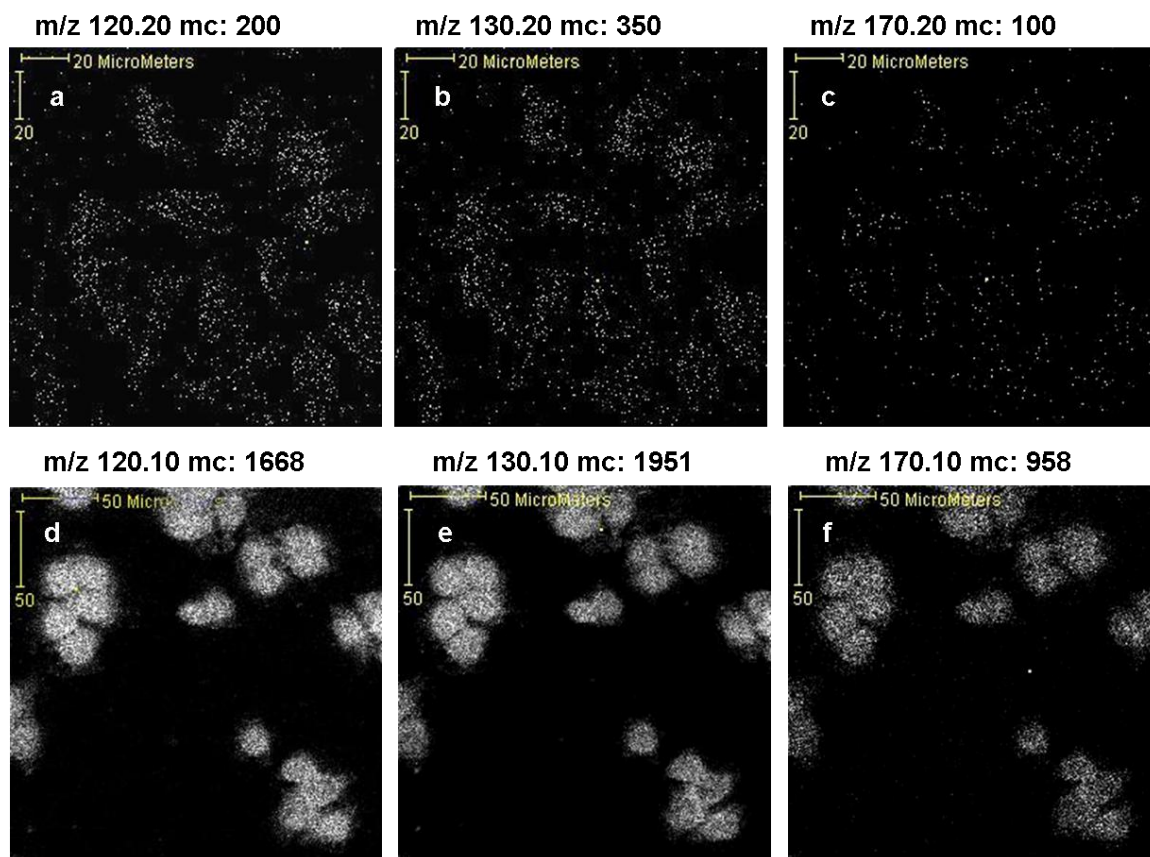


**Figure 5.16** 2D ToF-SIMS images amino acids of rapidly frozen freeze-dried HeLa cells acquired on the J105 with cluster  $\text{Au}_3^+$  (a-c) and  $\text{C}_{60}^+$  (d-f). (a) and (d)  $m/z$  120 fragment of phenylalanine, glycine or methionine; (b) and (e)  $m/z$  130, fragment of glutamic acid, glutamine or tryptophan; (c) and (f)  $m/z$  170 fragment of tryptophan. Maximum counts per pixel (mc) for each mass is displayed.

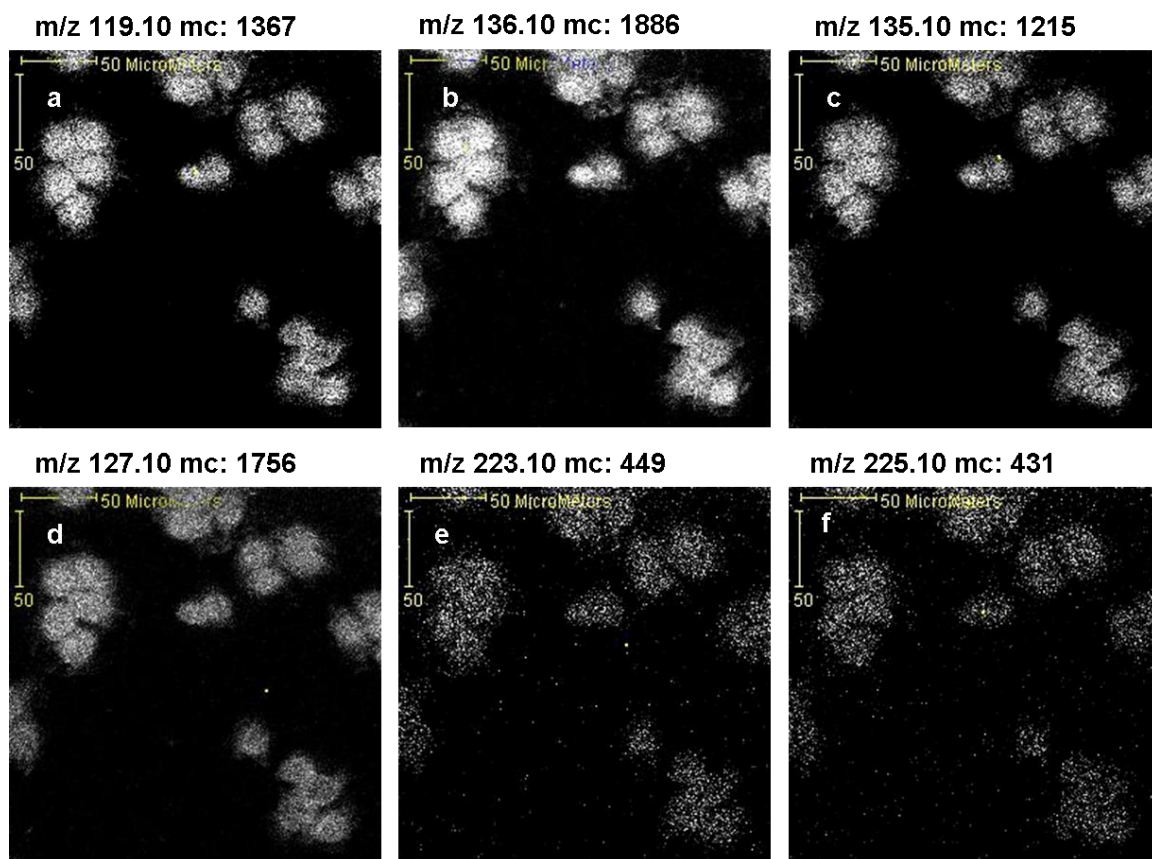


**Figure 5.17** 2D ToF-SIMS images of DNA and RNA nitrogenous bases of rapidly frozen freeze-dried HeLa cells acquired on the J105 instrument using 40 keV  $C_{60}^+$  primary ion beam. Adenine fragments (a)  $m/z$  119  $[C_5H_3N_4]^+$ , (b)  $m/z$  136  $[C_5H_6N_5]^+$ ; guanine fragment (c)  $m/z$  135  $[C_5H_3N_4O]^+$ ; thymine fragment (d)  $m/z$  127  $[C_5H_7N_2O_2]^+$ ; cytosine (e)  $m/z$  223  $[C_8H_{11}N_6O_2]^+$ ; and uracil (f)  $m/z$  225  $[C_8H_9N_4O_4]^+$ . Maximum counts per pixel (mc) for each mass is displayed.

The 2D images of HeLa cells in which a whole cell is analysed using the 40 keV  $C_{60}^+$  on the J105 are more comparable to the 3D imaging of normal rat kidney cells (NRK) reported by Hagenhoff and co-workers. In this study NRK cells were analysed in 3D using  $C_{60}^+$  beam as a sputtering and  $Bi_3^+$  as the analysis beam. The images

generated show PC head-group  $m/z$  184 to localise to the cell membrane and amino acids to the inside of the cell after 45<sup>th</sup> sputter cycle, Figure 5.11. Although similar images are produced, the NRK study was completed using dual beam experiment in which a valuable sample has been wasted during the etch cycle. This is where the J105 shows the potential benefits of analysing cells using a dc polyatomic beam in which a whole sample is consumed without needing to etch. Further, this data also highlights that the  $C_{60}^+$  can now be used to detect molecular species on a sub-cellular scale over a suitable time frame (3.5 hrs) by exceeding the static primary ion fluence.

HeLa cells were also analysed on the conventional ToF-SIMS, the BioToF using monoatomic,  $Au^+$  primary ion beam, Figure 5.18. The analysis was completed under static conditions in which it has not been possible to detect the nuclear material, Figure 5.18b and the PC signal is homogenous over the cell, characterised to the outer membrane, Figure 5.18c. These images are similar to the images of cells found in literature when analysed using conventional ToF-SIMS under static conditions. A study by Ewing and Winograd show the PC head-group to homogeneously localise to the top surface of the *Tetrahymena* protozoa cells [Ostrowski *et al.*, 2004].

Additionally, if a single beam experiment in which a whole cell is consumed was repeated on the conventional ToF-SIMS system running at 10 kHz with 100 nsec pulse would take 1000 times longer to accomplish due to the pulsed nature of the primary beam.

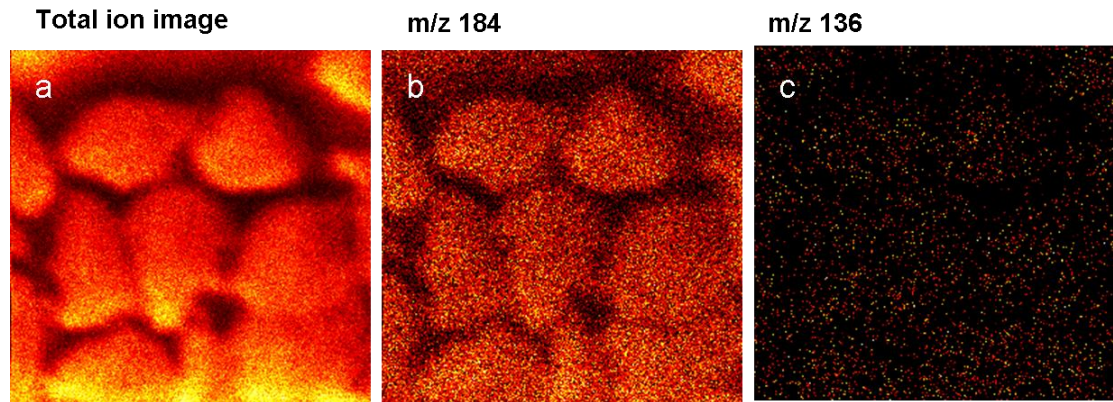


**Figure 5.18** 2D surface image of HeLa cells acquired on the conventional ToF-SIMS instrument, the BioToF using monoatomic 20 keV Au<sup>+</sup> primary ion beam over a field of view  $105 \times 105 \mu\text{m}^2$  and ion dose of  $5 \times 10^{12}$  ions/cm<sup>2</sup>.

#### 5.4.2.2 3 D analysis

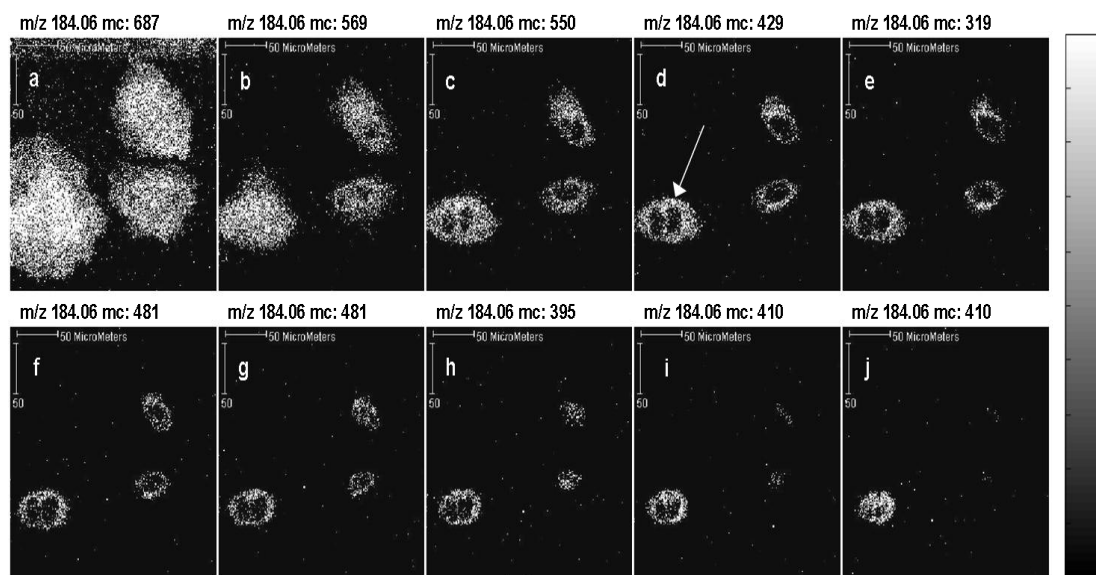
Although a whole cell analysis can be performed in a routinely workable analysis time (3.5 hrs), there is still a need to follow the evolution in biochemistry with depth, hence the need for 3D analysis. On the conventional ToF-SIMS, 3D imaging is accomplished using the interleaved mode in which one beam based on a LMIS is used for imaging and the second such as polyatomic ion is used to remove the damage caused by the LMIS. These dual beams approach produces very successful results although there is a loss of valuable sample during the etch cycle, motioned above. However, on the J105 a continuous polyatomic primary ion beam is used which allows all the material to be sampled and recorded, hence increasing the sensitivity.

Figure 5.19 shows 3D analysis of formalin fixed HeLa M cells in which the PC signal  $m/z$  184 is monitored with depth. This method of sample preparation is

extensively applied to fix live cells prior to analysis by microscopy. Fixation can either be performed using organic solvent such as 70% ethanol or cross-linking agents such as formalin. The former can result in dehydration of cells, eradication of lipids and precipitate proteins on the cell surface. The latter, formalin fixation only fixes the proteins by forming intermolecular bridges between the free amino acids but does not fix the lipids or the carbohydrates. However, it can preserve the cell morphology better than the organic solvent [IHC].

Under static conditions, the PC signal is distributed homogeneously over the cell as seen above, Figure 5.18. However, in 3D imaging the PC signal although is homogeneous in layer 1, Figure 5.19a, but it becomes localised to regions surrounding nucleus, Figure 5.19d as the depth profile progresses. This increase in the signal is attributed to the organelle membranes and lipid rich regions that extend from the nucleus which specify the presence of the endoplasmic reticulum. This image shows that one of the cells is at the dividing stage, mitosis, in the cell cycle as indicated by the arrow. Only two of the three cells are fully consumed by layer 10. Clearly the dividing cell will need higher ion fluence to be fully removed [Rabbani *et al.*, 2010].

The ion at  $m/z$  120 fragment of amino acids also follows the same distribution, it is diffused at the surface in layer 1 but becomes localised to the centre of the cell as it is sputtered by etching, Figure 5.20. This data demonstrates the benefits of 3D imaging as it allows one to retrospectively examine the chemistry at every point of the cell as a function of depth, which would not be possible if only 2D images are acquired at pre-determined depths using the interleaved dual beam experiment described above.



**Figure 5.19** 3D analysis of formalin fixed HeLa cells on the J105 using continuous 40 keV  $C_{60}^+$  primary ion beam in which  $m/z$  184.06 is imaged from layer 1 (a) to layer 10 (j), each layer acquired with a fluence of  $3 \times 10^{13}$  ions/cm<sup>2</sup>, over a field of view of  $256 \times 256 \mu\text{m}^2$  and  $256 \times 256$  pixels. Maximum counts per pixel (mc) for each layer is displayed. Reproduced from Rabbani *et al.* 2010.

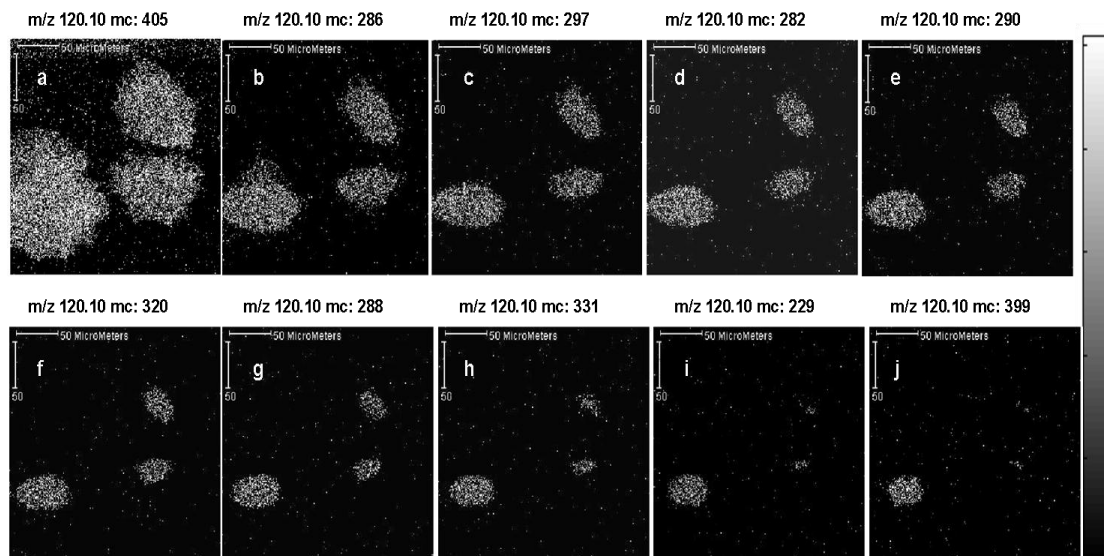


**Figure 5.20** 3D analysis of formalin fixed HeLa cells on the J105 using continuous 40 keV  $C_{60}^+$  primary ion beam in which  $m/z$  120.10 is imaged from layer 1 (a) to layer 10 (j), each layer acquired with a fluence of  $3 \times 10^{13}$  ion/cm<sup>2</sup>, over a field of view of  $256 \times 256 \mu\text{m}^2$  and  $256 \times 256$  pixels. Maximum counts per pixel (mc) for each layer is displayed.

Another feature of this instrument is that the analysis can be performed at a high mass resolution as illustrated in Figure 5.21. At the nominal mass  $m/z$  104 there are three different peaks which when imaged localise at three different locations. The inorganic peak  $m/z$  103.95 is assigned to a salt  $\text{NaKCNO}^+$ , Figure 5.21 d-f which localises within the cell. An unknown organic  $m/z$  104.05, Figure 5.21 a-c can be localised both inside and at lower intensity, around the cell. Another organic ion at  $m/z$  104.10, Figure 5.21 g-i localises around the lipid membrane which would suggest that it is a fragment of the PC head- group  $m/z$  184.06. This differentiation between the organic peak  $m/z$  104.05 and the PC fragment  $m/z$  104.10 is achieved at mass resolution

of 4000, which demonstrate the ability to maintain good mass resolution along with good spatial resolution. Furthermore, the spatial separation can only be visualised because the data was acquired as a series of layers as part of a 3D analysis. The inorganic peak  $m/z$  103.95 appears broad compared to other peaks which suggest that there are multiple species of similar masses present and mass resolution higher than 4000 is required to resolve them.

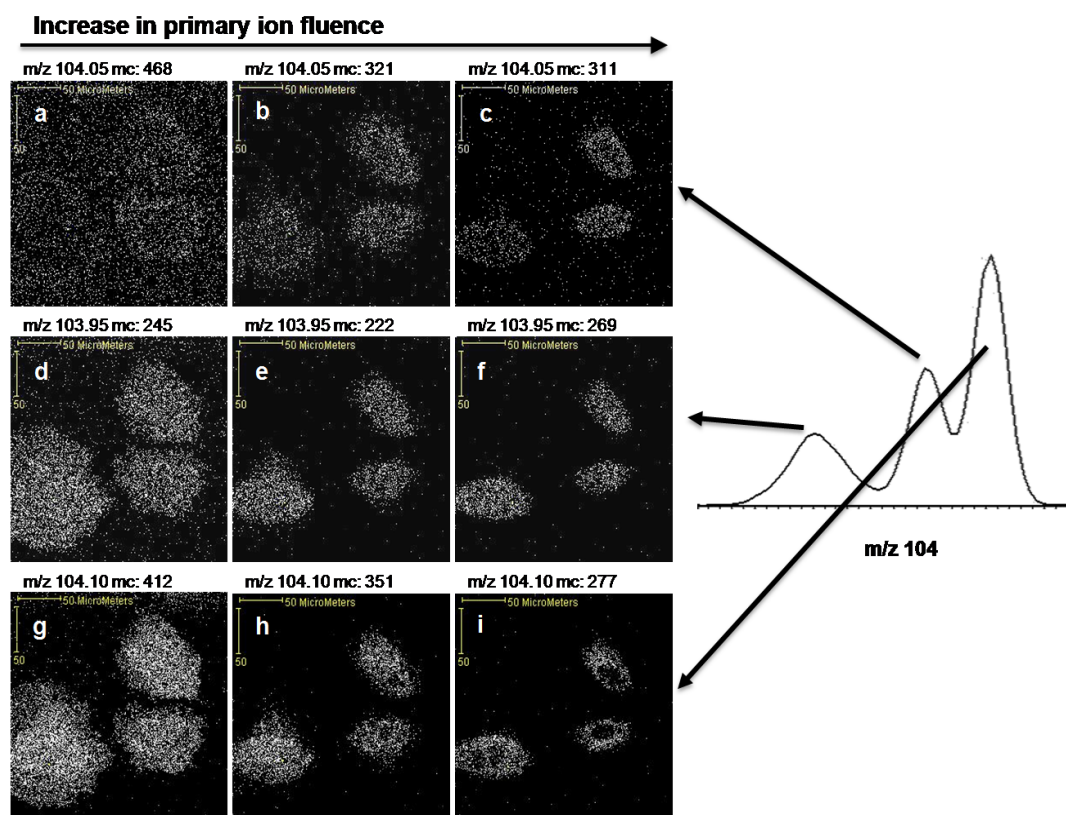


**Figure 5.21** Illustrates the importance of maintaining high mass resolution during analysis and 3D imaging. (a-c)  $m/z$  104.05 unknown (d-f)  $m/z$  103.95  $\text{NaKCNO}^+$  and (g-i)  $m/z$  104.10 fragment of PC head-group. Maximum counts per pixel (mc) for each mass and each layer is displayed. Reproduced from Rabbani *et al.* 2010.

Another aspect of this study was to investigate the different sample preparation procedures, formalin fixed, freeze-dried and freeze-fractured analysed in frozen hydrated state. As mentioned above, sample preparation plays a vital role in ToF-SIMS analysis of biological samples as the integrity and distribution of chemical species has to be maintained in a high vacuum. There are many different sample preparations under investigation but yet there is no agreement on the optimum procedure the analyst can follow during ToF-SIMS analysis of biological samples.

Figure 5.22 shows a comparison between the three different sample preparations explored for the analysis of HeLa cells. Two ions  $m/z$  184 and  $m/z$  136 were used to illustrate changes occurring in the distribution of nuclear and membrane as a function of depth. The nuclei appear to be similar for all three sample preparations but there is significant difference in the lipid distribution. The data shows that when the cells are analysed in freeze-fractured frozen-hydrated state, the peak  $m/z$  184 (green) can be localised around the lipid membrane of the cell on layer 1, Figure 5.22a, whereas in the freeze-dried and formalin fixed cells the  $m/z$  184 is more diffuse and extends outside the cells, Figure 5.22d and Figure 5.22g. This effect was observed because the formalin fixation preserves the morphology of the cell through cross linking the proteins but does not fix the lipids and carbohydrates. Thus, these molecules are free to move and when the sample is placed in high vacuum they may become redistributed or migrate to the top surface of the sample. Similar effect is also observed when the cells are analysed in the freeze-dried state, Figure 5.22d. However, a clear localisation of the lipids initially in the freeze-fractured frozen-hydrated state suggests that during the fracturing process the top membrane may have been removed and the nucleus has been exposed, or the

redistribution of lipid membrane and other components is avoided by maintaining the sample cold and fully hydrated. Following 1<sup>st</sup> layer acquisition, all samples show the similar distribution of PC which increases around the nucleus as the depth profile progresses until all the material is consumed.

The adenine fragment  $m/z$  136 has been perceived to behave differently in the three sample preparation methods. In the formalin and freeze-dried cells it spreads over the whole cells, representing their shape. However, with respect to the freeze-fractured frozen hydrated, the signal can be mapped to the centre of the cell which increases as the profile progresses towards the nucleus.

Further observing the spectra of the three sample preparation techniques it can be concluded that high signal levels are achieved when the sample is analysed in the frozen hydrated state as compared to the formalin fixed and freeze-dried, Figure 5.23. When 1<sup>st</sup> layer is acquired the intensity of  $m/z$  184 is  $1.6 \times 10^6$  for freeze-fractured frozen hydrated,  $5.0 \times 10^5$  for fixed and  $3.0 \times 10^6$  for freeze-dried. Overall high signal levels are obtained when the cell is analysed in frozen-hydrated state as compared to the other two sample preparation methods.

This increase in the signal levels could be due to increase in the ionisation efficiency due to the presence of water matrix. In the presence of water matrix, an increase in the amount of proton is seen during the sputtering process which helps to promote the formation of  $[M+H]^+$ , thus increasing the secondary ion signal. A number of studies have been published which show that the presence of water matrix results in an increase in the secondary ion yields of molecular species [Roddy *et al.*, 2003],

[Piwowar *et al.*, 2010]. Thus, the data validates that the spatial integrity and chemical distribution of the cells is preserved when they are analysed in a frozen hydrated state.

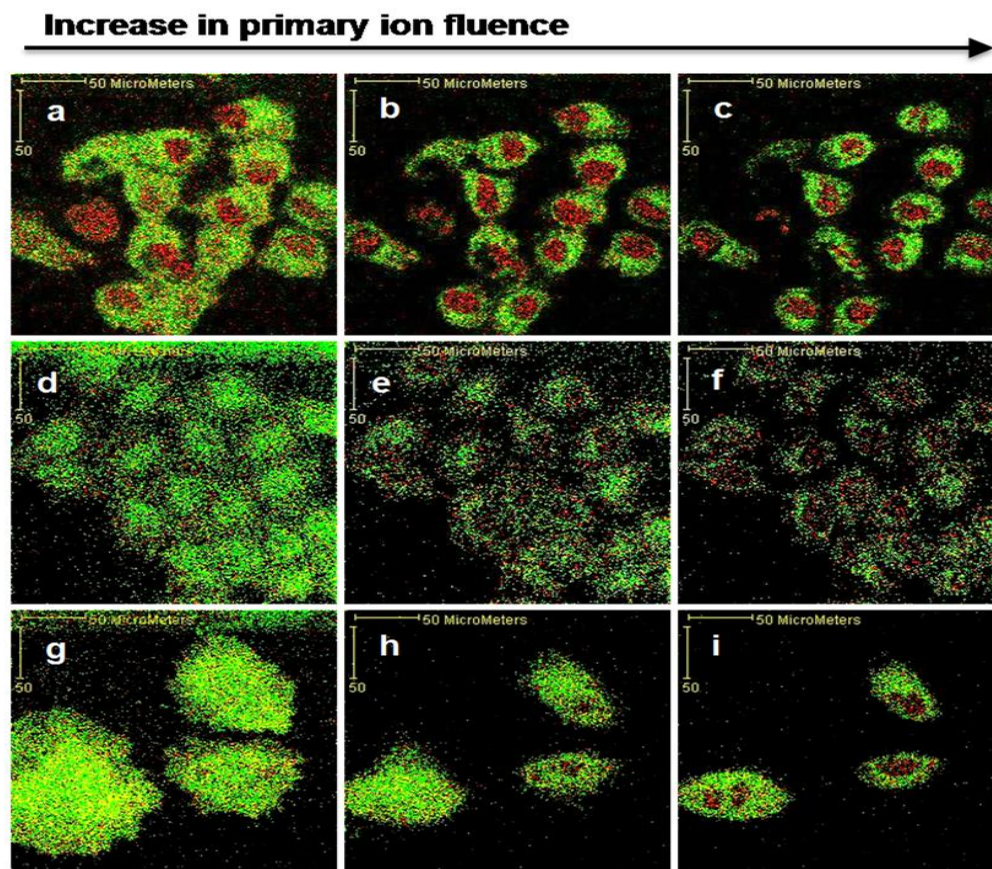


**Figure 5.22** A comparison of three different sample preparations, freeze-fracture frozen-hydrated (a-c), freeze-dried (d-f) and formalin fixed (g-i) for the  $m/z$  184.06 (green) and  $m/z$  120.10 (red) shown in colour-overlay. The figure shows an increase in primary ion fluence from left to right with each layer obtained using a fluence of  $3 \times 10^{13}$  ions/cm<sup>2</sup> acquired over a field of view  $256 \times 256 \mu\text{m}^2$  and  $256 \times 256$  pixels. Maximum counts per pixel (mc) for each mass and each layer are: (a)  $m/z$  184.06 mc:604;  $m/z$  120.10 mc:401 (b)  $m/z$  184.06 mc:552;  $m/z$  120.10 mc:367 (c)  $m/z$  184.06 mc:588;  $m/z$  120.10 mc:402 (d)  $m/z$  184.06 mc:1096;  $m/z$  120.10 mc:301 (e)  $m/z$  184.06 mc:481;  $m/z$  120.10 mc:263 (f)  $m/z$  184.06 mc:400;  $m/z$  120.10 mc:285 (g)  $m/z$  184.06 mc:687;  $m/z$  120.10 mc:405 (h)  $m/z$  184.06 mc:569;  $m/z$  120.10 mc:286 (i)  $m/z$  184.06 mc:550;  $m/z$  120.10 mc:297. Reproduced from Rabbani *et al.* 2010.

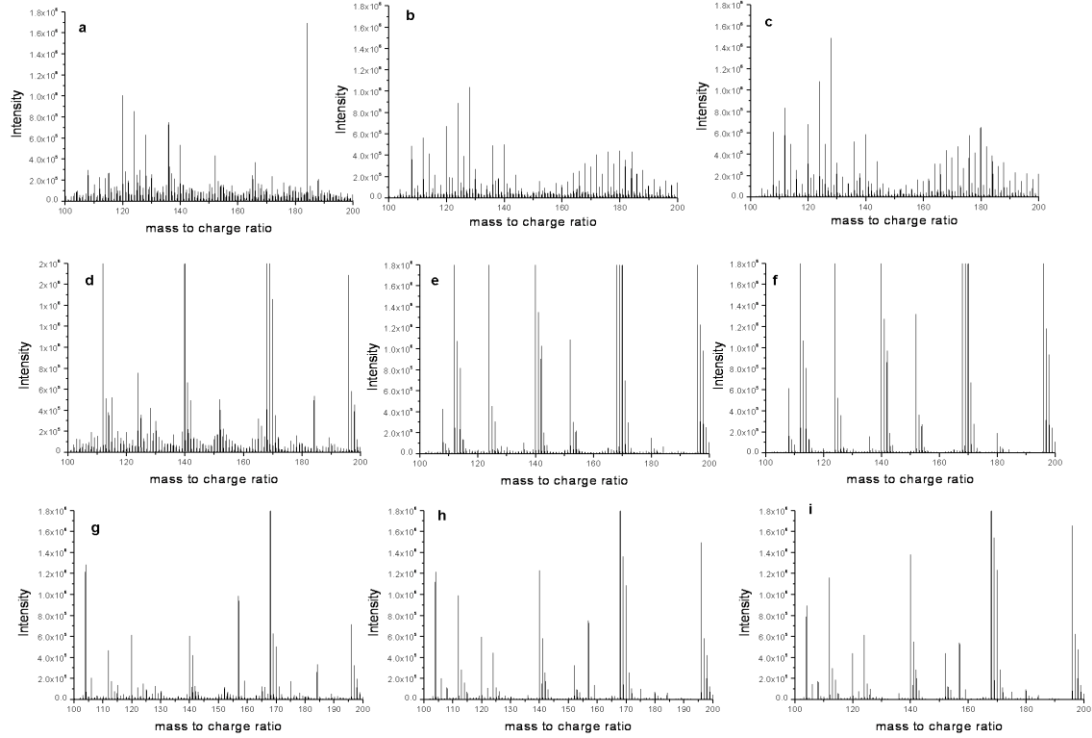


**Figure 5.23** ToF-SIMS spectra of HeLa cells analysed on the J105 layer 1 to later 3. (a-c): Freeze-fractured frozen hydrated cells. (d-f): Formalin fixed cells. (g-i): Freeze-dried cells.

### 5.4.3 Data Analysis tools

The spectral data of the biological samples acquired on ToF-SIMS can be very complex due to the complex nature of the sample and can present many challenges to the analyst. Further, acquiring data at high mass and spatial resolution at the same time, particularly with 3D analysis can be difficult to manipulate and visualise due to the large size of the data set. Various data analysis tools are being developed to reduce the dimensionality of the data set in which multivariate analysis is proving to be a successful and is routinely being used.

Multivariate allows simplification of the data set so that valuable and constructive information can be obtained from complex spectra and images. It allows enhancement of image contrast, recognize and classify significant areas as well as output the variables in  $m/z$  values associated with these areas so they can be chemically identified [Fletcher *et al.*, 2006], [Vaidyanathan *et al.*, 2008], [Lee *et al.*, 2008]. A number of studies have been published in which multivariate analysis has proven to be a valuable tool to differentiate between ToF-SIMS data for categorising proteins [Wagner *et al.*, 2001], as well as identify different microorganisms [Thompson, *et al.*, 2006] .

The two most common processing tools used in multivariate analysis include principal component analysis (PCA) and maximum autocorrelation factor (MAF). Comparative studies of PCA and MAF on SIMS data have indicated that for SIMS imaging MAF generates better images. MAF transforms the data set by maximising autocorrelation between the neighbouring pixels and offers the advantages of enhanced image contrast as it is independent of pre-processing and recognises fine features that

can be visualised in single image peaks, often limited in the PCA [Tyler *et al.*, 2007], [Wagner *et al.*, 2004], [Larsen, *et al.*, 2002], [Nielsen, *et al.*, 1998].

MAF was performed on the HeLa cells data acquired using  $\text{Au}_3^+$  ion beam. MAF 5 is able to capture some variations in signal between the cell membrane and nuclear material. However, the loading plot does not show any clear separation on the peaks responsible for this variation due to the limitation of signal per pixel, Figure 5.24.

Conversely, MAF analysis on the  $\text{C}_{60}^+$  image data generates better results. MAF 4 produces a variation in signal between the cell membrane and nuclear material, Figure 5.25. Since there is more signal per pixel, the loading plot can now be interpreted and individual peaks can be imaged. Figure 5.25 shows that the two masses responsible for the differentiation between the nucleus and the plasma membrane are,  $m/z$  136 adenine found in the nucleus and  $m/z$  184 PC head-group present in the plasma membrane.

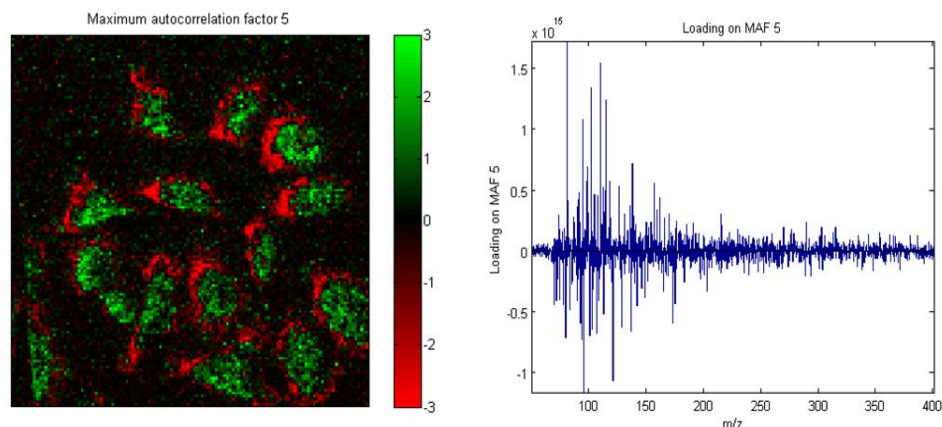


**Figure 5.24** MAF performed on HeLa cells data acquired using 40 keV  $\text{Au}_3^+$ .

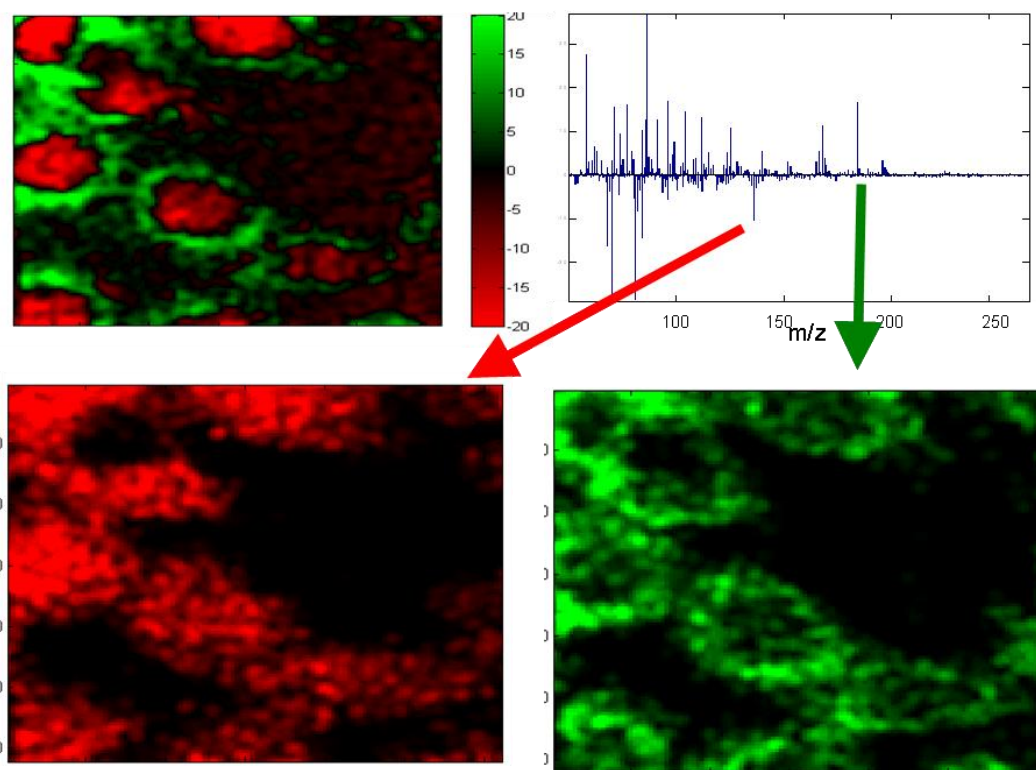


**Figure 5.25** MAF performed on HeLa cells data acquired using 40 keV  $C_{60}^+$ .

New software, 4D ToF-SIMS for the visualisation and analysis of 3D data set acquired on the J105 is currently being developed by the Vickerman group in collaboration with Reichenbach and co-workers. Currently the J105 instrument produces 3D data set with tens of thousands of ToF channels which cannot be managed in a fast memory of normal computer system and general imaging software are limited. Thus for 3D visualisation and analysis, software which is memory and computational efficient is required. According to Reichenbach *et al.* (2009) there are three issues which need to be addressed for rapid, real time visualisation of a large 3D hyperspectral data:

- Compression of the data set for rapid visualisation;

- 3D hyperspectral interactivity;
- clustering and categorising of spatial and spectral information.

Two ions,  $m/z$  184 and  $m/z$  120 were selected and imported into the 4D ToF-SIMS software for 3D visualisation, Figure 5.26. This software is still under development and new tools are being developed for enhanced visualisation of the 3D data set.

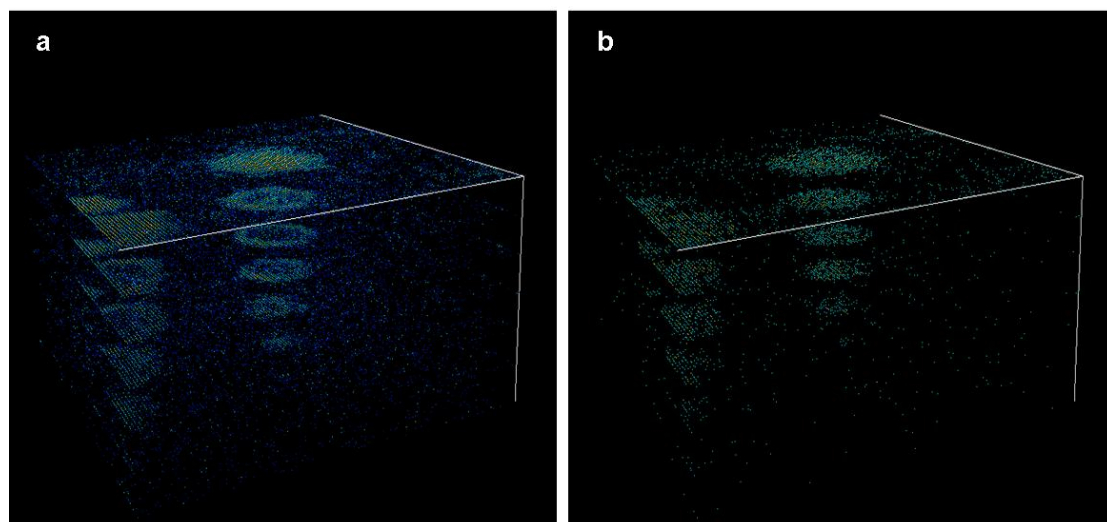


**Figure 5.26** 3D images visualised in 4D ToF-SIMS software, (a) PC head group  $m/z$  184 and (b) fragment of amino acids  $m/z$  120.

### 5.4.3 Conclusion

A model cell line, HeLa cells have been used to prove concept and the success of the instrument **J105 3D Chemical Imager** for high mass resolution, high sensitivity and sub-cellular imaging. The polyatomic primary ion beam  $C_{60}^+$  offers the possibility of much better if not good sensitivity in 2D imaging at sub- $\mu\text{m}$  spatial resolution together with the opportunity of delving into the chemistry below the surface over a suitable time frame (3.5 hrs). Using a dc primary beam and decoupling it from the mass spectrometry allows one to fully explore the potential of the  $C_{60}^+$  for imaging and a clear differentiation between the material within the nuclei and the lipid membrane can be made. By maintaining high mass resolution during imaging enables much greater chemical information to be obtained from the data, but this in turn will place greater demands on data processing tools. 3D analysis of cells allows one to monitor the distribution and change in chemistry with depth.

Sample preparation will be a key issue in future cell analyses and initial studies suggest that the formalin fixed can preserve the cell to some degree but redistribution of lipids may occur. Additionally, the analysis in frozen hydrated state reveals better localisation of nuclear material with an increase in signal levels, thus is a preferable method for the analysis of biological samples.

## 5.5 Summary

The aim of this chapter was firstly to highlight the limitations associated with the conventional ToF-SIMS for single cell imaging and secondly how this can be overcome by capitalising on the features of  $C_{60}^+$  polyatomic ion for imaging on the new instrument, **J105 3D Chemical Imager**. A standard cell line, HeLa cells have been used to emphasise key features of the instrument: sensitivity, imaging at high mass resolution with high spatial resolution and high throughput analysis with greatly reduced time. The data presented shows the clear capability to produce mass spectrometric images of single cells and identify cellular compartments such as the nucleus, the endoplasmic reticulum and plasma membrane in 2D and 3D modes.

Three different sample preparation techniques, formalin fixed, freeze-dried and freeze-fractured frozen hydrate were also investigated and the preliminary data suggests that frozen-hydrated may be beneficial in analysing cells in a lifelike form.

Since a large data set is being generated on the J105, new tools and methods are required for the manipulation and visualisation of the data which has been briefly touched on.

## References

Baker, M.J.; Zheng, L.; Winograd, N.; Lockyer, N.P.; Vickerman, J.C. **Mass spectral imaging of glycopospholipids, cholesterol, and glycophorin A in model cell membranes.** *Langmuir* (2008) 24 (20), 11803-11810

Bennett, B.D.; Zha, X.; Gay, I.; Morrison, G.H. **Intracellular boron localization and uptake in cell cultures using imaging secondary ion mass spectrometry (ion microscopy) for neutron capture therapy for cancer.** *Biology of the Cell* (1992), 74 (1), 105-108

Berman, E.S.F.; Fortson, S.L.; Checchi, K.D.; Wu, L.; Felton, J.S.; Wu, K.J.J.; Kulp, K.S. **Preparation of Single Cells for Imaging/Profiling Mass Spectrometry** *Journal of the American Society for Mass Spectrometry* (2008), 19 (8), 1230-1236

Börner, K.; Malmberg, P.; Månsson, J.-E.; Nygren, H. **Molecular imaging of lipids in cells and tissues** *International Journal of Mass Spectrometry* (2007), 260 (2-3), 128-136

Braun, R.M.; Blenkinsopp, P.; Mullock, S.J.; Corlett, C.; Willey, K.F.; Vickerman, J.C.; Winograd, N. **Performance characteristics of a chemical imaging time-of-flight mass spectrometer.** *Rapid Communications in Mass Spectrometry* (1998), 12 (8), 1246-1252

Breitenstein, D.; Rommel, C.E.; Möllers, R.; Wegener, J.; Hagenhoff, B. **The chemical composition of animal cells and their intracellular compartments reconstructed from 3D mass spectrometry.** *Angewandte Chemie - International Edition* (2007), 46 (28) 5332-5335

Castaing, R.; Slodzian, G. **Analytical microscopy by secondary ion imaging techniques.** *Journal of Physics E: Scientific Instruments* (1981), 14 (10), 1119-1127

Chandra, S. **3D subcellular SIMS imaging in cryogenically prepared single cells.** *Applied Surface Science* (2004), 231–232, 467–469

Chandra, S. **Quantitative imaging of subcellular calcium stores in mammalian LLC-PK1 epithelial cells undergoing mitosis by SIMS ion microscopy.** *European Journal of Cell Biology* (2005), 84 (9), 783-797

Chandra, S.; Lorey II, D.R. **SIMS ion microscopy imaging of boronophenylalanine (BPA) and <sup>13</sup>C<sup>15</sup>N-labeled phenylalanine in human glioblastoma cells: Relevance of subcellular scale observations to BPA-mediated boron neutron capture therapy of cancer** *International Journal of Mass Spectrometry* (2007), 260 (2-3), 90-101

Chandra, S.; Morrison, G.H. **Sample preparation of animal tissues and cell cultures for secondary ion mass spectrometry (SIMS) microscopy.** *Biology of the Cell* (1992), 74 (1), 31-42

Chandra, S.; Smith, D.R.; Morrison, G.H. **Subcellular Imaging by Dynamic SIMS Ion Microscopy by imaging isotopes, the transport of ions, molecules, and therapeutic drugs can be studied in single cells.** *Analytical Chemistry* (2000), 72 (3),104A-114A

Chandra, S. **Challenges of biological sample preparation for SIMS imaging of elements and molecules at subcellular resolution** *Applied Surface Science* (2008), 255 (4), 1273-1284

Clerc, J.; Fourré, C.; Fragu, P. **Sims microscopy: Methodology, problems and perspectives in mapping drugs and nuclear medicine compounds.** *Cell Biology International* (1997), 21 (10), 619-633

Cliff, B.; Lockyer, N.; Jungnickel, H.; Stephens, G.; Vickerman, J.C. **Probing cell chemistry with time-of-flight secondary ion mass spectrometry: Development and exploitation of instrumentation for studies of frozen-hydrated biological material.** *Rapid Communications in Mass Spectrometry* (2003), 17 (19), 2163-2167

Colliver, T. L.; Brummel, C. L.; Michaelleen L. Pacholski, M. L.; Swanek, F. D.; Ewing, A. G.; Winograd, N. **Atomic and Molecular Imaging at the Single-Cell Level with TOF-SIMS.** *Analytical Chemistry* (1997), 69, 2225-2231

Davies, N.; Weibel, D.E.; Blenkinsopp, P.; Lockyer, N.; Hill, R.; Vickerman, J.C. **Development and experimental application of a gold liquid metal ion source.** *Applied surface science* (2003), 203-204, 223-227

Davies, S.G., Kurczy, M.E., Roddy, T.P., Winograd, N., Ewing, A.G. **Secondary ion MS imaging to relatively quantify cholesterol in the membranes of individual cells from differentially treated populations.** *Analytical Chemistry* (2007), 79 (10) 3554-3560

Fletcher, J. S. **Cellular imaging with secondary ion mass spectrometry.** *Analyst* (2009), 134, 2204–2215

Fletcher, J.S.; Lockyer, N.P.; Vaidyanathan, S.; Vickerman, J.C. **TOF-SIMS 3D biomolecular imaging of *Xenopus laevis* oocytes using buckminsterfullerene (C60) primary ions** *Analytical Chemistry* (2007) 79(6) 2199-2206

Fletcher, J.S.; Lockyer, N.P.; Vickerman, J.C. **Developments in molecular SIMS depth profiling and 3D imaging of biological systems using polyatomic primary ions.** *Mass Spectrometry Reviews* (2010)

Fletcher, J.S.; Vickerman, J.C. **A news SIMS paradigm for 2D and 3D molecular imaging of bio-systems**. Analytical and Bioanalytical Chemistry (2010), 396, 85-104

Fletcher, J.S.; Handerson, A.; Jarvis, R.M.; Lockyer, N.P.; Vickerman, J.C.; Goodacre, R. **Rapid discrimination of casual agents of urinary tract infection using ToF-SIMS with chemometrics cluster analysis**. Applied Surface Science (2006) 252 (19), 6869-6874

Fletcher, J.S.; Rabbani, S.; Henderson, A.; Blenkinsopp, P.; Thompson, S.P.; Lockyer N. P.; Vickerman, J.C. **A new dynamic in mass spectral imaging of single biological cells**. Analytical Chemistry, (2008), 80 (23), 9058-9064

Gazi, E.; Dwyer, J.; Lockyer, N.; Gardner, P.; Vickerman, J.C.; Miyan, J.; Hart, C.A.; Brown, M.; Shanks, J.H.; Clarke, N. **The combined application of FTIR microspectroscopy and ToF-SIMS imaging in the study of prostate cancer**. Faraday Discussions (2004), 126, 41-59

Grovenor, C.R.M.; Smart, K.E.; Kilburn, M.R.; Shore, B.; Dilworth, J.R.; Martin, B.; Hawes, C.; Rickaby, R.E.M.; **Specimen preparation for NanoSIMS analysis of biological materials**. Applied Surface Science (2006), 252 (19) 6917-6924

Guerquin-Kern, J.-L.; Wu, T.-D.; Quintana, C.; Croisy, A. **Progress in analytical imaging of the cell by dynamic secondary ion mass spectrometry (SIMS microscopy)**. Biochimica et Biophysica Acta - General Subjects (2005), 1724 (3),228-238

IHC website: [http://www.ichworld.com/\\_protocols/general\\_ICC/fixation.htm](http://www.ichworld.com/_protocols/general_ICC/fixation.htm)  
accessed on 6-08-2010

Jackson, E.R.J.; Vickerman, J.C.; Lockyer, N.P. **A Systematic Evaluation of Cytospinning as a Novel Technique for the preparation of Cells for ToF-SIMS Analysis**. Surface and Interface Analysis submitted

Jones, E.A.; Lockyer, N.P.; Vickerman, J.C. **Depth profiling brain tissue sections with a 40 keV C60+ primary ion beam**. Analytical Chemistry (2008), 80 (6), 15, 2125-2132

Jones, E.A.; Lockyer, N.P.; Vickerman, J.C. **Mass spectral analysis and imaging of tissue by ToF-SIMS—The role of buckminsterfullerene, C<sub>60</sub><sup>+</sup>, primary ions** International Journal of Mass Spectrometry (2007), 260, 146–157

Kollmer, F. **Cluster Primary Ion Bombardment of Organic Materials**. Applied Surface Science (2004), 231-232, 153-158

Kötter, F.; Benninghoven, A. **Secondary ion emission from polymer surfaces under Ar<sup>+</sup>, Xe<sup>+</sup> and SF<sub>5</sub><sup>+</sup> ion bombardment**. Applied Surface Science (1998), 133, 47-57

Kozole, J.; Szakal, C.; Kurczy, M.; **Winograd, N. Model multilayer structures for three-dimensional cell imaging.** Applied Surface Science (2006), 252 (19), 6789-6792

Kurczy, M.E.; Piehowski, P.D.; Parry, S.A.; Jiang, M.; Chen, G.; Ewing, A.G.; Winograd, N. **Which is more important in bioimaging SIMS experiments-The sample preparation or the nature of the projectile?** Applied Surface Science (2008), 255 (4), 1298-1304

Lanekoff, I.; Kurczy, M.E.; Hill, R.; Fletcher, J.S.; Vickerman, J.C.; Winograd, N.; Sjövall, P.; Ewing, A.G.; **Time of flight mass spectrometry imaging of samples fractured in situ with a spring-loaded trap system.** Analytical Chemistry (2010), 82 (15) 6652-6659

Larras-Regard, E.; Mony, M.-C. **Scanning ion images; analysis of pharmaceutical drugs at organelle levels.** International Journal of Mass Spectrometry and Ion Processes (1995), 143 (C), 147-160

Larsen, R. **Decomposition using maximum autocorrelation factors.** Journal of Chemometrics (2002), 16, 427-435

Lechene, C.; Hillion, F.; McMahon, G.; Benson, D.; Kleinfeld, A.M.; Kampf, J.P.; Distel, D.; Luyten, Y.; Bonventre, J.; Hentschel, D.; Park, K.M.; Ito, S.; Schwartz, M.; Benichou, G.; Slodzian, G. **High-resolution quantitative imaging of mammalian and bacterial cells using stable isotope mass spectrometry.** Journal of Biology (2006) 5

Lee, J.L.S.; Gilmore, I.S.; Seah, M.P. **Quantification and methodology issues in multivariate analysis of ToF-SIMS data for mixed organic systems.** Surface Interface Analysis (2008), 40 (1), 1-14

Levi-Setti, R.; Gavrillov, K.L.; Strissel, P.L.; Strick, R. **Ion microprobe imaging of <sup>44</sup>Ca-labeled mammalian chromosomes.** Applied Surface Science (2004), 231-232, 479-484

Liebl, H.J. **Ion microprobe mass analyser.** Journal of Applied Physics (1967), 38(13), 5277-5283

Malm, J.; Giannaras, D.; Riehle, M.O.; Gadegaard, N.; Sjövall, P. **Fixation and drying protocols for the preparation of cell samples for time-of-flight secondary ion mass spectrometry analysis** Analytical Chemistry (2009), 81 (17), 7197-7205

Malm, J.; Giannaras, D.; Riehle, M.O.; Gadegaard, N.; Sjövall, P. **Fixation and drying protocols for the preparation of cell samples for time-of-flight secondary ion mass spectrometry analysis.** Analytical Chemistry (2009), 81 (17) 7197-7205

Malmberg, P.; Kriegeskotte, C.; Arlinghaus, H.F.; Hagenhoff, B.; Holmgren, J.; Nilsson, M.; Nygren, H. **Depth profiling of cells and tissues by using C<sub>60</sub><sup>+</sup> and SF<sub>5</sub><sup>+</sup> as sputter ions.** Applied Surface Science (2008), 255 (4), 926-928

McQuaw, C.M.; Sostarecz, A.G.; Zheng, L.; Ewing, A.G.; Winograd, N. **Investigating lipid interactions and the process of raft formation in cellular membranes using TOF-SIMS.** Applied Surface Science (2006), 252 (19), 6716-6718

McQuaw, C.M.; Sostarecz, A.G.; Zheng, L.; Ewing, A.G.; Winograd, N. **Lateral heterogeneity of dipalmitoylphosphatidylethanolamine - Cholesterol langmuir - Blodgett films investigated with imaging time-of-flight secondary ion mass spectrometry and atomic force microscopy.** Langmuir (2005), 21 (3) 807-813

Morrison, G.H.; Slodzian G. **The ion microscope opens new vistas in many fields of science by its ability to provide spatially resolved mass analysis of solid surfaces,** Analytical Chemistry (1975), 47 (11)

Nielsen, A.A; Conradsena, K; Simpson, J.J. **Multivariate Alteration Detection (MAD) and MAF Postprocessing in Multispectral, Bitemporal Image Data: New Approaches to Change Detection Studies.** Remote Sensing of Environment (1998), 64 (1) 1-19

Nygren, H.; Börner, K.; Malmberg, P.; Tallarek, E.; Hagenhoff, B. **Imaging TOF-SIMS of rat kidney prepared by high-pressure freezing.** Microscopy Research and Technique (2005), 68 (6), 329-334

Nygren, H.; Eriksson, C.; Malmberg, P.; Sahlin, H.; Carlsson, L.; Lausmaa, J.; Sjövall, P. **A cell preparation method allowing subcellular localization of cholesterol and phosphocholine with imaging TOF-SIMS.** Colloids and Surfaces B: Biointerfaces (2003), 30 (1-2), 87-92

Nygren, H.; Hagenhoff, B.; Malmberg, P.; Nilsson, M.; Richter, K. **Bioimaging TOF-SIMS: High resolution 3D imaging of single cells.** Microscopy Research and Technique (2007) 70 (11), 969-974

Nygren, H.; Malmberg, P.; Nilsson, M.; Kriegeskotte, C.; Arlinghaus, H.F. **The cytochemistry of anaplastic thyroid tumour cells and differentiated thyrocytes analysed by TOF-SIMS and depth profiling.** Applied Surface Science (2008), 255 (4), 1285-1288

Ostrowski, S.G.; Van Bell, C.T.; Winograd, N.; Ewing, A.G. **Mass Spectrometric Imaging of Highly Curved Membranes During Tetrahymena Mating.** Science (2004), 305, 71-73

Pacholski, M.L.; Cannon Jr, D.M.; Ewing, A.G.; Winograd, N. **Static time-of-flight secondary ion mass spectrometry imaging of freeze-fractured, frozen-hydrated biological membranes.** *Rapid Communications in Mass Spectrometry* (1998), 12 (18) 1232-1235

Parry, S.; Winograd, N. **High-resolution TOF-SIMS imaging of eukaryotic cells preserved in a trehalose matrix.** *Analytical Chemistry* (2005) 77 (24), 7950-7957

Parry, S.A.; Kurczy, M.E.; Fan, X.; Halleck, M.S.; Schlegel, R.A.; Winograd, N. **Imaging macrophages in trehalose with SIMS.** *Applied Surface Science* (2008), 255 (4), 929-933

Piehowski, P.D.; Kurczy, M.E.; Willingham, D.; Parry, S.; Heien, M.L.; Winograd, N.; Ewing, A.G. **Freeze-etching and vapor matrix deposition for ToF-SIMS imaging of single cells.** *Langmuir* (2008) 24 (15), 7906-7911

Piwovar, A.M.; Fletcher, J.S.; Kordys, J.; Lockyer, N.P.; Winograd, N.; Vickerman, J.C. **Effects of Cryogenic Sample Analysis on Molecular Depth Profiles with TOF-Secondary Ion Mass Spectrometry** *Analytical Chemistry* (2010), published online

Rabbani, S.; Fletcher, J.S.; Lockyer, N.P.; Vickerman, J.C. Exploring subcellular imaging on the buncher-ToF J105 3D chemical imager. *Surface and Interface Analysis* (2010), submitted

Reichenbach, S.E.; Tian, X.; Lindquist, R.; Tao, Q.; Henderson, A.; Vickerman, J.C. **Visualization and analysis of large three-dimensional hyperspectral images.** *Proceedings of SPIE - The International Society for Optical Engineering* (2009), 7341, Article number 734108

Roddy, T.P.; Cannon Jr. D.M.; Ostrowski, S.G.; Ewing, A.G.; Winograd, N. **Proton transfer in time-of-flight secondary ion mass spectrometry studies of frozen-hydrated dipalmitoylphosphatidylcholine.** *Analytical Chemistry* (2003), 75 (16) 4087-4094

Roddy, T.P.; Cannon Jr., D.M.; Meserole, C.A.; Winograd, N.; Ewing, A.G. **Imaging of freeze-fractured cells with in situ fluorescence and time-of-flight secondary ion mass spectrometry.** *Analytical Chemistry* (2002), 74 (16) 4011-4019

Römer, W.; Wu, T.-D.; Duchambon, P.; Amessou, M.; Carrez, D.; Johannes, L.; Guerquin-Kern, J.-L. **Sub-cellular localisation of a <sup>15</sup>N-labelled peptide vector using NanoSIMS imaging.** *Applied Surface Science* (2006), 252 (19), 6925-6930

Rothman, J.E.; Lenard, J. **Membrane asymmetry. The nature of membrane asymmetry provides clues to the puzzle of how membranes are assembled.** *Science* (1977), 195 (4286), 743-753

Sjövall, P.; Lausmaa, J.; Johansson, B. **Mass Spectrometric Imaging of Lipids in Brain Tissue**. *Analytical Chemistry* (2004), 76, 4271-4278

Sjövall, P.; Lausmaa, J.; Nygren, H.; Carlsson, L.; Malmberg, P. **Imaging of Membrane Lipids in Single Cells by Imprint-Imaging Time-of-Flight Secondary Ion Mass Spectrometry**. *Analytical Chemistry* (2003), 75, 3429-3434

Slodzian, G.; Daigne, B.; Girard, F.; Boust, F.; Hillion, F. **Scanning secondary ion analytical microscopy with parallel detection**. *Biology of the Cell* (1992), 74 (1), 43-50

Smith, D.R.; Chandra, S.; Barth, R.F.; Yang, W.; Joel, D.D.; Coderre, J.A. **Quantitative imaging and microlocalization of boron-10 in brain tumors and infiltrating tumor cells by SIMS ion microscopy: Relevance to neutron capture therapy**. *Cancer Research* (2001), 61 (22), 8179-8187

Strissel, P.L.; Strick, R.; Gavrilov, K.L.; Levi-Setti, R. **Specific Mg<sup>2+</sup> binding at human and Indian muntjac chromosomal Giemsa bands**. *Applied Surface Science* (2004), 231-232, 485-489

Thompson, C.E.; Ellis, J.; Fletcher, J.S.; Goodacre, R.; Henderson, A.; Lockyer, N.P.; Vickerman, J.C. **ToF-SIMS studies of Bacillus using multivariate analysis with possible identification and taxonomic applications**. *Applied Surface Science* (2006), 252 (19), 6719-6722

Tortora, G.J.; Grabowski, S.R. *Tortora Grabowski Principles of Anatomy and Physiology* (2000), US: John Wiley

Tyler, B.J.; Rayal, G.; Castner, D.G. **Multivariate analysis strategies for processing ToF-SIMS images of biomaterials**. *Biometrics* (2007) 15, 2412-2423

Vaidyanathan, S.; Fletcher, J.S.; Henderson, A.; Lockyer, N.P.; Vickerman, J.C. **Exploratory analysis of TOF-SIMS data from biological surfaces**. *Applied Surface Science* (2008), 255, (4), 1599-1602

Wagner, M.S.; Castner, D.G. **Characterization of adsorbed protein films by time-of-flight secondary ion mass spectrometry with principal component analysis**. *Langmuir* (2001), 17 (15), 4649-4660

Wagner, M.S.; Castner, D.G. **Simplifying the interpretation of ToF-SIMS spectra and images using careful application of multivariate analysis**. *Applied Surface Science* (2004), 231, 366-376

Wong, S.C.C.; Hill, R.; Blenkinsopp, P.; Lockyer, N.P.; Weibel, D.E.; Vickerman, J.C. **Development of a C<sub>60</sub><sup>+</sup> ion gun for static SIMS and chemical imaging**. *Applied Surface Science* (2003), 203-204, 219-222

Zheng, L.; McQuaw, C.M.; Baker, M.J.; Lockyer, N.P.; Vickerman, J.C.; Ewing, A.G.; Winograd, N. **Investigating lipid-lipid and lipid-protein interactions in model membranes by ToF-SIMS**. *Applied Surface Science* (2008), 255 (4), 1190-1192

## 6 Overall Conclusions and Future Work

Time of flight secondary ion mass spectrometry has progressed in the last century and is now more widely utilized for a range of applications. Advances in the instrumentation, particularly the development of cluster and polyatomic sources have extended the capabilities of ToF-SIMS for the analysis of complex biological samples. It has become a powerful technique to monitor the distribution of native biomolecules and xenobiotics at a very high spatial resolution, <100 nm with high selectivity and without need to label.

Chapter 1 and chapter 2 discuss the current state of ToF-SIMS instrumentation and applications. It was identified that although *high lateral resolution* molecular imaging can be obtained using the highly focused liquid metal ion sources, it results in low secondary ion yields and causes damage to the surface of a sample. Thus, the ion dose of these sources has to be kept at or below the static limit, which limits sensitivity. The SIMS community has been looking into ways for increasing the sensitivity such as using high mass primary ion beams, silver printing, matrix enhanced SIMS and laser post-ionisation. Significant enhancement in the secondary ion yields was observed with the introduction of polyatomic ion beams which also offer the benefit of low sub-surface damage and analysis at high ion dose. However to take full advantage of the polyatomic sources, the current ToF-SIMS instrumentation has to be customized. As a result a new instrument, the Ionoptika **J105 3D Chemical Imager** was designed and built which seeks to address these issues and allows the use of the polyatomic beam in a dc mode. This instrument has been described in some detail in chapter 2.

In chapter 3, the concept of the new instrument is validated. Initially standard organic samples were analysed and secondary ion signals were compared with a conventional ToF-SIMS instrument, the BioToF. A more quantitative comparison can be made by calculating the yields to evaluate the performance of both instruments.

The tandem MS capability of the new instrument was also demonstrated with standard organic samples and a lipid mixture of brain extract. In this project it was only possible to identify two unknown ions from the lipid mixture, but MS/MS of other ions will need to be completed to identify them.

A sensitivity test was also undertaken using a standard organic sample, arginine and it was established that currently the limit of detection on the J105 is  $3 \times 10^{-5}$  M which is equivalent to  $1.807 \times 10^{13}$  molecules of arginine. This study could benefit from examining a range of concentrations between  $3 \times 10^{-5}$  M and  $3 \times 10^{-6}$  M as well as investigating a variety of samples.

In chapter 4 molecular depth profiling using ToF-SIMS was reviewed. It was shown that the dual beam approach in which a highly focused liquid metal beam is used for analysis and a polyatomic ion beam for sputtering is frequently utilized when performing *high lateral resolution* 3D imaging. However, this method results in a loss of valuable sample during etch cycles. It has been shown that the polyatomic C<sub>60</sub> beam can be used for molecular depth profiling in dc mode on the J105. This study could be developed further by depth profiling multilayer systems to identify the depth resolution. Furthermore, the experiments could be performed at different energies and temperature to determine how these parameters affect the secondary ion yields, topographic roughness and depth resolution.

In chapter 5, the ability of ToF-SIMS to map the distribution of biological components in tissues and cells has been evaluated. It was identified that issues such as low duty cycle and imaging at high spatial and mass resolution at the same time are limiting this technique from reaching its full potential. The dual beam approach allows analysis to be completed in reasonable time with high spatial resolution but results in much of the material from a sample being wasted during etch cycles. These problems can be addressed by using the polyatomic beam in a dc mode on the new instrument. A standard cell line (HeLa) was used to show clearly the capability of the polyatomic beam,  $C_{60}$  to produce mass spectrometric images of single cells. The data shows that it is possible to identify and differentiate between lipid membrane and nucleus of single cells in a single 2D image and as a function of depth via 3D imaging.

Three different cell preparation methods, formaldehyde fixing, freeze-dried and freeze-fractured frozen hydrated were investigated. The data suggests that the freeze-fractured frozen hydrated method is beneficial as compared to the other two. It is intended that the systematic investigation of different sample preparations will be extended to other cell lines to confirm these findings. Also multivariate analysis can be performed on data generated from different sample preparations to identify the peaks that are responsible for different observations. Furthermore, to determine if the cells have been fractured, fluorescent reagents can be used to image sub-cellular structures using complementary imaging methods.

It has been demonstrated through the work on HeLa cells that it is possible to examine the evolution of biochemistry in the cells with depth using 3D imaging. This

presents the opportunity to begin to localise the distribution of drugs in the cells thereby investigating whether a drug has been transported to its target within the sample.

The amount and the size of the data generated on the J105 are very high and new data processing tools are required for the management, manipulation and interpretation of the information. This includes tools such as multivariate analysis, data compression and new software for visualisation of 3D data set.

In conclusion, imaging of cells and tissues has become the centre point of research in the SIMS community. The work presented in this thesis shows the immense potential of ToF-SIMS using the new instrumental configuration for the analysis of tissues and single cells. However, issues such as the matrix effect, optimum sample preparation and low ionisation still need to be addressed to progress forward and aid research in wider biological problems.